Sidereal Filtering for Multi-GNSS Precise Point Positioning and Deformation Monitoring

Philippa Catherine Cowles

Thesis submitted for the Degree of Doctor of Philosophy

School of Civil Engineering and Geosciences
Newcastle University
June 2017

Abstract

For earthquake and tsunami early-warning, it is crucial that displacements resulting from earthquakes are recorded with speed and accuracy. Traditional methods based on seismometer data often suffer from errors during integration which results in the maximum displacement not being accurately recorded. In contrast, Global Navigation Satellite Systems (GNSS) can measure permanent static displacement directly; however it too is subject to errors, the main error of which is multipath. Multipath can lead to errors in the measurement of small displacements or mask the displacement completely.

Multipath is dependent on the geometry of the GNSS constellation orbits and the antenna's surrounds. GPS satellites have an orbital period of half a sidereal day with a near-sidereal repeating ground track. Similarly, the GLONASS constellation geometry repeats about once every eight sidereal days thus the satellite-reflector geometry will repeat with these same periods. By accurately determining the repeat periods it is possible to remove the multipath error by analysing data from the previous repeat periods. This method is known as sidereal filtering and can be used to improve the precision of GNSS coordinate time series and hence improve displacement measurements.

This thesis looks to find the optimum geometry repeat period for the GLONASS constellation, which was found to be 689248 s and combine GPS and GLONASS for observation domain near-sidereal filtering. GLONASS-only filtering improves GLONASS coordinate solution standard deviations, on average, by 22.3%, 18.1% and 17.6% in the East, North and Up, whereas GPS and GLONASS combined filtering improves GPS and GLONASS standard deviations by 21.2%, 23.4% and 25.1%. The average maximum stability improvement, in terms of Allan deviation for all components is approximately 21.0% for GLONASS-only and 29.0% for combined filtering. Combined filtering produces more stable coordinate time series for averaging intervals over a few hundred seconds. It also reduces coordinate time series standard deviations and thus aids the measurement of small coordinate displacements and reduces the number of false alarms by half during displacement detection. Filtering improves the accuracy and precision of displacement estimates on average by about 2 mm, in terms of the difference between filtered and unfiltered RMSD and mean displacement values.

Acknowledgements

I would like to thank ESA and CODE for their orbit and clock products and Wuhan University for the PANDA software. Dr Ian Martin is acknowledged for his advice, help and implementation of sidereal filtering into the PANDA software.

NERC BIGF is acknowledged for providing 1 Hz GPS and GLONASS data from the OS Network. I would like to thank Martin Robertson for his technical support and guidance during data collection. This project was aided by financial support from a UK Natural Environment Research Council (NERC) studentship.

Huge thanks goes to my supervisors, Professor Peter Clarke and Dr Nigel Penna for their continuous guidance, support and feedback on my research methods.

Finally, thanks to my family, friends and colleagues for their support throughout the PhD process.

Table of Contents

List of Figures

List of Tables

List of Abbreviation

ARTA	Aspect Repeat Time Adjustment
CDMA	Code Division Multiple Access
CMT	Centroid Moment Tensor
CODE	Center for Orbit Determination
ECEF	Earth-Centred, Earth-Fixed
ESA	European Space Agency
FCB	Fractional Cycle Biases
FDMA	Frequency Division Multiple Access
FOC	Full Operational Capability
GDOP	Geometric Dilution Of Precision
GEO	Geostationary Orbit
GLONASS	Globalnaya Navigatsionnaya Sputnikovaya Sistema
GMF	Global Mapping Function
GNSS	Global Navigation Satellite Systems
GPS	Global Positioning System
GR	GPS and GLONASS
IAC	Information Analytical Center
IDS	International DORIS Service
IGS	International GNSS Service
IGSO	Inclined Geosynchronous Orbit
IRC	Integer-Recovery Clocks
IRNSS	Indian Regional Navigation Satellite System
ITRF	International Terrestrial References Frame
IVS	International VLBI Service
JMA	Japan Meteorology Agency
JPL	Jet Propulsion Laboratory
MAC	Master Axillary Concept
MAD	Median Absolute Deviation
MEDLL	Multipath Estimating Delay Lock Loop
MEO	Medium Earth Orbit

NEIC	National Earthquake Information Centre
NTRIP	Network of Transport of RTCM by Internet Protocol
PDOP	Position Dilution Of Precision
PPP	Precise Point Positioning
PRN	Pseudo-Random Noise
PTWC	Pacific Tsunami Warning Centre
QZO	Quasi-Zenith Orbit
QZSS	Quasi-Zenith Satellite System
RMS	Root Mean Square
RMSD	Root Mean Square Difference
RTCM	Radio Technical Commission for Maritime Services
RTK	Real-Time Kinematic
RTS	Real-Time Service
SNR	Signal to Noise Ratio
SSP	Single Point Positioning
SSR	State Space Representation
TEC	Total Electron Content
UPDS	Uncalibrated Phase Delays
VMF1	Vienna Mapping Function 1
VRS	Virtual Reference System

Chapter 1. Introduction

1.1 Chapter Overview

This chapter begins with describing the main driving force behind this thesis: to improve the accuracy and speed of displacement measurements from earthquakes, to aid earthquake and tsunami early-warning, using Global Navigation Satellite Systems (GNSS), as opposed to more traditional methods based on accelerometer and seismometer data. The limitations of current early-warning methods are given in section 1.2.1 and the requirements for GNSS enabled methods given in section 1.2.2.

1.2 Motivation

Over the past 10 years there have been a large number of high magnitude earthquakes that have occurred, as seen in Table 1.1. Considering the fact that tsunamis typically occur when an earthquake is larger than 6.3 in moment magnitude, shallow in depth and in close proximity to the ocean there are many earthquakes annually that could potentially trigger a tsunami event (Roger and Gunnell, 2012). When tsunamis do occur they cause destruction on a national scale, statistics of which can be seen in Table 1.2. Take the 2011 M 9.0 Tohoku-oki earthquake in Japan for example: it ruptured a fault area of approximately 500 km by 200 km causing fault displacement at the Japan Trench of up 50 m, sea-floor uplift of nearly 9 m and sea-floor subsidence of up to 2 m. This resulted in a tsunami with peak height of 40.5 m and run-up of 10 km inland, 24,000 people being reported as dead or missing, a nuclear disaster and an estimated ¥25 trillion (£18.6 trillion) worth of damage (Mimura *et al.*, 2011; Simons *et al.*, 2011).

Even though Japan does have a tsunami warning system in place the people in Tokyo only received a warning one minute before the earthquake was felt in Tokyo and the tsunami in coastal areas propagated inland in just 8 minutes. The Japan Meteorological Agency (JMA) originally estimated the earthquake at m_b7.2 just 30 seconds after the event. However it took 20 minutes for longer period seismic waves to propagate to further afield stations for the true earthquake size to be realised (M_w 9.0), using the W-phase method (Melgar *et al.*, 2013). The W-phase is a very long period wave (100-1000 s) which arrives in between the P and S-waves, described in more detail in section 1.2.1.

The 2004 M 9.2 Sumatra-Andaman earthquake which triggered an ocean wide tsunami, was also initially underestimated, and resulted in over 250,000 deaths (Sobolev *et al.*, 2007). The tsunami waves swept the Indian Ocean at speeds of 700 km/h and inundated the coast of Indonesia in under 30 minutes and the coast of Sri Lanka and Thailand in just 2 hours. The tsunami caused maximum run-up heights in these areas of 10.9 m, 20.0 m and 48.9 m respectively (Choi *et al.*, 2006). The initial earthquake size estimate, 11 minutes after rupture was M_w 8.0; it took a further 50 minutes for surface wave data to arrive which increased the estimate to M_w 8.5 which is powerful enough to cause an ocean-wide tsunami (Blewitt *et al.*, 2006). It was not until days later that the actual size of the earthquake was fully realised. If the full tsunami potential of the earthquake had been realised sooner, the lives of many people in neighbouring coastal areas, such as Indonesia could have been saved.

As demonstrated there is a need for a rapid and more reliable early-warning system to help with future disaster mitigation and relief. Melgar *et al.* (2013) demonstrate how the Global Positioning System (GPS) could be used to enhance early-warning by supplementing seismic data with GPS displacements reducing accurate magnitude determination time to 2 minutes.

Table 1.1: Earthquake Statistics (USGS, 2016)

Magnitude	Total Number of Earthquakes between 2005-2015
8.0+	16
7.0-7.9	161
6.0-6.9	1,608
5.0-5.9	19,475

Table 1.2: Tsunami Statistics from 1995 to 2015 (Centre for Research on the Epidemiology of Disasters, 2016).

Event	Number of Deaths	Number of People Affected
22 Other Events	1,695	695,747
1998 Papua New Guinea	2,182	9,867
2004 Sumatra	226,402	2,426,783
2011 Tohoku-oki	19,846	368,820

1.2.1 Current Warning System Limitations

Before the use of GNSS, earthquake and tsunami warning systems relied on seismometer data. A seismometer's response to ground acceleration is dependent on the amplitude and time period of the incoming elastic waves produced during the energy release from an earthquake. Due to this, seismometers are designed to record a specific frequency range. The principle of measuring the relative displacement of the mass in a passive seismometer is only used in short-period seismometers. At low frequencies it becomes harder to maintain an inertial reference of a seismometer as the mass tends to move with the base, resulting in the ground motion appearing smaller. Therefore broadband seismometers, which are commonly used for early-warning, use a force balancing mechanism in order to keep the mass stationary. This is normally in the form of an electrically generated compensating force from a feedback system that acts as a damper to reduce nonlinearity and increase sensitivity. The feedback force applied is proportional to the ground acceleration experienced, thus allowing ground motion displacement to be calculated through integration. Hence the dynamic range of the seismometer is imposed by the dynamic range of the electronic feedback system.

However, even with a feedback mechanism, seismometers can saturate (clip), due to delays in the electronics of the system and high frequency interference developing from the resonance effects of the system. This results in peak displacement remaining constant once the frequencies exceed a certain size. Hence, the maximum displacements will not be accurately recorded and the signal becomes distorted during the time interval where clipping happens (Wielandt, 2012).

To add to this there are numerous ways to compute the size of an earthquake. The concept of a logarithmic magnitude scale was introduced by C.F Richter in 1935, based on maximum amplitude (in microns) recorded by a 12 Hz Wood-Anderson seismometer. This magnitude scale is referred to as a local Magnitude scale, (M_L) for the Southern California region only. Seismometers tend to saturate for large earthquakes above M_L 7.0, hence this magnitude scale has limited use and is unsuitable for large magnitude earthquakes (Crowell *et al.*, 2013). Since then, the measurements of magnitude have expanded worldwide to earthquakes of all manner of depths, distances and to both surface and body waves (Aki and Richards, 2002). For example, short-period body wave magnitude (m_b), is determined at periods of 1-5 s from teleseismic P-waves, whereas the surface wave magnitude (M_s), is determined at a period of 20 s from teleseismic surface waves. The scales take into account ground motion amplitude, wave period, angular distance and focal depth of the earthquake as outlined by Geller (1976). Hence, different magnitude scales are used to measure the seismic energy released at different time periods.

A limitation of the magnitude scales mentioned is that they saturate once earthquakes exceed a certain size; m_b > 6.2 and M_s > 8.3 or when the spatial extent of the rupture exceeds 100 km in length (Geller, 1976; Kanamori, 1977). Saturation of the magnitude scale occurs because the seismometers become non-linear and leads to an underestimation of the earthquake magnitude. Saturation can also be caused by using a time window that is smaller than the duration of the rupture during calculation and/or the length scale of the rupture being bigger than the wavelength of the data causing the amplitude of the wave to be insensitive to the rupture extent. To estimate the size of larger earthquakes, magnitude scales that use longer period waves are thus required (Bormann and Saul, 2009). The quick and accurate magnitude estimation and slip distribution for large undersea earthquakes is especially vital for reliable tsunami early-warning, due to seafloor displacement being directly related to the tsunami size (McCloskey *et al.*, 2007).

The Moment magnitude (M_w) is obtained from the scalar seismic moment (M_o), and therefore, unlike the empirical scales previously discussed, expresses the earthquake size in relation to physical earthquake source parameters as given overleaf (Hanks and Kanamori, 1979):

(1.1)

$$M_w = \frac{2}{3}\log_{10} M_o - 10.7$$

where the total inelastic energy (Nm), required for rupturing and ground displacement from an earthquake can be defined as the Seismic Moment given by:

(1.2)

$$M_o = \mu A u$$

where μ is shear modulus (Pa), A the area of the fault (m²) and u the average permanent displacement (m) on the fault (Fowler, 2004). The constant value in equation (1.1) was chosen to be consistent with the magnitude values produced by earlier scales, such as the Richter scale. The required parameters are determined from waveform analysis of multiple seismograms created by an earthquake. The permanent displacement of the ground caused by an earthquake is also referred to as coseismic displacement. Note this is different from the transient displacement caused by the passage of seismic waves as depicted in Figure 1.1.

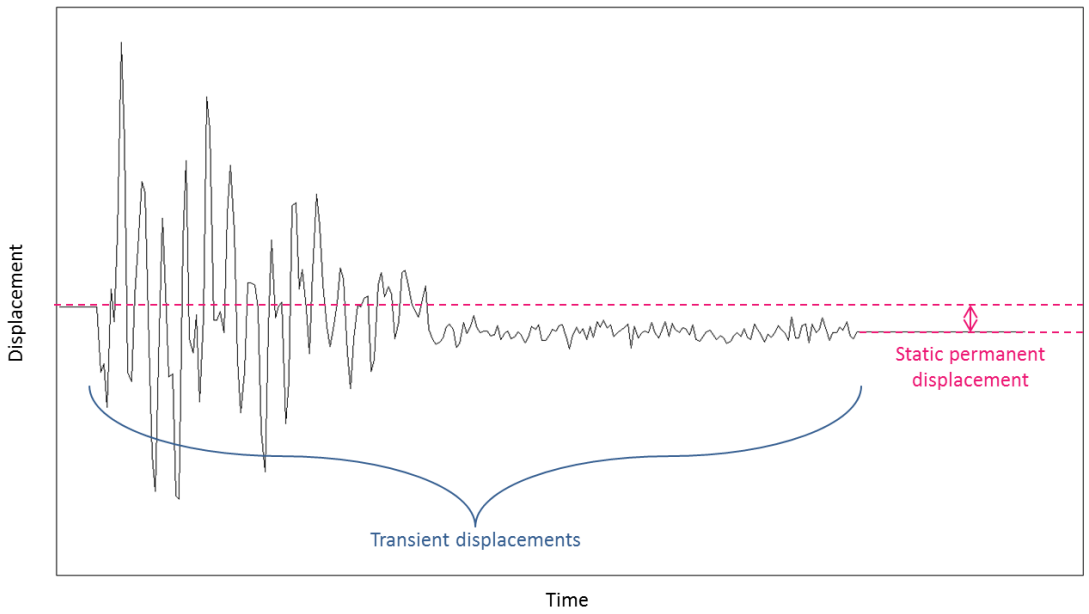

Figure 1.1: Illustration of static and transient earth surface displacement, applicable to any East, North or Up component from a seismogram.

The moment magnitude can be seen as a more reliable measure of earthquake size and does not saturate towards the top of the scale compared with other forms of magnitude, as fault geometry and observer azimuth are included in the computation and moment does not have an inherent upper bound. Also relations to the tectonic effects of an earthquake, such as average permanent displacement, make it more suitable for tsunami potential assessment.

Earthquake deformation which causes strain over a region to be localised into a fault can be described in the form of fault geometry and used as an input for tsunami generation. Faults are normally approximated as a plane whose orientation is described by its strike, dip and rake. As seen in Figure 1.2, the strike is the angle at the intersection of the fault plane and a horizontal plane, whereas the dip describes the inclination of the plane above or below the horizontal measured perpendicular to the strike. The rake on the other hand measures the slip direction on the fault plane. As much of the energy from an earthquake is released as teleseismic waves the Earth can be seen as having elastic behaviour over short time periods, which allows static deformation to be modelled in terms of static-elastic dislocation theory. Hence, earthquake induced sea-floor displacements can be calculated using the Okada Static dislocation point-source solution for multiple points across the fault which requires the following inputs: fault plane location, depth, strike, dip, slip, length, width, seismic moment and rigidity (Okada, 1985).

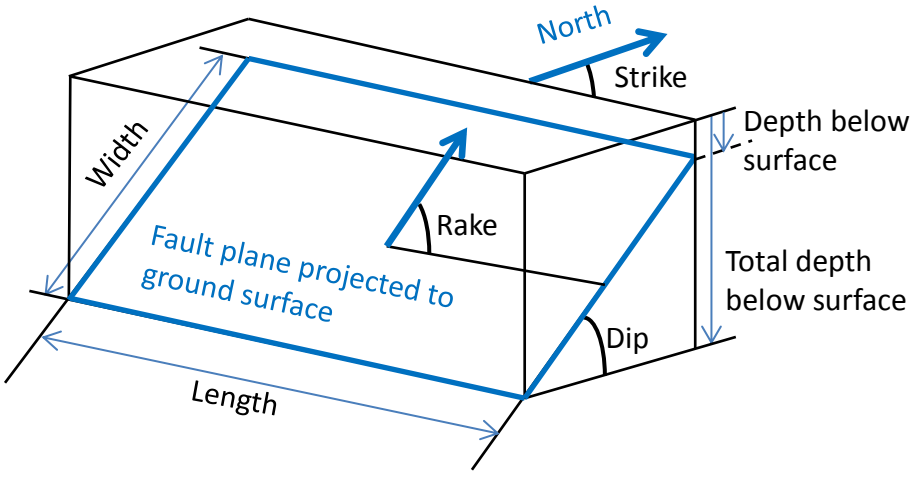

Figure 1.2: Earthquake Fault Geometry

Tsunami wave height calculations are based on the equations of motion and continuity requiring sea-floor displacement as an input, which can be gained with reduced computational power and time from GNSS direct displacement measurements during seismic moment computation, as opposed to inverted data from seismic sources. Due to the

assumptions made during seismic moment computation, however, such as using a single point source model, a minimum seismic wave period of 200 s, and an average rupture velocity, the wavelength used can be much shorter than the total rupture length for large earthquakes. This can still result in the underestimation of moment magnitude in extreme cases which can have devastating consequences (Bormann and Saul, 2009). Due to the use of a logarithmic scale an underestimation of one unit of magnitude is equivalent to an increase of 10 times the amplitude recorded by a seismograph and about 30 times the energy.

In addition to this, moment magnitude takes a few tens of minutes to calculate as it relies on long-period surface waves reaching distant seismometer sites. For early-warning where time is of the essence, the moment magnitude from P-waves (M_{wp}) can be calculated quickly as an alternative, at a period of 10-200 s, just after the arrival of the first P-waves. The Pacific Tsunami Warning Centre (PTWC), for example, is able to derive M_{wp} estimates within 2-3 minutes for local events and in under 10 minutes for teleseismic events (Hirshorn *et al.*, 2013). The P-wave seismic moment is calculated from either the first peak or first peak and trough (p_p, p_t) of the integrated vertical component of a seismogram, given by:

$$M_o = Max(|p_p|, |p_p - p_t|)\frac{4\pi\rho\alpha^3 r}{F^P} \tag{1.3}$$

where ρ and α are the density and velocity along the propagation path of the P-wave, r is the distance from the earthquake's epicentre and F^P the radiation pattern. When compared to high accuracy, but slower M_w estimates, Whitmore *et al.* (2002) found that M_{wp} tends to overestimate the magnitude of earthquakes less than 6.8, but underestimate earthquakes with magnitudes over 6.8. Hence the addition of a linear correction to the P-wave moment magnitude formula:

$$Mwp_c = (((logM_0 - 9.1)/1.5) - 1.03)/0.843 \tag{1.4}$$

Although faster to compute, this technique still underestimates the magnitude for earthquakes larger than 8.0. Therefore for large earthquakes, seismic moment estimation can benefit from using GNSS as it does not have this problem of saturation. There is also no

need to wait for longer period waves to propagate to further afield sites when using GNSS as GNSS can directly measure static permanent displacements rather than relying on integrated acceleration and velocity data, as outlined fully in section 2.1.

1.2.2 GNSS Early-Warning System Requirements

Recent advancements in GNSS hardware and software have made 1 Hz and higher GNSS data collection and near-real-time processing now routinely possible; hence the use of GNSS for rapid and reliable earthquake monitoring and tsunami early-warning systems such as those operated by JMA and NASA Jet Propulsion Laboratory (JPL).

Blewitt *et al.* (2006) demonstrated in a simulated real-time scenario, that a magnitude estimate of M_w 9.0 for the 2004 Sumatra earthquake could have been obtained using 30 s GPS data from 38 sites, within 7,500 km of the earthquake epicentre within just 15 minutes of earthquake rupturing. They were able to estimate static displacement with a ~10 mm accuracy to determine the magnitude, mechanism and earthquake rupture extent.

Melgar *et al.* (2012) demonstrated for the 2011 Tohoku-Oki event, how 1 Hz GPS displacement estimates can aid accurate inversion of the moment tensor much quicker than existing seismic methods alone. By replaying recorded GPS data of the event in a simulated real-time mode, they obtained a M_w value of 8.2 just 170 seconds after the initial rupture of the earthquake. In comparison it took the National Earthquake Information Centre (NEIC) 90 minutes to achieve a final Centroid Moment Tensor solution of M_w 8.3, from seismic only data. Also, for the Tohoku-Oki earthquake, Wright et al. (2012) showed how 1 Hz GPS data from 414 sites, post-processed in real-time PPP mode can give an accurate earthquake moment in under 2 minutes by using static displacements, as outlined fully in section 2.1.

For early-warning systems a high accuracy short-term GNSS station position computed from carrier-phase measurements at a continuous static receiver is required in order to prevent the occurrence of false alarms, the period of a few tens to hundred seconds is of most interest for a rapid solution. The ability of GNSS to measure accurate ground displacements is improved by using multiple satellite constellations to increase sky coverage but is limited by several GNSS errors, the most problematic source of error being multipath interference. Multipath can mask transient displacement signals and introduce phase measurement errors at frequencies and amplitudes similar to seismic waves produced by earthquakes and

tsunamis, which thus results in earthquake and tsunami magnitude being initially underestimated. Multipath can also overestimate earthquake size which gives rise to false alarms leading to reduced confidence in the system. An underestimation of earthquake and resulting tsunami size can lead to delays and inefficient evacuation warnings being given which could mean the difference between life or death.

1.3 Aims and Objectives

Multipath is still one of the main limiting errors of GNSS accuracy. Research to date has focused mainly on the mitigation of GPS multipath. This project looks to mitigate multipath in Globalnaya Navigazionnaya Sputnikovaya Sistema (GLONASS) and a combined GPS and GLONASS solution based on the orbital repeat geometry of both constellations with applications for earthquake and tsunami early-warning. A combined solution is desirable as it offers a more robust solution for short-term positioning. To achieve the project's aims, the objectives of this study are as follows:

- ~ Validate GPS satellite multipath geometry repeat periods and sidereal filtering in the observation domain using the Precise Point Positioning (PPP), approach.
- ~ Investigate GLONASS satellite multipath geometry repeat periods using correlation methodology.
- ~ Combine GPS and GLONASS filters for use in PPP.
- ~ Investigate filter use based on satellite elevation angle thresholds.
- ~ Explore the effect of multipath mitigation for use in earthquake and tsunami early-warning using a case study simulation.

1.4 Chapter Outline

This thesis is organised as follows:

Chapter 1 gives a brief introduction to the nature of this work, the motivation behind it and outlines the main aims and objectives.

Chapter 2 presents an introduction to GNSS and reviews the GNSS positioning techniques that are currently available. The major error sources limiting GNSS for high accuracy applications, such as early-warning systems, are also outlined.

Chapter 3 reviews previous research and multipath mitigation techniques for GPS. Methodology for determining optimum multipath orbital geometry repeat for GPS and filter creation is outlined and validated against previous GPS sidereal filtering studies.

Chapter 4 investigates the optimum multipath orbital geometry repeat for GLONASS and tests the successfulness of GLONASS multipath filtering. The considerations and results of combining GPS and GLONASS multipath filters are also assessed. It also details investigations of filter optimisation by using lag correlation strength and satellite elevation thresholds.

Chapter 5 evaluates the use of multipath mitigation for earthquake and tsunami early-warning using an antenna on a moving platform as a case study. It investigates the use of GNSS to measure small static displacement measurements, such as those likely to occur from an earthquake.

Chapter 6 summarises the research presented and details conclusions drawn. Recommendations for future work building on the results provided by this project are also included.

Chapter 2. GNSS, Processing Strategies and Error Sources

2.1 Use of GNSS in Seismology

Earthquake magnitude has traditionally been computed from seismometer data in the immediate aftermath of an earthquake. Improvements in satellite coverage from the introduction of GLONASS, receiver technology and data storage capabilities, has made it possible for near-real-time GNSS observations to be made with sampling rates up to 50 Hz with sub-decimetre accuracy, which is suitable for seismic studies (Genrich and Bock, 2006). There are a number of studies that have successfully used GNSS for seismic research, using a variety of different positioning techniques. The two most commonly used positioning techniques are relative positioning and PPP which are described later in section 2.3. As shown by Elósegui *et al.* (2006), 1 Hz GPS relative displacements computed from a static antenna and an antenna on a moving platform, on average, agree within 2.5 mm of displacements simulated by a shaking platform, with <5% having a difference of over 5 mm. Using the instantaneous positioning method over three short baselines with a common reference station, Bock *et al.* (2004) observed surface waves from the 2002 M_w 7.9 Denali earthquake at 3900 km away from the epicentre of the earthquake using 1 Hz GPS data. They similarly found that relative horizontal displacements agree with integrated velocities recorded by nearby broadband seismometers, with a Root Mean Square (RMS) difference of 2 to 3 mm at periods longer than 1 s. However, the reference station used was also affected by the earthquake and hence displacements at the other sites were biased by this ignored movement.

A GNSS receiver is able to directly measure ground displacements, whereas accelerometers are more useful at recording strong ground shaking but accumulate errors over time, which can introduce biases after double integration to displacements. It has been demonstrated that errors associated with the double integration of the noise inherent in accelerometers, from instabilities in sampling rates, for example, increase with the square of the integration time and vary with the system's sampling frequency (lower sampling frequencies suffer greater from numerical integration than high sampling rate), as described in Thong *et al.* (2002); Stiros (2008). Broadband seismometers on the other hand are more sensitive to ground motion but may become saturated during large earthquakes, causing the instrument

to be unable to record the full amplitude of the earthquake signal. GNSS does not suffer from this effect, nor is it greatly affected by tilt offsets which can introduce horizontal acceleration biases into seismometer readings due to a change in gravity surrounding the instrument. The effect of tilt can be reduced in seismometers by applying a high-pass filter, as described by Allen and Ziv (2011). However this can remove genuine static permanent displacement which can lead to erroneous earthquake and tsunami magnitude estimates being made.

Blewitt *et al.* (2009) demonstrated using corner frequencies (the frequency at the intersection between low and high frequency trends in the amplitude of radiated waves), how seismometer magnitude scales saturate for large earthquakes as the corner frequencies move to the lower end of the frequency spectrum which are below those used for M_s and m_b magnitude scales. This is due to larger earthquakes' sources taking more time to occur and causing destructive interference between separate source parameters at frequencies larger than the corner frequency of the source. On the other hand, GNSS can measure the static permanent displacement of a GNSS receiver which can be seen as a zero frequency wave, allowing the actual strength of the earthquake to be computed without saturation in agreement with long-period seismic source information, hence demonstrating the suitability of using GNSS for seismic studies (Wang *et al.*, 2007).

Blewitt *et al.* (2006) showed for the 2004 M_w 9.2 Sumatra earthquake, how relative positioning from 38 GPS stations up to 7500 km from the epicentre, with a sampling rate of 30s, could be used to estimate static co-seismic displacements averaged over a 15 minutes, with a ~10 mm accuracy, in a simulated real-time scenario. They were then able to use these displacements to accurately determine the magnitude, mechanism, and spatial extent of the earthquake rupture from just the first 15 minutes of GPS data following the earthquake.

More recently, for the 2011 M_w 9.0 Tohoku-Oki earthquake, Wright *et al.* (2012) showed how 1 Hz GPS data from 414 sites, post-processed in real-time PPP mode can give an accurate earthquake moment in under 2 minutes by also using static co-seismic displacements. The earthquake moment was able to be estimated quickly by using an evolving slip model that treats the displacements derived at each epoch as if they were the final, static displacement, removing the need to wait for the earthquake to fully rupture. For the smaller 2010 M_w 7.2 El Mayor-Cucapah earthquake, GPS was able to compute, in under

a minute, a comparable magnitude of M_w 7.0 for the much smaller rupture zone, demonstrating that the period of interest for GNSS early-warning applications is the first tens to hundred seconds (Allen and Ziv, 2011). PPP can provide centimetre to decimetre accuracy without the need of a nearby reference station, as is the need for relative positioning. In relative positioning one station acts as a reference and is tightly constrained to known coordinates and the relative displacement of each station is computed with respect to the reference. Biases often propagate into relative displacement measurements due to the reference station experiencing seismic motion during large earthquakes. PPP is hence often preferred as it does not suffer from this effect, as explained fully in section 2.6.

These studies demonstrate the ability of a GPS only solution to quickly and accurately determine the magnitude of seismic events using static permanent displacements varying from a few centimetres to a few metres in size. However, GNSS is still less receptive to small ground motion, when compared to seismometers as GNSS can only detect displacement of a few centimetres. In order to prevent false alarms from noisy GPS data, Wright *et al.* (2012) suggested waiting until at least one GPS site experiences a displacement of over 8 cm before sending out a warning, which is sufficient for earthquakes over magnitude 7.0.

A number of studies have also outlined the feasibility of using high-rate GPS to reconstruct seismic waves caused by earthquakes, such as for the 2008 M_w 8.0 Wenchuan earthquake (Shi *et al.*, 2010). For the 2011 M_w 9.0 Tohoku-Oki, Psimoulis *et al.* (2015) showed how 1 Hz PPP GPS data was able to reconstruct seismic displacement waveforms to within 1-2 cm of closely spaced strong-motion sensors, for stations further than 400 km away from the earthquake epicentre. Other studies combine high-rate GPS with strong motion seismographs and recommend filtering and smoothing techniques to improve the accuracy of displacements recorded by 1 Hz GPS receivers (Davis and Smalley, 2009; Bock *et al.*, 2011). Davis and Smalley (2009) also showed how 1 Hz GPS data from kinematic relative positioning can be used to measure surface wave dispersion curves from the 2004 M_w 9.2 Sumatra earthquake with results comparable to those from broadband seismometers.

More notably, high-rate GPS derived displacements have been used for earthquake source parameters and fault slip distribution inversions as described fully in section 5.3. Allen and Ziv (2011) used on-the-fly 1 Hz relative displacements to explore the use of high-rate GPS displacement data for the 2010 M_w 7.2 El Mayor-Cucapah earthquake. They found that most

collated seismic instruments (broadband velocity channels) clipped due to the arrival of S-waves. The GPS antennas at the same location however were unaffected. In comparison with double integrated accelerometer data, the horizontal components of the GPS waveforms showed a great degree of similarity, with aligned phase and comparable amplitudes. Using a short-term average/long-term average-type algorithm, they were able to extract static offsets shortly after the S-wave arrival and compute the magnitude of the earthquake. Their algorithm was based on a short-term average window of 2 s and a long-term average window of 100 s, where the short-term average needed to be 10 times greater than the long-term average to signify an earthquake had been triggered. This was done using a static slip inversion scheme requiring a priori knowledge of the fault plane geometry. The first seismic P-wave magnitude estimate was 5.9, 13 s after the earthquake, whereas the first GPS magnitude estimate was 6.9, 36 s after the earthquake. Hence, they showed how earthquake early-warning becomes more reliable with the contribution of GPS-based magnitude estimates. This is particularly notable for larger earthquakes such as the 2011 M_w 9.0 Tohoku-oki event, where the rapid P-wave-based magnitude method faces greater limitations.

Melgar *et al.* (2012) demonstrated also how 1 Hz GPS displacements can be used to accurately invert for the moment tensor much quicker than existing seismic methods for the 2011 Tohoku-oki event. The National Earthquake Information Centre (NEIC) took 90 minutes to achieve a final Centroid Moment Tensor (CMT) solution of M_w 8.3. The centroid in this method refers to the centre of the earthquake moment distribution in time and space, defined by four parameters (centroid latitude, longitude, depth, and centroid time), in addition to six moment-tensor elements (linear vector dipoles and force couples with moment) which provides a point-source CMT model of an earthquake (Ekström *et al.*, 2012). Replaying recorded GPS data of the event in a simulated real-time mode, Melgar *et al.* (2012) obtained a M_w value of 8.2 just 170 seconds after the initial rupture of the earthquake. The delay from using seismic data alone is due to having to wait for very long W-phase waves to reach further afield stations before a robust seismic estimate of magnitude can be computed. As static permanent displacement is essentially a zero-frequency wave, GPS data can provide improved resolution at these lower frequencies in comparison to seismic data. Melgar *et al.* (2012) used P-wave data to compute origin time and hypocentre of the earthquake, the CMT solution is then computed using coseismic

displacement measurements extracted from the seismic waveforms at each station. This information along with a Green's functions mathematically describing the layered Earth is used to determine the centroid, as outlined fully in the study. Seismic data is often unstable at stations in close proximity to the earthquake, due to the reasons mentioned earlier in section 1.2; hence these measurements are supplemented by GPS data which offers greater robustness, allowing more accurate magnitude estimates to be computed in a shorter amount of time.

In addition to using the CMT solution which requires no prior knowledge of a region, Crowell *et al.* (2012) also investigated the benefit of using predefined fault planes for earthquake parameter inversions, in regions with known, well-defined faulting. They found that both methods are capable of rapidly and reliably modelling both the 2003 M_w 8.3 Tokachi-oki and the 2010 M_w 7.2 El Mayor-Cucapah earthquake in under 2 minutes, thus demonstrating the feasibility of using GPS to obtain accurate earthquake solutions within the first minutes of rupture.

Smalley (2009) indicated the importance of having a GPS sample rate high enough to capture the complete temporal history of Earth surface displacements, especially when stations are close to the earthquake epicentre. To ensure aliasing does not happen, most applications oversample the data, digitally low-pass filter the oversampled time series, and then decimate the time series to the desired lower sampling rate. Genrich and Bock (2006) showed how sub 1 mm relative displacement time series precision is possible at 1 Hz, by using this method with data originally sampled at 50 Hz. Sampling at rates higher than required however, increases the cost of data transmission, processing and storage. It can also cause latency issues for real-time applications, such as in earthquake early-warning.

Smalley (2009) demonstrated that 1 Hz GPS recordings of displacements from sites less than 10 km from the epicentre of small magnitude 6 earthquakes are aliased, and affect the reliability of earthquake source parameters from GPS data inversions. At stations over 10 km away from the epicentre, aliasing does not occur at 1 Hz sampling rates, as the Earth attenuates the signal by naturally applying an anti-alias low-pass filter. Hence 1 Hz GPS data is reliable for earthquake studies provided that sites are over a certain distance away from the epicentre; which is largely dependent on earthquake size as outlined fully in Smalley

(2009). For sites closer to the epicentre, there is a trade-off between using higher rates but at a higher economic and logistical expense.

All the studies mentioned so far only use GPS which can suffer from poor satellite geometry due to a limited number of satellites in the constellation. The geometry of the satellite constellation is often quantified using the Geometric Dilution Of Precision (GDOP) or Position Dilution Of Precision (PDOP). GDOP is an easily calculated function involving the formal errors of the relative coordinates of the GNSS receiver and satellites $\sigma_e^2, \sigma_n^2, \sigma_u^2$, the formal errors of the measured range, σ_ρ, receiver clock bias estimate, σ_t , and speed of light, c as given below:

$$GDOP(\sigma) = \sqrt{\sigma_e^2 + \sigma_n^2 + \sigma_u^2 + c^2 \cdot \sigma_t^2} \Big/ \sigma_\rho \tag{2.1}$$

It is often used to indicate how errors in the observations will affect the final coordinate solution; it is a measure of the quality of the satellite configuration which can increase or reduce other GNSS errors. Satellites arranged close together with small angular separation have a high GDOP value as similar positional information is relayed from each satellite. Satellites spaced more evenly and further apart with larger angular separation help to minimise trilateration error and therefore have a smaller GDOP value which is more desirable.

The addition of other satellite constellations as outlined in full in section 2.2, is set to increase the number of visible satellites in the future by 70%, from the currently available 70 satellites to over 120 new satellites originally planned for 2020. This addition increases the potential of receiving satellite signals with strong geometry and offers redundancy in a solution, hence the use of GLONASS satellites in this study. Pandey *et al.* (2016) for example, show how the addition of GLONASS with GPS in a PPP static solution improves satellite geometry by more than 30% when compared with a GPS only solution, due to, on average, increasing the number of visible satellites by 60%.

2.2 GNSS

At present there are four planned or fully operational Global Navigation Satellite Systems. The US GPS, Russian GLONASS, European Galileo and Chinese BeiDou. In addition to global coverage systems, regional satellite systems, such as the Indian Regional Navigation Satellite System (IRNSS) and the Japanese Quasi-Zenith Satellite System (QZSS) also exist. All systems aim to deliver global or regional positioning, navigation and time transfer services self-sufficiently. In this section the contrasts between the systems are outlined and considerations that must be made to integrate multiple GNSS are examined.

The IRNSS which became fully operational in 2016 is a 7 satellite constellation consisting of 3 Geostationary Orbit satellites (GEO) and 4 Geosynchronous Orbit satellites (GSO) which cover an area range of 30° to 130° longitude and 30° South to 50° North latitude. A comparative analysis of IRNSS and GPS by Vasudha and Raju (2017) showed that the IRNSS consists of sufficient number of satellites for regional positioning and can improve positioning performance when combined with GPS. The QZSS on the other hand, is expected to consist of 4 satellites in Quasi-zenith orbits (QZO) by 2018 with the intention that at least 3 satellites will be visible in the Asia-Oceania regions at all times. Again this system is intended to compliment the GPS constellation, bringing the total number of satellites in the area to eight or more (six GPS satellites and three QZSS) enabling more stable and higher-precision positioning (Cabinet Office, 2017).

BeiDou is China's second generation satellite navigation system which is planned to consist of 35 satellites in total made up from: 5 Geostationary Orbit satellites, 3 inclined Geosynchronous Orbit satellites (IGSO) and 27 Medium Earth Orbit satellites (MEO), with the latter two satellite groups being arranged in 3 orbits inclined at an angle of 55°. The first BeiDou satellite was launched in April 2007, 20 operational satellites are currently available with the completion of a global coverage system planned by 2020 (http://www.beidou.gov.cn.html). The BeiDou GEO satellites are roughly situated over the Equator, covering the longitude of the whole area of China, whereas the IGSO satellites move from the northern to the southern hemispheres over the same region, improving the regional accuracy of the system over China and its neighboring countries.

Similar to BeiDou, the completion date for the Galileo constellation is planned for 2020. The Galileo system is planned to consist of 30 MEO satellites with an orbit inclination of 56°. The

first four satellites were designed to validate the ground and space segments of the Galileo system and reached the In-Orbit Validation phase in October 2012. In August 2014 the first two of the fully operational satellites were launched but unfortunately did not successfully reach their intended orbital positions (European-Commission, 2015). As of 2016 there are now 14 full-operational capability satellites in orbit. As BeiDou and Galileo are not currently fully operational and IRNSS and QZSS only regional, they will not be discussed further and their data are not considered in this thesis.

GLONASS originally reached Full Operational Capability (FOC) in January 1996. However, due to funding issues satellite availability soon declined to under eight satellites (Hofmann-Wellenhof *et al.*, 2008). In the early 2000's restoration began and the system since December 2011 has been restored to FOC with 24 satellites.

GPS on the other hand was declared FOC in July 1995 with 24 satellites and since 2010 has been modernised to include 32 satellites in total. The main properties of the GPS and GLONASS systems can be seen in Table 2.1 and are discussed below.

GLONASS satellites transmit the same pseudo-random noise code signal but on their own carrier frequencies, implementing the Frequency Division Multiple Access (FDMA) technique to identify each satellite. Satellites that are positioned in antipodal slots of a single orbital plane share the same frequency. Each satellite transmits two frequencies, L1 and L2, centered on two base frequencies. The nominal values of the FDMA carrier frequencies are defined as:

$$f_{1k} = f_1 + \Delta f_1 k \qquad (2.2)$$

$$f_{2k} = f_2 + \Delta f_2 k$$

where k is the frequency channel number of each satellite. The constants are $f_1 = 1602\ MHz$ for the GLONASS L1 band, $\Delta f_1 = 562.5\ kHz$ the frequency separation between GLONASS carriers in the L1 band, $f_2 = 1246\ MHz$ for the GLONASS L2 band and $\Delta f_2 = 437.5\ kHz$ the frequency separation between GLONASS carriers in the L2 band. Since 2005 the channel numbers, for any given satellite, provided in the almanac as part of the GLONASS navigation message, were limited to the range of -7 to +6. This was due to the original channel numbers (+1 to +24) causing interference with radio astronomy and satellite

communication frequency bands. The ratio between the two carrier frequencies $f_{1k}/f_{2k} = 9/7$ is constant for all values of k (Hofmann-Wellenhof *et al.*, 2008).

Table 2.1: Main characteristics of GPS and GLONASS (Groves, 2013).

	GPS	GLONASS
Constellation		
Orbital Planes	6	3
Orbital Height	20,180 km	19,100 km
Orbital Period	11 hr 58 min	11 hr 15 min 48 sec
Inclination	55°	64.8°
Semi-Major Axis	26,580 km	25,500 km
Satellite Differentiation	CDMA	FDMA
Ground Track Repeat Periods	1 Sidereal Day	8 Sidereal Days
Signal Properties		
Carrier frequencies	1575.42 MHz 1227.60 MHz	1602+0.5625**k* MHz 1246+0.4375**k* MHz
Code Frequencies	C/A code: 1.023 MHz P code: 10.23 MHz	C/A code: 0.511 MHz P code: 5.11 MHz
Reference System		
Reference Frame	WGS-84	PZ-90
Time System	GPS time	GLONASS time

The FDMA technique has the advantage of being more resistant to narrowband interference due to the wider radio spectrum band used. It also has low cross-correlation between different GLONASS signals. The new GLONASS-K satellites, launched from 2011, include a new L3 band with Code Division Multiple Access (CDMA) capabilities in addition to the system's traditional FDMA signals, and hence they will have similar signals to the GPS constellation. This will improve integration with GPS which also uses CDMA, so the systems will share more similar processing strategies.

Unlike GLONASS, GPS satellites all transmit on the same carrier frequency. Satellites are identified by unique pseudo-random noise (PRN) codes generated by each satellite and transmitted with the navigation message using CDMA. For GPS, due to the CDMA signal structure, any receiver hardware frequency dependent biases in the signal will be the same for all satellites. As the bias is the same for all satellites the biases are absorbed into the receiver clock biases.

The biases for GLONASS on the other hand are different for each satellite and, if ignored, will increase the error of the observed pseudoranges and hence affect the positioning solution. The code inter-frequency biases can reach up to 5 m and the carrier-phase biases can surpass the L1 and L2 wavelength values and reach up to 73 cm (Yamada *et al.*, 2010; Wanninger, 2012). Receiver dependent calibration values have been proposed to mitigate the contribution of these biases, Wanninger (2012) found that in general carrier-phase biases for different manufacturers' equipment can be modelled by linear functions of frequency. They also found that biases were similar between different manufacturer's equipment for both L1 and L2 frequencies, and stable over a 6 month period.

GPS and GLONASS also use different underlying coordinate systems to reference satellite positions and likewise satellite offsets are referenced to different time systems. Using satellite orbit and clock products in the same reference frame removes the need to transform between the two coordinate systems. For example, The European Space Agency (ESA) products are given in the International Terrestrial Reference Frame (ITRF), the current version is called IGb08.

The orbit repeat and inclination also differs between GPS and GLONASS. GLONASS has a higher inclined orbital plane for better coverage over higher latitudes such as Russia, and the coverage of the GLONASS constellation can be seen in Figure 2.1.

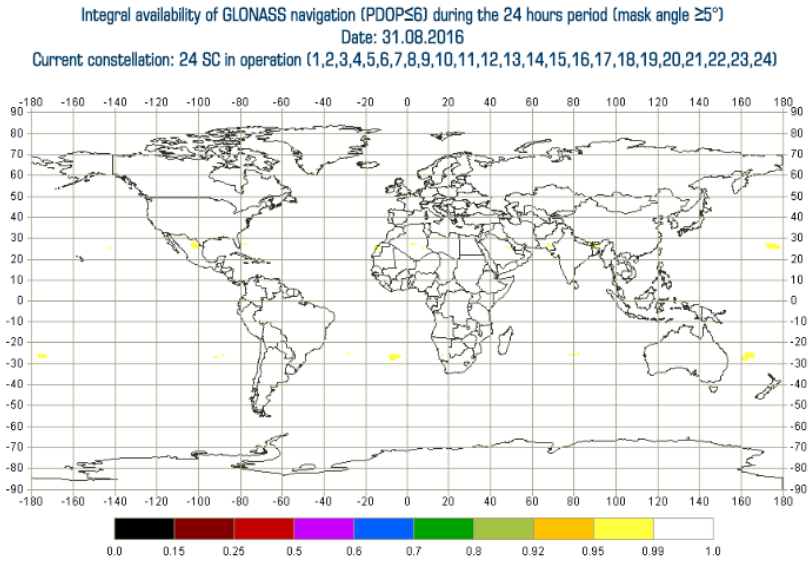

Figure 2.1: GLONASS availability: (https://www.glonassiac.ru/en/GLONASS/CumulativeAvailability.php)

The GPS orbital repeat period is such that the GPS satellites circle the Earth twice during one Earth rotation causing the satellites to be in resonance with the Earth's gravitational potential. Resonance can cause daily drift rates in the satellite semi-major axis of up to 7 m per day and orbital perturbations of up to 4 m per day (Ferreira and de Moraes, 2009). Due to this resonance regular satellite manoeuvres are necessary to maintain them in their nominal orbits. The closer the inclination of the GNSS satellite is to 56.06° or 63.40°, the stronger the effect of resonance will be hence, the GLONASS satellites experience weaker resonance, as their ground track repeats every eight days and their orbits are at a higher incline (Sanchez *et al.*, 2015).

In brief, the GLONASS FDMA method causes GLONASS to have additional receiver inter-frequency biases and, if combining GLONASS and GPS, an additional time system offset parameter in the solution. Although they have different terrestrial reference frames, precise orbit and clock products from the International GNSS Service (IGS), are provided in the same frame for both. Both constellations can be used for GNSS positioning, as outlined in the next section.

2.3 GNSS Positioning

The location of a GNSS receiver can be determined by using known modulated codes from a group of four or more GNSS satellites orbiting the Earth and measuring the range from the receiver to each of the satellites.

The satellites are able to generate and transmit single or multiple coded signals on single or multiple radio frequencies using high precision clocks. Provided that the time of generation and signal code are known by the receiver, the receiver can measure the reception time of the code against its own less precise clock and hence determine the propagation time of the code between the satellites to the receiver. The propagation time measured can be converted to a range measurement by multiplying by the speed of light in space.

The range measurement contains the receiver to satellite range plus additional biases and random noise. Therefore the observed range measurement is known as a 'pseudorange'. A single pseudorange measurement relates to the surface of a sphere upon which the receiver could lie. A minimum of three pseudoranges would be required to determine the coordinate position of a receiver based on trilateration. However, to account for the receiver clock

offset a fourth pseudorange is in reality required. Biases present in the pseudorange decrease the accuracy of the position and are often considered as errors. These errors can be split into three main categories: satellite dependent errors, receiver dependent errors and signal propagation errors, which will be discussed later in this chapter.

To gain the most accurate position possible the errors affecting the observations must be reduced. Numerous GNSS positioning methods can be used to try to mitigate or recognise and ignore the restrictions of these errors. These methods are described in the following sections: 2.4, 2.5 and 2.6.

2.4 Single Point Positioning

Single Point Positioning (SPP) was the first positioning technique GNSS was designed for and the most simplistic form which only requires a GNSS receiver and no other apparatus. The receiver computes the pseudorange to four or more satellites by measuring the code observation, allowing the receiver clock offset and receiver position to be solved for. The satellites broadcast orbital and clock navigation data, which is computed by the master control station and uploaded to each satellite every four hours. The infrequency of the navigation data upload period limits the accuracy and quality of the satellite orbit data and makes it the most significant restriction in this positioning technique, leading to other error sources being ignored. Typical accuracies for static SPP over a 24 hr period, using dual-frequency GPS and precise orbit products, is around 1 m in all coordinate components. For kinematic single-epoch solutions the accuracies worsen, to 5.2 m and 9.7 m in the horizontal and vertical components respectively. Thus, this approach is not accurate enough for earthquake studies (Satirapod *et al.*, 2001) .

The other major error source is caused by the ionosphere. However, satellites also broadcast the Klobuchar ionosphere model which decreases about 50% RMS of the ionospheric range error worldwide when using single frequency receivers (Klobuchar, 1987).

2.5 Relative Positioning

Relative positioning relies on the assumption that many of the biases in the pseudorange measurements are spatially and temporally correlated. Using one or more reference receivers with known positions the biases on rover receiver measurements can be mitigated

by differencing the measurements, when the receivers are observing the same satellites simultaneously. Inadequate determination of relative error parameter modelling will degrade the position accuracy of the rover as will larger baselines, as the biases are no longer correlated with the rover biases. Hence, reference receiver specific biases such as multipath must be mitigated before data differencing is computed. For real-time applications a data link is also required, such as radio links at frequencies ranging from below 300 kHz to 2000 MHz and higher, or an internet connection (Kaplan and Hegarty, 2006).

2.5.1 Carrier-phase Based Positioning

Relative positioning can either be computed from the code or carrier-phase observations. Multipath and tracking errors are the main limiting factors of using code-based positioning when a rover and reference receiver are in close proximity, due to the frequency of the code chipping rate. Carrier-phase tracking where the number of phases of the incoming carrier wave is counted, however, if more precise and less susceptible to multipath errors due its shorter wavelength. Hence only carrier-phase positioning is mentioned in this study. The observation error of carrier-phase is <2.5 mm compared with ~2.9 m observation error from the code signal (Hofmann-Wellenhof *et al.*, 2008). It is possible to measure both the code and the phase of the carrier wave on which the code signal is modulated.

The carrier-phase is inherently ambiguous due to the sinusoidal nature of the carrier wave making successive waveforms indistinguishable from one another. The addition of a time-free phase bias allows pseudoranges to be computed from the carrier-phase. The phase bias ($\bar{N}$) is comprised of three parts, $\bar{N} = N + b_{\varphi r} + b^{\varphi s}$ where N is the integer carrier-phase ambiguity, and $b_{\varphi r}$ and $b^{\varphi s}$ are the Fractional Cycle Biases (FCBs) for the receiver and satellite respectively. The integer carrier-phase ambiguity is unknown and different for each receiver-satellite pair. Provided that the receiver does not lose lock with the satellite signal during observation, N will remain constant. The loss of signal lock between receiver and satellite is called a cycle slip and if a slip occurs a new integer ambiguity must be solved for, separately from the original integer ambiguity.

The method of resolving the phase bias is used to categorise carrier-phase positioning techniques. If $\bar{N}$ is estimated with other parameters then it is known as a float solution, if it can be separated from the fractional parts, it known as a fixed solution. If the bias can be

successfully estimated or resolved then more precise positioning is possible. The following sections outline different carrier-phase positioning techniques.

2.5.2 RTK

Local area Real-Time Kinematic (RTK) positioning involves a single reference station transmitting its location and code and carrier-phase observations at frequencies L1 and L2 for each visible satellite to the rover. The rover station uses the reference station information to remove the satellite clock bias by differencing observations made to the same satellite by each receiver, assuming that the bias is the same at the marginally different times that the signal was transmitted to the reference and rover receiver. A single difference observation is formed and satellite and atmospheric delay biases are reduced. The receiver clock bias still remains; therefore, single difference observations to each satellite are differenced to form double-difference observations. In the double-difference combination the carrier-phase ambiguity is an integer and can be solved quickly, assuming the two receivers are sufficiently close enough so that the ionospheric differential delay is small when compared with the carrier-phase wavelength. If the reference and rover receiver are however further apart, or have a large altitude difference the atmospheric delay biases are no longer similar enough for the integer ambiguity to be resolved, limiting this technique to baseline lengths of less than 20 km (Hofmann-Wellenhof *et al.*, 2008).

2.5.3 Network RTK

Network RTK allows larger distances between rover and reference receivers by reducing the distance dependent biases in the RTK solution by using multiple reference stations in a network to observe the spatial distribution of these biases.

Garrido *et al.* (2011) demonstrated that both the Virtual Reference System (VRS) and the Master Auxiliary Concept (MAC) techniques, when used in a five station network with maximum radius between stations of 15 km, can provide accuracies of <2.5 cm and <5.0 cm in the horizontal and vertical respectively. The VRS solutions on average, however, have a smaller range in precision in the East, North and Up compared to the MAC solution.

Similarly Edwards *et al.* (2010) showed that the accuracy of NRTK in large networks with average inter-station spacing of over 60 km, can also reach the level of <2 cm in the horizontal and <3.5 cm in the vertical, at one-sigma. However, NRTK solutions were found to

degrade for sites at the network extents due to extrapolating rather than interpolating corrections. Hence, the baseline length is limited to the extent covered by the reference station network.

2.6 Precise Point Positioning

Precise Point Positioning has grown in popularity as it provides centimetre to decimetre accuracy without the need for a nearby reference station. PPP was first created for static applications as an enhancement of the SPP technique (Zumberge *et al.*, 1997), but has advanced recently to be used for kinematic applications e.g. Kouba and Héroux (2001a).

In PPP, undifferenced code and carrier-phase observations from dual-frequency receivers are combined with external network derived correction products and models to reduce GNSS errors and estimate coordinates. Carrier-phase ambiguities are often difficult to calculate due to the initial carrier-phase offset in satellites and hardware biases in the receiver. Therefore, most PPP techniques estimate the ambiguity as a float solution. The time taken for ambiguities to be adequately determined in static PPP to allow decimetre level accuracy is roughly 30 minutes and over twice as long for centimetre level accuracy (Bisnath and Collins, 2012). The initialisation time is often referred to as the convergence period and can depend on factors such as satellite geometry, environmental conditions, receiver quality and observation rate and duration. When using continuously operating reference stations for monitoring (where stations positions are constantly being computed) convergence is less of an issue.

Soycan and Ata (2011) demonstrated, using 30 second data from 60 GPS Ordnance Survey stations, how the accuracy of static PPP improves with observation time. After 1 hour of observation, the mean values of RMS errors are 27 mm, 84 mm and 55 mm in latitude, longitude and ellipsoidal height respectively; after 3 hours they reduce to 15 mm, 23 mm and 17 mm. After 24 hours these errors are reduced further to 3 mm, 7 mm and 7 mm which is comparable to values gained by relative positioning of long baselines from IGS stations over the same time period (2 mm, 6 mm and 4 mm). Hence, PPP can provide centimetre level precision, with a few hours of observation data, comparable in precision to relative positioning.

The IGS regularly generates a variety of precise orbit and clock products, which differ primarily by their latency and the coverage of the tracking network used for their calculation as seen in Table 2.2. Products from different analysis centres which use solutions based on different networks are compatible; Springer and Dach (2010) showed that GLONASS clock products from ESA and Information-Analytical Center (IAC) of Roscosmos, Moscow, Russia agree at the 80 picosecond level. The final IGS products have the highest accuracy, for GPS only (<3 cm orbits) and interval rate (orbits: 15 mins, satellite clocks: 30 s), but the longest latency (12-18 days). ESA alternatively offer combined GPS and GLONASS products with interval rates also of 15 mins and 30 s for the orbits and clock respectively. The achievable accuracy of PPP is hence limited by accuracy of the products used.

PPP encounters large ionospheric effects which can cause metre level range errors. To compensate for these effects, un-differenced code and carrier-phase observations at two frequencies are used in an ionospheric-free linear combination. Combined with precise orbit and clock products along with models for other error sources, Zumberge *et al.* (1997) were the first to demonstrate it was possible to reduce the main contributing errors to allow centimetre accuracy static positioning. The main influencing factor on accuracy was the improvement in clock quality.

With improvements in the IGS satellite orbit and clock products over the last 20 years, the accuracy of the final orbit product has improved from 30 cm to <2 cm, the clock quality has also improved to <2 cm (Kouba, 2009). Kinematic PPP is increasingly being used in research and applications, particularly in sparsely populated areas with no local reference network or receivers. Kinematic applications include building structural monitoring (Yigit, 2014), airborne surveying (Zhang *et al.*, 2008), glaciology (Zhang and Andersen, 2006), offshore tidal studies and tsunami and earthquake detection (Li *et al.*, 2014; Takahashi *et al.*, 2014).

Zhang and Andersen (2006) for example, outline how a PPP approach overcomes the limitations of a double-difference approach for ice flow and tidal investigations of the Amery ice shelf in Antarctica. The main three limitations were said to be firstly, the lack of a base station under 200 km away to collect synchronised GPS observations at the same time as the receiver on the Amery ice shelf. Secondly, the propagation of errors during static processing due to the observed site not being static but moving at a rate of a few metres per day on the ice shelf. Lastly, due to previous observations only taking place a couple of times a year due to logistical constraints, the instantaneous velocities of the ice shelf are not retrieved; only

the average yearly velocities are recorded. Their study demonstrated how PPP can be used to reduce logistic complexity and used to explore short-timescale kinematics, similar to those required in earthquake monitoring.

Takahashi *et al.* (2014) outlined how PPP on a buoy-based system can be integrated with seafloor pressure sensors and an array of seafloor transponders for tsunami and crustal deformation monitoring. Their system was designed to sense tsunami and crustal deformation of ± 8 m with a resolution of <5 mm. Previous studies for high precision sea surface observations using a double-difference approach have had limited geographic coverage due to the need for short baselines, restricting the studies to within the vicinity of coasts, lakes and rivers. Fund *et al.* (2013) showed that PPP coordinates from a buoy-based system within close proximity to a radar gauge are not significantly biased with respect to radar gauge data and are consistent with double-difference processing at the sub-centimetre precision level in the horizontal plane.

Table 2.2: A review of a variety of orbit and clock products (Enderle and Springer, 2015; IGS, 2015; Dach et al., 2016).

Provider and Type	Latency	Clock RMS (ns)	Orbit RMS (cm)	Clock interval (s)	Orbit interval (s)	Constellation
IGS Ultra Rapid	Predicted	3	5	900	900	GPS
IGS Rapid	17 h to 41 h	0.15	2.5	300	900	GPS
IGS Final	12 d to 18 d	0.075	2.5/3	30	900	GPS and GLONASS
ESA Final	12 d to 18 d	-	-	5	900	GPS and GLONASS
CODE Rapid	10 h	-	-	300	900	GPS and GLONASS
CODE Final	12 d	-	-	5	900	GPS and GLONASS

Use of PPP for kinematic applications is more complicated as the station location is not assumed to be fixed over time. The majority of PPP software handles estimating parameters with a changing state by using a Kalman filter estimation technique which is recursive and estimates the state of a process by minimising the mean of the squared error of the residuals (Welch and Bishop, 1995). A dynamic model aims to describe the time evolution of a set of observables, formed from modelling position, velocity, receiver clock offsets, atmospheric corrections, ambiguities using precise orbit and clock products and additional models as described later in this chapter. The modelled and real measurements, along with the estimated system describing parameters (state vector) and measurement covariances, are combined by the Kalman filter to update the state vector with the information gained from the current epoch's observations. Its recursive nature means it can be used in real-time using only the current input measurements and previously calculated state and covariances. A selection of different PPP software is reviewed in Table 2.3 and the PANDA software, used in this Thesis, is discussed in detail later in section 3.7.

Colombo *et al.* (2004) evaluated the performance of kinematic PPP at fixed sites and on a moving vehicle using 30 second clock rate products. They noted 3D RMS position errors of 4.3 cm to 9.3 cm at the fixed sites and 5.5 cm to 7.7 cm on the moving vehicle with typical convergence times of 40+ minutes. They also noted the importance of using clock products at the same rate as positioning so that short term variability in the satellite clocks could be corrected for. An improvement in static PPP of 30% was found when 30 second clock products were used in comparison with 5 minute clock products when comparing results with a baseline solution. Interpolated clock rates faster than 30 seconds, however, were found not to further improve positional error or convergence times in kinematic PPP when using 1 second carrier-phase observations (Hesselbarth and Wanninger, 2008).

Table 2.3: A review of a variety of currently available PPP software.

Software	GNSS Observation	Processing mode	Institute	Online Service	Reference
PANDA	GPS+GLONASS+BeiDou+Galileo	Static/Kinematic	Wuhan University	-	(Jing-nan and Mao-rong, 2003)
GIPSY	GPS+GLONASS	Static/Kinematic	JPL/NASA	APPS	(Zumberge *et al.*, 1997)
Bernese	GPS+GLONASS	Static/Kinematic	University of Bern	-	(Dach *et al.*, 2015)
gLAB	GPS+GLONASS	Static/Kinematic	ESA/UPC	-	(Hernandez-Pajares *et al.*, 2010)
GAPS	GPS+BeiDou+Galileo	Static/Kinematic	University Of New Brunswick	GAPS	(Leandro *et al.*, 2007)
Magic	GPS+GLONASS+Galileo	Static/Kinematic	GMV	MagicGNSS	(Tobías *et al.*, 2014)

The IGS has also been at the forefront of real-time product development since 2007, when the IGS Real-Time Pilot Project was initiated. In April 2013 they launched the Real-Time Service (RTS), allowing subscribed users to stream PPP orbit and clock corrections in the Radio Technical Commission for Maritime Services (RTCM), State Space Representation (SSR) format. The IGS RTS products are received by the users via the Network Transport of RTCM by Internet Protocol (NTRIP) and have a sampling rate of 5 seconds, typical latency of 25 seconds and orbit accuracy of ~5 cm (Grinter and Roberts, 2013).

The reliability of the reception of the orbit and clock corrections is essential for real-time PPP to work. In kinematic PPP especially, signal interruption is more likely, preventing the receiver from receiving corrections and causing a disruption in satellite tracking. Any disruption in satellite tracking, such as an impeded sky view, high receiver dynamics or interference causing discontinuity in the system (cycle slips), requires the carrier-phase biases to be re-estimated in a period of reconvergence.

Before advancements in PPP, relative kinematic positioning was used to measure seismic waves, as described in Bock *et al.* (2004) , where one station acts as a reference and is tightly constrained to known coordinates and the relative displacement of each station is computed with respect to the reference. For large earthquakes however, the reference station may also be affected by seismic motion and hence introduce biases into the other station's relative displacement measurements. Positioning accuracy of relative positioning degrades with increasing baseline length as discussed in Ge *et al.* (2006). PPP is usually considered to be free from this limitation; however PPP relies on network-based satellite products which could affect PPP positioning accuracy in a similar way. For example, Geng *et al.* (2010b) investigated the effect of satellite clock product and uncalibrated phase delays (UPDs) accuracy in PPP, when the radial distance of a circular reference network, centred around a receiver on a marine vessel, is increased. Satellite clock estimates were differenced from the Center for Orbit Determination (CODE) 'Final' clock products, for a large, medium and small circular reference network, with radii of approximately 3,600, 2,000 and 900 km. The mean RMS of all three networks was within $\pm$0.02 ns of each other, with the smallest circular network having the largest mean RMS of ≈0.041 ns. Hence, the increase in distance from reference network does not worsen satellite clock estimates as they are extremely close to those produced by CODE from a global network. The UPD estimates however were affected by the increase in network radius.

Additionally, Geng *et al.* (2010b) also compared the positioning accuracy of kinematic PPP and relative positioning on the same marine vessel. The RMS values for ambiguity-fixed PPP using the large circular reference network are 55.6%, 56.6% and 13.5% smaller in the East, North and Up respectively than those from relative ambiguity-fixed positioning for a 2,800 km baseline. When using an ambiguity-float solution however, relative positioning performs better in the East and Up; this could be attributed to the longer distance used for PPP between receiver and reference network. The RMS values for relative positioning increased at a higher rate than for PPP as the base station distance to reference stations grew. Hence ambiguity-fixed PPP out performs relative positioning for separation distances over a few thousand kilometres away.

Therefore, PPP is the preferred technique for large station separation distances. Even though ambiguity-float PPP can be less accurate than relative positioning and orbit and clock errors can propagate into the PPP solution, as they are held fixed, these factors are out weighted by the cost effective advantages of PPP. PPP only requires a single dual-frequency GNSS receiver, without the need for communication to multiple GNSS stations in a network for their data and error corrections. PPP is not limited by separation distance to other sites, so can be used in remote and hostile environments, such as on buoys at sea. For relative positioning, Bock *et al.* (2011) showed that a dense network with site separation distance of 20-40 km is required for the computation of large earthquake magnitudes. Whereas for PPP, Wright *et al.* (2012) were able to sufficiently compute magnitude estimates using just 10 stations separated by 100 km, which makes GNSS for early-warning more economically feasible.

PPP also does not suffer from reduced satellite availability, due to the need of relative positioning to simultaneously see the same set of satellites. This possibly gives PPP an advantage when used in an urban environment, when satellite visibility is already limited due to high rise buildings impeding the sky view. Hence PPP has reduced equipment and logistical costs when compared to relative positioning, as well as providing absolute station coordinates, unaffected by reference station movement which can occur during large earthquakes. Thus PPP has been deemed most suited for this study.

Recent advancements in satellite orbit and clock products has made PPP accuracies comparable with relative positioning techniques with the advantage of positioning in a dynamic global reference frame without the need for reference receivers nearby. However,

long convergence times are required for centimetre accuracy to initially be reached and similar length re-convergence times required when the sky view is impeded and reconvergence is necessary due to loss of lock with satellites, causing a reduction in satellite numbers and hence poor satellite geometry which further increases convergence times. The convergence period occurs as the solution changes from a pseudorange-only solution to a float ambiguity carrier-phase solution and can be seen as the time necessary for the ambiguity estimates to reach a unique set of ambiguity parameters with a certain level of accuracy. Despite this, PPP has a wide range of uses and below two approaches to reduce convergence time are discussed. Fixing the ambiguities to integer values to form a fixed ambiguity solution is discussed in the next section; integrating GPS with other navigation systems, in particular GLONASS, is covered in section 2.6.2.

2.6.1 PPP with Fixed Ambiguity Resolution

As mentioned in section 2.5.1, carrier-phase ambiguities are computed of the integer part and FCBs associated with the receiver and satellite. Provided that the FCBs can be determined, the integer part can be fixed to the correct value and the carrier-phase used as an unambiguous measurement allowing centimetre accuracy PPP to be obtained. Float solutions can only reach centimetre accuracy after long convergence periods.

Ge *et al.* (2008) and Laurichesse *et al.* (2009) showed that it is possible to fix undifferenced carrier-phase ambiguities to integer values for receivers not in the additional network solution by utilizing network-estimated FCBs for each satellite, which were shown to be fairly stable in time and space.

Ge *et al.* (2008) estimated the satellite and receiver ambiguity by deconstructing the ambiguities into widelane and narrowlane ambiguities by differencing and adding the L1 and L2 phase observations. The RMS of the East component compared to the IGS weekly solutions was improved by 30% using this method, as outlined fully in Ge *et al.* (2008).

Collins *et al.* (2008) and Laurichesse *et al.* (2009) further developed and simplified the approach by redefining the satellite clock products, known as integer-recovery clocks (IRCs), by absorbing the corresponding narrowlane FCBs into the clock products to ensure that the narrowlane biases have integer characteristics that can be directly fixed. Their methods differ slightly as Collins *et al.* (2008) estimate the receiver clock carrier-phase and code-phase FCBs separately before fixing the wide and narrowlane ambiguities, sometimes

referred to as the Decoupled Satellite Clock method, which requires post-processing. Laurichesse *et al.* (2009) on the other hand do not decouple the receiver clock estimates and their method can be implemented in real-time.

Geng *et al.* (2010a) investigated the effects of increasing static observation periods on ambiguity-fixed PPP position accuracy and found that after one hour the 3D RMS of a float solution is 5.0 cm, and reduced to 1.6 cm by a fixed solution and after 4 hours reduced from 1.4 cm to 0.9 cm. They indicated that an observation period of 3 hours or more is required for vertical components to achieve better than 1 cm accuracy. Laurichesse *et al.* (2009) also noted long convergence times of around 30 minutes for static positioning and 90 minutes for kinematic positioning. The long period of time is required for the narrowlane biases to be estimated as float values so that the ambiguities can be fixed to integers from the relatively noisy pseudoranges.

2.6.2 GPS and GLONASS PPP

The addition of GLONASS increases the number of satellites in view and hence strengthens satellite geometry and redundancy in the PPP solution and therefore can speed up the convergence time of ambiguity float PPP. The additional of GLONASS reduces the effect of random errors, which has the potential to improve the position solution in terms of accuracy, provided that there are no systematic errors present. However, GLONASS orbit products, for example, are less accurately determined than GPS products, as seen in Table 2.2 and there is more uncertainty surrounding GLONASS signal biases, predominantly due to using FDMA for satellite identification. When comparing GPS-only and GPS and GLONASS PPP solutions in a non-optimal environment, Alkan *et al.* (2015) found that positioning precision only improves if the overall satellite geometry is improved with the addition of GLONASS satellites. If the geometry is not improved there is little improvement in the positioning estimate. Furthermore, Chen *et al.* (2016) show how, in a dynamic setting, a GPS and GLONASS PPP solution provides more accurate and robust coseismic displacements in a non-optimal environment when compared to GPS-only.

Li and Zhang (2014) used a single difference approach, selecting a GPS satellite with high elevation and a healthy epoch as a reference to cancel out GPS receiver clock offsets. Thus, it left just the GPS and GLONASS time offset to be estimated for the GLONASS observations. They investigated the effect of using GLONASS on ambiguity float and ambiguity fixed

solutions where GLONASS is kept as float but the GPS is fixed, in both static and kinematic scenarios. From 178 IGS stations over a 7 day period the convergence time on average for ambiguity float PPP was reduced by 45.9% from 22.9 to 12.4 minutes in static mode and by 57.9% from 40.6 to 17.7 minutes in kinematic mode with the addition of GLONASS. For fixed ambiguity PPP, the time taken to gain the first ambiguity fix was also reduced, by 27.4% from 21.6 to 15.7 minutes in static mode and by 42.0% from 34.4 to 20.0 minutes in kinematic mode. Li and Zhang (2014) also investigated the extent of improvement in convergence time with the number of satellites visible in the sky and found that adding GLONASS reduces the convergence time more when fewer GPS satellites are visible.

Similar results were found by Cai and Gao (2013) using an undifferenced approach. The approach assigns the code observations a comparatively small weight compared with that assigned to the carrier-phase observations, allowing the inter-frequency bias to be neglected and error assimilated into the code residuals instead. Using five IGS stations the convergence time on average for ambiguity float PPP was reduced by 39%, 30% and 60% for the East, North and Up coordinate components respectively in kinematic mode.

Banville *et al.* (2013) suggest that carrier-phase biases can be modelled as formal integer parameters to allow natural convergence to integer values instead of calibrating observations to allow for GPS and GLONASSS ambiguity fixed solutions. However, they found that their method degraded the solution compared with using external calibrations but showed potential for use in real-time network processing without the reliance on external corrections. In a GLONASS float PPP solution the constant biases can be combined with the ambiguity term so does not degrade the positioning solution. This method is commonly used in GLONASS PPP software as the development in GLONASS fixed PPP is still on going.

It has been demonstrated that in practice it is possible to decrease the convergence time of GPS ambiguity float and fixed PPP by the addition of GLONASS. At present there are no publicly available combined GPS and GLONASS ambiguity fixed PPP products. Therefore, only ambiguity float PPP is used in this study. As a consequence of only using a float PPP solution the coordinate estimates computed by PPP will be less precise than those from relative positioning over short baselines. However, for measuring earthquake static displacements over short periods of time (several seconds to minutes) the relative change of the Earth's surface position is of more importance than the absolute accuracy of the coordinate solution. Considering the majority of PPP errors vary slowly in time, such as satellite orbits

and clocks, as outlined next in section 2.7, and phase biases remain constant, these errors can be assumed to be stable over a short period of time. Therefore, a float PPP solution is still able to measure small static displacements with the required sub decimetre accuracy for earthquake and tsunami early-warning applications.

Even though GPS ambiguity fixed products (FCB and IRC) can be used in real-time and increase positioning accuracy once converged, positioning errors can still occur due to the assumptions made when products are estimated within a network. Different conventions adopted in the network solution and by the user may result in erroneous ambiguities being fixed. It is also common when using products in real-time for the fixed ambiguities to change, when satellites move in and out of view, which can cause large coordinate shifts (Seepersad and Bisnath, 2015). These shifts could be detected as genuine Earth surface movements and give rise to false alarms, which is undesirable and hence best avoided.

2.7 Satellite Dependent Errors

As mentioned in the previous section, GNSS signals are subjected to various error sources. In order to achieve high-accuracy positioning results it is necessary to understand these error sources and how to mitigate their effect in PPP. Most of these errors can be mitigated to some extent by modelling, estimating as an unknown parameter or forming different linear observables. The key errors and their handling strategies for PPP are now described.

2.7.1 Satellite Orbits and Clocks

The PPP technique relies on the use of precise GNSS orbit and clock products. Each GPS satellite transmits Keplerian orbital elements (rate, drift and clock offset parameters) which have been computed by the GPS ground segments and uploaded to the satellites on a daily basis. The ephemeris is available at the time of observation with accuracies of about 100 cm for the orbit and 5 ns for the clocks (IGS, 2015). The GLONASS satellites transmit coordinates, velocities and accelerations which are also immediately available at the time of observation. Accuracies in the coordinates range from 20 m in the along track to 1.5 m in the radial component and velocities range from 0.2 cm/s to 0.05 cm/s (GLONASS, 2008).

The accuracy of the broadcast ephemeris is limited by the control segment upload frequency, downlink bandwidth and satellite storage capabilities. For more accurate positioning post-processed ephemerides are required.

Precise ephemerides are calculated from data collected by a globally distributed network of continuous receivers whose coordinates are precisely known. These products are available from IGS Analysis Centres or commercially at a range of different latencies and accuracies as mentioned earlier in this chapter and outlined in Table 2.2.

Real-time products are produced by extrapolating satellite orbits and clock products forward over a small period of time which reduces the accuracy of the product.

In this thesis, ESA GPS and GLONASS combined 'Final' orbit and clock products are used as ESA was one of the first agencies to produce combined products, and the first agency to provide 30 second clock products for GLONASS. The products are calculated in 24 hour periods from a network of 150 receivers and uploaded weekly in daily files with a clock sampling rate of 30 seconds (Jean and Dach, 2013). The importance of using clock products at the same rate as positioning was noted in Colombo *et al.* (2004) to capture the high frequency noise that occurs in satellite clocks. Therefore the clock products used in this study are the highest rate currently available which is unfortunately not at the same rate as positioning (1 Hz) due to product computation time and storage issues. Bock *et al.* (2009) showed how using 30 second clocks for 1 Hz positioning degraded 3D coordinate RMS by 30%, whereas deterioration was <2% when 5 second clock rates were used.

2.7.2 Satellite Orientation

For PPP it is important to know the GNSS satellite orientation as precise orbit and clock products are estimated using dynamic force models which refer to the satellite's centre of mass; the code and carrier-phase observations from satellites however refer to the antenna phase centre so must be corrected. To correct for this difference in reference point the offset between the centre of mass and antenna phase centre (phase centre offset) of the satellite must be known. The IGS provides GPS satellite antenna offset corrections that have been used in this study.

2.8 Signal Propagation Errors

A major error component of PPP is due to the impact of the atmosphere on GNSS transmitted signals. As GNSS signals pass through the atmosphere layers they are delayed and deflected, these propagation effects and time offsets need to be accounted for in order to achieve high-accuracy positioning, as described in this section.

2.8.1 Tropospheric Delay

The electrically-neutral atmosphere (troposphere) is the lower part of the Earth's atmosphere which extends to a height of about 40 km and contains the majority of the atmosphere's mass (80%). It is non-dispersive with respect to radio waves for frequencies below 15 GHz, therefore propagation is frequency independent and the effect cannot be eliminated by L1 and L2 linear combinations (Hofmann-Wellenhof *et al.*, 2008).

The tropospheric path delay is often separated into hydrostatic dry and wet components as shown by Hopfield (1969). The former accounts for roughly 90% (240 cm zenith delay at sea level), of the tropospheric path delay and is a function of pressure and temperature. The latter is related to water vapour in the troposphere, which is a function of humidity, and only contributes around 10% (40 cm zenith delay at sea level), of the total tropospheric path delay but causes the most difficulty in forming tropospheric path delay mitigation models as it is highly variable in time and space (Leick, 2004). The magnitude of the wet delay is larger at lower elevation angles due to traveling a longer path through the troposphere.

The difficulty in modelling this tropospheric path delay is dependent on many factors such as water vapour pressure, atmospheric pressure, temperature, site altitude and satellite elevation angle. The delay occurs due to the refractive index of the neutral atmosphere slowing down the radio waves, contrary to the assumption that the waves are traveling at the speed of light in a vacuum.

The tropospheric path delay is normally expressed as a product of the zenith path delay scaled by a mapping function for a given elevation angle. There are many different tropospheric models such as Hopfield, UNB3 and Saastamoinen, with minor differences between models for zenith angles less than 75° (Hopfield, 1969; Saastamoinen, 1972; Collins, 1999). There are also many mapping functions used to determine the amount of error that occurs from traveling longer path lengths when the satellite is not at the zenith. Modern mapping functions such as the Vienna Mapping Function 1 (VMF1) seek to reduce errors by using a large temporal range of input data (6 hour resolution) not limited by seasonal or constant values. VMF1 was originally site specific for IGS, International VLBI Service (IVS) and International DORIS Service (IDS) stations only, but around a year later the more widely used global gridded version became available at 2.5° by 2.0° resolution with a latency of less than 24 hours (Boehm and Schuh, 2004). The Global Mapping Function (GMF) is a lower resolution (15° by 15°) version of the VMF1 created by a spherical harmonic fit to the

seasonal average VMF1 parameters. The GMF has the advantage that no external input files are required and only the approximate station coordinates and day of the year are required as input parameters, making it suitable for real-time PPP (Boehm *et al.*, 2006).

In PPP the hydrostatic tropospheric path delay error is corrected through tropospheric modelling, whereas the wet component is estimated as an unknown parameter due to its high variability which makes it difficult to model. The zenith delays are mapped to satellite elevation angles using a mapping function and elevation dependent weighting is often applied to reduce errors at lower elevation angles where higher levels of error occur (Luo *et al.*, 2009).

2.8.2 Ionospheric Delay

The ionosphere is the upper part of the Earth's atmosphere which extends between about 70 km and 1000 km above the Earth's surface and is a dispersive medium at radio frequencies. Within this layer are charged particles, electrons and positive ions, which are produced by coronal mass ejections and ultraviolet solar radiation causing ionization of the gas molecules in the layer. These free electrons affect radio wavelengths in a frequency dependent way. The carrier-phase is advanced so satellites appear closer (phase advance), whereas the code signal is delayed so satellites appear further away (group delay). The magnitude of the ionospheric delay is equal for both carrier-phase and code signal but in opposite directions and can cause range errors of around 0.1 m at night and up to 100 m during the day (Hofmann-Wellenhof *et al.*, 2008).

The ionospheric delay is directly proportional to the Total Electron Content (TEC) encountered along slant paths from the satellite to receiver location, meaning that the delay is larger at lower elevation angles. TEC however is highly spatially and temporally variable and is a function of geographical location, local time, season and geomagnetic and solar activity, making it difficult to remove by modelling.

For dual-frequency receivers, the first order ionospheric effects can be eliminated through forming the ionospheric-free linear combination (LC) of L1 and L2 measurements, making use of the ionosphere's dispersive properties as outlined in Kouba and Héroux (2001b).

The higher order effect usually contributes to less than 0.1% of the total ionospheric delay so is often ignored in PPP and is absorbed by the satellite clock corrections. The second-order

ionospheric delay terms and the difference of slant TEC (STEC) between the actual slightly bent paths versus the straight line propagation terms are the main contributors to the remaining ionospheric delay. Their combined effect on the precise GNSS satellite products cause errors in the satellite Z coordinates of up to 11 mm and more than ±20 ps in the satellite clocks and therefore need to be mitigated if obtaining coordinate with sub-decimetre accuracy (Hernández-Pajares *et al.*, 2014).

2.8.3 Differential Code Biases

The differential code bias is a pseudorange bias between the C1 and P1 code signals transmitted, unique for each satellite as the signals travel different routes to get from satellite to antenna. The magnitude of the P1-C1 biases is of the order 2 ns (0.6 m) for GPS; however biases have a significant time varying component. Satellite differential code biases remain stable over one day but can vary by 0.5 ns between consecutive days. Receiver differential code biases are more variable and can vary by 1.0 ns between days (Sardón and Zarraoa, 1997). Therefore, pseudorange biases need to be continuously monitored over time and are hence estimated on a monthly basis for GPS by the IGS (Kouba, 2009).

GLONASS differential code biases are more complex to calculate as they are unique to each satellite-receiver pair as signals are transmitted at different frequencies, resulting in different code biases to be computed for each channel, as previously mentioned in section 2.2.

2.9 Receiver Dependent Errors

Receiver dependent errors are often caused by receiver hardware and electronic limitations. These include receiver clock drifts due to receivers containing less stable oscillators, and errors arising from the difference between the physical and electrical antenna phase centre.

2.9.1 Receiver Clock Offset

As previously stated in section 2.3, receiver clock biases affect the ranges of all receiver signals equally. This is due to receivers using cheap quartz crystal oscillators to keep cost, size and power consumption to a minimum. The receiver clocks drift according to the quality of the oscillator by about 0.1 ns/s relative to the stable atomic clocks used in the GNSS satellites. The majority of receivers aim to keep the offset below a predefined magnitude,

usually within 1 ms of GPS time. The receiver can steer the internal oscillator to push the clock drift to close to zero or alternatively the receiver introduces discrete jumps in the receiver's clock time estimates (Hofmann-Wellenhof *et al.*, 2008).

In PPP the receiver clock offset is estimated as an unknown parameter along with the receiver position. For combined GPS and GLONASS receivers the receiver clock offset between the two different time systems is handled by solving for two separate clocks offsets, one for each system, or by solving for one receiver clock offset and then the offset to the other time system (Cai and Gao, 2009).

2.9.2 Antenna Phase Centre Variation

The receiver antenna phase centre is an electromagnetic property which is dependent on the elevation and azimuth angle, intensity and frequency of an incoming signal. A mean position of the electrical antenna phase centre is determined for the purpose of offset calibration. Numerous different calibration methods exist, such as relative, anechoic chamber and robot calibrations which agree with one another at the 1 mm level (Görres *et al.*, 2006). Without correcting for antenna phase offsets and variations, potential errors of up to 8 cm in the vertical and 4 cm in the horizontal can occur which could lead to Earth surface displacement being undetected (El-Hattab, 2013).

The IGS provides GNSS receiver antenna phase calibrations tables at 5° elevation intervals and satellite calibrations at 1° intervals which can be interpolated for the required elevation angle and found in the IGS08.atx file, available from: https://igscb.jpl.nasa.gov/igscb/station/general/igs08.atx. The satellite calibrations are calculated from 17 years of GPS data from five analysis centres. In comparison, only 8 years and 2.5 years of GLONASS data from two analysis centres are used respectively, with only 70% of IGS station antennas having been robotically calibrated. The antenna phase offset and variation coordinate vector corrections can be applied to the receiver position vector after conversion to geocentric coordinates. However, GLONASS corrections are not yet widely available and are hence often not used in PPP processing.

2.9.3 Phase Windup

Radio wave signals transmitted from GNSS satellites are right-hand circularly polarized and can be pictured as a rotating electric vector field propagating from satellite to receiver which

rotates 360° with every wave cycle. Phase-windup occurs due to relative rotations of the receiver or satellite antenna around their bore axis which influences the carrier-phase measurements as an apparent variation in range. Satellites can rotate up to one revolution in less than half an hour during eclipse periods when reorienting their solar panels towards the sun (Wu *et al.*, 1993).

The effect of phase windup for relative positioning is around 1 cm so is often ignored, but for PPP the effect is significant as over half a wavelength (>10 cm for GPS) can be reached. A phase windup correction can be applied as outlined by Wu *et al.* (1993).

For kinematic receivers there is an additional windup error due to receiver motion, which for GPS satellites will apply to all satellites by roughly the same magnitude. This is therefore normally ignored and absorbed into the receiver clock bias estimate or is sometimes estimated as an additional parameter (Hernández-Pajares *et al.*, 2004).

GLONASS signals however are transmitted at different frequencies; therefore phase windup error will be different for each satellite carrier-phase and can range from 1.9 mm to 0.5 mm with one rotation. In PPP satellite phase windup is normally mitigated by modelling using the above mentioned correction, whereas receiver phase windup is often not accounted for. As static sites are being used for this study, receiver phase windup does not need to be accounted for as the receiver remains in the same orientation.

2.10 Relativistic Effects

PPP is based on effectively observing the time difference between the transmitted signal of a satellite and reception of the signal at a ground-based receiver. Relativity effects in GNSS measurements are caused by the motion of the satellite with respect to the receiver, causing the satellite clock to appear to run faster to an observer on the Earth than it would to an observer at the satellite due to the weaker effects of the Earth's gravity field on the satellite than on the Earth's surface.

2.10.1 Sagnac Effect

The Sagnac effect occurs due to GNSS satellites having a coordinate frame in an inertial system but observations in an Earth-Centred, Earth-Fixed (ECEF) system, causing the receiver to rotate, with a velocity up to 500 m/s at the equator with the Earth whilst satellite signals

propagate to the receiver. The magnitude of the satellite clock error due to this effect can reach 10 ns in 3 hours which is equivalent to 30 cm range error (Hofmann-Wellenhof *et al.*, 2008). The Sagnac effect for the receiver clock can be modelled as outlined by Ashby (2003) and the correction applied in precise orbit and clock products. Therefore, it must also be corrected for in PPP processing to maintain uniformity (Kouba, 2009).

Also in PPP processing the space-time curvature of the satellite signal caused by the gravitational field must be accounted for as errors can reach up to 18.6 mm (Hofmann-Wellenhof *et al.*, 2008).

2.11 Geophysical Errors

Sub-daily periodic signals at different frequencies can propagate into GNSS position estimates due to unmodelled geophysical forces acting on the Earth. These include earth tides and ocean tide loading which can cause large localised variation in surface displacements which could be misinterpreted as movements caused by an earthquake and give rise to false alarms.

2.11.1 Earth Tide

Earth tides occur due to the response of the pliable Earth to the gravitational attraction and temporal variations of the Sun, Moon and other celestial bodies. The solid Earth tide generates periodic site displacements which can reach up to 30 cm in amplitude and 5 cm in the vertical and horizontal components respectively. Neglecting Earth tide effects can result in systematic position errors of up to 12.5 cm in the radial and 5 cm in the North direction (Kouba, 2009).

Diurnal and semi-diurnal tides dominate and can be partially averaged out of static positioning over 24 hours. However, the is not the case for short observation periods of PPP (Kouba and Héroux, 2001b). The effect of the Earth tide is dependent on station latitude, tide frequency and sidereal time and can be computed and corrected using models, such as provided in the IERS Conventions 2010.

2.11.2 Ocean Tide Loading

Ocean tide loading similarly occurs due to the redistribution of ocean water from ocean tides, deforming the sea floor and coastal land. Stations along the coastline such as in

Cornwall can experience peak-to-peak localised surface displacements of up to 15 cm in the vertical and 2 cm in the horizontal direction over a 6 hour period. The extent of displacement varies globally and changes slowly over time with a dominant period of around half a lunar day (12hr 25mins). This error is normally mitigated by applying ocean tide loading corrections, such as FES2012, computed from tidal hydrodynamic equations, altimetry and tide gauge data assimilations, convolved with a solid Earth response model (Kouba and Héroux, 2001b; Lyard *et al.*, 2006). Ocean tide loading could be interpreted as apparent ground displacement caused by an earthquake over short time periods if not corrected for.

2.12 Multipath Overview

This section gives a brief introduction to multipath error; Chapter 3 next, describes multipath and techniques for mitigating multipath in full.

Multipath error occurs due to reflecting surfaces near the receiving antenna causing transmitted signals to arrive via more than one path (Hofmann-Wellenhof *et al.*, 2008). The reflected signals impede the reception and processing of the direct signal at the receiver, causing errors to occur in both the code and carrier-phase measurements, which produce errors in the final position solution. For precise applications, such as seismology, the carrier-phase multipath is of most importance to mitigate, as code measurements are often weighted lower during GNSS data processing. It is vital that carrier-phase multipath error is mitigated as it has very similar characteristics to the surface waves generated by an earthquake, such as a cyclic nature over small periods of a few seconds with amplitudes of a few centimetres, as described below.

Carrier-phase multipath φ can be represented by the additional multipath signal path, carrier wavelength and the ratio of direct signal amplitude to multipath indirect signal amplitude (damping factor) as:

$$\varphi = arctan\left\{\frac{\beta sin\theta}{1 + \beta cos\theta}\right\} \tag{2.3}$$

where θ is the phase shift of the reflected multipath signal with respect to the direct signal phase and β is the damping factor of the reflected signal to the direct signal $(0 \leq \beta \leq 1)$,

where 0 represents no reflection and 1 represents that the reflected signal is the same strength as the direct signal.

The phase shift (ψ) of the reflected multipath signal can be described by S, the separation distance between the antenna and reflecting object and E, the satellite incident angle of the reflected point from an entirely vertical or horizontal surface, i.e. tilt = zero, as seen in Figure 2.2:

$$\psi = \frac{4\pi}{\lambda} 2S \sin E \tag{2.4}$$

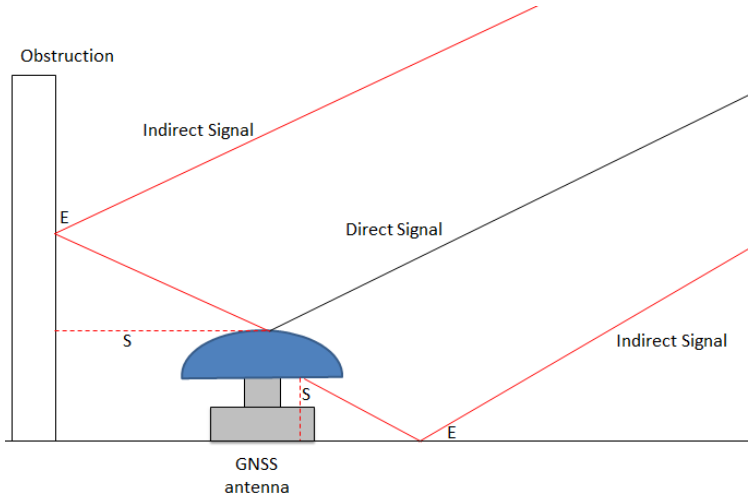

Figure 2.2: Multipath geometry of satellite signal, receiver antenna and reflecting obstructions.

If however the reflecting surface is tilted, additional parameters α, angle of incident at the surface, and γ, tilt angle of the surface, are required to compute the elevation angle as given by:

$$E = \alpha - \gamma \tag{2.5}$$

As satellites are constantly on the move the geometry of the reflector with respect to the satellite and receiver does not stay constant over time. This causes the carrier-phase multipath error to have cyclic variations as the phase difference θ changes gradually.

Characteristically, carrier-phase multipath can reach up to 4.8 cm on the L1 carrier-phase and 6.1 cm on the L2, which equates to roughly a quarter of the signal cycle. This occurs when $\beta = 1$ and $\theta = 90°$, in reality a multipath signal with an amplitude this big is very unlikely. Code-phase multipath on the other hand is essentially limitless (Wanninger and May, 2001).

For use of GNSS in seismology, these oscillating small multipath errors can hinder the accurate measurement of small static permanent displacements, in particular those from small earthquakes or stations far from the earthquake epicentre. There is also a risk that transient surface waves at far away stations (>1000 km) can be mistaken as multipath interference when small in amplitude and over periods of tens of seconds (Ogaja and Satirapod, 2007).

There are numerous different techniques that can be used to mitigate multipath including signal modelling and multipath signal absorption, as described in Chapter 3.

2.13 Summary

This chapter has given an overview of several GNSS positioning techniques, their achievable accuracies and methods used to reduce error sources. It illustrates the practicalities and benefits of using PPP for seismic studies, the only positioning method capable of delivering centimetre accuracy positioning on a global scale. Research into recent PPP developments, such as GPS ambiguity-fixed PPP, has been considered and found to offer high levels of accuracy but at the expense of long initial convergence periods. Convergence periods can be reduced in the future with the addition of GLONASS, which also improves accuracy.

The contrast between the GLONASS and GPS systems has been discussed and the considerations that must be implemented when integrating the two systems for PPP multipath mitigation. A review of combined GPS/GLONASS PPP demonstrates improved accuracy and convergence times compared with GPS only, and the benefits it brings when there is low satellite availability which has provided motivation for using this combined system for earthquake ground displacement derivation.

The main error sources affecting positioning accuracy in PPP have also been outlined. The ionosphere introduces the largest range bias; the first order effects are removed by using ionosphere free linear combinations of code and carrier-phase observations due to the

absence of appropriate models. Models are however effective for removing solid Earth tides, phase centre variation and offset, phase windup and relativistic effects. Other parameters such as receiver clock offsets, hardware bias and wet troposphere zenith delay are estimated during the PPP solution instead.

Given that there is not yet a universal way of mitigating multipath error, Chapter 3 and Chapter 4 investigate the use of a combined GPS and GLONASS sidereal filtering approach to mitigate the effect of multipath at stationary receivers.

Chapter 3. Sidereal Filtering

As mentioned in the previous chapter, one of the main remaining errors that still exist in PPP is multipath. This chapter outlines the characteristics of multipath, reviews the currently applicable mitigation techniques and validates the application of a sidereal filter for GPS carrier-phase observations using the PANDA implementation of PPP.

3.1 Multipath

Multipath is caused by transmitted signals arriving at an antenna via more than one path, preventing the receiver from accurately determining the range. The multipath effect on the carrier-phase is lower than in pseudorange measurements. The maximum multipath effect on the carrier-phase occurs when the multipath attenuation factor is less than or equal to unity, which corresponds to a maximum range error of roughly a quarter of the signal cycle, as discussed in section 2.12. When multipath delay after the direct signal is brief (tens or hundreds of nanoseconds) and reflected signal strength strong, the receiver cannot resolve the signal due to distortion of the correlation function between the received and receiver-generated reference carrier-phase signal (Kaplan and Hegarty, 2006). As well as being delayed, the reflected signal arrives at the antenna with weakened amplitude, caused by travelling additional path lengths (Axelrad *et al.*, 2005). The extent of the above mentioned processes occurring depends on the incidence angle of the reflector, its material and polarization properties.

Materials with high multipath reflectance located close to an antenna, under 1 m away, will cause multipath signals with long periods to occur and conversely short wavelength signals occur from distant objects over 50 m away (Yi *et al.*, 2011). This can be demonstrated by incorporating the time-dependant behaviour of the multipath phase into equation (2.4), i.e. taking the time derivative of ψ.

$$\frac{d\psi}{dt} = \frac{4\pi}{\lambda} S\, cosE\, \frac{dE}{dt} \tag{3.1}$$

For example, as seen in Figure 3.1, the GPS satellite rises from 10° to 80° in 2 hours and 45 minutes or at a mean rate ($\frac{dE}{dt}$) of 0.007°/s. Consider this satellite rising E = 10° over a horizontal reflector at a distance of 2 m from a receiving antenna (S = 2 m). For the GPS L1 carrier signal (λ = 0.19 m) the rate of change of multipath phase ($\frac{d\psi}{dt}$), as given by the equation above, is approximately 0.91°/s, i.e. a period of 395 s (6m 35s). If the same reflector were placed further away (20 m) the rate of change of the multipath phase would be much bigger (9.1°/s) and which has a shorter period of 40 s. Hence signals reflected from nearby objects results in $\frac{d\psi}{dt}$ being small, therefore frequency is low and wavelength long, when $\frac{d\psi}{dt}$ is large the opposite is true; the multipath signal frequency is high with a short wavelength (Bilich and Larson, 2007). It can be seen how carrier-phase multipath from strong but far-away reflectors needs to be mitigated for PPP to be used in seismic studies, due to the frequency of this multipath error being very similar to the frequency of seismic waves, or even low enough to be mistaken for static displacement.

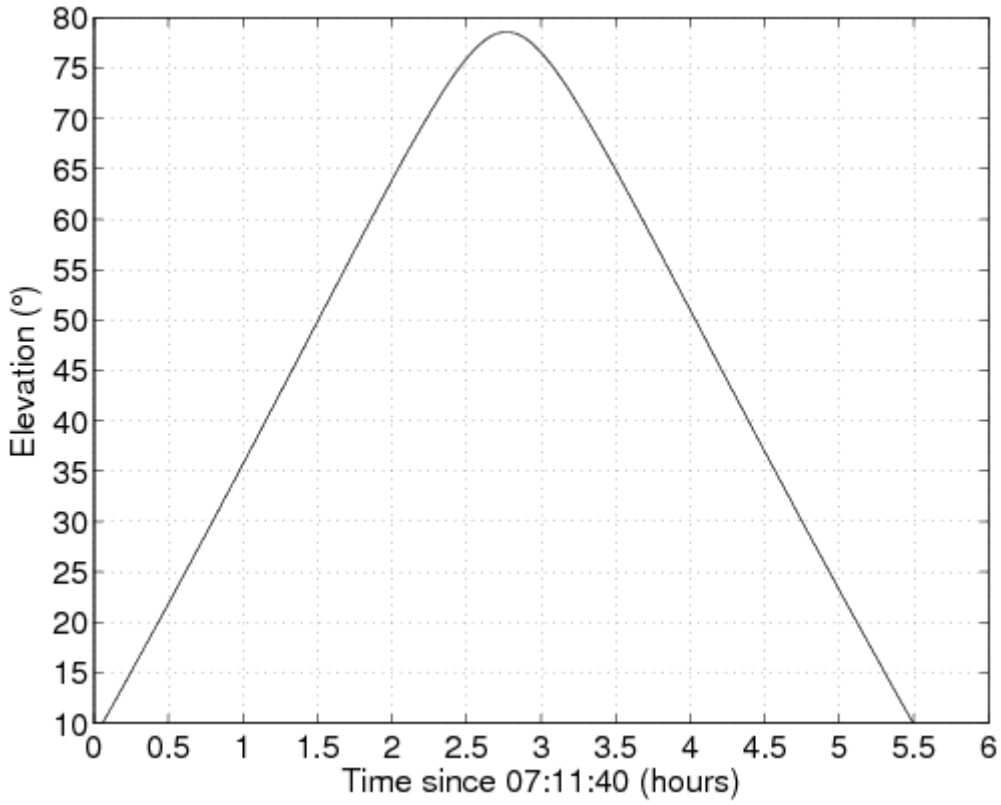

Figure 3.1: Elevation of GPS satellite 24 from OS Net receiver OBAN, 2014, day 306.

Assuming that the GNSS antenna remains static in the same environment, the multipath effect will essentially depend on the satellite's orientation in the sky (azimuth and elevation angle). Multipath error generally increases as satellite elevation decreases due to signals reflected from glancing incidence angles producing strongly reflected signals. Transmitted signals from low elevation satellites near the horizon are also more affected by tropospheric path delay than high elevation satellites due to travelling through the troposphere for longer (Leick, 2004). For this reason it is common to process GNSS data with an elevation cut off angle of 10° or more to remove the strong multipath signals from low elevation satellites. However, this reduces the GDOP and the number of observations available, which results in reduced redundancy in a position solution, or in a worst case scenario, the solution failing to compute if satellite numbers drop below the minimum of four.

Reflections from rough surfaces produce 'diffuse multipath' which is uncorrelated in time and has random noise-like properties which typically produce rapidly fluctuating errors of several millimetres. This kind of multipath can be removed by the receivers' hardware and by filtering through averaging over long observation periods of several days; this however does not benefit seismic studies.

Reflections from large, smooth surfaces with consistent electrical properties, on the other hand, produce specular multipath. This causes systematic time-correlated errors in both the pseudorange and carrier-phase measurements due to the relative motions of the satellites, receiver and reflectors. Extensive specular error may lead to range errors in the order of metres for the pseudorange and several centimetres for the phase measurements (Kamatham *et al.*, 2012). This type of multipath unfortunately cannot be dealt with by dynamic filtering as used for diffuse multipath, so presents a larger problem. Numerous different techniques however have been proposed by researchers to mitigate and reduce this error as outlined in the following sections.

3.2 Mitigation

3.2.1 Antenna Mitigation

A simple multipath mitigation method is to reduce or avert reflections in the area of the antenna with appropriate site selection or using microwave absorbing materials. Elósegui *et al.* (1995) demonstrated how using microwave absorbing materials between the user and reference station antenna could reduce code multipath errors in the vertical antenna

position coordinates by 75%. Similarly Ning *et al.* (2011) showed that over 80% of multipath effects could be removed by placing a microwave absorber ring under the antenna on a microwave absorber sheet. They saw vertical coordinate component variations reduced from 27 mm to 4 mm.

Other mitigation methods can be related to the design of the antenna to improve the antenna gain pattern. Choke-ring antennas are common practice and reduce the majority of the code multipath by modifying the radiation patterns of the receiver antenna by using careful design and microwave absorbing materials. They are designed to attenuate reflected signals coming from negative elevation angles with respect to the antenna horizon. They do this by having a sharp cut off point below a certain elevation angle and lower gain for Left Hand Circular Polarized (LHCP), reflected signals. As mentioned in section 2.9.3, GNSS satellite signals are circularly polarized; incoming signals that have been reflected a single time from a highly specular reflector have their polarisation changed from right-hand to left-hand circular. This however only occurs if their angle of incidence with the reflector is less than Brewster's angle, as outlined in Groves (2013). Choke-ring antennas, however, do not mitigate multipath signals coming from positive elevation angles very well. The concentric ring formation of the antenna allows control over the acceptance and rejection of low elevation, direct and indirect signals and the balance between phase pattern features, gain and polarisation segregation with more recent designs using variable choke ring depth (Tranquilla and Al-Rizzo, 1994; Filippov *et al.*, 1998). The antennas, however, do not mitigate the carrier-phase multipath as effectively, as the code and multipath signals that have been reflected more than once and have been poorly attenuated, are still able to pass through the polarization filter and cause ranging errors.

Multiple closely-spaced antennas (<2 cm apart), can also be used to reduce multipath by forming small antenna arrays. Based on the assumption that reflected signals are highly correlated between closely-spaced antennas, the relative multipath amplitude, phase, as well as the geometry of the reflector, can be estimated at each of the antennas in the array, thereby reducing the number of unknown parameters in the Least-Squares Adjustment. The carrier-phase error due to the multipath signal can then be calculated and subtracted from the carrier-phase residuals of each antenna. Using this method, Ray *et al.* (1998) showed that 73% of carrier-phase multipath could be removed.

Signal processing techniques that take place within the receiver architecture can also be used to reduce this type of error. The initial approach of this category demonstrated that long additional multipath signals could be filtered out by reducing the spacing of the early and later correlators in the receiver hardware from 1 chip to 0.1 chip. Provided that the early and late correlators are processed simultaneously the noise element of the early and late signals caused by multipath are correlated so can be cancelled out. This technique is recognised as the narrow-correlator and reduces multipath and noise by over 80% (Van Dierendonck *et al.*, 1992).

Other receiver approaches use a mixture of correlator spacing and numerous early and late correlators. The Strobe correlator, for example, uses two contrasting narrow correlator discriminators but originally only provided code correlation for C/A code (Garin *et al.*, 1996). The Enhanced Strobe correlator however provides carrier-phase correction as well as code correction for C/A code and showed improved performance over previous methods (Garin and Rousseau, 1997).

Similarly to the techniques mentioned above, the Multipath Estimating Delay Lock Loop (MEDLL) approach can reduce the delay-lock-loop code multipath error by 90%. MEDLL utilises the maximum likelihood criterion and recursive Least-Squares method to estimate features of the multipath signal (magnitude, phase and delay) and remove them from the received signal (Van Nee *et al.*, 1994). Nevertheless, receiver internal mitigation techniques still have difficulties in mitigating short extra multipath signals (less than 30 m or 0.1 PN code chip) and introduce noise and interference to the signals, which is not desirable (Kaplan and Hegarty, 2006).

3.2.2 Post Processing

The majority of approaches mitigate multipath error at the post-processing stage. Wanninger and May (2001) proposed an estimation procedure to approximate carrier-phase multipath by using double-difference residuals from regional networks, using the correlation of multipath effects spaced one sidereal day apart. Carrier-phase corrections were applied to undifferenced observations that were used to form the double-difference residuals at the two stations to reduce the multipath error in the linear combinations. Corrections were stored as gridded azimuth and elevation hemisphere site templates of average double-difference standard deviations. However, multipath is not reduced in the original L1 and L2

observations and it is not always possible to allocate the multipath signature to a specific site or satellite due to the use of double-differencing and the need to ideally have a multipath free site or low multipath site in the network.

The concept of station calibration for multipath mitigation has also been presented, where antennas are moved robotically to try to randomize the multipath effect. Although operational costs are high for this method so it is not often used, in-situ calibration has been successful in removing far-field multipath effects which gives an insight into near-field multipath effects (Wübbena *et al.*, 2010).

Analysing the Signal-to-Noise Ratio (SNR) of GPS signals can also be used to produce time-constant azimuth and elevation multipath correction maps for GPS raw data on both the L1 and L2 frequencies. This is due to SNR being related to multipath error. The frequency and magnitude content of various multipath elements of the SNR time series can be extracted using wavelet analysis and any changes in the SNR linked to phase multipath, which can be used to determine which satellites and segments of the antenna environment are contributing most to multipath error and at which frequencies. The error patterns can then be projected on to hemisphere templates representing the antenna's reflective surroundings. The method is useful when observation periods are short as it does not rely on data from previous days. The method shows a 20% reduction in post-fit residual RMS at elevation angles lower than 20° and reduced spectral power in kinematic positions (Bilich and Larson, 2007; Bilich *et al.*, 2008b). The method is restricted by unavailability, inconsistency and precision in SNR units and definitions from different antenna/receiver manufacturers. Errors using wavelet analysis can also occur if aliasing occurs between multipath and genuine site movement frequencies, as it becomes difficult to separate the two components using frequency thresholds as this method employs. The phenomenon of aliasing can occur when signals with different frequencies are sampled at a uniform rate, leading to the under sampling of each signal, causing signal reconstruction substitution mistakes which could mask genuine site movement.

More advanced correction-mapping approaches account for the arc of the horizontal circle decreasing with increasing elevation angle by using congruent cells which allow for finer resolution at high elevation angles where signals can be heavily affected by near-field multipath effects. The standard deviations of carrier-phase observation residuals were found to reduce by up to 35% in high multipath environments, as defined in Knöpfler *et al.* (2010),

using dynamic cells (Fuhrmann *et al.*, 2015). However, even with varying cell size, high-frequency multipath effects are not captured effectively using this method of averaging measurement residuals into cells (Atkins and Ziebart, 2015).

SNR-based observation weighting in improved stochastic modelling has proved effective in reducing multipath effects by down-weighting phase data affected by multipath. Wieser and Brunner (2002) used conventional outlier detection methods with additional measured SNR values as a quality indicator to reweight parameter estimations in an iterative Least-Squares Fuzzy system. However, this approach does not account for the fact that although multipath error and SNR are correlated, there is a 90° or 270° phase difference between the two and they are orthogonal to one another. Due to this phase difference, data without multipath is often down-weighted by mistake as the cyclic nature of the signal is unaccounted for. Hence, the use of SNR can provide incorrect information for the quality of the phase measurement.

The cyclic nature of the phase multipath can be seen by expressing the damping factor of the reflected signal to the direct signal (β), from equation (2.3) in terms of the amplitude of the direct signal (A_d), and multipath signal (A_m), as given below:

$$\varphi = arctan\left\{\frac{A_m sin\theta}{A_d + A_m cos\theta}\right\} \tag{3.2}$$

The amplitude of the combined direct and multipath signal, A_c is given in Lau and Cross (2006) as:

$$A_c^2 = A_d^2 + A_m^2 + 2A_d^2 A_m^2 cos\theta \tag{3.3}$$

Figure 3.2 shows this relationship between the direct and multipath signal in terms of amplitude and phase. As explained in detail by Lau and Cross (2006), when the multipath signal is orthogonal to the direct signal ($\theta = 90°$ or $270°$), the amplitude of the combined multipath and direct signal is closest to the nominal signal and the carrier-phase multipath error is at a maximum and hence modulation distortion is at a minimum. The measured SNR

signal however is also close to the nominal SNR when no multipath is present, thus the incorrect weighting of multipath free signals occurs.

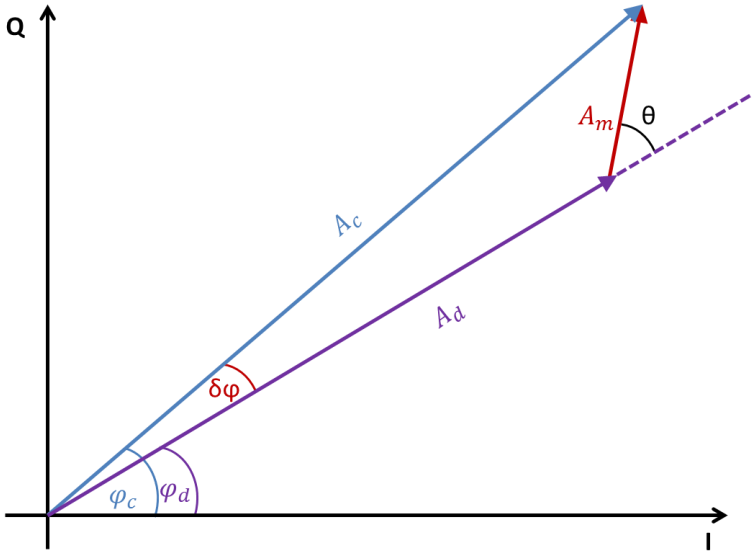

Figure 3.2: Phasor diagram showing the relationship between the direct, multipath and composite signals. The multipath phase errors depend on the amplitude (A) and carrier- phase (ϕ) of the multipath phasor where relative phase is denoted by θ *and I and Q refer to the in-phase and quadrature components.*

Lau and Cross (2006) described an SNR-based stochastic model which applies a modified SNR to form the stochastic model and phase measurement quality checker, which is determined by using empirical and calibrated data. The modified SNR accounts for the fact that phase multipath errors and SNR are orthogonal. Improvements of up to 35% were noted in the RMS of the coordinates in comparison with the standard Least-Squares method when used in a double-differencing positioning approach.

A Vondrak filter with cross-validation can also be used for mitigation. The filter can be used to separate carrier-phase signal from noise and cross-validation used to find the optimum smoothing factor. Improvements in the coordinate RMS values are between 20% and 40%. However, this approach can only be used when the noise level is lower than the magnitude of the signal. Genuine high-frequency signals related to station movement from an earthquake, for example, could be filtered out at high noise levels (Zheng *et al.*, 2005).

The approaches identified all have their disadvantages as outlined, making them inapplicable or inappropriate for real-time situations. For real-time early-warning an accurate GNSS displacement measurement is required within a few minutes of an earthquake rupturing. Station movement due to an earthquake can produce high-frequency signals, which fall into

the same frequency range as multipath. When SNR levels are high, approaches using SNR or the Vondrak filter can remove signals from actual station movement, which could result in earthquake size being underestimated or worse, not being registered. Using a double-difference approach also limits the effectiveness of these approaches, as pre-computed multipath maps cannot be assigned to a certain satellite or site which could cause complications if communications of multiple sites in a network are affected by an earthquake. The main limitation of using SNR techniques for PPP however, is the need to have up to date hardware data of entire networks. This makes multipath mitigation very computationally intensive as different parameters are needed to reflect each individual station's hardware. Bilich and Larson (2007) also noted that raw SNR observables can suffer from quality issues such as quantisation, the process of converting a signal into a signal with a smaller set of values that closely approximates the original signal, which can complicate power spectral map creation.

3.3 Sidereal Filtering

Other approaches to these described above, take advantage of the sidereal day (nominally 23h 56m 04s, 86164 s) repeating patterns of the GPS geometry, causing multipath at a site to be highly correlated across successive sidereal days. This is due to GPS satellites having an orbital period of half a sidereal day with a daily repeating ground track. This means that satellite visibility from any point on earth is the same from day to day and satellites appear in the same positions approximately 4 minutes (236 s) earlier each day, due to the time difference between the sidereal and solar day. Similarly, the GLONASS constellation geometry repeats about once every eight sidereal day so consecutive satellites will be seen in the same position as the previous satellite on consecutive days in each orbital plane and the same satellite will be in the same position eight sidereal days later.

Provided that the station remains fixed, the surroundings and antenna should not change significantly across consecutive days, therefore multipath signals are expected to strongly repeat over sidereal periods over the short time period of the filter's lifetime, as explained later in this section. The day to day repeatability of the multipath can hence be exploited using 'sidereal filtering' to improve positioning accuracies and mitigate the multipath error (Genrich and Bock, 1992; Nikolaidis *et al.*, 2001). This method allows an estimate of multipath signal at every epoch to be constructed and then subtracted from the time series

of subsequent days. The filters may also be stacked (averaged), before subtraction to improve precision and robustness. The technique can be used to filter errors either in the observations or the coordinate components and does not suffer from the effect of frequency aliasing. Coordinate domain filtering refers to extracting the coordinates of the previous day, with no significant station displacements occurring. Then shifting the extracted coordinates by the optimum sidereal repeat period and subtracting the extracted coordinates from the coordinate time series lagged by the optimum repeat period. In observation domain filtering on the other hand, the multipath filter is computed and subtracted from the carrier-phase observations, not the coordinate time series.

Bock *et al.* (2000) used coordinate sidereal filtering in continuous GPS crustal deformation monitoring with a set sidereal period of 86160 s to correlate positional errors. They investigated the effect of using different size stacking windows and found that a 3-sidereal day stack provided optimum noise reduction in the coordinate time series by about 50% in all components, when using instantaneous relative positioning with 30 second data.

As described in Choi *et al.* (2004), however, filtering is more effective when the correct satellite geometry repeat interval is used. They proposed a modified sidereal filter technique that uses the mean sidereal day of the GPS satellite constellation to correct positional errors. Due to the Earth's oblateness a secular nodal drift is produced westwards by 14.665° per year which affects the ground track repeat of the GPS orbit (Axelrad *et al.*, 2005). In order to compensate for this orbital plane motion, the average semi-major axis of the satellite orbits is set marginally lower, causing the orbital period to be about 4 seconds shorter than half a sidereal day. The satellite geometry hence does not repeat sidereally and the correct satellite geometry repeat interval can be used to improve filtering. An accurate repeat interval is particularly important for high-accuracy positioning at high rates (greater than 1 Hz), as multipath can change considerably over a few seconds; it can however also affect lower rate positioning. Ragheb (2007) showed how using the optimum repeat interval can improve observation domain filtering by 4% compared to when using the nominal repeat period for double-difference 1 Hz data.

Other studies have focused on determining the actual GPS satellite geometry repeat interval of individual satellites using satellite orbits and satellite residuals and found that applying the correct time shift is crucial for effective multipath mitigation. Axelrad *et al.* (2005) analysed three different methods of estimation for the correct individual sidereal repeat

period per satellite. The first method involves finding the average orbit repeat time shift (T_a) using the broadcast ephemeris and the orbital mean motion (Δn) deduced from Kepler's third law of planetary motion, as outlined below:

$$n = \sqrt{GM/a^3} + \Delta n \tag{3.4}$$

$$T_a = 86400 - 2(2\pi/n) \tag{3.5}$$

where GM is the Earth's universal gravitational parameter, a is the orbit semi-major axis and n the mean motion.

The second method finds the orbital time shift by using a Lagrangian interpolator to interpolate precise orbit products (SP3 files) to the equator crossing on successive days.

The third approach is based on the local geometry at the receiver on the ground. The optimum time shift is found when the dot product between the two receiver-to-satellite unit vectors associated with the current epoch measurement, and the prospective correction derived from the previous day's measurement, is at a maximum, as outlined fully in Axelrad *et al.* (2005).

Agnew and Larson (2007) used the broadcast ephemeris in the same way to find orbit repeat periods but compared their results to the aspect repeat method. The aspect repeat method is similar to the third approach outlined by Axelrad *et al.* (2005) but uses the topocentric instead of the geocentric-vector position of satellites to find the repeat interval. Similarly, Hung and Rau (2013) obtained the optimum average repeat times of GPS satellites by estimating the repeat time for each satellite using polynomial interpolation from the ECEF positions of each satellite.

Ragheb (2007) on the other hand used the day-to-day autocorrelation of coordinate and double-differenced 1 second carrier-phase residuals. Due to using a double-difference approach however, the repeat times computed are associated to satellite pairs, so do not fully represent each individual satellite's ground track repeat period.

Larson *et al.* (2007) developed an Aspect Repeat Time Adjustment (ARTA) method, based on the cross-correlation of coordinate residuals to determine the best GPS satellite repeat intervals, which can be varied to accommodate changes in the multipath environment. This approach emphasizes the fact that the application of coordinate component filtering will degrade the positioning solution if the repeat periods of the satellites differ greatly. Also satellites experience different levels of multipath and therefore contribute differently to the position estimates, something which will need to be considered when post-processing GNSS data.

The studies mentioned show that the repeat period for individual satellites can be computed by different methods which agree with each other to three seconds very often and to one second most of the time. Agnew and Larson (2007) mentioned that the optimum correction from filtering is obtained by using separate repeat times for individual satellites as opposed to the mean for the whole constellation. Most individual satellite lag periods were found to be within 5 seconds of the mean and remain fairly stable over an extended period of time, as shown by Agnew and Larson (2007) who computed the orbital periods for a ten year period. However, it can also be seen in Figure 3.3 how some orbital periods are very different, this is most likely due to orbit maintenance manoeuvres required to ensure the satellite's trajectory stays within a specified tolerance. When manoeuvres do occur satellites are flagged as unhealthy and are not used in a positioning solution.

Ragheb (2007) suggested that the optimum precision of a sidereal filter can be achieved from a 7-day stack, which saw a reduction in the time series variance of 61%. This study also highlighted the importance of the sidereal filter lifetime, the time period in which the filter remains useful in improving the precision of site coordinates. The filter lifetime starts to degrade from day 1, at day 30 there is no difference in precision from unfiltered cases. This could have a significant effect on the effectiveness of using a GLONASS filter created using data 8 sidereal days apart. Dai *et al.* (2014) showed how systematically updating the sidereal filter on a daily basis benefits its effectiveness by an improvement difference in coordinate accuracy of over 50% in comparison with traditional wavelet filtering techniques.

As well as investigating sidereal filter lifetime, Ragheb *et al.* (2007b) also compared coordinate and observation domain filtering approaches. They use 1 second GPS data with a double-difference strategy, for three short baselines formed from four sites across the Newcastle University campus. Due to using a double-differenced approach, as mentioned

earlier, the observation domain filtering orbit repeat periods are the averaged orbit repeat periods of the satellites. They are not the optimum orbit repeat period for each individual satellite, as maybe the case in PPP strategies. Ragheb *et al.* (2007b) found that there is little difference in 3D coordinate standard deviation improvement between the coordinate and observation domain filtering with average variance reduction of the three baselines being 35% and 32% respectively. Although the coordinate domain filter performance is slightly better, the computation time for this method was found to be longer and varied greatly with the severity of the multipath at the site. For a high multipath scenario, the total coordinate filtering time was about 6 times longer than observation domain filtering. Observation domain filtering computation time was unaffected by multipath severity or low sky visibility and resulting loss of lock of satellites. Hence, if using a double-difference approach for tsunami early-warning, observation domain filtering would be the preferred method in terms of speed, accuracy and adaptability to the multipath environment.

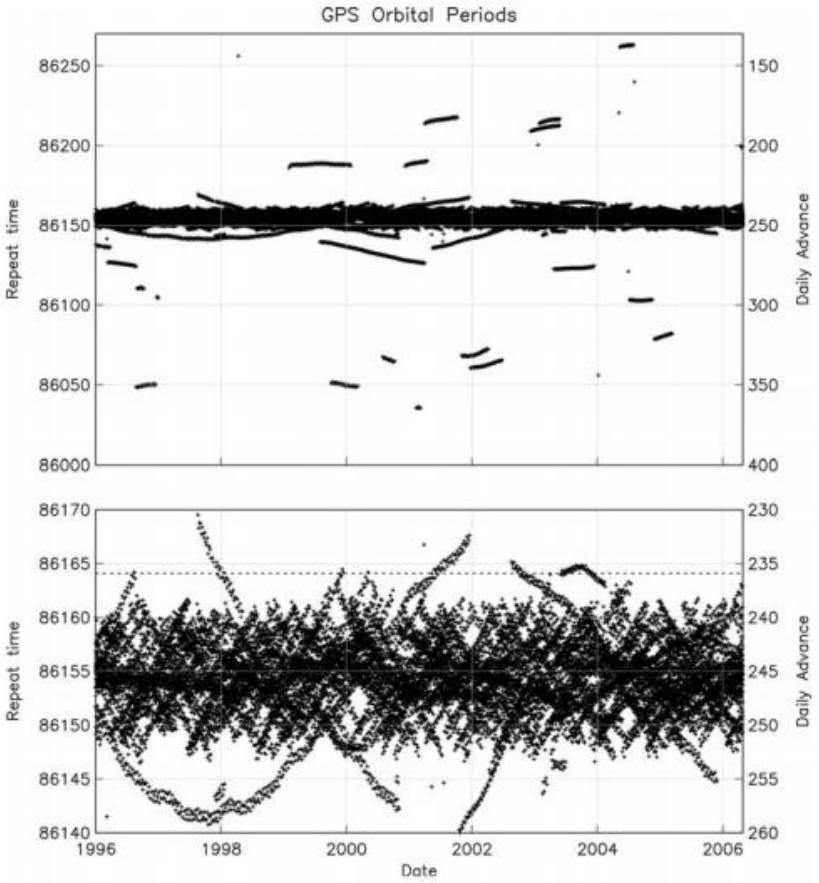

Figure 3.3: Orbital repeat times of the GPS satellite constellation found from broadcast ephemerides for the period between January 1st 1996 and April 3rd 2006 (Agnew and Larson, 2007). The top plot shows the full range of periods, whereas the bottom plot zooms in to show the most common repeat periods in relation to the sidereal-day repeat period, given by the dashed line. Both axes are in seconds where the left axis shows the daily advance relative to 24 hours.

Lau (2012) showed that positioning improvements for observation domain and coordinate domain filtering are very similar to one another (less than 7% difference) when a double-difference positioning approach over a short baseline is used. In contrast to Ragheb *et al.* (2007b), the mean and individual satellite orbit repeat periods were obtained by Lau (2012) from the broadcast ephemeris using the semi-major axis and the correction to the mean motion.

The lack of enhanced improvement from the observation domain filtering was speculated to be due to lack of high-frequency multipath occurring at the selected sites. Furthermore, on average, they found that positioning accuracy can be improved by about 40% with either filtering approach with efficiency being greatly dependent on the severity of multipath effects. The limiting factor of the sidereal filtering technique was shown to be changing weather conditions that affect the wetness of surfaces near the antenna. However, sidereal filtering has been shown to be more suitable for high-rate GNSS applications where high-frequency multipath is present compared to techniques such as hemispheric mapping which suit lower-frequency multipath mitigation (Dong *et al.*, 2015).

More recently Atkins and Ziebart (2015) compared the effectiveness of observation and coordinate domain filtering in undifferenced carrier-phase measurements, using 1 Hz data and with a PPP approach for two different receivers and multipath environments. They used the same methodology as in Lau (2012) to compute mean and individual orbit repeat periods. The observation domain filtering was out-performed by the coordinate domain filtering for time periods longer than 1000 s. This is believed to be due to the low frequency components of observation domain filtering corrections being applied inside the Kalman filter and probably being absorbed during the Kalman filter process into other parameters rather than into the residuals. Over short time periods (<1000 s) however, they found that the observation domain filter on average was 5%-16% more stable in terms of Allan deviation than the coordinate domain filtering. Hence, observation domain filtering would be more suitable when analysing periods of just a few minutes, which is the requirement for earthquake and tsunami early-warning systems.

Atkins and Ziebart (2015) also confirmed the findings of Larson *et al.* (2007) and Agnew and Larson (2007), that there is little difference between using different methods to calculate satellite repeat times. Conversely, they argued that techniques that use mean corrections from multiple days to improve filter robustness, such as the technique used by Ragheb *et al.*

(2007b), could reduce filter effectiveness of correcting for high-frequency multipath. This is due to satellite sky tracks changing slightly over adjacent days, causing corrections to be out of phase. This is something that even an accurate satellite repeat time cannot correct for and is due to the complex nature of multipath itself and has yet to be accounted for in multipath mitigation techniques.

As mentioned, sidereal filtering can be applied to the observation or coordinate components and it can also be applied using residuals from double-, single- or un-differenced approaches. Instead of using double-differenced residuals as in Ragheb (2007), Zhong *et al.* (2010) used a satellite-specific single-differenced approach to establish multipath models to be subtracted from single-differenced residuals of subsequent days. Coordinates were processed using the corrected single-differenced residuals in a double-differenced solution. Based on this method, Ye *et al.* (2015) went on to show how the method can be applied to satellite systems with vastly different orbital repeat periods within the same satellite constellation and applied to more than one satellite system at the same time.

The individual orbital repeat times for each BeiDou satellite in orbit at the time were calculated by Ye *et al.* (2015) using the method described in Agnew and Larson (2007), where periods of the GEO and IGSO were found to be near 1 sidereal day, but roughly 7 sidereal days for the MEO satellites. Multipath mitigation improved the RMS error of the coordinate components of the BeiDou satellites on average by 51% and the combined GPS and BeiDou solution by 65%. This demonstrates the adaptability of sidereal filtering for combined satellite systems for use in high-rate seismological studies that require a high level of precision.

Using a double- or single-difference approach requires the multipath model to be frequently updated when observed satellites differ between subsequent days. The measurement residuals are also associated with satellite pairs meaning certain generalisations have to be made in order to calculate the repeat period for individual satellites. Using an approach such as PPP removes the limitation mentioned as measurements are commonly undifferenced. Geng *et al.* (2013), however, alternatively used a single-differenced PPP approach to help remove clock and receiver hardware delay errors. PPP is also not limited by the need to completely remove any mutual atmospheric, clock or orbital errors prior to multipath mitigation as for a double-difference solution (Reuveni *et al.*, 2012). This is due to PPP using

global orbit and clock products and modelling atmospheric corrections for each site individually, thus the majority of the residuals are due to the contribution of multipath error.

As reviewed above sidereal filtering is an effective way of removing multipath error. The effectiveness relies on sites having a strong multipath signal, with the surrounding environment remaining relatively unchanged over successive days with comparable weather conditions.

Coordinate and observation domain filtering both prove to be effective in mitigating multipath error in either a double-difference or PPP positioning approach. Observation domain filtering however is shown to be more stable over short time periods and quicker to implement (Ragheb *et al.*, 2007a; Atkins and Ziebart, 2015). Hence, for early-warning systems, observation domain filtering is the preferred choice as a displacement measurement is required rapidly at the slight expense of accuracy.

The performance of observation domain filtering, particularly for high-rate data, relies on the ability to accurately determine the individual repeat time for each satellite. The various methods mentioned for finding the optimum repeat time for GPS satellites are in agreement with one another by +/- 3 seconds. The double-difference correlation approach used in Ragheb *et al.* (2007b) was limited due to using mean repeat periods. In contrast, orbital parameter methods are not universal for different satellite constellations which make GLONASS orbital repeat methodology harder to validate. Therefore, correlation of the day to day carrier-phase residuals in a PPP solution has been deemed the most suitable method for this thesis as it can be used for both GPS and GLONASS constellations to find individual satellite repeat times.

3.4 GPS Sidereal Lag Investigation

As discussed above satellite geometry repeat periods are not the same as the sidereal day (23h 36m 04s) therefore it is necessary to calculate the lag of the repeating errors in the residuals caused by the receiver's reflective environment. The GPS constellation geometry repeats once every near sidereal day, so the same satellite is seen about the same time every day from a fixed location.

Accordingly a script was established in MATLAB for the GPS satellite constellation to determine the optimum value of the 'sidereal' lag for the filtering application. For this, a

correlation methodology is used, where satellite residuals (carrier-phase and code) are correlated against subsequent epochs. This is straightforward as each satellite residual is correlated against the residual in the same data set that is roughly a sidereal day apart. Correlation C, a value between -1 and 1 for each lag value k, can be calculated as follows:

$$C(k) = \frac{\sum_{i=1}^{N} X_i X_{i+k}/N}{\sqrt{\sigma_i^2 \sigma_{i+k}^2}} \tag{3.6}$$

$$\sigma_i^2 = \frac{\sum_{i=1}^{N} (X_i - \mu_i)^2}{N} \tag{3.7}$$

$$\mu_i = \frac{\sum_{i=1}^{N} X_i}{N} \tag{3.8}$$

where X_i is the carrier-phase residual from the current epoch, X_k is the lagged carrier-phase residual and N is the number of epochs in each window. σ_i^2 and σ_k^2 give the variance for the current epoch and lagged residuals in each window, and similarly μ_i is the mean, given here just for the current epoch as the lagged variance and mean are computed in the same way.

The correlation value is computed for all valid epochs for chosen lag values ranging around the nominal lag. 60 lag values were considered for GPS with one second separation, ranging from 23h 55m 30s (86130 s) to 23h 56m 30s (86190 s) based on previous research (Ragheb, 2007). The correlation was computed from 8 days of GPS data. A 2 hour window size ($N = 7200\ s$ in the above equations) was used as Ragheb (2007) deemed usable values could be obtained for a 2 hour window with at least 97% of the values being the same as those computed from longer window sizes which are more computationally intensive. The highest mean correlation value closest to 1 from all windows hence corresponds to the optimum value of lag and the lag value to be used in the filter. Optimum lag values were calculated and applied individually for each site, satellite and signal.

3.5 Stacking Methodology

Once the sidereal lag is known, the residuals can be stacked to create a sidereal filter. Stacking is the process of averaging residuals at epochs separated by multiples of the optimum sidereal value, over a selected number of days. A stack of 7 days for GPS has been used in this thesis as Ragheb *et al.* (2007a) showed how the 24 hour coordinate variance of a time series decreases with the number of days added into the filter stack and is at a minimum at 7 days. A 5 second moving average is also applied to smooth the filter values, to help minimise the amplification of high-frequency measurement noise when the correction filter is applied.

3.6 Application of Filter

The stacking of residuals at all epochs for each individual satellite forms a sidereal filter which can be applied to each satellite carrier-phase and code residual during processing. Each residual is matched to the correct time tag and filter value in the filter file and the correction subtracted at the observation equation level as expressed below:

$$X_i^{fltr} = X_i - \Delta X_i \tag{3.9}$$

where i is the epoch, X_i^{fltr} is the filtered residual, X_i is the observed residual, and ΔX_i is the sidereal filter as mentioned previously. The station coordinates are then computed from the corrected observation residuals in PPP using the exact same approach as for unfiltered residuals. This methodology was implemented in to the PANDA software by Dr Ian Martin.

An outlier detection element to the filter to remove outliers, such as those due to the effects of the daily orbital products which lack continuity across the day boundaries, was required to ensure only multipath is being removed by the near-sidereal filter. This was created in MATLAB, based on the Median Absolute Deviation (MAD). This method was chosen over other outlier detection methods such as the mean and standard deviation, as it is not sensitive to the presence of outliers.

The MAD can be calculated as seen overleaf:

(3.10)

$$MAD = med\ |x_i - med\ x_{i=1}^{n}|$$

where med refers to calculating the median of the data set $x_{i=1}^{n}$, $\{x_1, x_2 \dots x_n\}$, where x_i is an individual value in the data set. The MAD can additionally be multiplied by a constant value (b) of 1.4826 which ensures that the MAD will converge to σ for a normally distributed data set. For data that follows another distribution, b is equal to the inverse of the 75th centile of the raw MAD (Leys *et al.*, 2013).

If a value is more than a certain number of MADs away from the median of the residuals, that value is categorised as an outlier. Three rejection criteria, deviations of 3, 2.5 and 2, as outlined in Miller (1991), were tested. A deviation of 3 was found to remove the orbital defects from the time series most effectively and is a common deviation value used for outlier detection methods (Liu *et al.*, 2004). Using a threshold of 3 deviations, the decision criterion can be seen as:

(3.11)

$$med - 3 * MAD < x_i < med + 3 * MAD$$

Any epoch where a value fails to meet this criterion is rejected and does not contribute to the averaged values in the filter or contribute to any of the statistical analysis between unfiltered and filtered cases.

3.7 Data Handling and PPP Processing using PANDA Software

To assess the levels of multipath at the selected sites, characterisation of the multipath environment at each site was performed using carrier-phase residuals grouped in 3° by 3° bins of the sky; 30 bins for elevation angles between 0°-90° and 120 bins for the azimuth between 0°-360°. The RMS error was computed for each of these bins. Sites HUNG, KILN, OBAN, MACY and PADT from the OSGB GNSS network were selected due to their relatively high carrier-phase residual RMS and site REDU mentioned later in section 3.9.1, due to its lower RMS values, as seen in Figure 3.4. To ensure that the dominant signal in the residuals is in fact multipath and not say due to the troposphere, the carrier-phase residual RMS values were normalised and plotted against azimuth and elevation angles under 30° where multipath is strongest. As seen from Figure 3.5 and Figure 3.6, the normalised carrier-phase

residual RMS values are elevation dependent; they are higher at lower elevation angles, which are in keeping with multipath characteristics, as outlined in section 3.1. The gaps around the azimuth angle extents, particularly at higher elevation angles can be attributed to the lack of GPS satellites directly overhead due to the inclination of the GPS satellite orbits. The gap at site KILN at low elevation angles between azimuth angles 80°-160˚ is likely due to an obstruction blocking the satellite signals. The behaviour of the RMS values surrounding this gap again point to multipath being the dominant signal in the residuals, as the values are high, elevation and azimuth angle dependent and vary greatly, indicating multipath from signals reflecting of the obstruction. The troposphere on the other hand, although highly elevation dependent would not be expected to fluctuate this much between azimuth angles within such a small area and time.

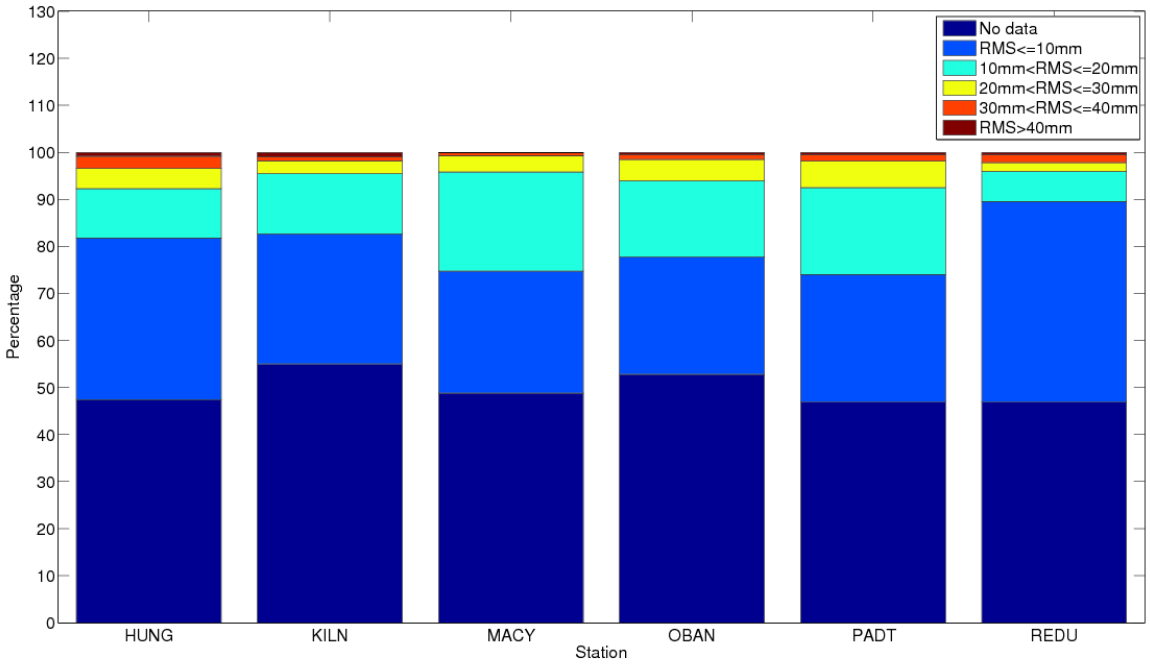

Figure 3.4: Percentage breakdown of GPS-only carrier-phase residuals RMS at all elevation angles. Empty bins occur when there is no data available due to no satellites being seen at a particular elevation and azimuth angle bin.

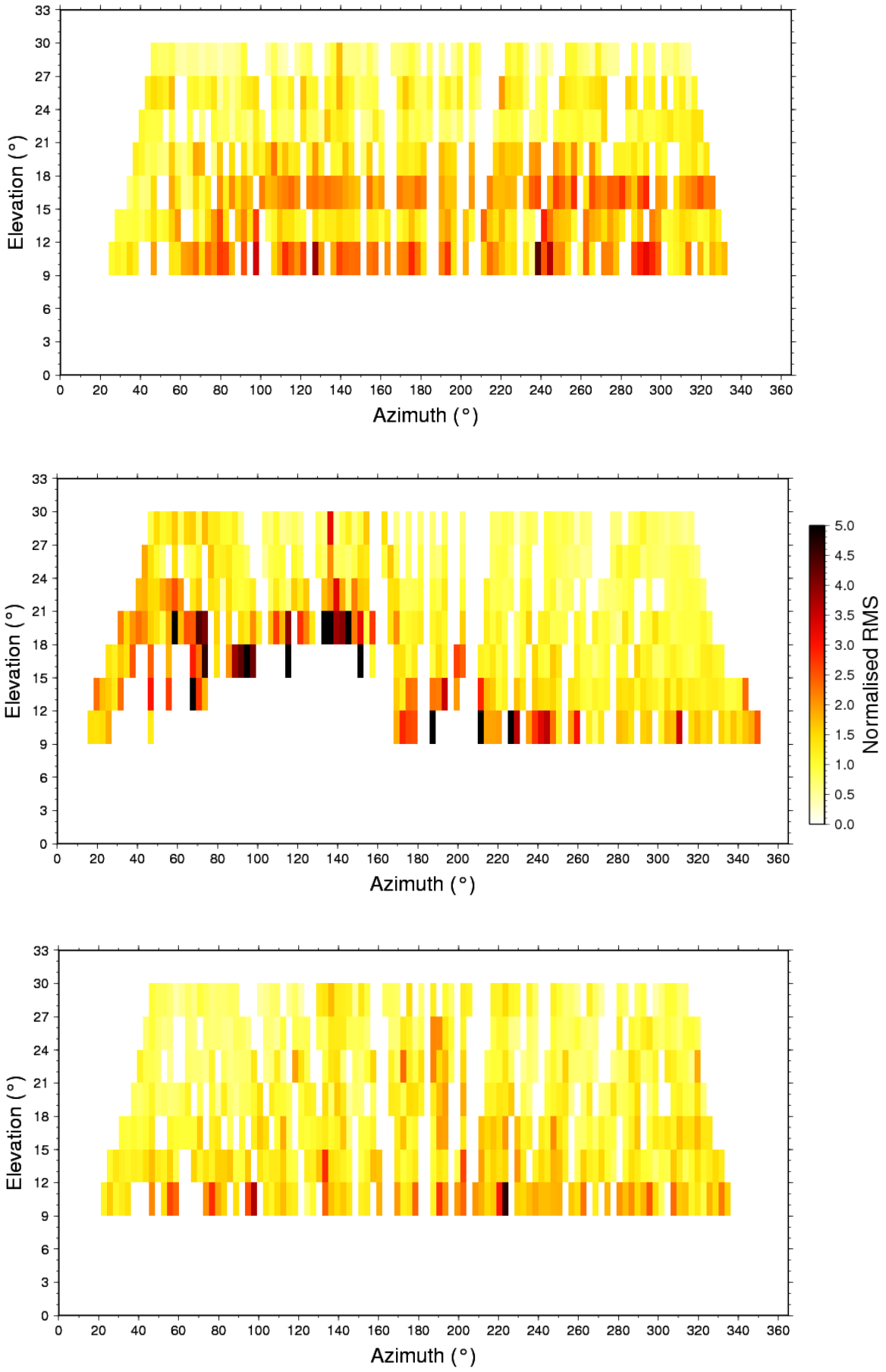

Figure 3.5: GPS-only carrier-phase residual normalised RMS variation with elevation angles up to 30° and azimuth angles, for sites HUNG (top), KILN (middle) and MACY (bottom).

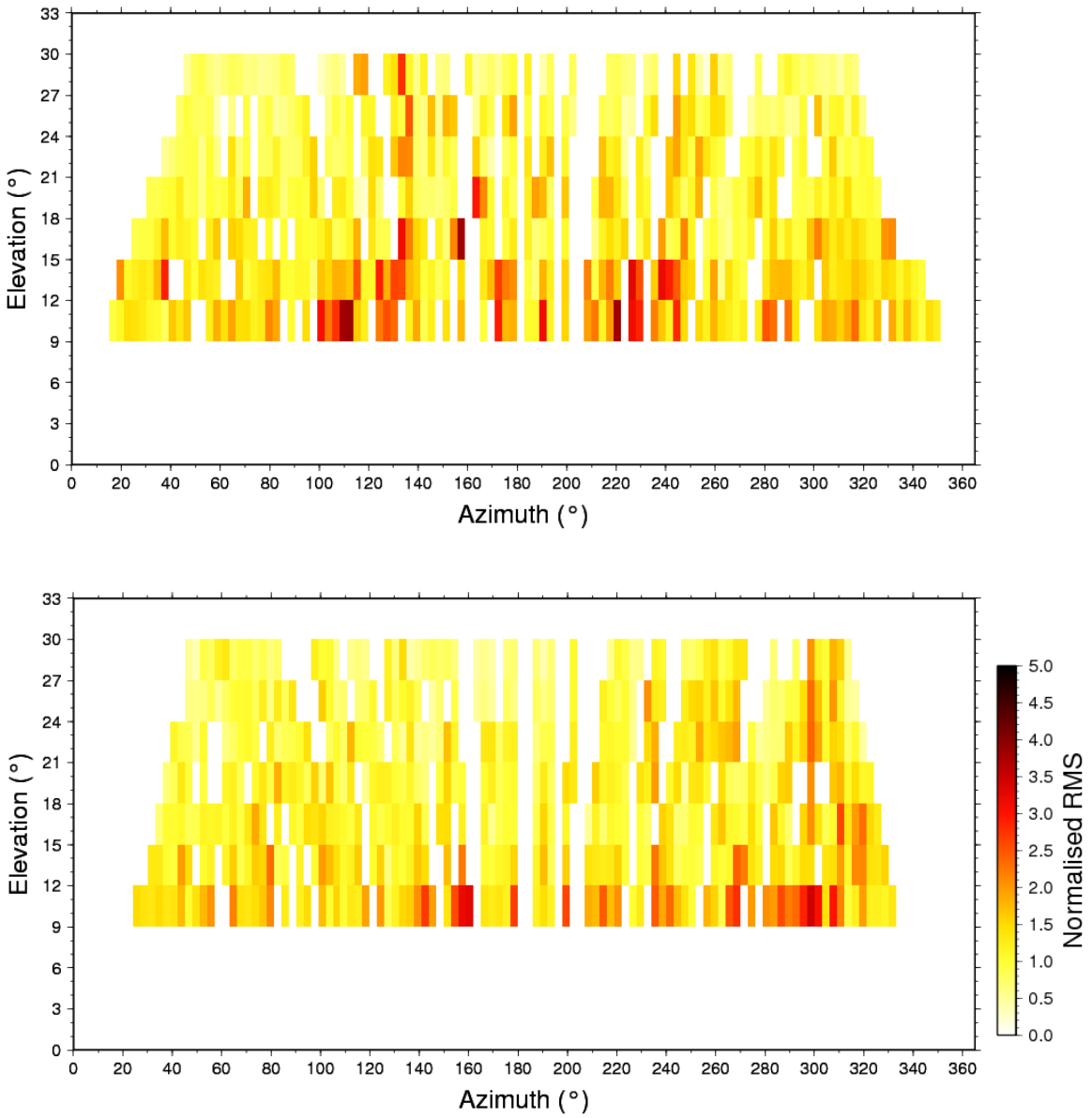

Figure 3.6: GPS-only carrier-phase residual normalised RMS variation with elevation angles up to 30° and azimuth angles, for sites OBAN (top), PADT (bottom).

The OS sites are installed with a Leica AR25 antenna, a Leica GRX1200+GNSS receiver which has full GNSS signal tracking capabilities and use firmware versions 8.20/MEv4.007. The location of the selected OS sites can be seen in Figure 3.7.

For accurate optimum lag period determination a 1 Hz data set was collected over a continuous 22 day window in November 2014 (days of the year, 306 to 327). A low elevation mask angle (10°) was used to allow typically higher multipath error generating low elevation satellites to be included, to ensure that the robustness of the sidereal filtering could be easily tested.

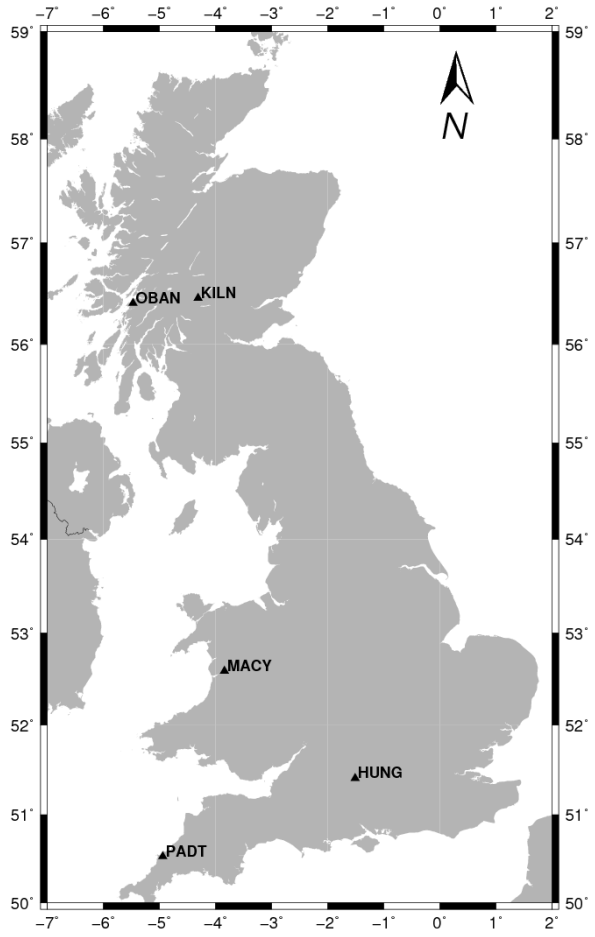

Figure 3.7: OS Net site locations in the UK

Data was firstly processed in static PPP mode using the PANDA (Positioning And Navigation Data Analyst) software which was developed by Wuhan University. As outlined in Table 2.3, PANDA is capable of processing GNSS data from multiple satellite constellations and has been used by numerous international research institutes to determine precise satellite orbits, such as for CHAMP (CHAllenging Minisatellite Payload), GRACE (GRAvity Climate Experiment) and COSMIC (Constellation Observing System for Meteorology Ionosphere and Climate). Hwang *et al.* (2009), for example, use PANDA to validate orbits determined by different software, the Bernese software. PANDA has also been used in numerous research studies; Geng *et al.* (2009) use PANDA to improve the speed of integer ambiguity resolution for single GPS receivers. Shi *et al.* (2010) use PANDA software to estimate the displacement from the 2008 Wenchuan earthquake using 1 Hz position time series from GPS data, and similarly, Chen *et al.* (2016) measure displacements from the 2015 M_w 8.3 Illapel earthquake using a combination of GPS and GLONASS data processed using PANDA software.

Like the majority of PPP software packages PANDA contains the following modules: data pre-processing (Turbo-Edit method used to remove gross outliers and detect large cycle slips) (Blewitt, 1990), orbit integration, residual-editing (used to remove smaller cycle slips and outliers), parameter estimation and the option for GPS ambiguity-fixing. The software is able to be used for real-time and post-mission processing and therefore has two different estimators, a Square Root Information Filter for real-time and a Least-Squares (batch) estimator for post. In this study the recursive Least-Square estimator was used with back smoothing. The structure and modules of PANDA are outlined in more detail in Shi *et al.* (2008b). The parameters estimated by PANDA for this study were the coordinates, receiver clock biases, wet tropospheric delay and an inter-frequency bias term to account for the difference in GPS and GLONASS signals at the receiver (inter-system bias), and satellite and frequency dependent code bias. ESA 'Final' orbit and clock products, as discussed in Table 2.2, were used for the majority of this study unless otherwise stated, to demonstrate the full potential (i.e. through the use of accurate orbit and high-rate GPS and GLONASS clocks) of the sidereal filtering methodology to remove multipath error. For a real-time application, such as tsunami early-warning, real-time products would need to be used; however erroneous satellite clock offsets could mask the true effectiveness of the sidereal filter so the real-time products have not been used in this study. It is expected that real-time orbit and clock products should improve with the addition of more stable clocks onboard future GNSS satellites, and hence, advance the use of sidereal filtering for real-time scenarios. Initial results for one hour real-time GPS orbit estimates are better than 5 cm and clocks better than 0.2 ns when compared to IGS 'Final' products, so improvement in the future looks promising (Shi *et al.*, 2008a). A cutoff elevation of 10° was used to remove multipath error from very low elevated satellites which typically produce higher levels of multipath, as outlined in section 3.1. The error sources discussed in Chapter 2 were also considered, Table 3.1 lists the relevant parameter estimation strategies and correction details used in PANDA for this study.

The GPS carrier-phase and code residuals output from PANDA were separately correlated to find the optimum for each satellite in the constellation, using the MATLAB script as described in section 3.4. Figure 3.8 shows a system diagram outlining the overall filtering process implemented using the PANDA software.

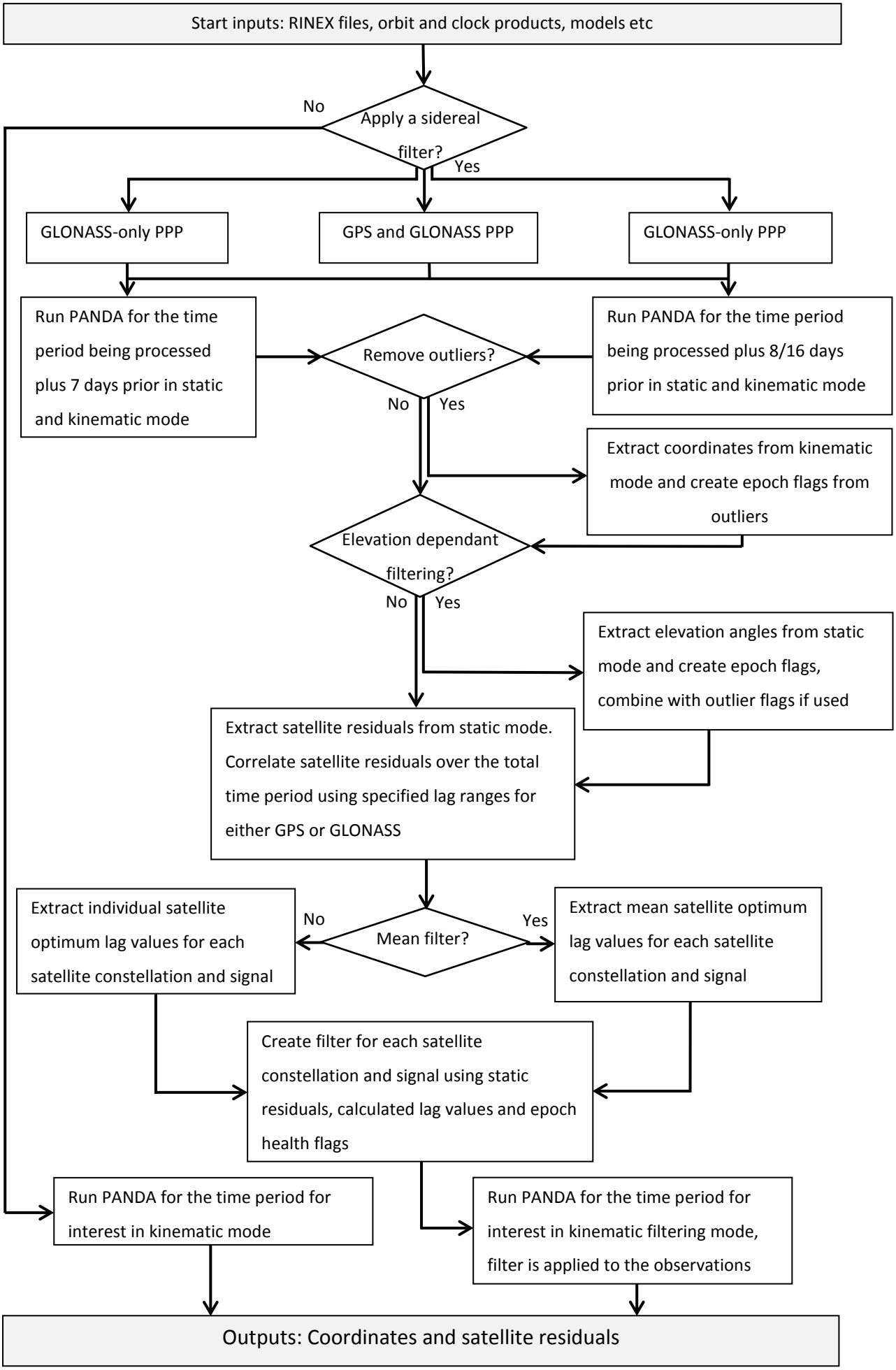

Figure 3.8: Diagram of filter implementation into the PANDA software. Please refer to the main text for description.

Table 3.1: GPS and GLONASS PANDA PPP processing strategy

Item	Models and Constraints
Observations	GPS and GLONASS LC/PC
Elevation Angle Cutoff	10°
Sampling Rate	1 s
Weighting Strategy	Elevation dependent weighting for observations under 30° according to: $w = {}^{1}/_{2} \sin E$
GPS and GLONASS Weighting Strategy	The GPS and GLONASS constellations both contribute equally to the overall positioning solution
Orbit and Clock Products	Fixed, ESA 'Final' GPS and GLONASS products (15 mins and 30 s)
Satellite Antenna PCO/PVC	igs08.atx
Phase Windup	Corrections applied
Receiver Antenna PCO/PCV	igs08.atx
Tropospheric Model	Saastamoinen model for wet and dry hydrostatic delay, estimated every 1 h
ZTD Process Noise	0.020 m/sqrt(s)
Mapping Function	GMF
Ionosphere	1st order eliminated by ionosphere-free linear combination
Solid Earth Tides	IERS Conventions 2010
Solid Earth Pole Tides	IERS Conventions 2010
Ocean Tides	FES2012
Time System	GPS Time
Terrestrial Frame	IGb08
Coordinate Sigmas	5 m
XYZ Process Noise	0.5 m/sqrt(s)
Receiver Clock Process Noise	900.0 m/sqrt(s)

3.8 Optimum GPS Lag Period

GPS filtering was conducted separately at first to validate the correlation methodology for finding the optimum lag period for individual satellites in the constellation. As seen from

Figure 3.9 the correlation curves for the carrier-phase residuals are generally broad, with the exception of site KILN, which has a steep sided curve, with correlation varying more rapidly with lag period. The difference in correlation pattern at KILN is likely due to the difference in site environment compared to the other sites. As seen in the photographs in Appendix A, KILN is located on a pillar above grassland next to a metal fence, whereas, the other antennas are mounted on top of roofs made with highly reflective manmade materials. It is expected that the rooftop sites will experience specular multipath where reflected signals are strong and systematic, KILN on the other hand, due to the vegetation, will experience diffuse multipath where signals are randomly scattered. The multipath at KILN is thus less systematic and hence shows weaker correlation values. The mean lag period for the whole GPS constellation for all 5 sites peaks between 86155 s and 86156 s for the 8 day time span considered. These are comparable to the mean values computed from previous studies, as outlined in Table 3.2. This validates that the correct correlation methodology has been implemented. The studies mentioned have all used varying methodologies, time periods and sites as outlined in Table 3.2, hence the slight variation in mean between them. The majority of the studies mentioned have used individual satellite orbits and satellite residuals to compute the optimum lag period. They include in brief: finding the average orbit repeat time using the broadcast ephemeris and the orbital mean motion; interpolating precise orbit products to the equator crossing on successive days; finding when the dot product between two receiver-to-satellite unit vectors associated with the current epoch measurement and the prospective correction derived from the previous day's measurement is at a maximum; and using the day-to-day autocorrelation of coordinate and carrier-phase residuals as explained in section 3.3.

Along with the mean for the whole constellation, the optimum lag periods per satellite were also computed to increase the filter's effectiveness, as mentioned in section 3.3. Tables 3.3 and 3.4 show how for all sites the individual satellites' optimum lag values only vary on average from the constellation mean by just over 3.5 s for the carrier-phase residuals and slightly higher for the code residuals. Figure 3.10 shows a visual representation of finding the optimum lag value for individual satellites using carrier-phase residual correlation for site MACY. It can be seen how the correlation strength is satellite dependent with variations within the constellation ranging from 0.4 to 0.85 for this site. The individual satellites' optimum lag values for the carrier-phase and code residuals for all sites can be seen in Tables 3.3 and 3.4 respectively. The carrier-phase and code residuals have slightly different

optimum lag values for individual satellites with the code values showing slightly more variations from the constellation mean, this is most likely due to the code being less accurate than the carrier-phase.

In order to validate the correlation methodology is able to correctly compute optimum lag values, the aspect repeat method, as outlined in Agnew and Larson (2007), was also used to computed lag values for this time period. The FORTRAN script 'asprep.f' taken from the above mentioned study was used to compute lag values for the aspect repeat method. As seen in Table 3.3, the correlation and aspect repeat method agree with one another within less than 2 s most of the time and the method was able to compute optimum lag values for satellites that the correlation method could not, such as G08. The aspect repeat lag values for satellites G04 and G13 however, are over a 100 s different to the mean values found by the correlation method and the constellation mean. As well repeat time, 'asprep.f' also computes the angular separation between repeated satellites passes which indicates how close the satellites positions are between each repeat period. The smaller the separation angle, the closer the satellite is to being in the same position, which hence shows a genuine repeat. Satellites G04 and G13 both show angular separation values ten times larger than the majority of the constellation, which indicates that the method has not calculated a genuine repeat period. This could be due to a satellite maneuver or the orbits being at a different incline or more elliptical than the rest of constellation which alters the orbit repeat period.

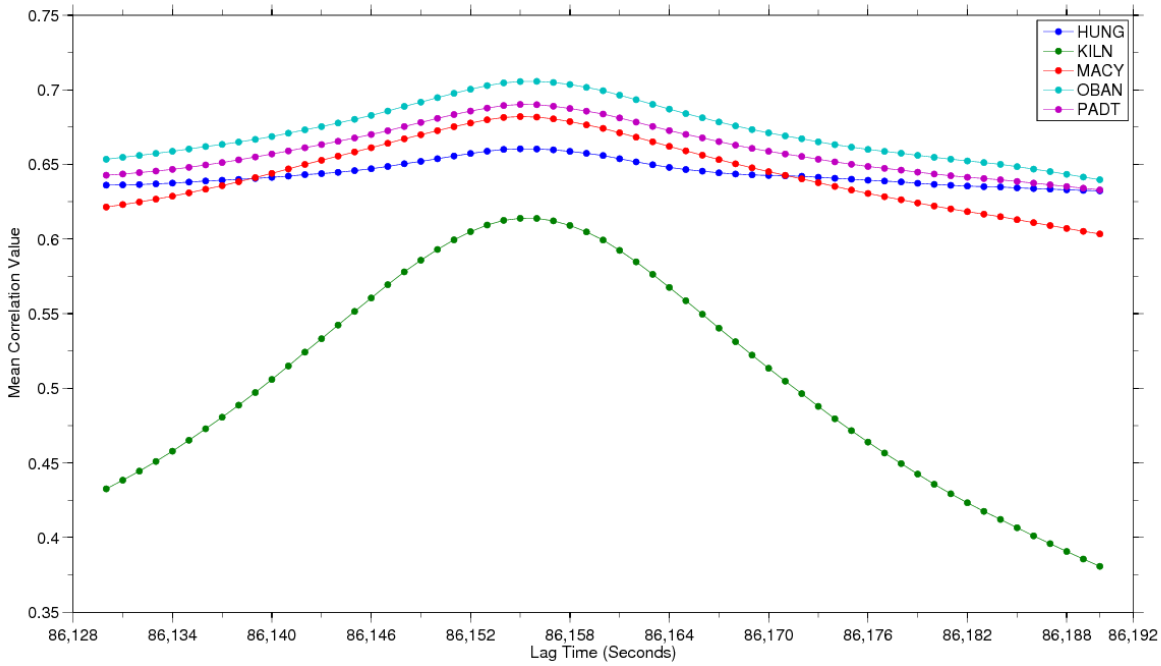

Figure 3.9: Mean GPS satellite constellation carrier-phase residual correlations at a range of near-sidereal lag values, for a selection of OS Net sites, 2014, days 320 to 327.

Table 3.2: Mean lag periods of the GPS constellation by different authors using a range of different methodologies for sidereal filtering.

Study	Methodology	Mean lag period	Calculation period
Axelrad *et al.* (2005)	Line-of-sight unit vector maximum dot product	86154 s to 86156 s	01/01/04-31/12/04
Larson *et al.* (2007)	Broadcast ephemeris average orbit repeat Line-of-sight unit vector maximum dot product Time of equator crossings interpolation from precise orbits	86155 s	25/09/04-29/09/04
Agnew and Larson (2007)	Broadcast ephemeris average orbit repeat Aspect repeat time	86153 s to 86154 s	01/01/96-30/04/06
Ragheb *et al.* (2007b)	Observation residuals correlation	86154 s	04/04/05-08/04/05 and 13/12/05-17/12/05
Hung and Rau (2013)	Aspect repeat time	86153 s	08/03/11-11/03/11
This Study	Observation residuals correlation	86155 s to 86156 s	02/11/14-23/11/14

Table 3.3: Standard deviations of the GPS carrier-phase residuals, optimum lag values per satellite at selected OS Net sites, and the optimum lag values calculated using the aspect repeat method, 2014, days 306-327. All values are given in seconds.

Site	HUNG	KILN	MACY	OBAN	PADT	Sat Mean	Sat St.dev	Aspect Repeat
Opt lag value St.dev	3.82	3.50	3.30	3.20	3.92	-	-	-
Sat 01	86154	86154	86154	86154	86154	86154.00	0.00	86154
Sat 02	86157	86157	86156	86157	86156	86156.60	0.49	86156
Sat 03	-	-	-	-	-	-	-	-
Sat 04	86142	86166	86145	-	86142	86148.75	10.03	86039
Sat 05	86158	86158	86158	86158	86157	86157.80	0.40	86157
Sat 06	86152	86152	86152	86152	86152	86152.00	0.00	86152
Sat 07	86151	86150	86151	86150	86151	86150.60	0.49	86151
Sat 08	-	-	-	-	-	-	-	86057
Sat 09	86156	86156	86156	86156	86157	86156.20	0.40	86157
Sat 10	86153	86152	86153	86153	86152	86152.60	0.49	86152
Sat 11	86157	86156	86156	86156	86156	86156.20	0.40	86156
Sat 12	86162	86161	86161	86162	86161	86161.40	0.49	86161
Sat 13	86160	86160	86160	86161	86162	86160.60	0.80	86290
Sat 14	86158	86160	86158	86159	86160	86159.00	0.89	86159
Sat 15	86160	86161	86158	86163	86162	86160.80	1.72	86162
Sat 16	86157	86157	86157	86157	86157	86157.00	0.00	86156
Sat 17	86155	86155	86155	86155	86155	86155.00	0.00	86154
Sat 18	86158	86159	86158	86159	86158	86158.40	0.49	86158
Sat 19	86155	86155	86154	86155	86154	86154.60	0.49	86154
Sat 20	86155	86155	86155	86156	86155	86155.20	0.40	86155
Sat 21	86152	86153	86153	86153	86153	86152.80	0.40	86153
Sat 22	86158	86158	86158	86158	86157	86157.80	0.40	86157
Sat 23	86157	86156	86156	86157	86157	86156.60	0.49	86157
Sat 24	86154	86155	86155	86155	86156	86155.00	0.63	86156
Sat 25	86160	86159	86160	86158	86159	86159.20	0.75	86160
Sat 26	86156	86156	86155	86156	86156	86155.80	0.40	86155
Sat 27	86155	86155	86155	86155	86155	86155.00	0.00	86155
Sat 28	86157	86156	86156	86156	86156	86156.20	0.40	86156
Sat 29	86152	86151	86151	86151	86151	86151.20	0.40	86150
Sat 30	86152	86153	86152	86152	86153	86152.40	0.49	86153
Sat 31	86155	86155	86155	86155	86154	86154.80	0.40	86154
Sat 32	86151	86151	86151	86151	86152	86151.20	0.40	86151

Table 3.4: Standard deviations of the GPS code residuals and optimum lag values per satellite at selected OS Net sites, 2014, days 306-327. All values are given in seconds.

Site	HUNG	KILN	MACY	OBAN	PADT	Sat Mean	Sat St.dev
Opt lag value St.dev	4.29	3.38	3.90	3.68	4.03	-	-
Sat 01	86160	86155	86154	86155	86154	86155.60	2.24
Sat 02	86155	86158	86157	86157	86155	86156.40	1.20
Sat 03	-	-	-	-	-	-	-
Sat 04	86142	86149	86142	-	86142	86143.75	3.03
Sat 05	86158	86156	86157	86158	86157	86157.20	0.75
Sat 06	86153	86153	86151	86152	86150	86151.80	1.17
Sat 07	86148	86151	86149	86150	86151	86149.80	1.17
Sat 08	-	-	-	-	-	-	-
Sat 09	86157	86155	86156	86157	86156	86156.20	0.75
Sat 10	86154	86157	86154	86152	86153	86154.00	1.67
Sat 11	86159	86154	86156	86156	86155	86156.00	1.67
Sat 12	86164	86159	86160	86161	86161	86161.00	1.67
Sat 13	86160	86146	86160	86160	86160	86157.20	5.60
Sat 14	86157	86160	86161	86160	86160	86159.60	1.36
Sat 15	86160	86161	86159	86165	86163	86161.60	2.15
Sat 16	86154	86156	86157	86157	86155	86155.80	1.17
Sat 17	86155	86155	86155	86154	86153	86154.40	0.80
Sat 18	86159	86160	86160	86160	86157	86159.20	1.17
Sat 19	86157	86155	86154	86154	86154	86154.80	1.17
Sat 20	86159	86155	86155	86155	86155	86155.80	1.60
Sat 21	86152	86151	86153	86152	86153	86152.20	0.75
Sat 22	86157	86156	86159	86158	86156	86157.20	1.17
Sat 23	86159	86157	86156	86157	86156	86157.00	1.10
Sat 24	86155	86155	86154	86157	86155	86155.20	0.98
Sat 25	86160	86159	86159	86162	86161	86160.20	1.17
Sat 26	86156	86155	86155	86156	86156	86155.60	0.49
Sat 27	86157	86156	86154	86156	86155	86155.60	1.02
Sat 28	86154	86156	86156	86157	86156	86155.80	0.98
Sat 29	86150	86153	86151	86150	86150	86150.80	1.17
Sat 30	86152	86151	86152	86152	86153	86152.00	0.63
Sat 31	86154	86154	86154	86154	86157	86154.60	1.20
Sat32	86153	86151	86152	86151	86151	86151.60	0.80

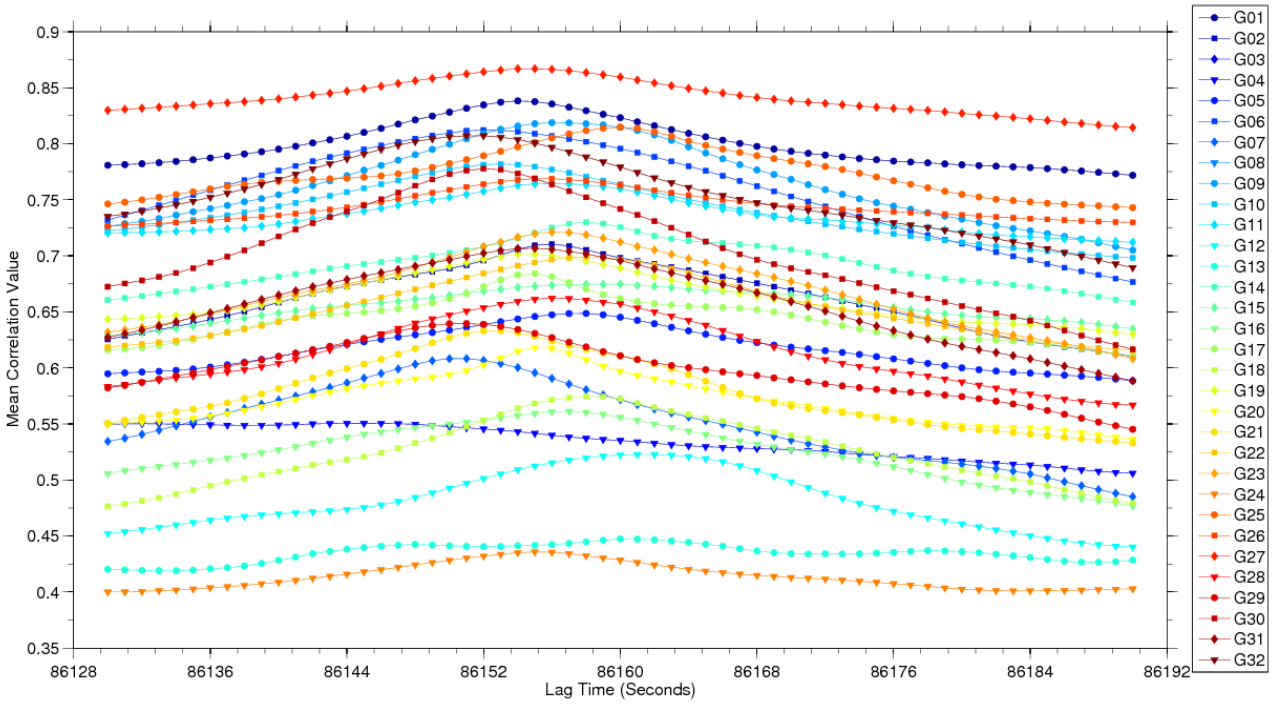

Figure 3.10: Mean correlation values of GPS carrier-phase residuals at different near-sidereal lag ranges at MACY, 2014, days 320 to 327.

3.9 GPS Sidereal Filter Performance

Once the optimum lag period was determined separately for each site, satellite and signal, individually, sidereal filters for carrier-phase and code residuals were made by stacking the static residuals at the individually computed lag periods for each site, as given in Table 3.3 and Table 3.4. The filters were then included into PANDA where they were subtracted from the original observation residuals, and processed in kinematic mode, as outlined previously in section 3.6.

The coordinate differences from the known coordinate positions of the filtered and unfiltered kinematic time series are shown for HUNG in Figure 3.11 after outlier detection. The best epoch from both scenarios, the coordinate closest to the known coordinate position (zero), is also plotted to act as a visual reference guide. The standard deviation and the coordinate RMS percentage decrease of each coordinate time series was computed along with the 3D RMS percentage decrease for statistical analysis. In addition to this the standard deviation of the unfiltered and filtered carrier-phase residuals for each individual

satellite are plotted along with the mean standard deviation for the whole GPS satellite constellation.

Upon examination of Figure 3.11, it can be seen how consecutive days show similar variations in coordinates in all three dimensions over periods of a few minutes and over larger periods of a few hours. For example there is a distinct sidereal repetition in the North coordinate at roughly 6.45am each day where the coordinate error fluctuates from ±7 cm in the space of about 20 minutes as highlighted by the red ellipse.

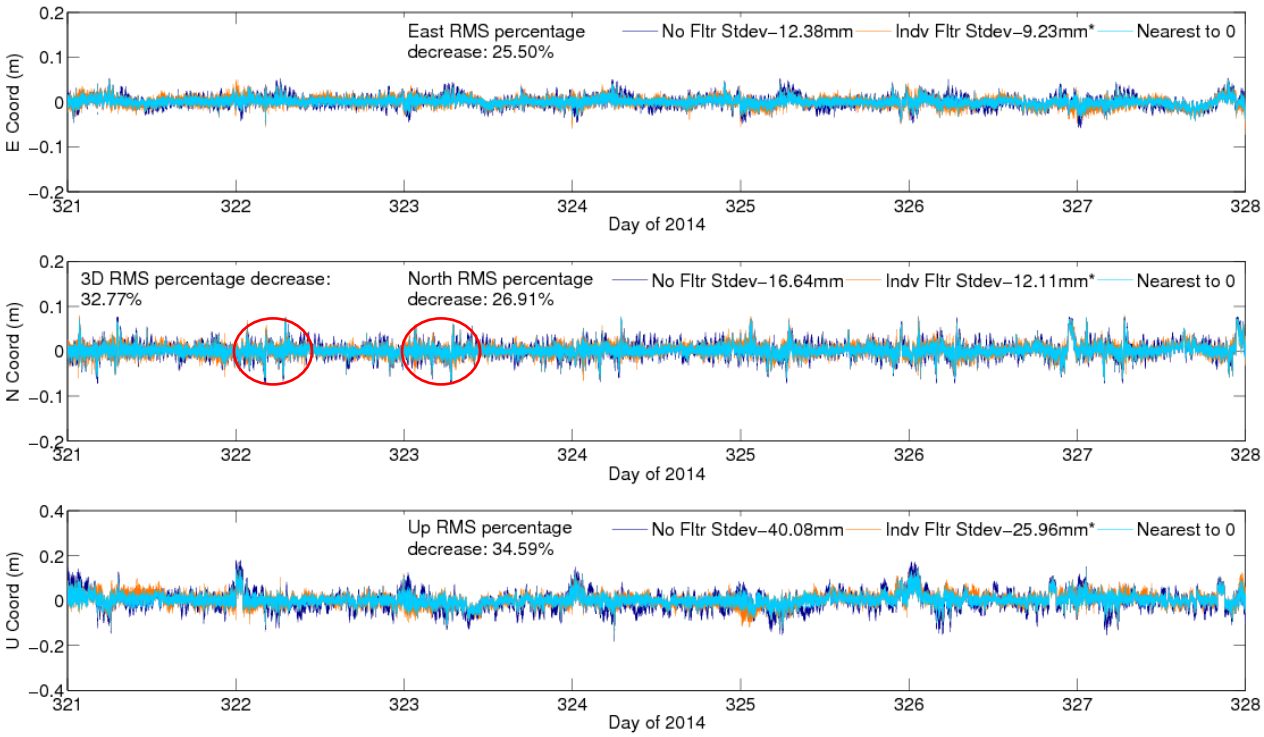

Figure 3.11: Coordinate comparison at site HUNG of unfiltered GPS PPP processing, in dark blue, and GPS-only sidereally filtered PPP processing, in orange, 2014, days 321 to 327. The best epoch from both scenarios, the coordinate closest to the known coordinate position (zero) is also plotted, in cyan.

The sidereal filter of individual lag values, computed per satellite and site, can be seen to produce more precise results than the unfiltered coordinates, indicating that the filter has been successful in reducing high-frequency errors of the order of a few minutes. The standard deviations for all three dimensions are significantly smaller according to an F-test conducted at the 95% confidence level when the filter is applied, as represented in the Figure 3.11 by an asterisk above the individual filter standard deviation. The standard deviations for the other sites can be seen in Table 3.5, and all show similar improvements

(decreases) in standard deviations, after individual filter application. The results also show as expected, how the vertical components of the OS sites are noisier than the horizontal due to only seeing satellites in one hemisphere overhead. The majority of the North coordinates, both unfiltered and filtered, are also noisier than the East coordinates. This is as a result of the high UK latitude in comparison to the GPS satellite inclination angle, resulting in less visible satellites in the North-South direction than the East-West. Table 3.5 also shows how individual filter values produce greater coordinate standard deviation improvement when compared with constellation mean filter values, which is consistent with the Agnew and Larson (2007) study. The 3D RMS has also decreased by 32.77% due to individual filter application for site HUNG. For all the sites it can be seen in Table 3.6 how the 3D RMS of the coordinates decrease on average by about 33.5% with individual filter application. Individual filter application, again, on average out performs mean filter application, hence why only individual filter values are from this point on used.

Table 3.5: Standard deviations, in millimetres, of coordinates from unfiltered GPS PPP processing and PPP processing with GPS-only mean and individual sidereal filtering.

Site	Processing Method	East St.dev	North St.dev	Up St.dev
HUNG	PPP unfiltered	12.38	16.64	40.08
HUNG	PPP Mean filtered	9.35	12.25	25.53
HUNG	PPP Indv filtered	9.23	12.11	25.96
KILN	PPP unfiltered	17.39	17.92	43.97
KILN	PPP Mean filtered	13.00	16.73	34.76
KILN	PPP Indv filtered	11.59	14.81	31.94
MACY	PPP unfiltered	11.83	16.50	39.00
MACY	PPP Mean filtered	9.63	11.47	27.15
MACY	PPP Indv filtered	9.60	11.47	27.08
OBAN	PPP unfiltered	18.17	16.63	37.08
OBAN	PPP Mean filtered	10.73	11.84	25.76
OBAN	PPP Indv filtered	10.58	11.66	25.73
PADT	PPP unfiltered	22.94	24.00	55.09
PADT	PPP Mean filtered	10.34	12.06	25.03
PADT	PPP Indv filtered	10.24	11.86	25.03

Table 3.6: 3D RMS percentage decrease of coordinates with PPP processing with GPS-only mean and individual sidereal filter application.

Site	3D RMS filter % decrease	
	PPP Mean filtered	PPP Indv filtered
HUNG	33.64	32.77
KILN	21.76	28.62
MACY	28.76	28.98
OBAN	32.47	32.68
PADT	44.56	44.30

Filtering can also be seen to reduce the standard deviation of the carrier-phase residuals to which it has been directly applied, as seen for site HUNG in Figure 3.12. The average percentage decrease in carrier-phase residuals' standard deviation for all five sites is about 29.5% as listed in Table 3.7 which is similar to the improvement seen in the coordinates. As demonstrated by the above statistics the precision of the coordinate time series for GPS has been improved by sidereal filtering, by a comparable amount to studies mentioned earlier in this section.

Although the standard deviation gives an indication of the overall variability of the data set as a whole, it does not take into consideration non-stationary noise processes. These non-stationary processes may exist in the time series and have time varying statistics, such as, variance and mean. Standard deviation is not able to converge when flicker noise is present for example; it increases with the number of epochs used to determine it.

The Allan deviation statistic, however, can be used to assess time series stability. For early-warning applications the improvement in stability of a period of a few hundred seconds to minutes is of most interest for rapid and reliable displacement measurements. The Allan deviation is also able to characterise non-stationary noise processes; it remains relatively constant in the presence of flicker noise (Riley, 2008). Standard deviation can be seen to be centered on individual measurements to mean measurement variation whereas the Allan deviation is centered on measurement to measurement variation. The stability of the time series is important to assess for early-warning applications, in order to prevent the occurrence of false alarms from erroneous time series measurements from an unstable data set.

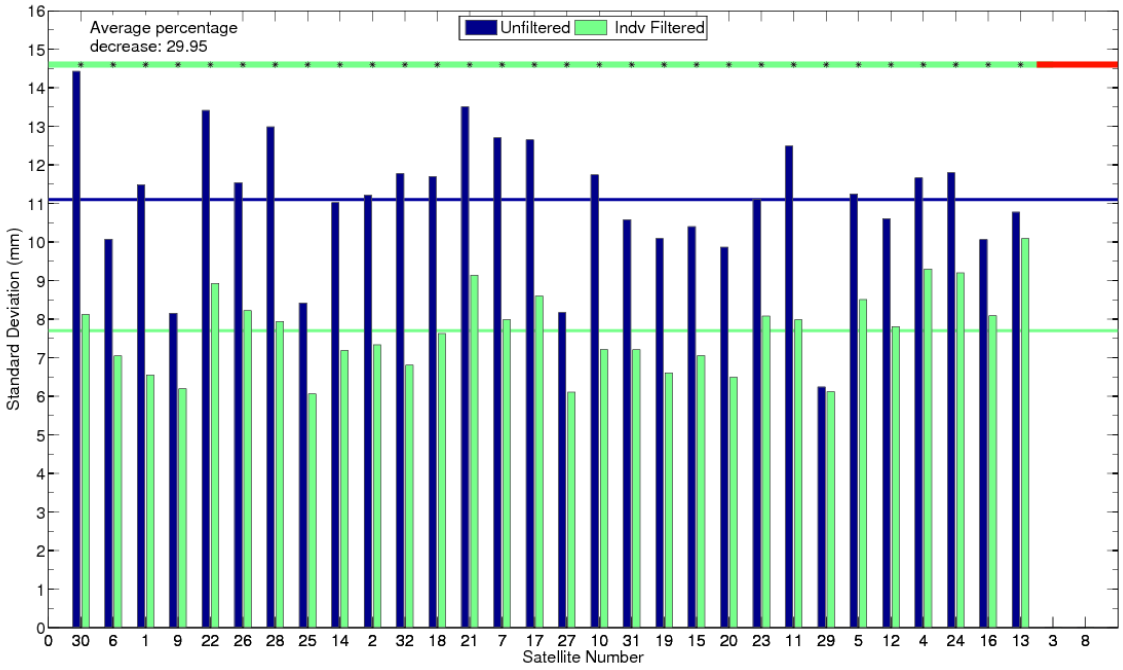

Figure 3.12: Comparison of standard deviations, at site HUNG, 2014, days 321 to 327 for unfiltered and GPS-only sidereally filtered carrier-phase residuals ordered by satellite correlation strength, strongest on the left, weakest on the right. Horizontal lines represent the mean of the constellation carrier-phase residuals standard deviations for the unfiltered, in blue and filtered in green, scenarios. The asterisk signifies that the filtered residuals' standard deviations are significantly smaller than the unfiltered, at the 95% confidence level and the horizontal line behind them indicates if a filter was applied to that particular satellite (green) or not (red).

Table 3.7: Carrier-phase residuals average standard deviation percentage decrease with GPS-only mean and individual sidereal filter application.

Site	**LC residuals average standard deviation % decrease**	
	PPP Mean filtered	PPP Indv filtered
HUNG	26.38	29.95
KILN	9.35	31.43
MACY	25.05	27.36
OBAN	26.42	29.61
PADT	26.09	29.03

The Allan deviation was first developed in the 1960s to analyse the frequency stability of precision oscillators (Allan, 1966), but has since been used to analyse the error characteristics of GNSS positioning solutions (Niu *et al.*, 2014). Allan variance (σ_y^2), the square of the Allan deviation, for N samples in a time series taken regularly, in this case every τ seconds, is defined in Ferre-Pikal and Walls (2005) as:

$$\sigma_y^2(\tau) = \frac{1}{2(N-2)\tau^2} \sum_{i=1}^{N-2} [x_{i+2} - 2x_{i+1} + x_i]^2 \tag{3.12}$$

To make maximum use of the data set the overlapping Allan deviation can be used where all available overlapping samples at each averaging time are formed. This is the most common measure of time-domain frequency stability and has a higher confidence estimate and performs better over long averaging intervals than the normal Allan deviation (Riley, 2008). For numerous sampling times $\tau = n\tau_0$, the overlapping Allan deviation is given by:

$$\sigma_y^2(\tau) = \frac{1}{2(N-2n)\tau^2} \sum_{i=1}^{N-2n} [x_{i+2n} - 2x_{i+n} + x_i]^2 \tag{3.13}$$

where n becomes a variable for the estimator whose value must remain less than the number of data epochs halved. The size of n increases with increasing averaging intervals which results in a less consistent average for the Allan variance value. This is due to a smaller number of terms being included in the summation and hence why averaging intervals between 1 s and 7200 s (2 hours), are only used in this thesis.

The overlapping Allan deviation is small for stable coordinate time series across the specified time intervals but large for less stable data sets. Hence, the filtered data should have a smaller Allan deviation as the mitigation of multipath is expected to increase time series stability. Ferre-Pikal and Walls (2005); Riley (2008); Friederichs (2010) all offer a more comprehensive overview of using the Allan deviation statistic for stability analysis if further information is required.

In order to quantify an increase in time series stability from filtering, Allan deviation values were computed across the above mentioned averaging intervals for each of the East, North and Up coordinate time series components, as seen for site HUNG in Figure 3.13. It can be seen that the filter is successful in increasing the stability of the coordinate time series over averaging intervals roughly larger than 300 s for the horizontal components and 250 s for the vertical component. The Allan deviation curve for the horizontal unfiltered components show an overall gradient of -1 at the lower averaging intervals, indicating that the dominant noise process is white or flicker noise. At the larger averaging intervals the unfiltered curve has peaks and troughs, indicating a periodic component to the signal which is most likely due to strong carrier-phase multipath interference as this pattern does not occur in the filtered curve.

To aid analysis the percentage reduction of the filtered Allan curve relative to the unfiltered Allan curve was computed for each averaging interval using the following equation:

$$Percentage\ Reduction = \frac{Unfiltered\ Allan\ Dev - Filtered\ Allan\ Dev}{Unfiltered\ Allan\ Dev} \text{ X } 100 \quad (3.14)$$

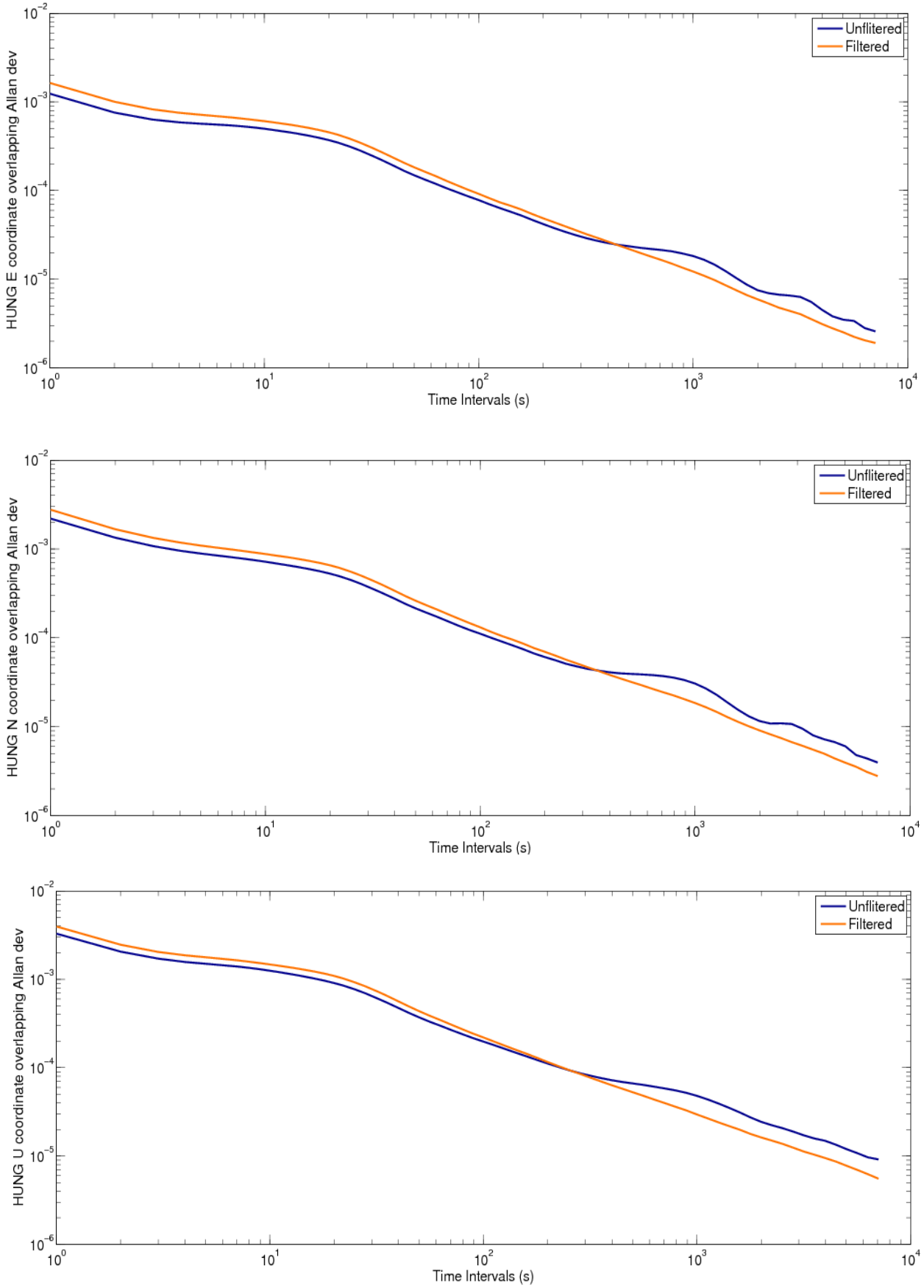

Figure 3.13: Allan deviation plots of the corresponding coordinate time series (East, North and Up) at site HUNG.

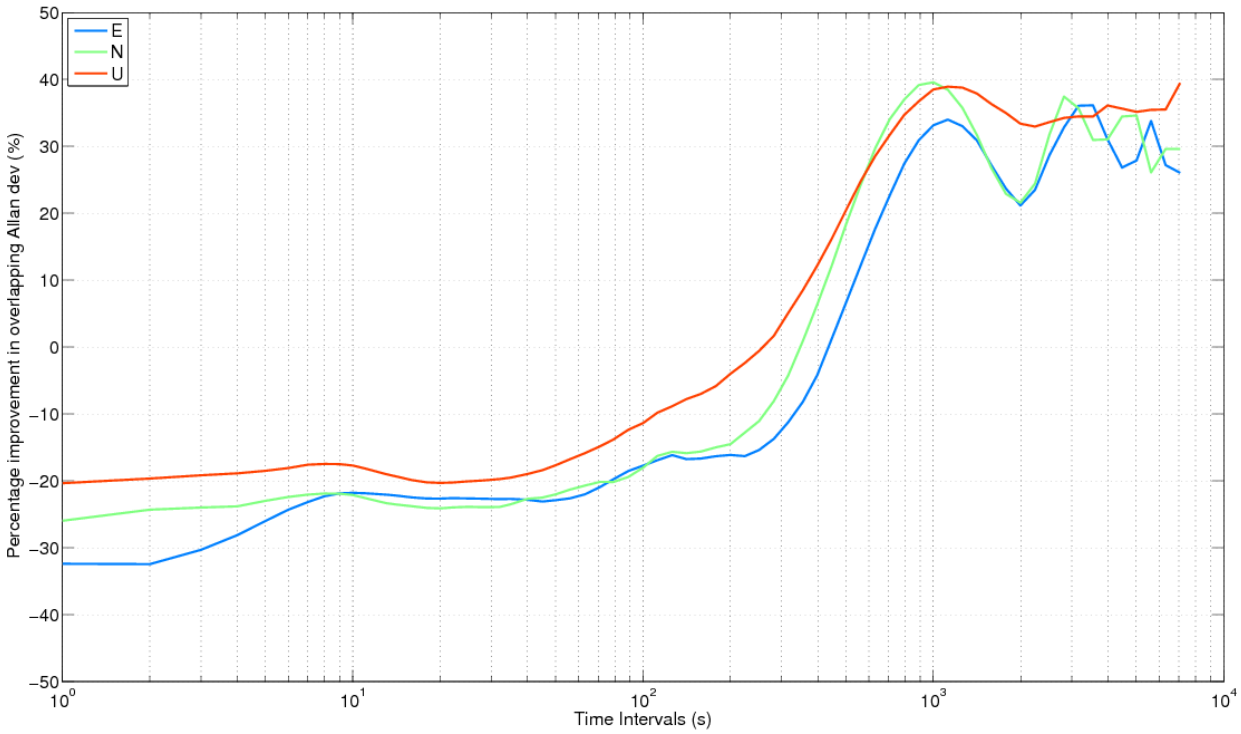

Figure 3.14: Percentage improvement (reduction), in Allan deviation at site HUNG after sidereal filtering corresponding to the Allan deviation curves.

Table 3.8: Maximum percentage improvement in Allan deviation with GPS-only sidereal filter application.

Site	Maximum percentage improvement in Allan deviation		
	East	North	Up
HUNG	36%	39%	39%
KILN	32%	20%	33%
MACY	28%	35%	35%
OBAN	40%	37%	31%
PADT	43%	45%	53%

As seen from Figure 3.14 the maximum improvement for all three components is about 38%, with a steady increase in percentage between the intervals of around 100-1000 s, which corresponds to typical periods of multipath error. At around interval 2000 s the improvement dips to 21% for the vertical component and 33% for the horizontal components and then continues to fluctuate for larger averaging intervals. The maximum

improvements of the other sites can be seen in Table 3.8 where the average maximum for all sites and coordinates is 35%-38%.

For intervals smaller than 300 s the filter degrades the stability of the time series, this is most likely due to the filter amplifying high-frequency noise during periods where there is little or no multipath hence effectively the filter could be adding noise rather than removing it.

The power spectral density of unfiltered and filtered solutions was also computed to evaluate filter performance at different frequencies. As seen in Figure 3.15 for site HUNG, and in Appendix B for all other sites, the filter substantially improves the position estimates at frequencies below 0.001 Hz, (the orange curve is lower than the blue), but increases noise at frequencies greater than 0.02 Hz, (the orange curve is higher than the blue). This indicates that the precision of the filter solution is improved at lower frequencies. The sidereal filter has also whitened the spectra of the positions, which is consistent with the results found by Bilich *et al.* (2008a).

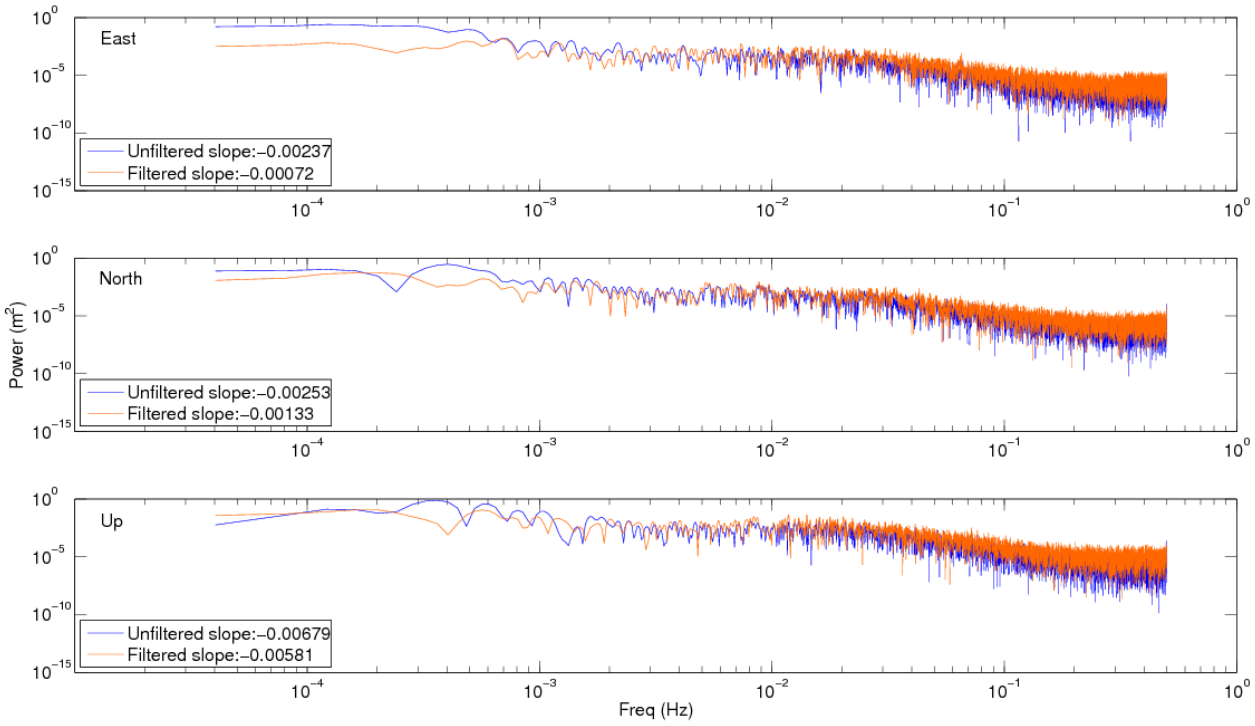

Figure 3.15: Power spectral density comparison of computed GPS coordinates at site HUNG, of unfiltered GPS PPP processing, in dark blue, and GPS-only sidereally filtered PPP processing, in orange, 2014, days 321 to 327.

3.9.1 Application of GPS Filter in a Low Multipath Environment

Prior to this section, the filter has only been applied to OS sites which experience high-level multipath (LC residuals RMS >20 mm) as seen in Figure 3.4. Sites like HUNG, which have a higher proportion of high-level multipath showed greater improvement with filtering than sites with lower levels of multipath, like site MACY. Hence, filtering effectiveness appears to be dependent on the amount of multipath present at the site. If there is little to no multipath the filter will be capturing noise rather than a genuine multipath signal and result in noise being added to the solution rather than multipath being removed. To explore this theory an IGS site REDU in Belgium was selected, as IGS sites are carefully chosen and equipped to have low multipath and interference environments. To ensure this was the case multipath levels at site REDU were assessed using the same method as described in section 3.7. As seen in Figure 3.4, REDU has a lower proportion of high-level multipath than the OS sites; the majority of multipath at REDU has a RMS value below 10 mm.

Figure 3.16 shows the coordinate solution at REDU for the same time period used for the OS sites (days 321 to 327, 2014), without filtering has much lower standard deviations, almost half the size of the OS site unfiltered standard deviations, as previously seen in Table 3.5. The effect of filtering at REDU is minimal; it only has a 3D RMS percentage decrease of 7.8% compared with an average decrease at the OS sites of 33.7% as seen in Table 3.6. The average percentage decrease in carrier-phase residual standard deviations as seen in Figure 3.17, is also about 10 percentage points less than the OS sites average in Table 3.7.

As seen from the Allan deviation plots in Figure 3.18 and Figure 3.19 the filter has been successful in improving the stability of the coordinate time series over averaging intervals of over about 145 s in all components. However, the maximum improvement in stability is only 16% and 22% in the horizontal and vertical components respectively, compared with 35% and 38% at the OS sites. Hence, multipath mitigation is very much site dependant as it depends on the multipath environment surrounding the antenna. High-level multipath sites like the OS sites benefit more from filtering than low multipath sites, such as REDU, which are in a low multipath environment.

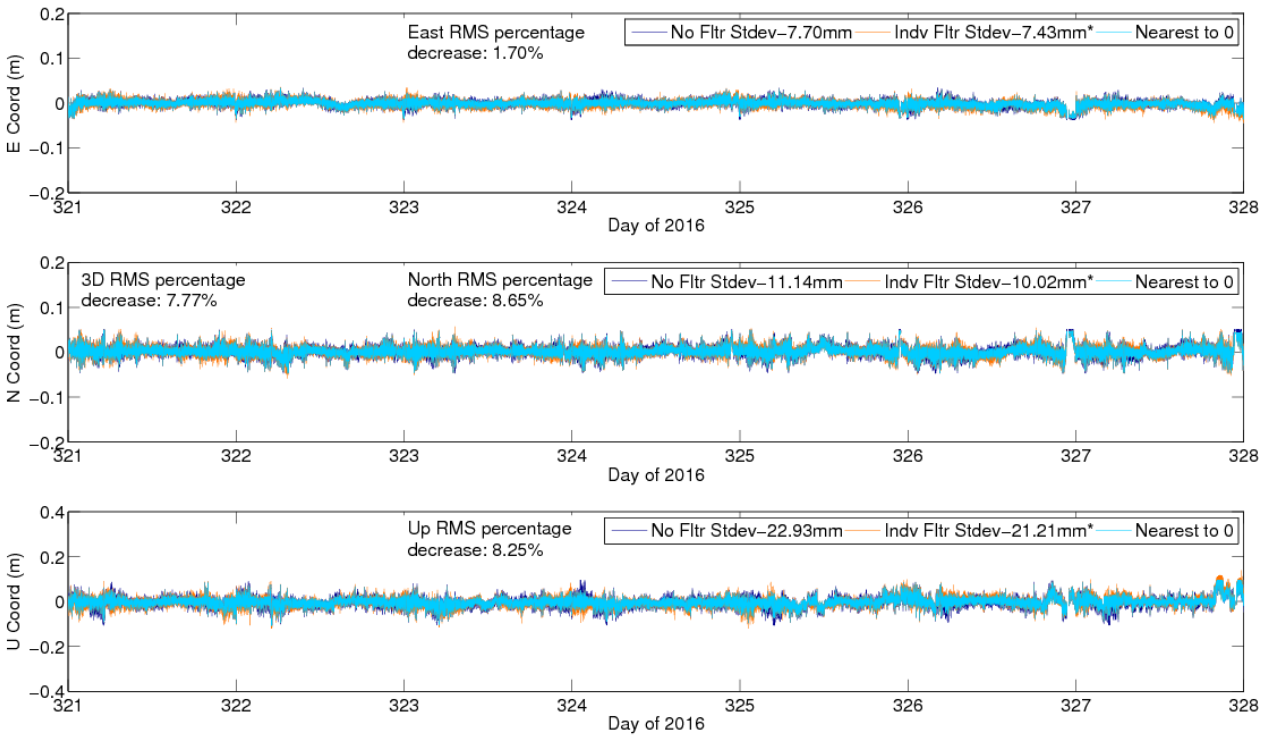

Figure 3.16: Coordinate comparison at site REDU of unfiltered GPS PPP and GPS-only sidereally filtered PPP processing, 2014, days 321 to 327. Symbology as explained in Figure 3.11.

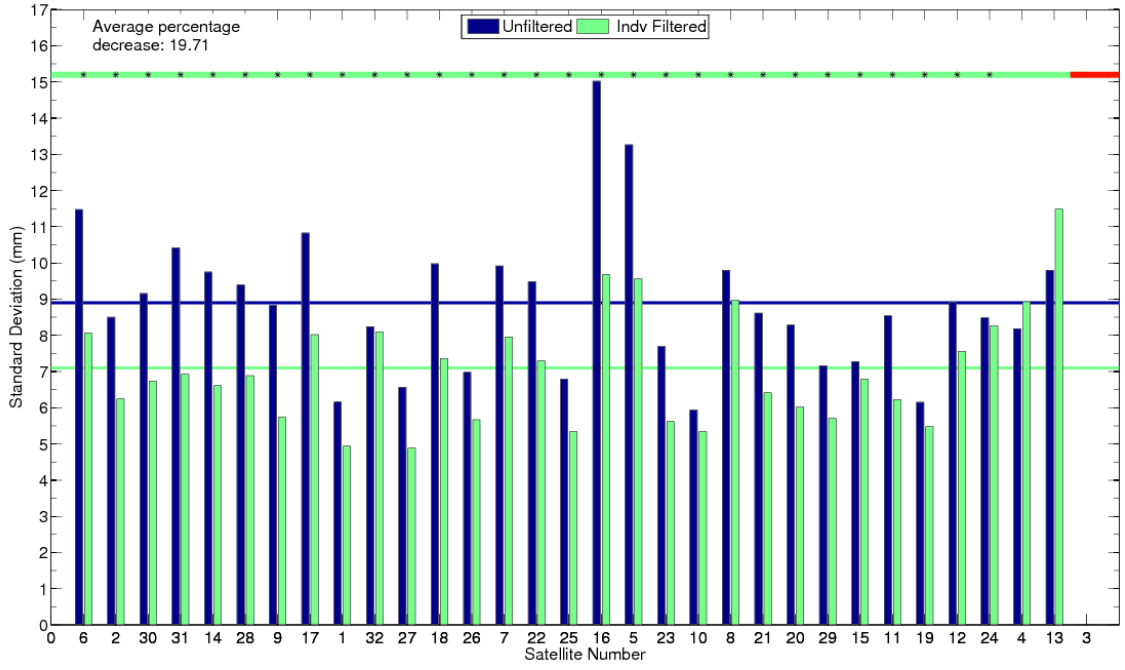

Figure 3.17: Comparison of standard deviations at site REDU, 2014, days 321 to 327 for unfiltered and GPS-only sidereally filtered carrier-phase residuals per satellite. Symbology as explained in Figure 3.12.

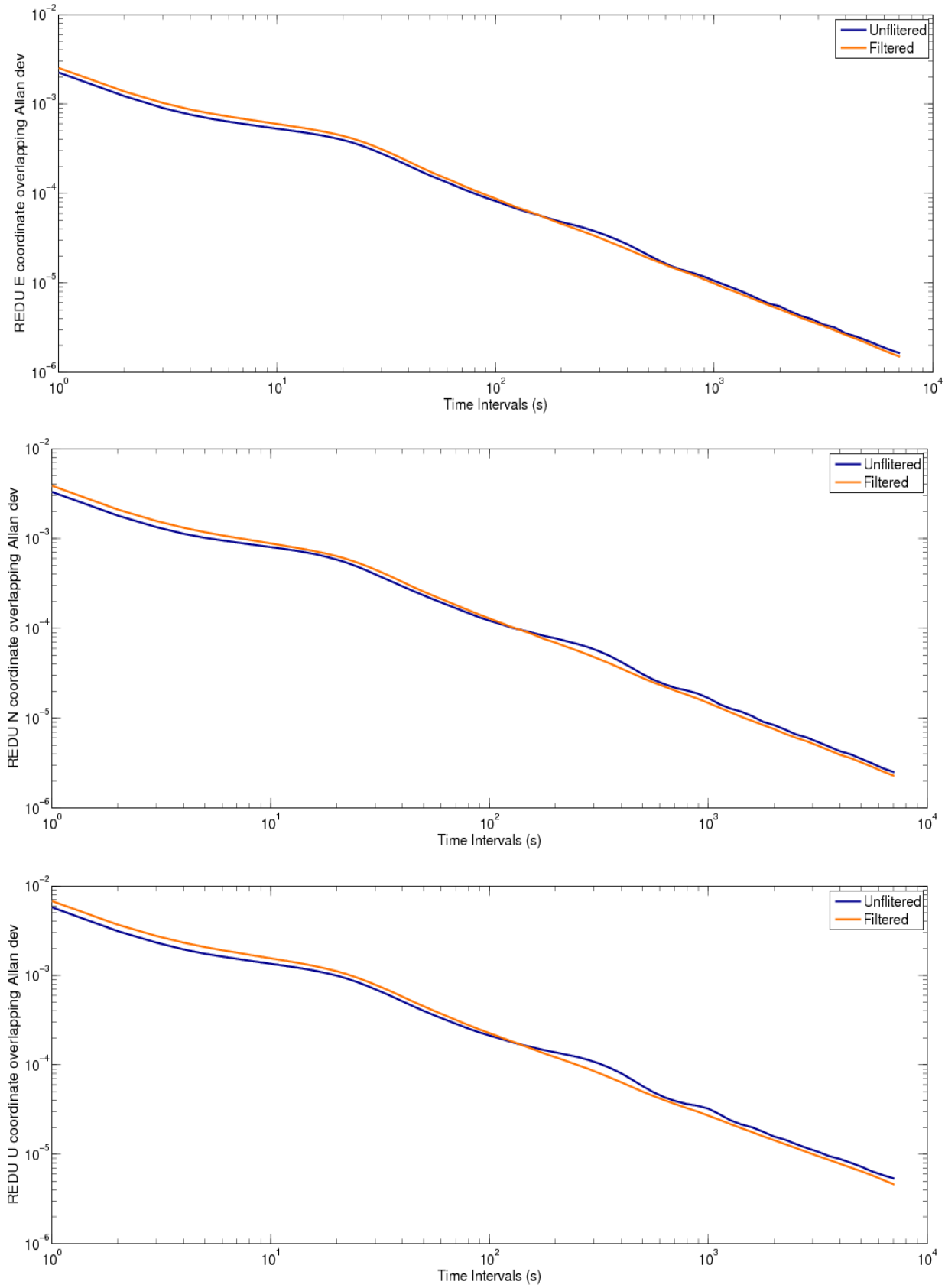

Figure 3.18: Allan deviation plots of the corresponding coordinate time series (East, North and Up) at site REDU.

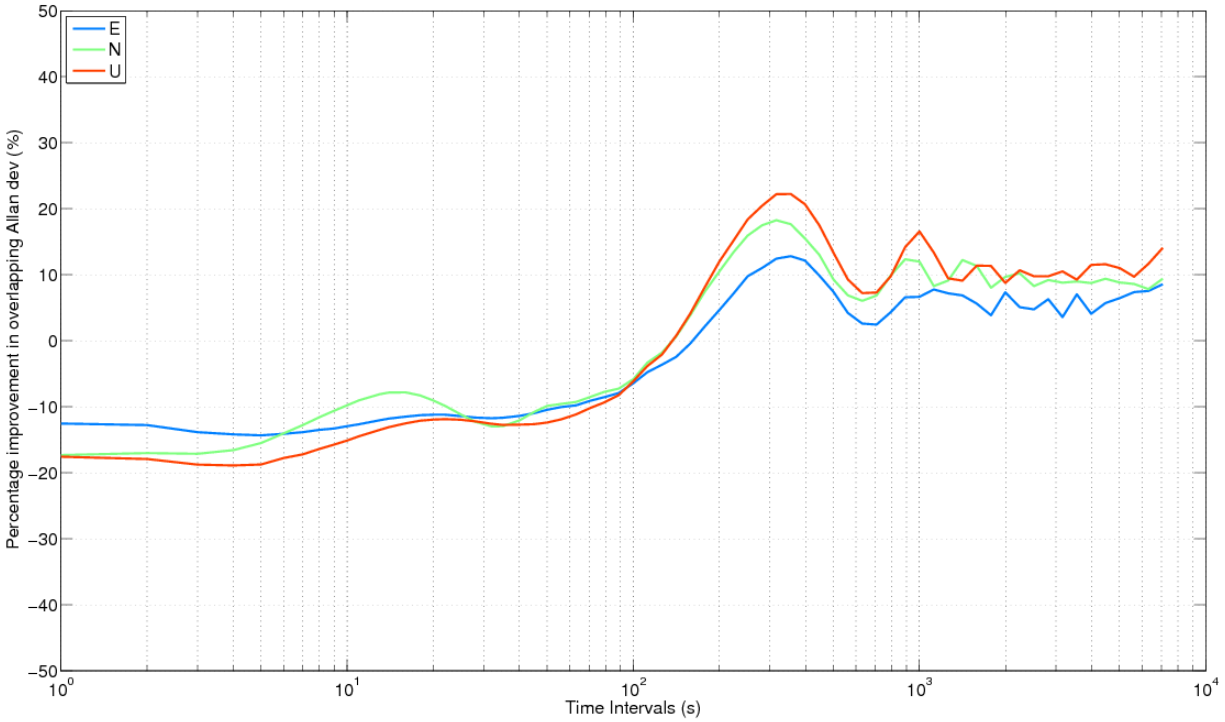

Figure 3.19: Percentage improvement (reduction), in Allan deviation at site REDU after GPS-only sidereal filtering.

3.10 Application of Filter using Elevation Angle Threshold

The effect of satellite elevation angle is taken into consideration when applying the GPS filter in this section. Prior to this section the filter has been applied to all elevation angles between 0°-90°. It is expected that when satellites are at lower elevation angles they will experience higher levels of multipath; therefore only applying the filter at times of low satellite elevation should prevent adding or amplifying noise at times experiencing little to no multipath. To explore this theory, high-level multipath (LC residual RMS >20 mm) for all five sites was sorted into two elevation angle categories, elevations of 30° or less and elevations of over 30° to 90°. The percentage of values in each category from the total was then computed. It is clear from Figure 3.20 that the majority of high-level multipath does occur at low elevation angles, on average 90.8% of the sites' high-level multipath occurs at elevation angles of 30° or less. This value is higher for site HUNG where about 98.2% of the total high level multipath occurs at elevation angles 30° or less compared to only 83.4% for site MACY. Both these sites were hence selected to test the effect of limiting filter application to epochs where satellite elevation is 30° or less.

The statistics in Table 3.9 show that the coordinates for site HUNG yield slightly higher standard deviations, about 2.15 mm on average for all three components, for 30° filter application (epochs with elevation angles of 30° or less) compared to the 90° filter (epochs with elevation angles between 0°-90°). The overall 3D RMS improvement of the time series has also been reduced by about 8.53%. MACY also shows that thresholding filter application to lower elevation angles has not improved filter performance, instead causing the coordinate time series standard deviations to increase by about 2.6 mm in the horizontal components and over 6 mm in the vertical component. The 3D RMS improvement is also ~17% less than for the 90° application.

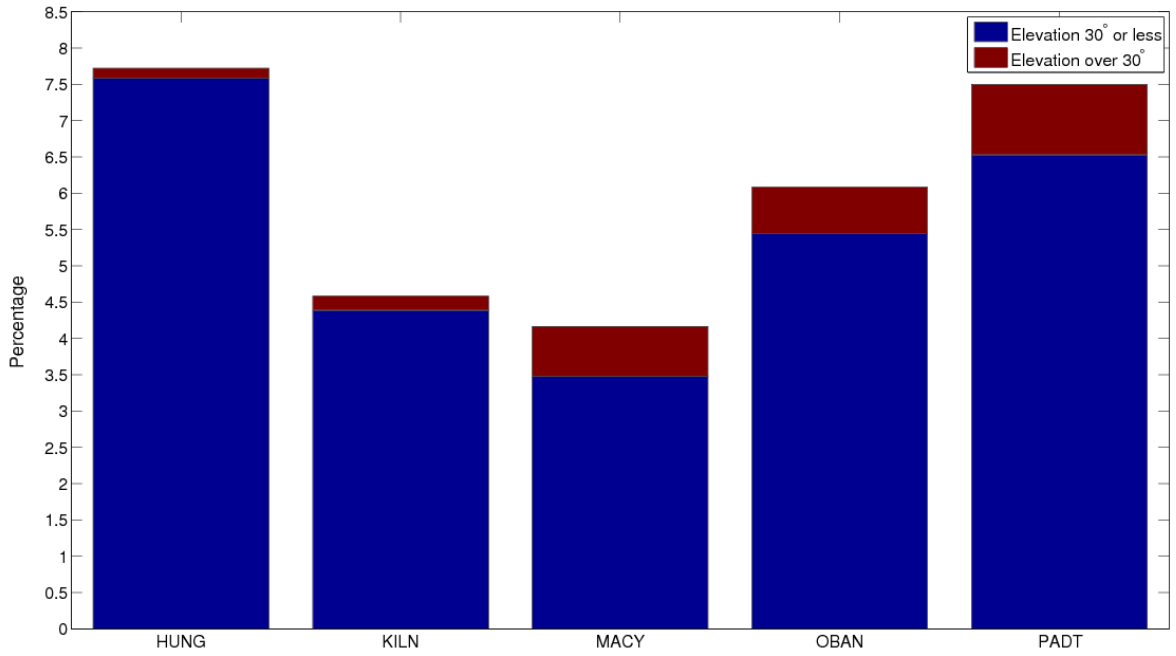

Figure 3.20: Percentage breakdown of elevation angles with GPS-only carrier-phase residuals RMS >20 mm.

Table 3.9: Comparison of elevation angle filter thresholding statistics; coordinate standard deviations, percentage decrease in 3D coordinate RMS and percentage decrease in GPS-only carrier-phase residuals standard deviations, for sites HUNG and MACY.

Site	Processing Method	East St.dev (mm)	North St.dev (mm)	Up St.dev (mm)	3D RMS filter % decrease	LC residuals St.dev % decrease
HUNG	90° filter	9.23	12.11	25.69	32.77	29.95
HUNG	30° filter	10.85	12.92	29.72	24.24	28.45
HUNG	35° filter	10.67	12.43	28.70	24.53	29.34
HUNG	Indv filter	10.32	12.66	29.28	24.47	29.03
MACY	90° filter	9.60	11.47	27.08	28.98	27.56
MACY	30° filter	11.64	14.56	33.21	11.59	12.82

As well as the precision in coordinate time series, the stability has also not improved at site HUNG when using a 30° filter. It can be seen from the Allan deviation plots in Figure 3.23 how the 30° filtered results consistently have a lower Allan deviation value than the 90° filter curve for all coordinate components under averaging intervals of 250 s. However, the unfiltered case has the lowest Allan deviation during these periods. Above this averaging interval both filters have a lower Allan deviation then the unfiltered case, but the 90° filter has the lowest. Around the averaging internal of 500 s the 30° filter shows similar stability improvement as the 90° filter, and again at round 2500 s in the East component. The percentage improvement in Allan deviation plot as seen in Figure 3.24, more clearly shows the comparison of stability improvement between the two filters. The improvement in stability at shorter averaging intervals using the 30° filter implies that the filter is not amplifying as much high-frequency noise at the higher elevated satellites as the 90° filter.

The Allan deviation curves seen in Figure 3.25 for site MACY, also show that the 30° filter reduces the amplification of high-frequency noise at the short averaging intervals. The stability of the 30° filter is lower than the 90° filter for averaging intervals smaller than about 100 s where both filters have greater Allan deviations than the unfiltered case. After this interval the 90° filter Allan deviations gets notably smaller than the unfiltered curve whereas there is very little reduction in Allan deviation from the 30° filter in comparison. Again this is more evident from the percentage improvement in Allan deviation plots as was seen in Figure 3.24, where both filters gradually increase before fluctuating at averaging intervals over 1200 s, with the 90° filter showing about 5% higher maximum improvements.

For site MACY this is mostly likely, as hypothesised, due to about 17% of the high-level multipath at MACY occurring at elevations greater than 30° so are not filtered when using the elevation angle threshold filter of 30° or less. Although site HUNG only has 2% of high-level multipath occurring at elevations greater than 30°, the effect of not mitigating this multipath error is noticeable.

3.10.1 Application of Filter at Elevation Angles of 35° or less

The lack of improvement at site HUNG from using a filter elevation of 30° or less indicates that the threshold used might have been too harsh as an arbitrary value was used. Therefore sidereal filtering elevation angle thresholding was investigated further by calculating the optimum elevation angle for filter application for the constellation as a mean and for

individual satellites at site HUNG. Optimum elevation angles were computed by correlating the optimum lag value for each satellite, first by using a broad range of elevation angles ranging between 20°-90° incremented by 10° intervals. Based on these results the range was then narrowed to 20°-50° incremented by 2° intervals. As with finding the optimum lag period, the elevation angle which gives the highest correlation value is deemed the optimum. As seen from Figure 3.21, the optimum elevation angle varies for each satellite and has a mean value of 35° at site HUNG. The filter was hence recomputed and only applied to epochs with elevation angles of 35° or less.

As seen from the statistics in Table 3.9, the 35° or less filter reduces the coordinate standard deviations in all three components on average by 0.5 mm in comparison with the 30° or less filter. However, the improvement is still less than the 90° filter. The 3D RMS improvement has decreased by 8.2% and the average reduction in carrier-phase residuals standard deviations has decreased to 29.3%, which is only 0.7 of a percentage point less than for the 90° or less filter. Due to one elevation threshold value for the whole constellation not improving the filter results, a filter with individual elevation thresholds for each individual satellite was computed to account for the variability of elevation between satellites, as seen in Figure 3.22.

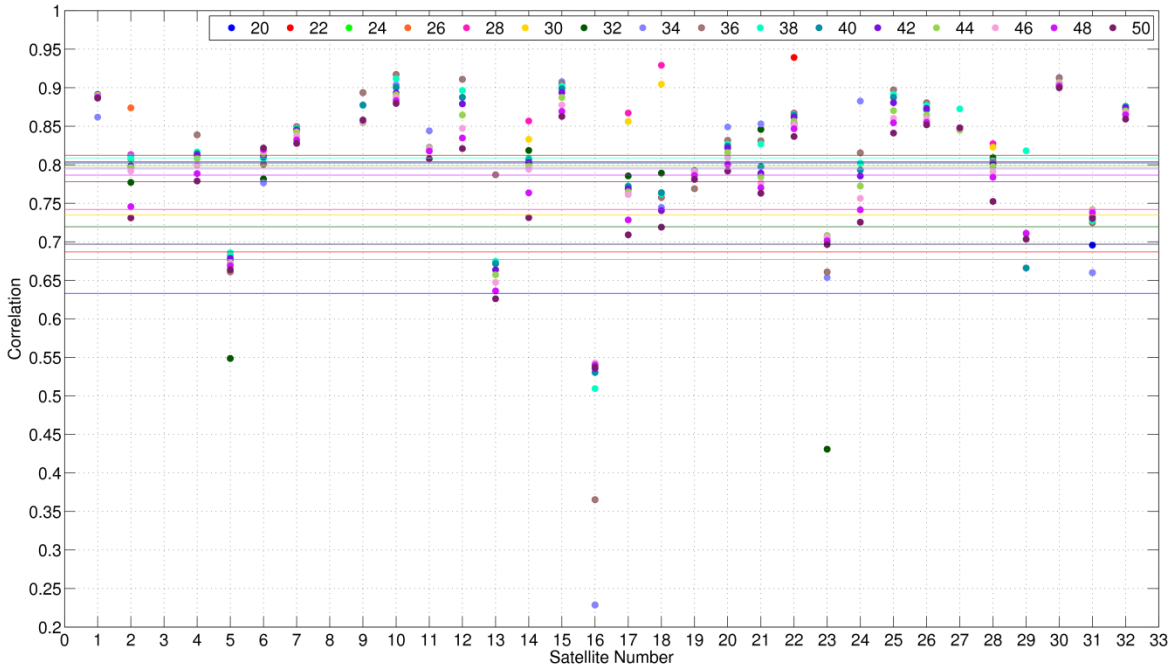

Figure 3.21: Correlation values of GPS carrier-phase residuals at a range of elevation angle thresholds at HUNG, 2014, days 320 to 327. Straight lines show elevation constellation mean values.

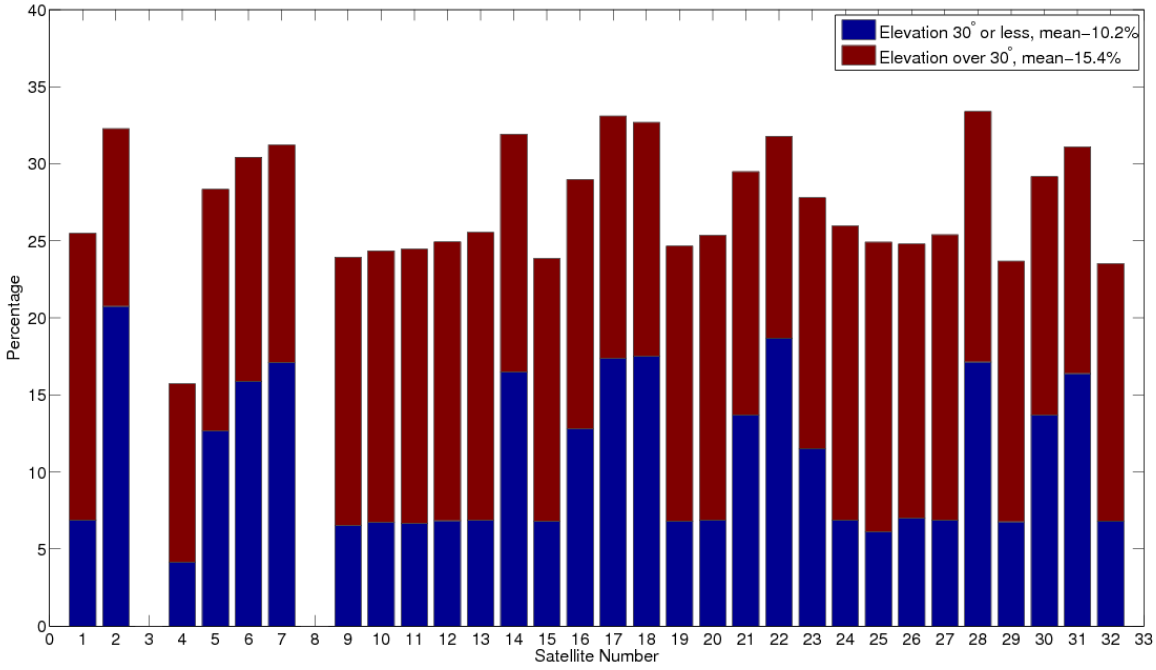

Figure 3.22: GPS satellite elevation angle variation at site HUNG, 2014, days 320 to 327 for RMS >20mm.

3.10.2 Application of Filter at Optimum Elevation Angles for each Satellite

As seen from Figure 3.21, the optimum elevation angles for the constellation at site HUNG vary from 22° to 50° for individual satellites. The statistics in Table 3.9 show that using individual elevation thresholds for individual satellites does not appear to improve the accuracy of the coordinate time series compared to using the constellation mean elevation angle threshold or no elevation threshold. This could be as optimum elevation angles are based on using the optimum lag periods calculated from using residuals with elevation angles from 0°-90° rather than recalculating the optimum lag value at the elevation threshold which could affect the results. These lag values were used because it would be unlikely that a lag value could be computed for all the satellites when only using for example, 30% of the available data during correlation. This is evident as data gaps in Figure 3.21, as correlations for some satellites could not be computed using the 0°-90° elevation angle optimum lag values with certain elevation threshold values. Lack of computed optimum lag values would lead to certain satellites not being filtered at all, which would heavily reduce filter effectiveness. By using the 90˚ lag values the same number of satellites will be filtered making the results more comparable.

The lack of improvement with elevation dependent filtering could be due to the way PANDA weights the satellites signals. As seen in Table 3.1, PANDA applies elevation dependent weighting on satellites below an elevation angle of 30˚. Weighting strategies such as this are normally applied to account for the increasing noise and modelling errors with increasing zenith distance. Hence, the filtering at lower elevation angles could be improving the residuals but not strongly contributing to the overall coordinate solution due to the weighting strategy.

Another thought is the tropospheric signal could be more dominant in the residuals than the multipath signal, which you would not expect to be vastly improved by elevation thresholding. As seen in Figure 3.5 and Figure 3.6 however, this does not seem to be the case as the residuals are strongly elevation dependent which is a characteristic of multipath.

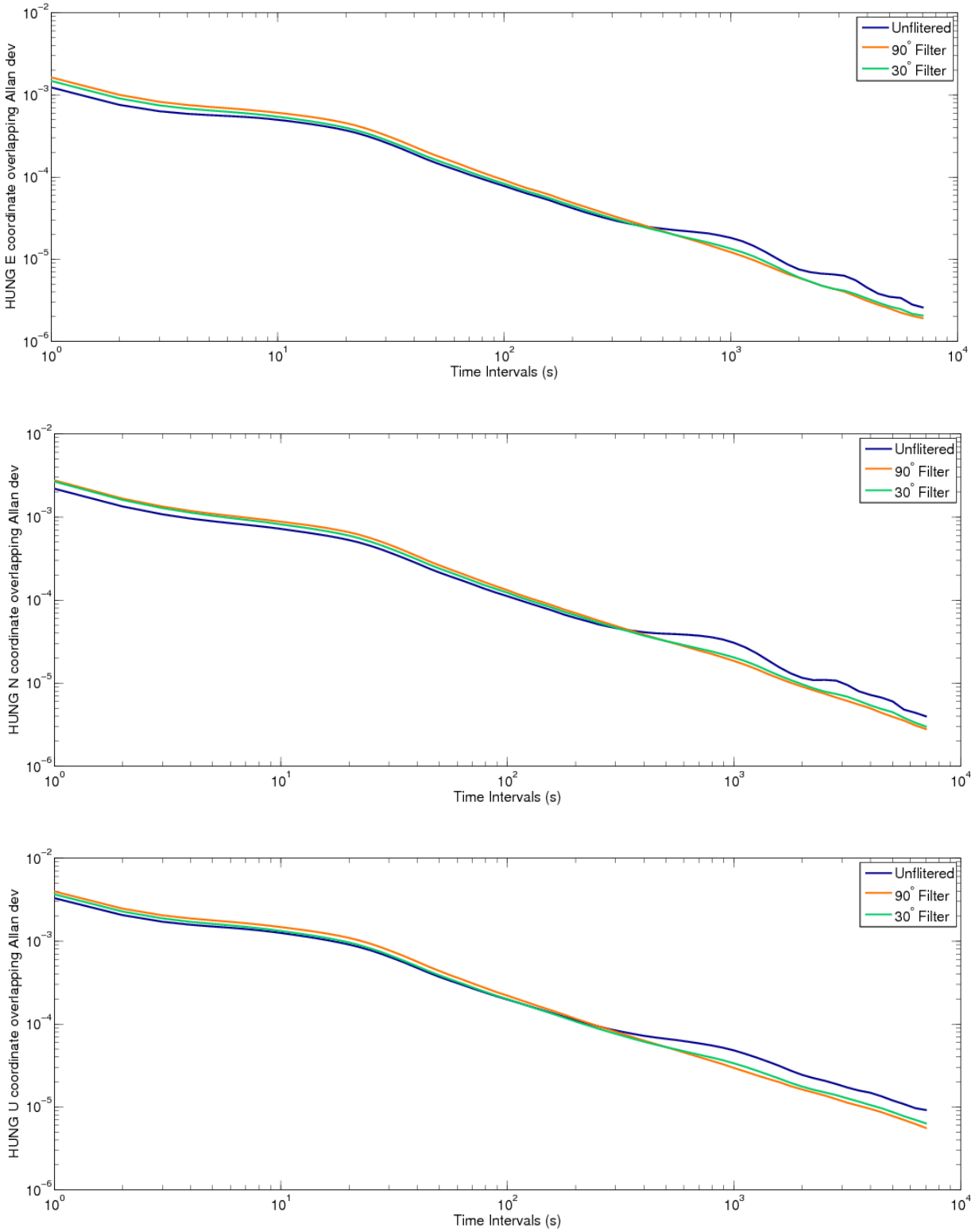

Figure 3.23: Comparison of elevation angle filter thresholding Allan deviation plots for GPS-only, site HUNG.

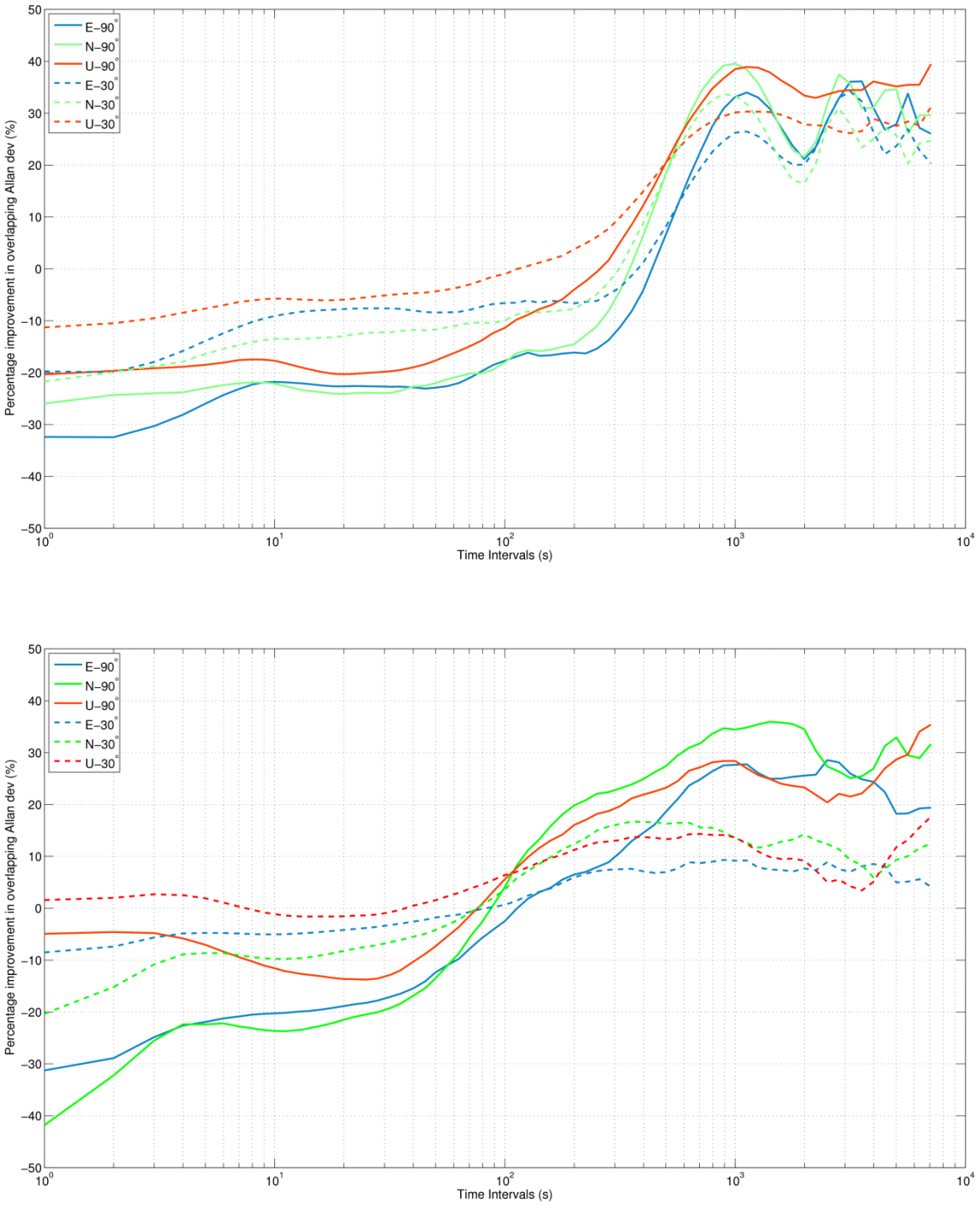

Figure 3.24: Comparison of elevation angle filter thresholding percentage improvement in Allan deviation for GPS-only, sites HUNG (top) and MACY (bottom) for a 90° and a 30° or less filter.

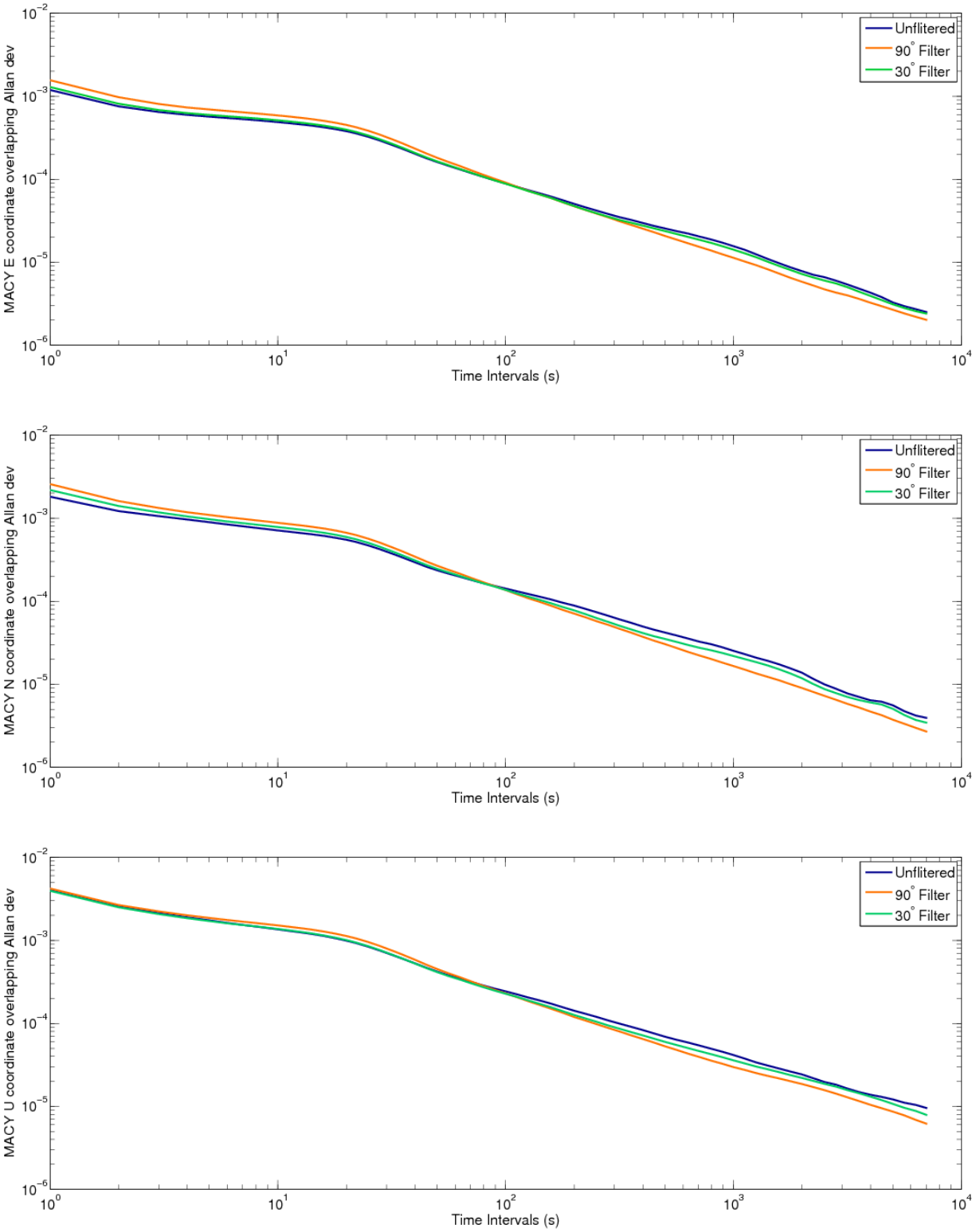

Figure 3.25: Comparison of elevation angle filter thresholding Allan deviation plots for GPS-only, site MACY.

3.11 Conclusion

From the above analysis it has been shown that the method implemented in this study is capable of finding the optimum repeat period of individual GPS satellites, as values are in keeping with those found from previous studies, as listed in Table 3.2.

Using a PPP processing strategy in the PANDA software has allowed each satellite to be filtered with an individual optimum repeat period which has improved the 3D RMS of coordinate difference values on average by 33.5% with filter application. The GPS sidereal filter has also increased the accuracy and stability of the PPP coordinate time series with sites showing an average maximum improvement in Allan deviation of around 35-38% in all coordinate components. This indicates that the filter has been implemented correctly and the methodology is valid. The filter has, hence, been developed further for use for GLONASS satellites as outlined next in Chapter 4.

Elevation angle filter thresholding was investigated to try and reduce the amplification of high-frequency noise, to increase time series stability at short averaging intervals. This was found not to be very effective for the GPS satellites; neither the individual elevation threshold or the constellation mean threshold improved the coordinate time series precision or stability better than when the filter was applied to all elevation angles at site HUNG and MACY. This could be due to the high variability of elevation between satellites or the lag periods not being optimum for the elevation thresholds used.

Chapter 4. GLONASS Sidereal Filtering

Chapter 3 outlined the successful use of GPS sidereal filtering in the observation domain using a PPP processing strategy in the PANDA software. This chapter develops the use of filtering further by including GLONASS observation domain filtering into the PPP solution. The benefit for GLONASS filtering and the feasibility of combining GLONASS and GPS multipath filters is investigated and analysed in this chapter.

4.1 GLONASS Sidereal Lag Investigation

Similar to the GPS constellation geometry repeat mentioned in the previous chapter, the GLONASS constellation geometry repeats about once every eight sidereal days. This means satellites will be in the same position relative to a receiver, eight sidereal days later. For GLONASS a longer time span is required for computing correlations to account for the larger lag separation period. Therefore, residuals were correlated over a 18 day period instead of the 8 day span used for GPS to allow at least two passes of the GLONASS satellites to have occurred. 80 lag values were considered for GLONASS ranging from 689210 s to 689290 s (7d 23h 26m 50s to 7d 23h 28m 10s). Due to a lack of prior research into GLONASS lag values a much larger lag range was initially used but then reduced to 80 values to reduce computation time. The larger lag range did extend to eight sidereal days (689312 s) but no peak correlations were found. Hence, it was not further considered.

The methodology used for GLONASS filter creation follows the same outline as described for GPS apart from a longer stacking window being required due to the longer lag periods. The GLONASS filter is, hence, created using 17 days of data prior to the week being processed so that the stack will include the average of two multipath residuals roughly eight and sixteen sidereal days prior to the epoch being processed. The same five sites and data collection period were used for GLONASS as for GPS, as outlined in section 3.7. The percentage breakdown of GLONASS-only carrier-phase residual RMS can be seen in Figure 4.1 and show a larger percentage of higher carrier-phase residual RMS (RMS >10 mm) than for GPS-only, as previously seen in Figure 3.4. This indicates either more multipath is present in the GLONASS observations or observations in general are noisier. Sites HUNG and KILN suffer more from extreme multipath (RMS >30 mm) whereas site MACY experiences very little extreme multipath, assuming multipath is the cause for the majority of the larger residuals.

As seen in Figure 4.2 and Figure 4.3 the normalised carrier-phase RMS values for GLONASS show a similar pattern to GPS in Figure 3.5 and Figure 3.6. Unlike a tropospheric signal which you would expect to remain fairly stable over a small area and time the RMS values fluctuate from one bin to the next across the azimuth angles and increase with decreasing elevation angles, which indicates multipath is the dominant signal in the residuals. GLONASS has more coverage over the azimuth extents than GPS due to its higher orbital inclination providing more coverage directly overhead in the UK. However, due to a fewer number of satellites in the GLONASS constellation there are more gaps in the sky coverage, as seen by the systematic stripped pattern.

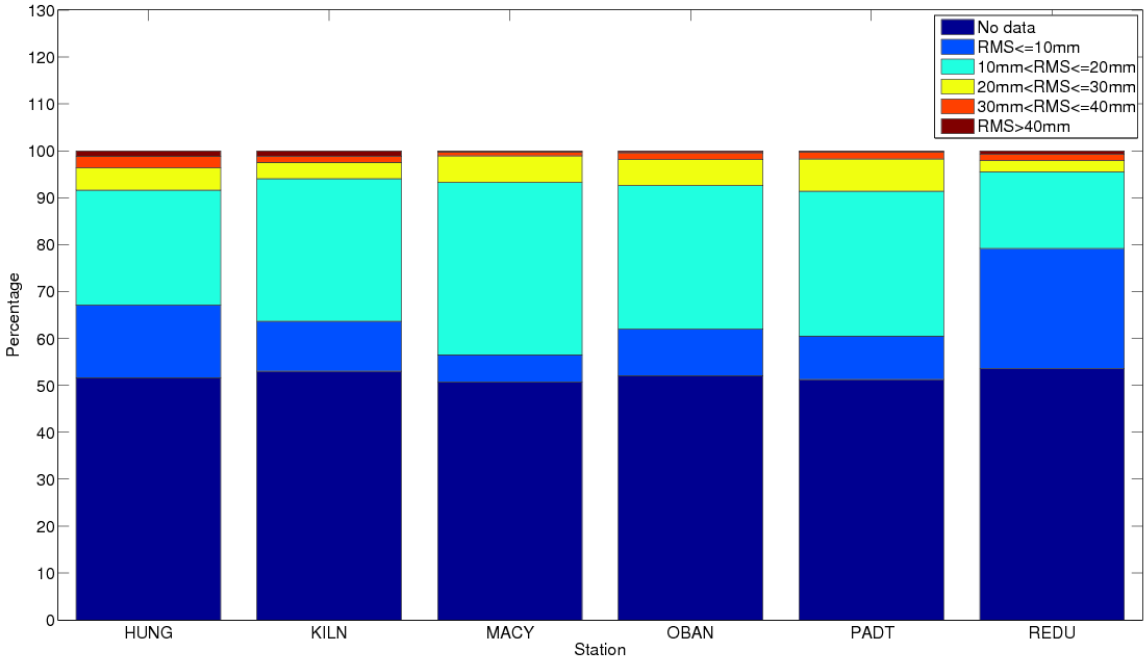

Figure 4.1: Percentage breakdown of GLONASS-only carrier-phase residuals RMS at all elevation angles.

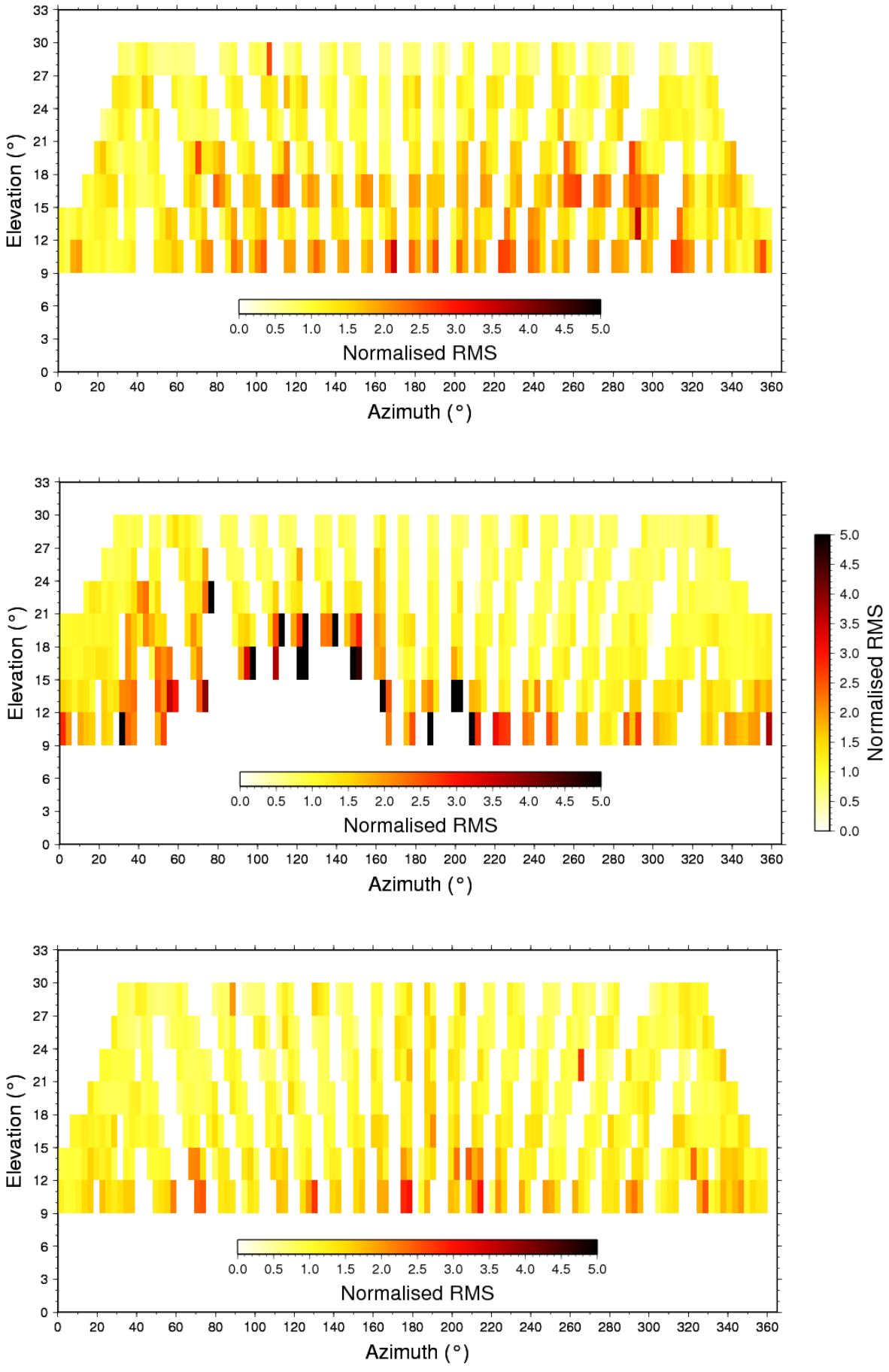

Figure 4.2: GLONASS carrier-phase residual normalised RMS variation with elevation angles up to 30° and azimuth angles, for sites HUNG (top), KILN (middle) and MACY (bottom).

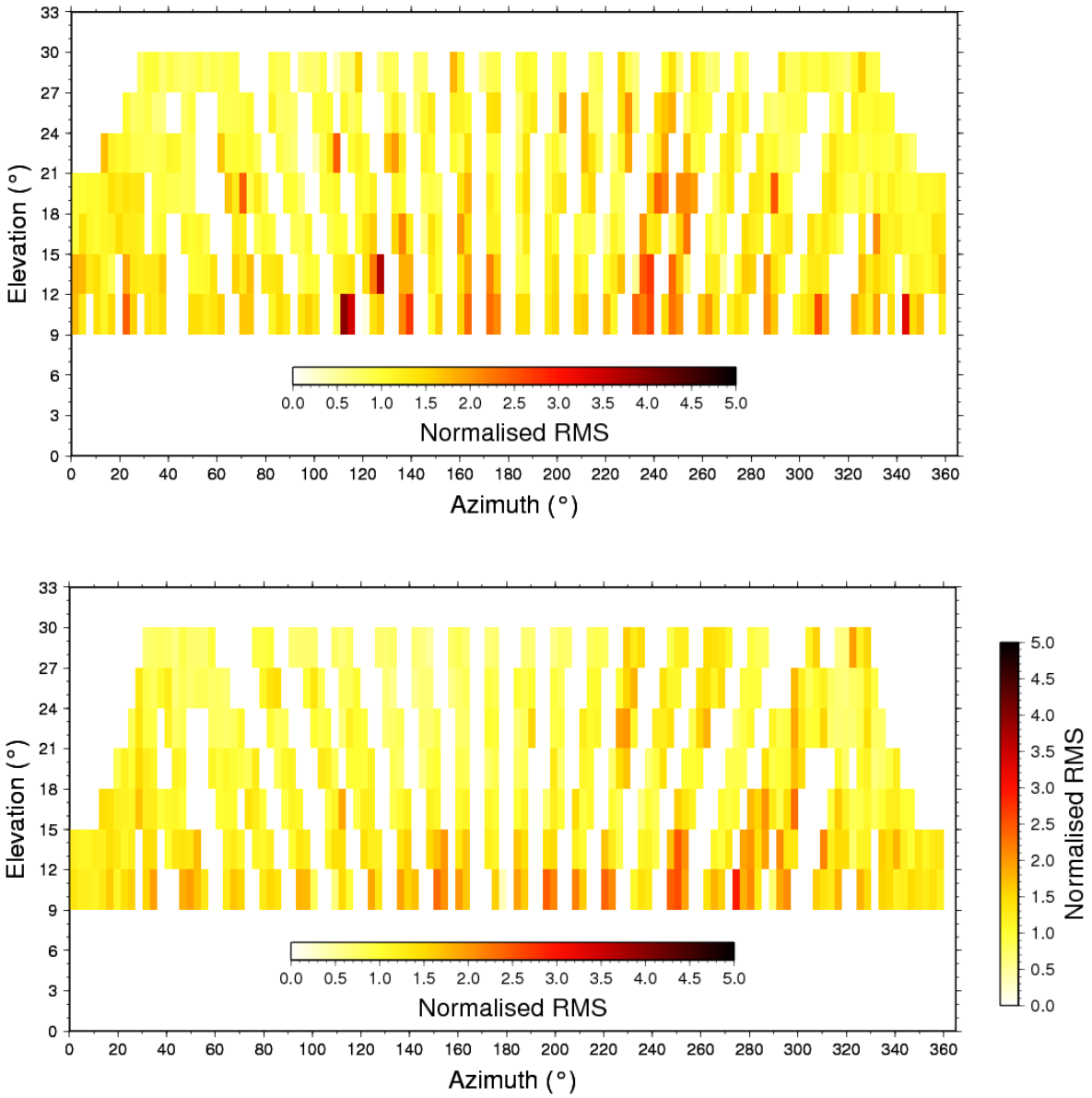

Figure 4.3: GLONASS carrier-phase residual normalised RMS variation with elevation angles up to 30° and azimuth angles, for sites OBAN (top), PADT (bottom).

4.2 Optimum GLONASS Lag Period

GLONASS filtering was conducted separately at first to find the correct lag period for individual GLONASS satellites. As seen from Figure 4.4 the correlation curves are generally broad with the exception of site KILN, which was also the case for the GPS satellites, as in Figure 3.9. As seen in the photographs in Appendix A, site KILN is the only site not situated on top of a roof; it is on a high pillar above grass covered ground with a metal railing close by which may explain the difference in correlation curve from the other sites. The mean lag period for the whole GLONASS constellation for all five sites peaks around 689248 s (7d 23h

27m 28s) for the 22 day time span correlated. This is roughly 8 times the sidereal period of 86156 s which is the mean repeat period found for the GPS-only satellites for the same data set. The mean peak correlation strength of the GLONASS constellation for all sites is roughly 0.51, ranging from 0.42-0.63, whereas for GPS the mean correlation is higher (0.67) and values between sites are less scattered. The lower correlation values for GLONASS are expected due to the longer lag periods used, which increases the potential for the environment around the site to change during the time span considered, reducing the correlation strength.

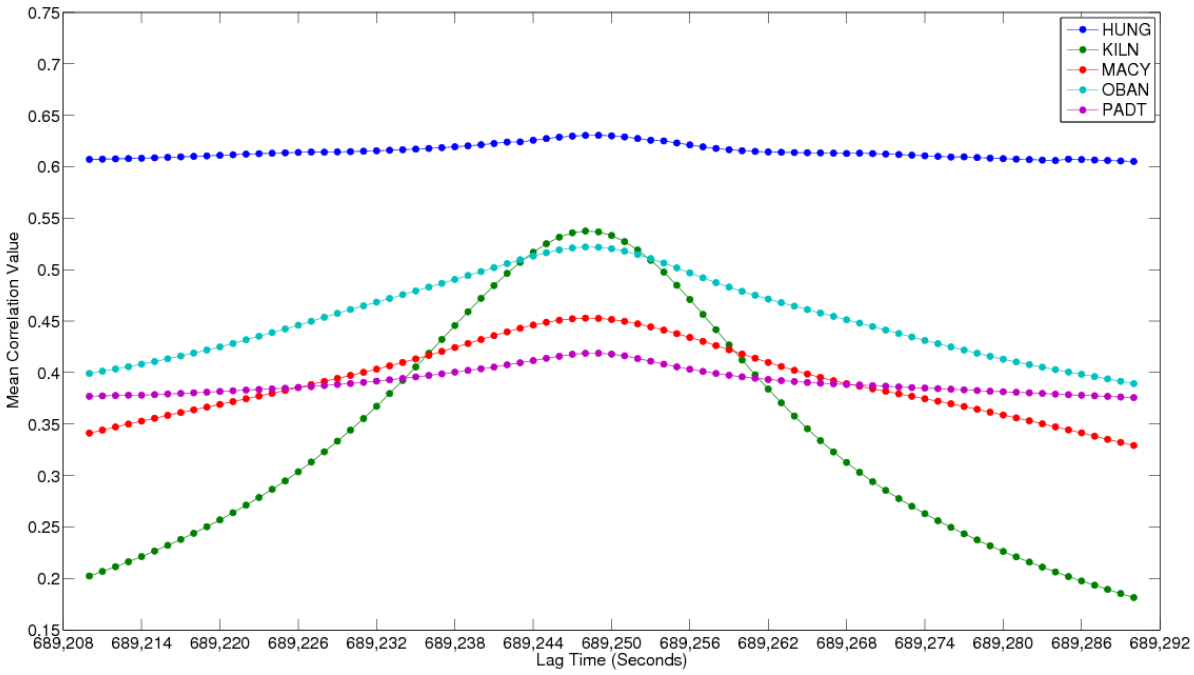

Figure 4.4: Mean GLONASS satellite constellation carrier-phase residual correlations at lag values near eight sidereal days, for a selection of OS Net sites, 2014, days 306 to 327.

It can be seen from Figure 4.5 which shows the carrier-phase residuals for satellite R01 at site OBAN, selected as the best example for clarity, how the residuals have a similar repeating pattern every near 8 sidereal days. Once lagged by 689248 s it can be seen how similar the residual pattern is at this repeat period from the zoomed in plot, bottom, hence the successful correlation of GLONASS-only residuals.

Along with the mean for the whole constellation, the optimum lag periods per satellite were also computed to increase the filter effectiveness. The individual GLONASS satellite optimum lag values for carrier-phase residuals for all the sites have a similar spread from the mean as those for GPS, a value just below 3.5 s, as given in Table 4.1. The code residual lag spreads

are also slightly higher, as for GPS, as seen in Table 4.2. Figure 4.6 shows the optimum lag values for individual satellites using carrier-phase residual correlation for site MACY. Site MACY has the most defined peaks, hence, used as the example here; the other sites also show similar peak correlation strengths at similar lag periods. The peak correlation strength ranges within the constellation from 0.25-0.60, which is slightly smaller than the GPS range in seen Figure 3.10. The correlation curves for GLONASS are also slightly steeper and more consistent within the constellation when compared to GPS.

As for GPS, in order to validate the correlation methodology the aspect repeat method, as outlined in Agnew and Larson (2007), was also used to compute lag values from ESA combined orbits, for this time period, for GLONASS. The FORTRAN script 'asprep.f' taken from the above mentioned study, was edited to allow for the addition of GLONASS and a near 8 day repeat period, then used to compute lag values for the aspect repeat method. As seen in Table 4.1, the correlation and aspect repeat method agree with one another within less than 2 s most of the time which indicates the correlation methodology has been implemented correctly and is thus valid.

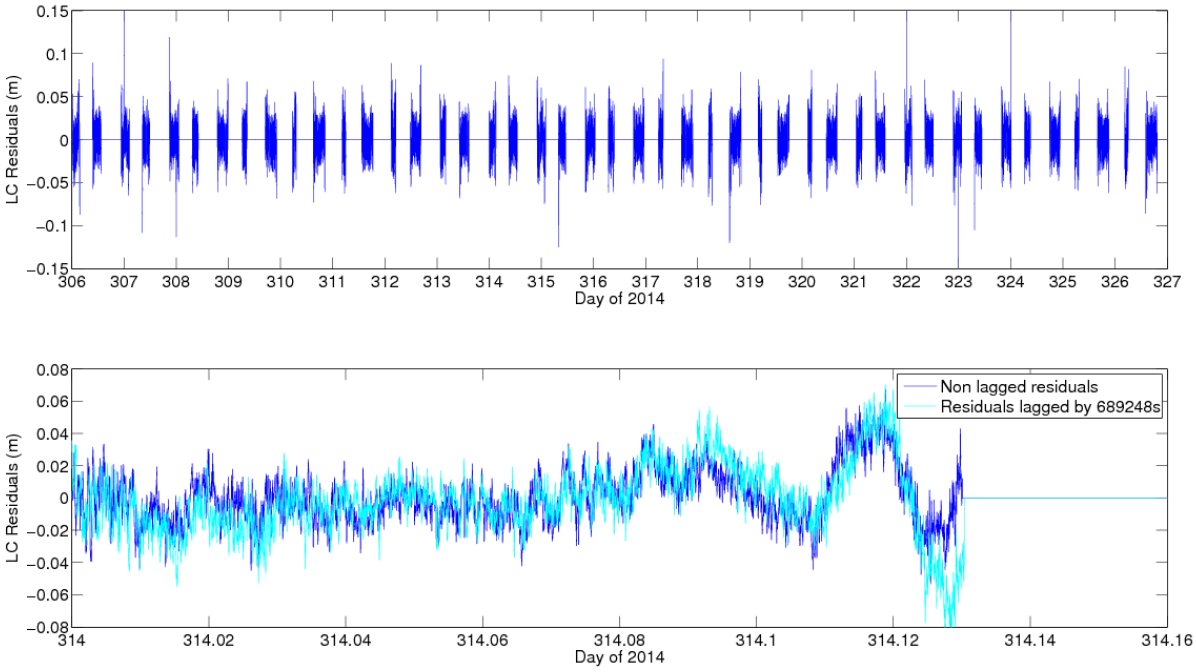

Figure 4.5: Satellite R01 carrier-phase residuals 8 sidereal day repeat pattern at site OBAN, 2014, days 306 to 327 (top). The same R01 carrier-phase residuals lagged by 689248 s, zoomed in at day 314 (bottom).

Table 4.1: Standard deviations of the GLONASS carrier-phase residuals, optimum lag values per satellite at selected OS Net sites and the optimum lag values calculated using the aspect repeat method, 2014, days 306-327. All values are given in seconds.

	HUNG	KILN	MACY	OBAN	PADT	Sat Mean	Sat St.dev	Aspect Repeat
Opt lag value St.dev	3.43	3.83	3.33	3.58	3.26	-	-	-
Sat 01	689245	689245	689245	689244	689244	689244.60	0.49	689245
Sat 02	689250	689250	689250	689249	689250	689249.80	0.40	689250
Sat 03	689250	689249	689249	689250	689250	689249.60	0.49	689250
Sat 04	689248	689250	689250	689250	689251	689249.80	0.98	689250
Sat 05	689248	689249	689249	689249	689249	689248.80	0.40	689249
Sat 06	689250	689251	689251	689250	689249	689250.20	0.75	689250
Sat 07	689251	689251	689251	689250	689251	689250.80	0.40	689250
Sat 08	689250	689249	689250	689248	689248	689249.00	0.89	689249
Sat 09	689248	689249	689248	689248	689248	689248.20	0.40	689248
Sat 10	689249	689249	689249	689249	689249	689249.00	0.00	689249
Sat 11	689249	689249	689250	689249	689249	689249.20	0.40	689249
Sat 12	689242	689248	689247	689248	689248	689246.60	2.33	689248
Sat 13	689249	689249	689248	689248	689249	689248.60	0.49	689249
Sat 14	689253	689252	689252	689253	689252	689252.40	0.49	689252
Sat 15	689246	689241	689243	689241	689243	689242.80	1.83	689242
Sat 16	689249	689250	689249	689250	689249	689249.40	0.49	689249
Sat 17	689248	689248	689248	689248	689249	689248.20	0.40	689248
Sat 18	689243	689243	689244	689243	689244	689243.40	0.49	689244
Sat 19	689240	689237	689238	689238	689239	689238.40	1.02	689239
Sat 20	689239	689240	689242	689241	689241	689240.60	1.02	689241
Sat 21	-	-	-	-	-	-	-	-
Sat 22	689248	689249	689249	689248	689248	689248.40	0.49	689248
Sat 23	689249	689250	689249	689249	689248	689249.00	0.63	689249
Sat 24	689248	689248	689249	689248	689248	689248.20	0.40	689248

Table 4.2: Standard deviations of the GLONASS code residuals and optimum lag values per satellite at selected OS Net sites, 2014, days 306-327. All values are given in seconds.

	HUNG	KILN	MACY	OBAN	PADT	Sat Mean	Sat St.dev
Opt lag value							
St.dev	5.46	4.18	4.02	3.74	4.90	-	-
Sat 01	689243	689245	689244	689244	689245	689244.20	0.75
Sat 02	689250	689250	689249	689249	689246	689248.80	1.47
Sat 03	689254	689247	689249	689250	689249	689249.80	2.32
Sat 04	689259	689251	689249	689248	689251	689251.60	3.88
Sat 05	689247	689247	689249	689248	689244	689247.00	1.67
Sat 06	689248	689249	689251	689250	689249	689249.40	1.02
Sat 07	689250	689250	689250	689249	689252	689250.20	0.98
Sat 08	689246	689250	689250	689248	689254	689249.60	2.65
Sat 09	689250	689249	689248	689247	689249	689248.60	1.02
Sat 10	689253	689249	689248	689249	689257	689251.20	3.37
Sat 11	689253	689250	689249	689249	689258	689251.80	3.34
Sat 12	689242	689247	689248	689249	689258	689248.80	5.19
Sat 13	689246	689249	689251	689248	689251	689249.00	1.90
Sat 14	689255	689252	689252	689252	689257	689253.60	2.06
Sat 15	689241	689240	689240	689240	689242	689240.60	0.80
Sat 16	689254	689250	689250	689247	689255	689251.20	2.93
Sat 17	689249	689250	689248	689247	689249	689248.60	1.02
Sat 18	689241	689243	689243	689243	689238	689241.60	1.96
Sat 19	689240	689237	689236	689237	689249	689239.80	4.79
Sat 20	689238	689237	689240	689239	689251	689241.00	5.10
Sat 21	-	-	-	-	-	-	-
Sat 22	689252	689249	689248	689247	689248	689248.80	1.72
Sat 23	689250	689248	689248	689249	689259	689250.80	4.17
Sat 24	689249	689247	689249	689247	689251	689248.60	1.50

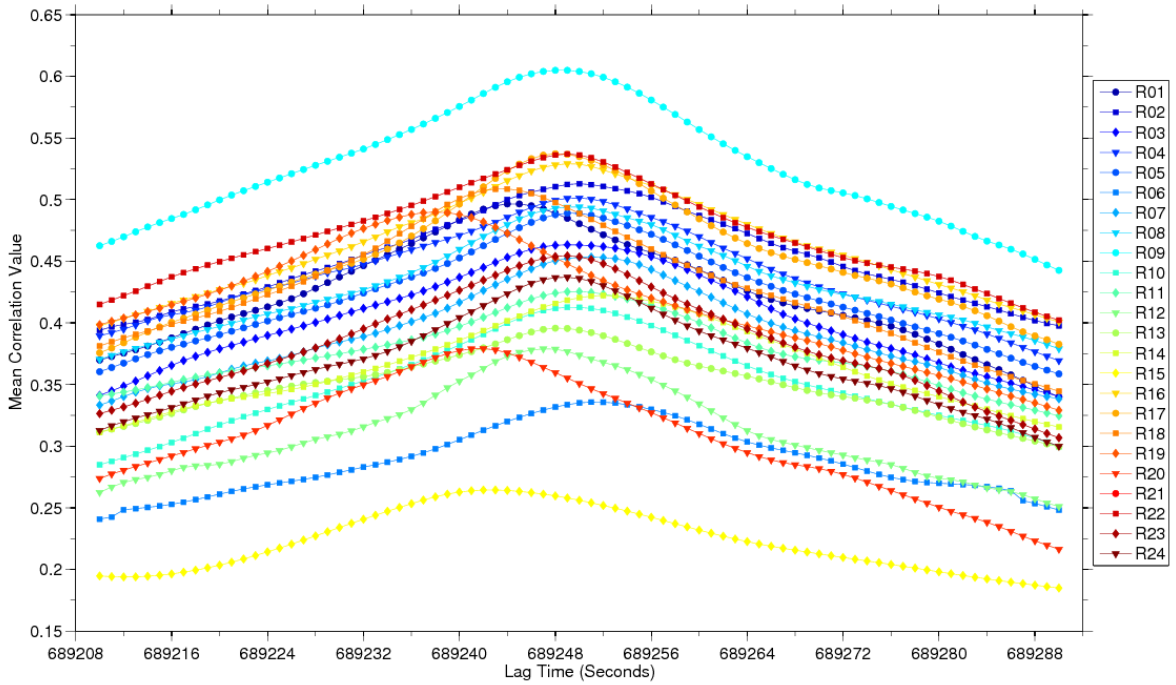

Figure 4.6: Mean correlation values of GLONASS carrier-phase residuals at different near 8 sidereal day lag ranges at MACY, 2014, days 306-327.

4.3 GLONASS Sidereal Filter Performance

Once the individual optimum lag periods were determined, sidereal filters for the carrier-phase and code residuals were made by stacking the static residuals at the desired lag periods as outlined before for GPS. Upon examination of Figure 4.5 which shows the coordinates for site OBAN as an example, the filter can be seen to produce less noisy results than the unfiltered coordinates, visually indicating that the filter has been successful in reducing multipath. For example, the rise and fall in the East component spanning about 7 hours starting around 09.30 on day 322 (322.4), as seen in the red ellipse, is reduced from a range of about +60 mm/-50 mm to +40 mm/-40 mm with filter application. The standard deviations for all three dimensions are significantly smaller and the 3D RMS decrease is 28.0% which is 4.5 percentage points less than the improvement from GPS-only filtering as seen in Table 3.4. The greatest improvement in RMS is in the East; the North and Up components have similar slightly smaller levels of improvement as one another, which is also the case for GPS-only filtering at this site.

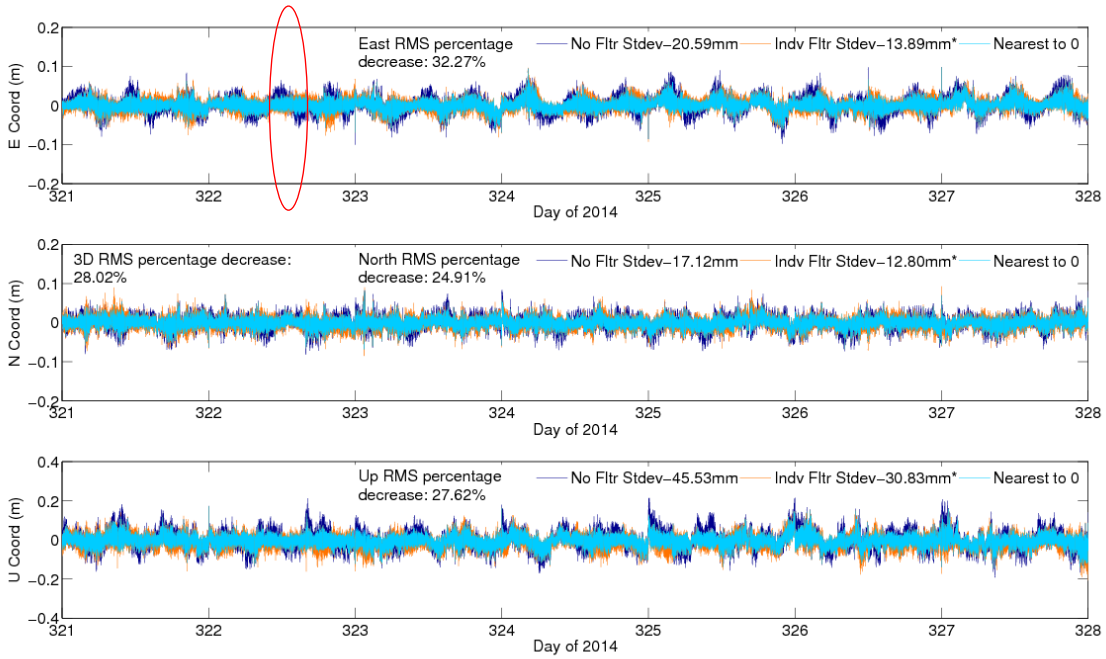

Figure 4.7: Coordinate comparison at site OBAN of unfiltered PPP and GLONASS-only sidereally filtered PPP processing, 2014, days 321 to 327.

For site HUNG, however, similar patterns of improvement from GLONASS-only filtering cannot be seen, as for GPS filtering. For GPS-only filtering, as previously seen in Figure 3.6, the Up coordinate benefited most from sidereal filtering, whereas in the GLONASS-only case the North coordinate shows most improvement for site HUNG, Figure 4.8. The 3D RMS decrease for GLONASS filtering at HUNG is also less, 27.4%, than for GPS filtering. For all sites it can been seen in Table 4.3 how the 3D RMS of the coordinates decreases on average by about 17.9% with GLONASS-only filter application. HUNG and KILN show the least 3D RMS improvement with filter application and reduce the mean decrease by nearly 6 percentage points. As mentioned earlier in this chapter, the performance of GLONASS-only filtering is expected to be less efficient than GPS filtering due to the longer lag periods used to create the multipath filters, so a smaller improvement in filtering in the coordinates is not a surprise.

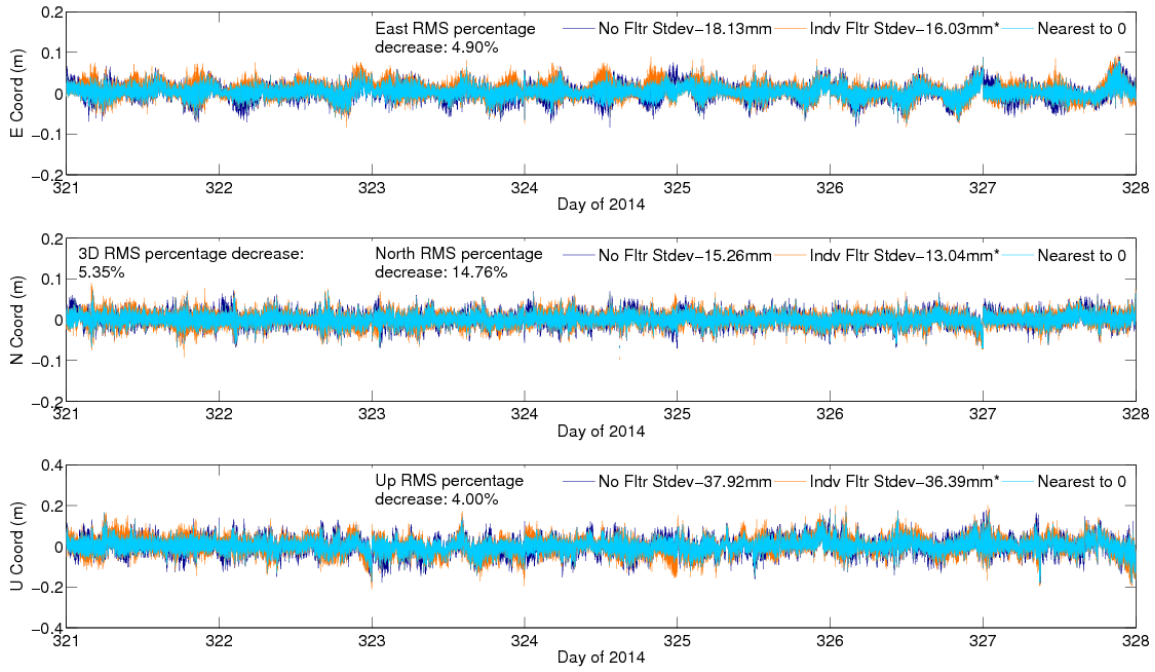

Figure 4.8: Coordinate comparison at site HUNG of unfiltered PPP and GLONASS-only sidereally filtered PPP processing, 2014, days 321 to 327.

The standard deviations of the coordinate time series for all the sites can be seen in Table 4.4; the standard deviations in the East component in general, are improved the most by GLONASS-only filtering and the Up component the least. This is due to the GLONASS constellation having a higher inclination angle than the GPS constellation; the North coordinates are on average less noisy than the East coordinates for the UK sites. The opposite is the case for the GPS coordinate time series as discussed in section 3.9.

The standard deviations for the Up component are larger for both the unfiltered and filtered time series when compared with the horizontal components, as is the case for GPS. This is attributed to poor satellite geometry resulting from only seeing satellites in one hemisphere, due to the Earth blocking the view of satellites from underneath the receiver.

The average decrease in carrier-phase residual per satellite standard deviation for all sites is about 14.7% as seen in Table 4.5. Site HUNG, which had the lowest 3D RMS coordinate improvement out of the five sites (5.35%), actually has the largest average reduction in carrier-phase satellite residuals standard deviation of 22.2%. In contrast, site PADT had a reasonable 3D RMS coordinate improvement of 21.7% but a low average reduction in carrier-phase satellite residuals standard deviation of 6.8%. Hence, for GLONASS, the

percentage reduction in satellite residuals does not seem to correlate with the overall improvement in the coordinate time series. On closer inspection it can be seen from Figure 4.9 how all the satellites at site HUNG in the GLONASS constellation, including R21 which had no filter applied, indicated by the red horizontal line, are improved by filter application. The improvement in R21 is likely a result of the overall improvement in all other satellite residuals from filtering. Also the amount of improvement at each satellite does not seem to correlate with the strength of the correlation of the residuals when finding the optimum lag period. For site PADT, however, as seen in Figure 4.10, even with filters being applied to them, not all satellite residuals are improved by filtering (take satellites R06 and R15 as an example). The lack of improvement in residual standard deviation from filtering could be due to the relatively low correlation of satellite R15 residuals (0.21). The difference in effectiveness of the filtering as seen at site HUNG and PADT between the coordinate and residual filtering could be due to the different contribution of each satellite to the overall coordinate solution during processing, as mentioned in Larson *et al.* (2007).

Table 4.3: 3D RMS filter percentage decrease of coordinates with PPP processing with GLONASS-only sidereal filtering application.

Site	3D RMS filter % decrease
HUNG	5.35%
KILN	13.03%
MACY	21.45%
OBAN	28.02%
PADT	21.66%

Table 4.4: Standard deviations, in millimetres, of coordinates from unfiltered PPP processing and PPP processing with GLONASS-only 8 sidereal day filtering.

Site	Processing Method	East St.dev	North St.dev	Up St.dev
HUNG	PPP unfiltered	18.13	15.26	37.92
HUNG	PPP filtered	16.03	13.04	36.39
KILN	PPP unfiltered	18.15	15.60	38.90
KILN	PPP filtered	15.28	14.32	33.53
MACY	PPP unfiltered	17.65	16.64	43.70
MACY	PPP filtered	15.64	13.60	32.90
OBAN	PPP unfiltered	20.59	17.12	45.53
OBAN	PPP filtered	13.89	12.80	30.83
PADT	PPP unfiltered	33.99	18.99	46.03
PADT	PPP filtered	20.30	14.42	39.90

Table 4.5: Carrier-phase residuals average standard deviation percentage decrease with GLONASS-only sidereal filter application.

Site	LC residuals average standard deviation %
HUNG	22.20%
KILN	16.09%
MACY	11.17%
OBAN	17.37%
PADT	6.79%

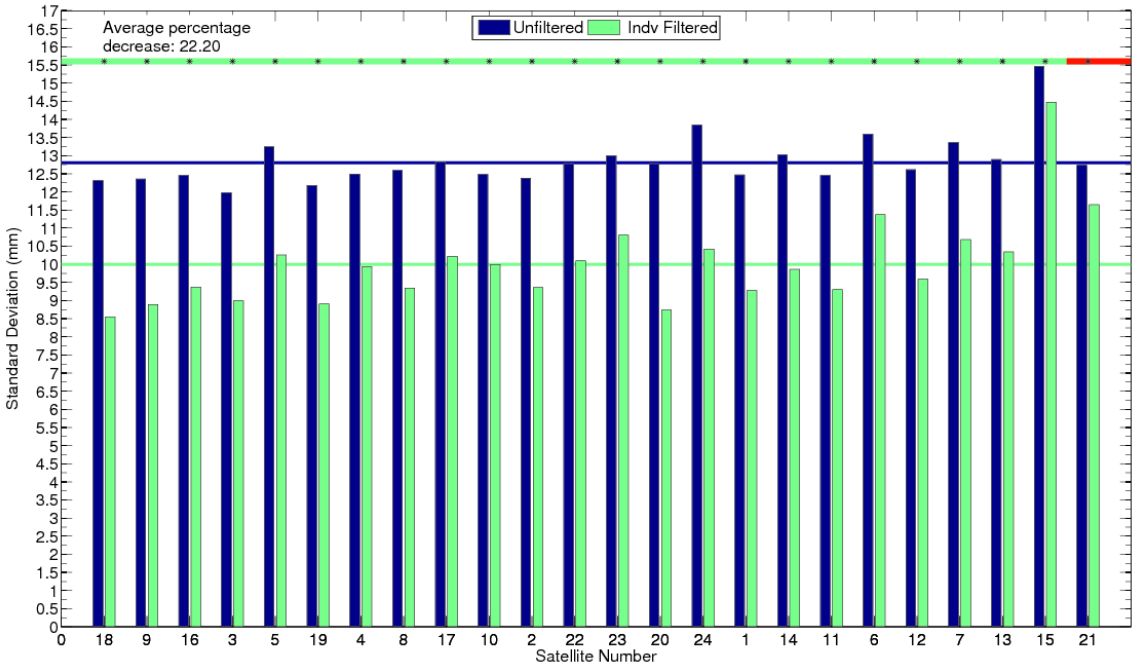

Figure 4.9: Comparison of standard deviations at site HUNG, 2014, days 321 to 327 for unfiltered and GLONASS-only sidereally filtered carrier-phase residuals per satellite. Symbology as explained in Figure 3.10.

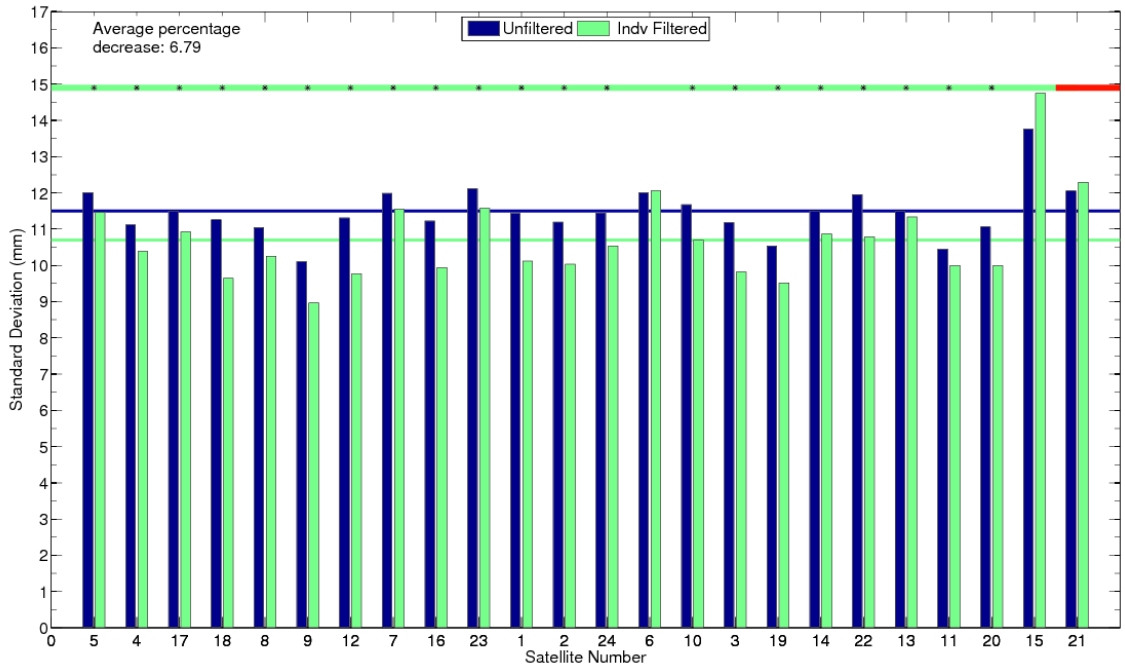

Figure 4.10: Comparison standard deviations at site PADT, 2014, days 321 to 327 for unfiltered and GLONASS-only sidereally filtered carrier-phase residuals per satellite. Symbology as explained in Figure 3.10.

As with the GPS analysis, the Allan deviation of the coordinate time series is used to assess the change in stability with filter application. An improvement in stability at periods of a few hundred seconds is beneficial for early-warning. Site PADT has the largest maximum percentage improvement in Allan deviation with GLONASS-only filter application whereas site HUNG shows the least improvement, as seen in Table 4.6. The East coordinate Allan deviation plots for PADT and HUNG can be seen in Figure 4.11 and show for PADT, increasingly larger improvements in the East coordinate stability for time intervals greater than 700 s, with the maximum improvement peaking at the maximum 2 hour averaging interval. Site HUNG, on the other hand, shows an increase in stability from averaging intervals over 450 s with maximum improvement around the averaging interval of 15 minutes. The filtered Allan deviation curve remains relatively smooth as it decreases with increasing averaging intervals. The unfiltered curve however oscillates at averaging intervals of over 450 s which causes a dip in the percentage improvement in stability at the 30 minute interval, as seen in Figure 4.14.

For the North coordinates, site MACY has the largest maximum percentage improvement in Allan deviation with GLONASS-only filter application, whereas site KILN shows the least improvement. The North coordinate Allan deviation plots for MACY and KILN can be seen in Figure 4.12. Both the unfiltered and filtered Allan deviation curves for MACY are smooth and

show an increase in the North coordinate difference stability from filtering after averaging intervals of just 90 s, which indicates GLONASS sidereal filtering is capable of reducing high-frequency multipath. The stability improvement increases steadily until the 1000 s averaging interval where it peaks then slowly plateaus before decreasing at the larger averaging intervals as shown in Figure 4.14. For KILN however, the filter shows improvement in stability from just 40 s but the improvement increases very slowly across the larger averaging intervals to a maximum of just 9%.

Table 4.6: Maximum percentage improvement in Allan deviation with GLONASS-only sidereal filter application.

Site	Maximum percentage improvement in Allan deviation		
	East	North	Up
HUNG	17%	21%	20%
KILN	18%	9%	13%
MACY	21%	24%	29%
OBAN	32%	23%	30%
PADT	43%	13%	5%

For the Up component, site OBAN has the largest maximum percentage improvement in Allan deviation with GLONASS-only filter application, whereas site PADT shows the least improvement. The Up coordinate Allan deviations plots for OBAN and PADT can be seen in Figure 4.13. The Allan deviation curve shows the stability of the Up coordinate improvement with filtering for averaging intervals of larger than 200 s for site OBAN. The improvement in stability (Figure 4.14) increases steadily until about averaging interval 700 s where it crests. This then forms a trough at 1400 s before continually fluctuating and coming to a maximum at the largest averaging interval of 2 hours. For site PADT however, the Allan deviation curve shows no improvement in stability for averaging intervals below 1 hour and 10 minutes. The maximum improvement of stability of 5% is at averaging interval 1 hour and 20 minutes which rapidly decreases to near zero again in just 20 minutes.

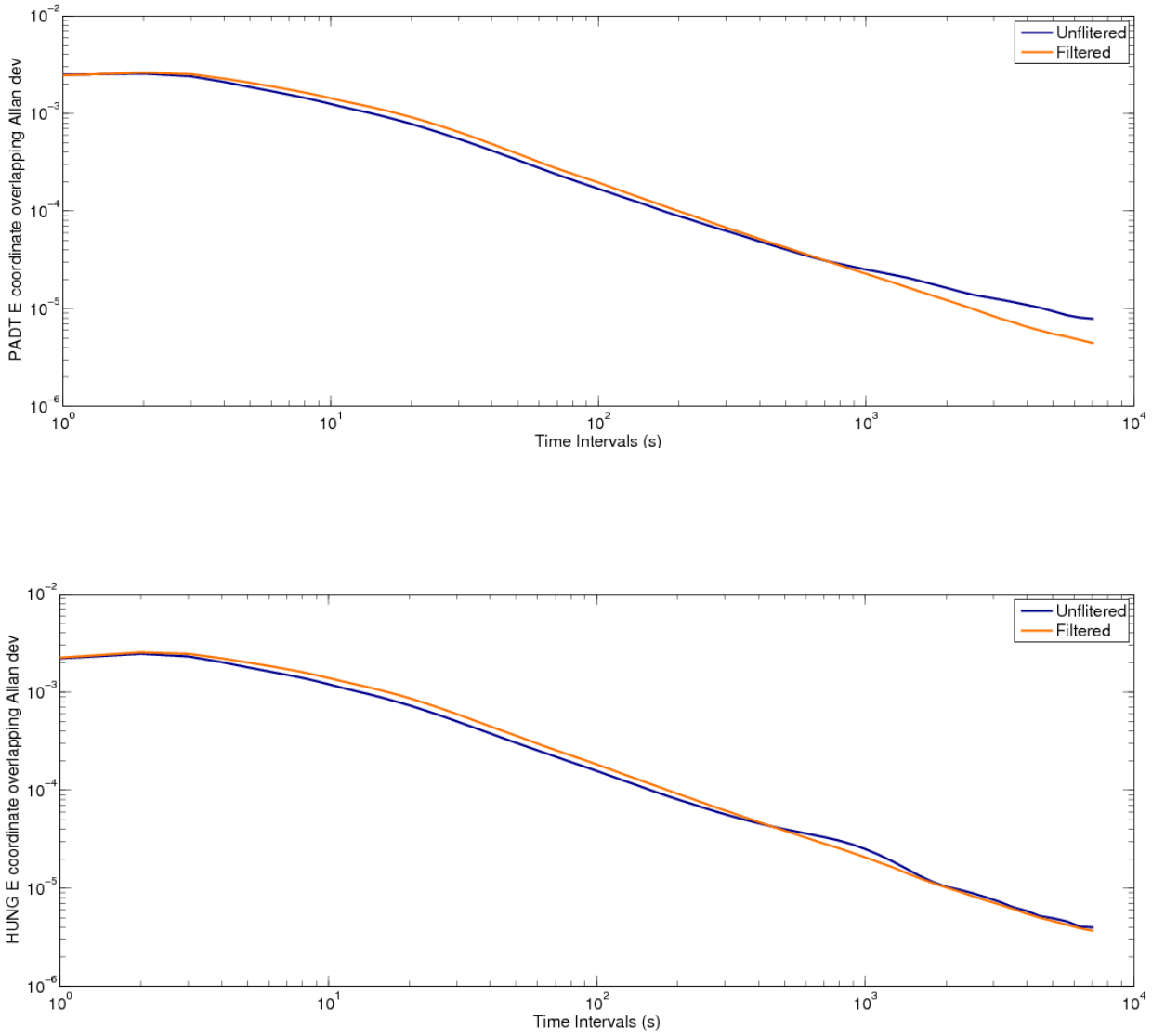

Figure 4.11: Allan deviation plots of the corresponding coordinate time series for the East coordinate at site PADT (top) and HUNG (bottom).

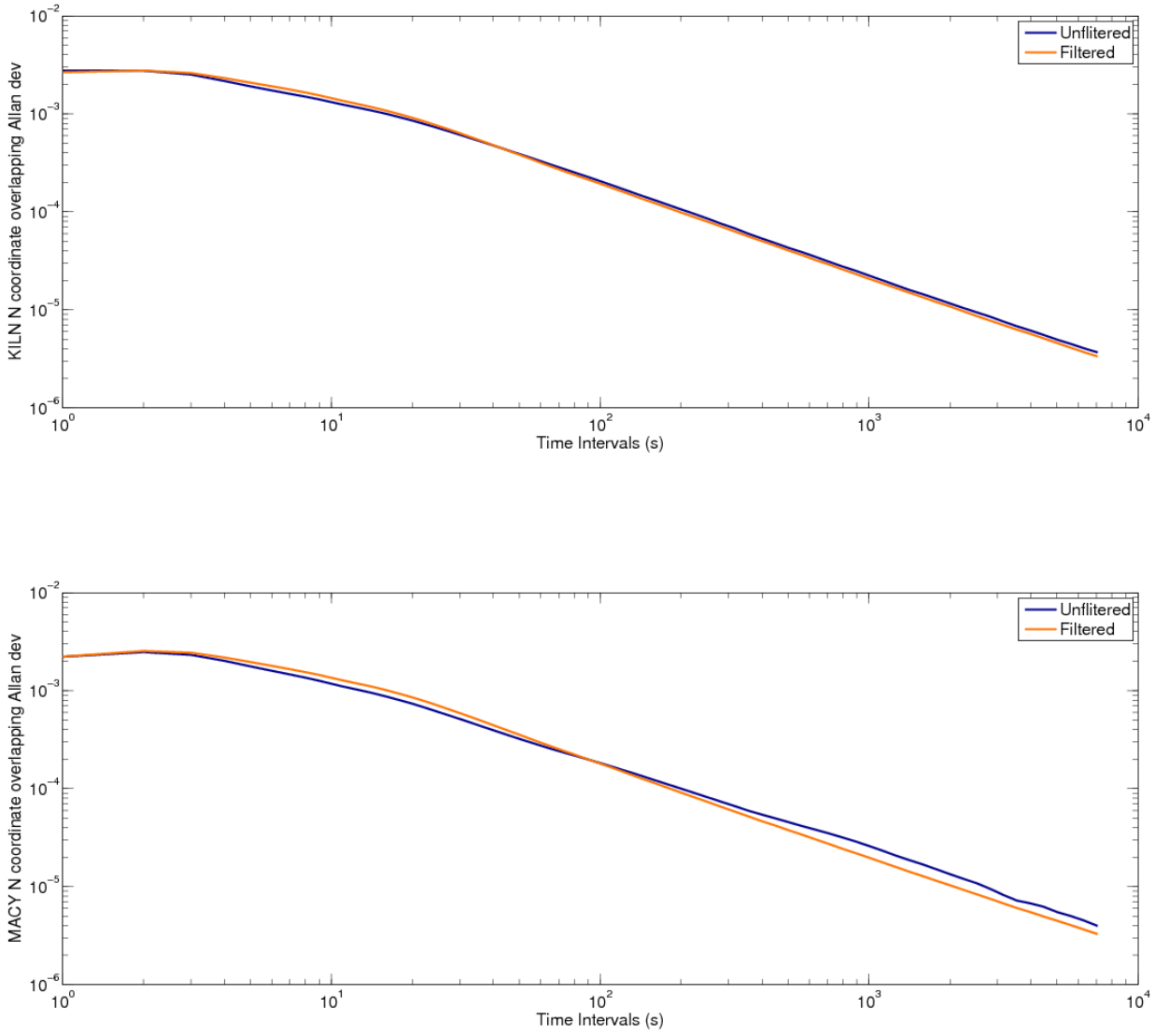

Figure 4.12: Allan deviation plots of the corresponding coordinate time series for the North coordinate at site MACY (top) and KILN (bottom).

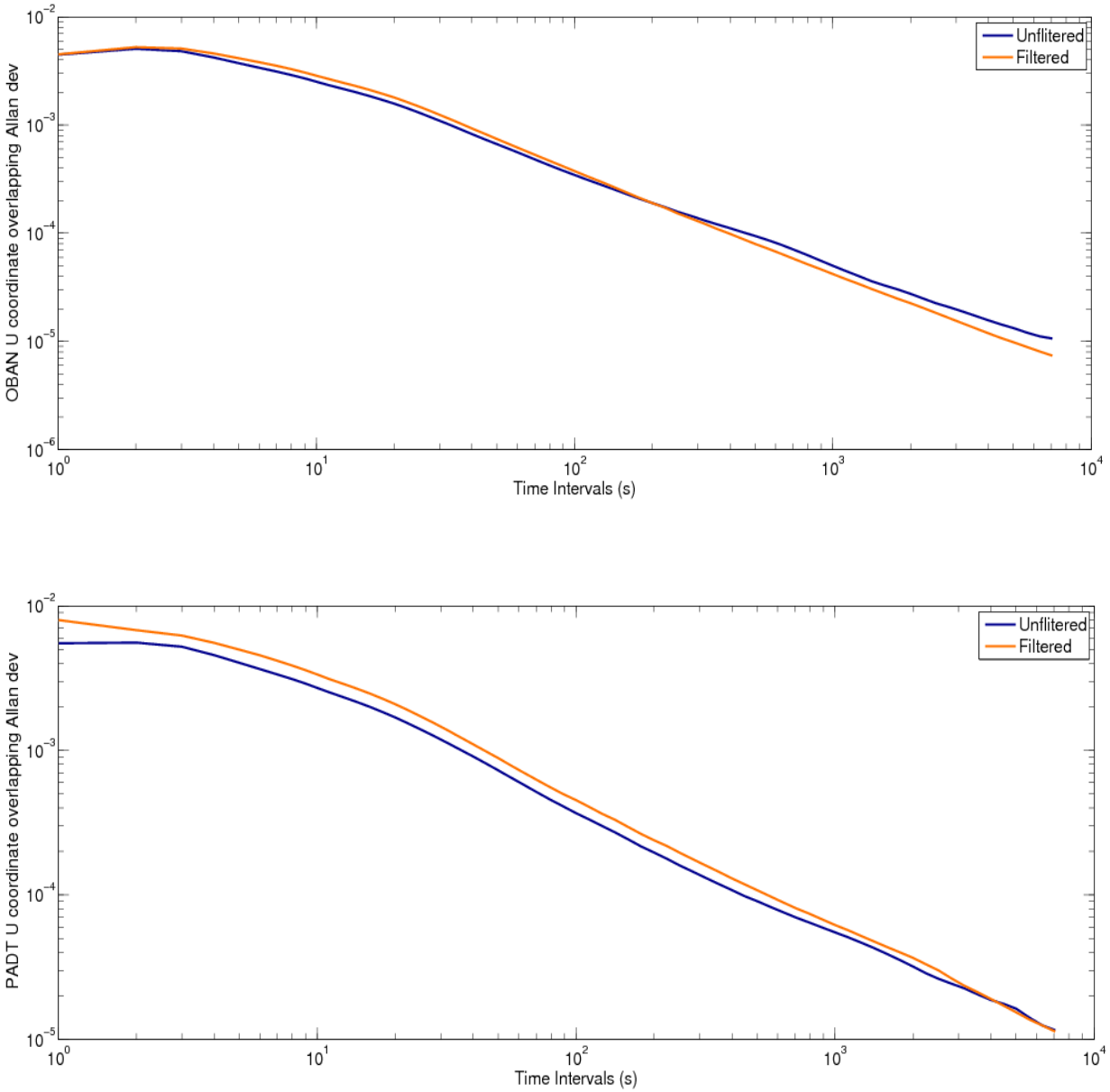

Figure 4.13: Allan deviation plots of the corresponding coordinate time series for the North coordinate at site OBAN (top) and PADT (bottom).

From looking at the percentage improvement in Allan deviation curves for all sites after GLONASS-only filtering shown in Figure 4.14, it can be seen how time series stability improvement is very much site dependent, showing similar patterns for all three coordinate components at an individual site. Sites HUNG, MACY and OBAN show an initial trough of deterioration in stability from filtering which steadily rises to a crest of near maximum improvement at around 1000 s, which then dips to lower levels of improvement before fluctuating at the larger averaging intervals. The variable performance of the filter at these larger averaging intervals of thousands of seconds could be due to more non-multipath errors contributing to the measurement residuals at these periods. It is plausible that lower-frequency multipath errors could be being soaked up by other slowly varying parameters, such as the wet tropospheric delay during the Kalman filter process. Hence, there is less multipath present at these periods in the residuals which are being used to create the multipath mitigation filters.

PADT also shows a similar pattern to the three sites previously mentioned, but only in the North and Up coordinates; the stability of the East coordinate on the other hand rapidly increases from time intervals 100 s to over 2500 s for GLONASS-only filtering. This difference at PADT could be due to the nature of the environment surrounding the antenna at this site; it has a large metal mast next to the GNSS antenna on a roof at one side, as seen in the antenna installation pictures in the Appendix A. Also, as mentioned earlier in section 4.1, the reduction in Allan deviation for site KILN is poor and hence has a different percentage Allan deviation curve in comparison to the other sites. This can be attributed to KILN having less high-level multipath (LC residual RMS >20 mm) in comparison to the other sites as seen in Figure 4.1. Thus it is expected to yield less striking results as there is less multipath to remove. The lower levels of multipath at this site can perhaps be attributed to the grassy surrounds of the antenna as opposed to smooth more reflective manmade materials surrounding the other sites' antennas, as seen in Appendix A.

Overall it can be seen how GLONASS filtering has, on average, reduced the standard deviations for all five sites by 5.5 mm, 3.1 mm and 7.7 mm in the East, North and Up coordinates, which is equivalent to about 22.3%, 18.1% and 17.6% improvement respectively. The 3D RMS of the coordinate time series has also been improved by just fewer than 18%. As well as improving the coordinate precision, GLONASS multipath filtering has also increased the stability of the coordinate time series in terms of a smaller Allan deviation

value. The average maximum improvement in Allan deviation for all five sites in the three coordinates is roughly 21% which indicates that the GLONASS filter has been successful in mitigating the majority of GLONASS multipath at these sites. The success of GLONASS multipath filtering appears to be site specific; OBAN shows the greatest improvement in coordinate standard deviations; 3D RMS and average maximum improvement in Allan deviation being 30%, 28% and 28% average values respectively. Whereas site HUNG shows the worst improvement; 10%, 5% and 19% values respectively, as previously stated. HUNG was also out-performed by site OBAN when considering all the statistics mentioned, when just using GPS observations and filtering was considered, as described in section 3.9. The main reason for this difference is that site OBAN has more high-level multipath (GLONASS LC residual RMS over 10 mm) than site HUNG as seen in Figure 4.1. This is evident from the surrounding environment at each site; OBAN is on top of a sloping roof with nearby reflecting objects, whereas HUNG is on a large flat roof with no obstructions nearby, as seen in the antenna installation pictures in Appendix A. Hence, it is expected that OBAN will experience more multipath from reflections from these nearby objects whereas site HUNG will only experience reflections from the roof itself from very low elevation angles, which should largely be reduced by the use of a choke ring antenna. Thus, OBAN yields more dramatic results as it is more strongly affected by multipath so there is more multipath to remove.

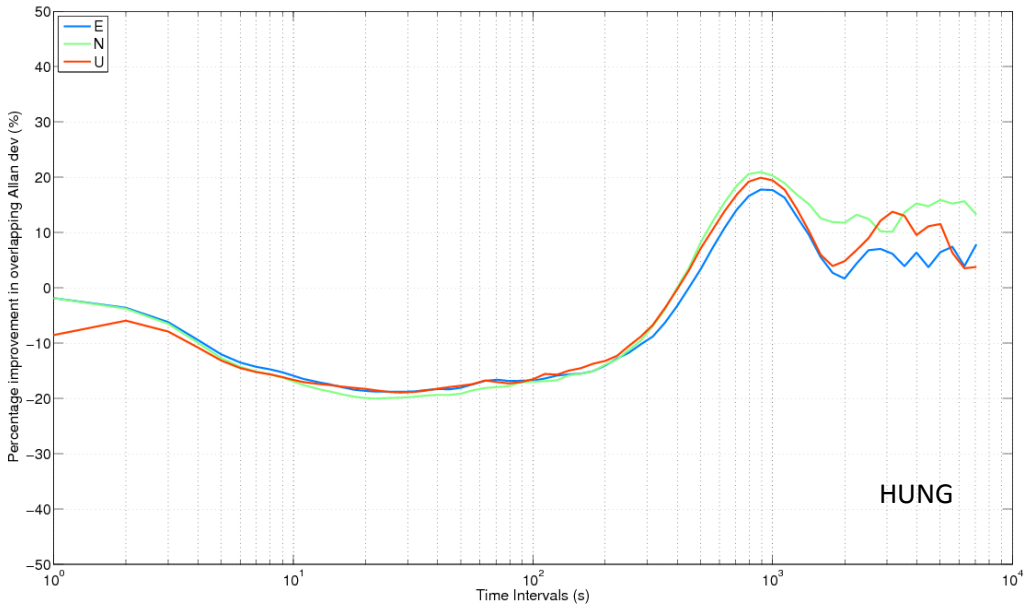
E
N
U
Percentage improvement in overlapping Allan dev (%)
Time Intervals (s)
HUNG

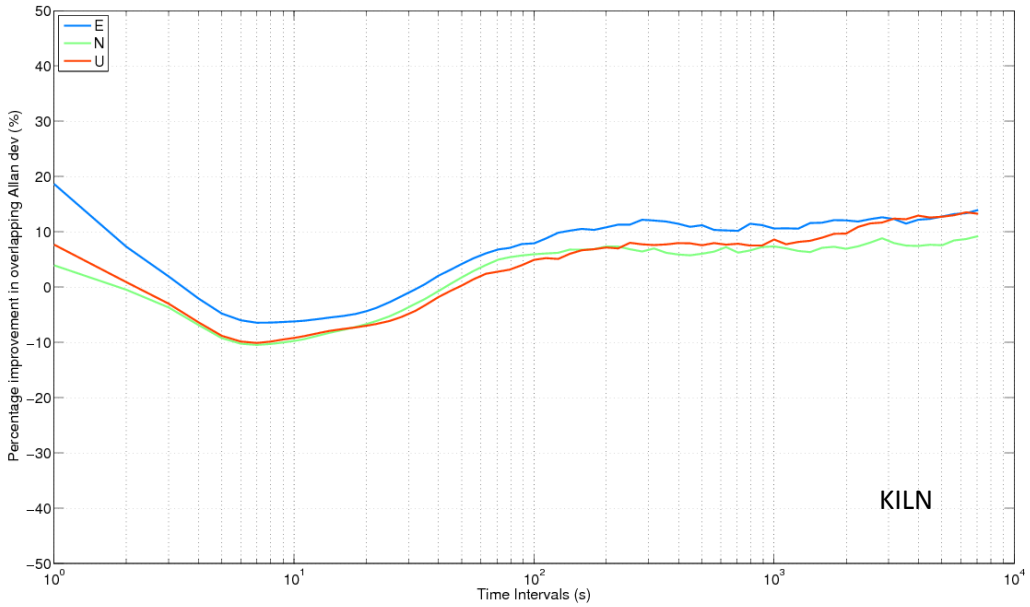
E
N
U
Percentage improvement in overlapping Allan dev (%)
Time Intervals (s)
KILN

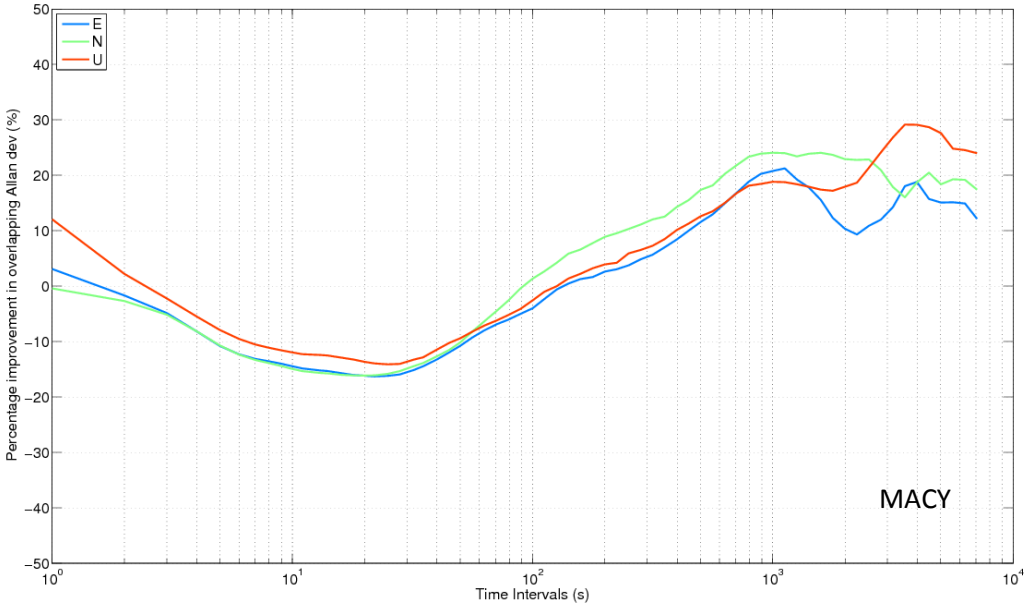
E
N
U
Percentage improvement in overlapping Allan dev (%)
Time Intervals (s)
MACY

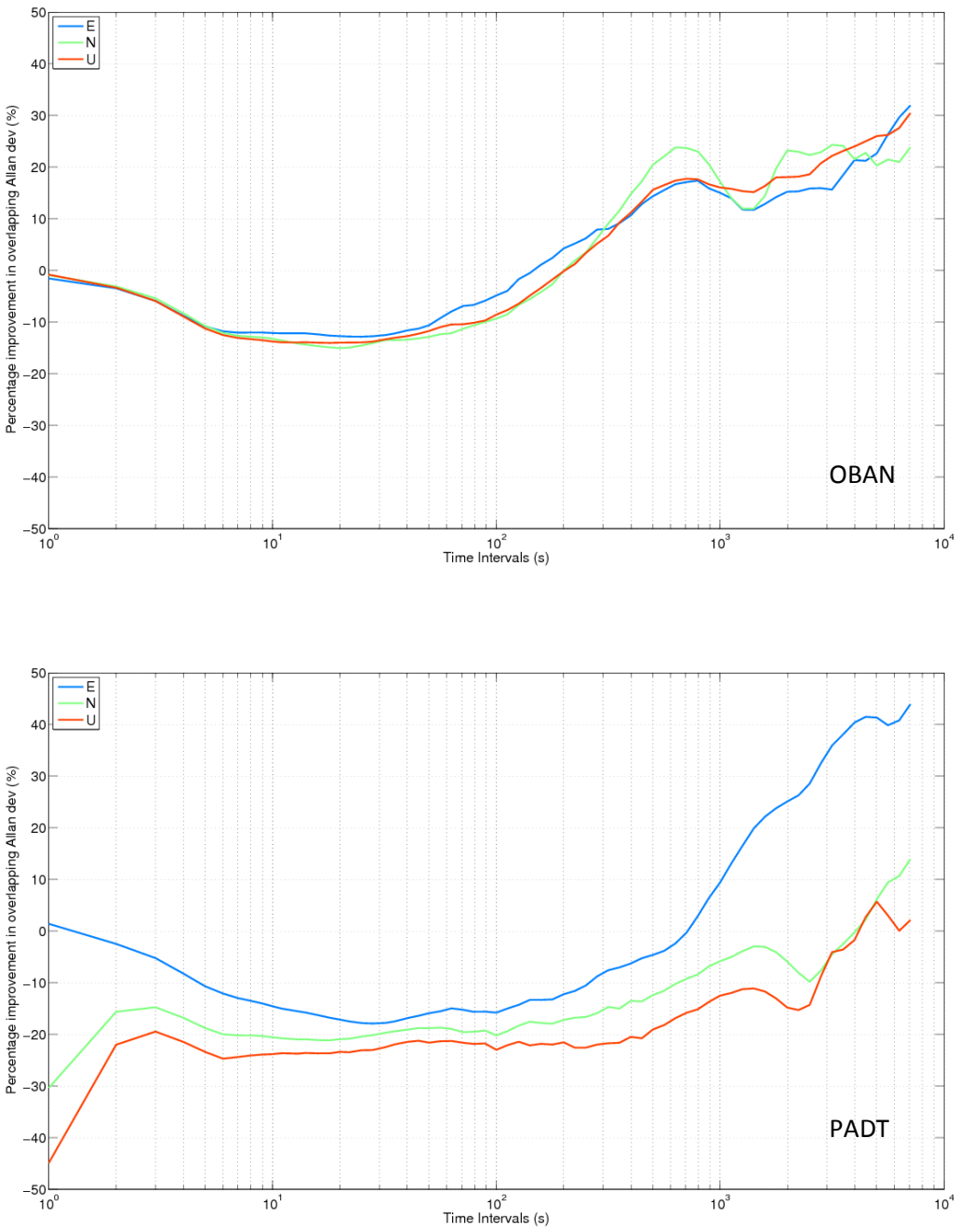

Figure 4.14: Percentage improvement (reduction), in Allan deviation for all sites, (HUNG, KILN, MACY, OBAN and PADT) after GLONASS-only filtering, corresponding to Allan deviation curves.

As seen in Figure 4.15 for site HUNG, and in Appendix C for all other sites, the GLONASS-only filter improves the position estimates at frequencies below 0.0001 Hz, (the orange curve is lower than the blue), but increases noise at frequencies greater than 0.0025 Hz, (the orange curve is higher than the blue). GLONASS filtering shows similar results to GPS filtering in the spectrum, however, it is effective over a smaller range, frequencies below 0.0001 Hz compared to 0.001 Hz, as seen for GPS in section 3.9.

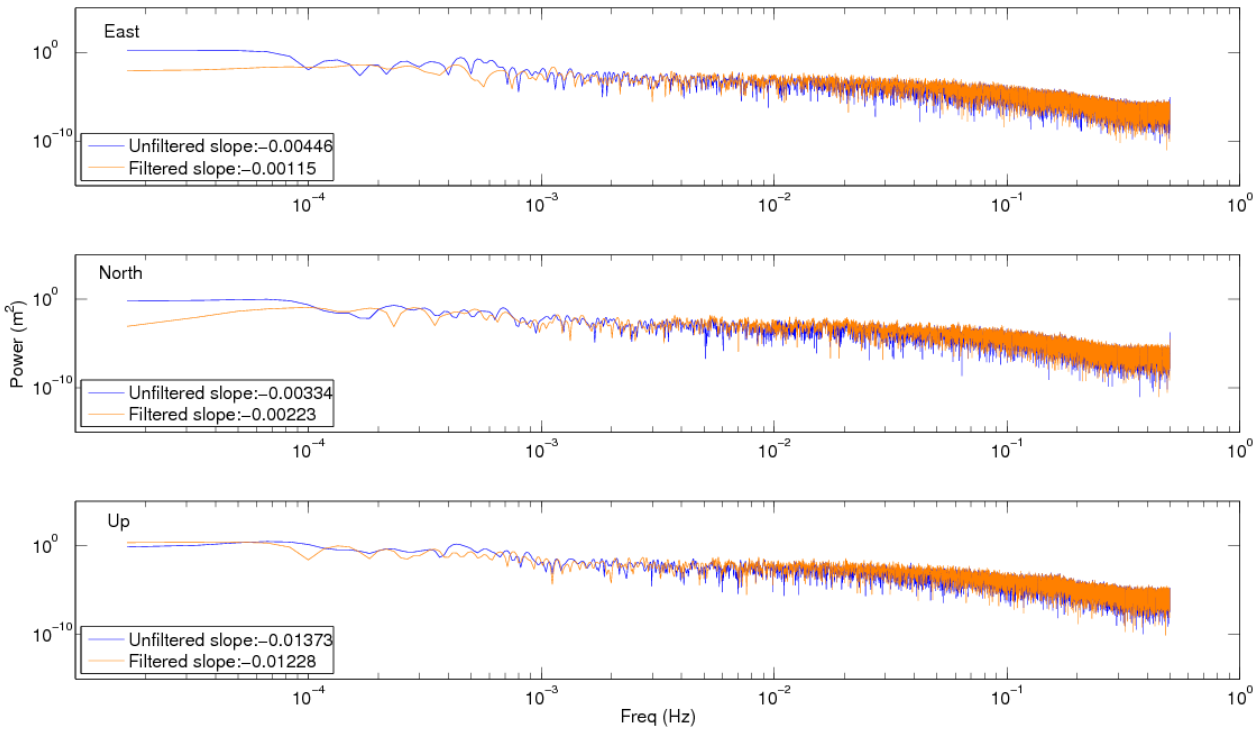

Figure 4.15: Power spectral density comparison of computed GLONASS coordinates at site HUNG of unfiltered GLONASS PPP processing, in dark blue, and GLONASS-only sidereally filtered PPP processing, in orange, 2014, days 321 to 327.

GLONASS-only filtering in general differs from GPS-only filtering, as the improvement with filtering in terms of 3D RMS and carrier-phase residual standard deviation improvement, varies more between sites. The standard deviations for GLONASS-only filtering between all five sites is 8.8 mm and 5.9% in terms of 3D RMS and carrier-phase residual standard deviation percentage improvement, compared to 6.4 mm and 1.5% for GPS-only filtering. One reason for more variation in improvement across sites could be due to more variation in GLONASS-only carrier-phase residuals with RMS values greater than 40 mm across sites, than compared with GPS-only residuals, as seen in Figure 3.4 and Figure 4.1. Additionally, due to the longer lag values used for GLONASS filter creation, certain sites may be more

prone to changing weather conditions, which affects the reflectance of surfaces near the antenna and hence the effectiveness of filtering, as mentioned in section 3.3.

4.3.1 Application of GLONASS Filter in a Low Multipath Environment

Prior to this section, the GLONASS filter has only been applied to OS sites which experience high-level multipath (LC residuals RMS >20 mm) as seen in Figure 4.1. The IGS site REDU was selected in section 3.9.1 to explore the application of GPS filtering in a low multipath environment. To ensure REDU also has a low-level of GLONASS multipath the GLONASS multipath levels at site REDU were assessed. Figure 4.1 shows how only 4% of the carrier-phase residual RMS values are over 20 mm and 16% between 10 mm and 20 mm at site REDU compared with 8% and 24% respectively, at site HUNG.

As seen in Figure 4.17, the unfiltered coordinate solution at REDU, for the same time period as used for the OS sites (days 321 to 327, 2014), standard deviations are on average 27 % lower than the OS site equivalents, as given in Table 4.4. Filtering at REDU has not improved the coordinate solution but instead has made the standard deviations larger in all components and caused the 3D RMS to worsen by 14.7 percentage points. This is due to the GLONASS carrier-phase satellite residual standard deviations only being improved by 3.8%, as seen in Figure 4.16. As discussed in the previous section, GLONASS filtering is naturally less effective than GPS filtering due to the longer lag periods used in filter creation. In a low multipath environment especially, the multipath signal is even harder to replicate which explains why the GLONASS filter has been less effective at site REDU than the GPS filter in section 3.9.1.

As seen from the Allan deviation plots in Figure 4.18 and Figure 4.19 the filter has not improved the coordinate solution stability, in fact it has caused the stability to worsen by over 20% in the East component. The lack of improvement in neither precision nor stability by GLONASS filtering at REDU is likely due to the filter being unable to distinguish the low multipath signal from noise, coupled with the high potential of the environment changing between long lag periods. This thus causes noise to be added to the signal rather than the true multipath signal being subtracted during filter application. Hence, GLONASS filtering effectiveness suffers greater than GPS filtering in a low multipath environment and filtering should only be used if a high-level of multipath is expected.

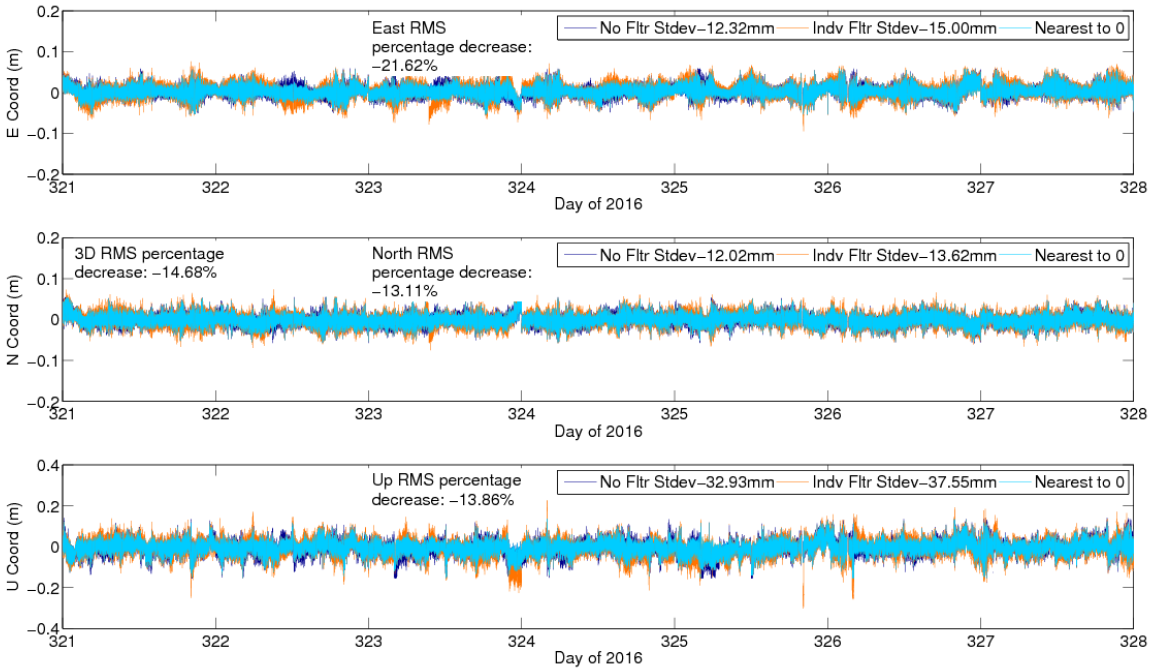

Figure 4.17: Coordinate comparison at site REDU of unfiltered PPP and GLONASS-only sidereally filtered PPP processing, 2014, days 321 to 327. Symbology as explained in Figure 3.11.

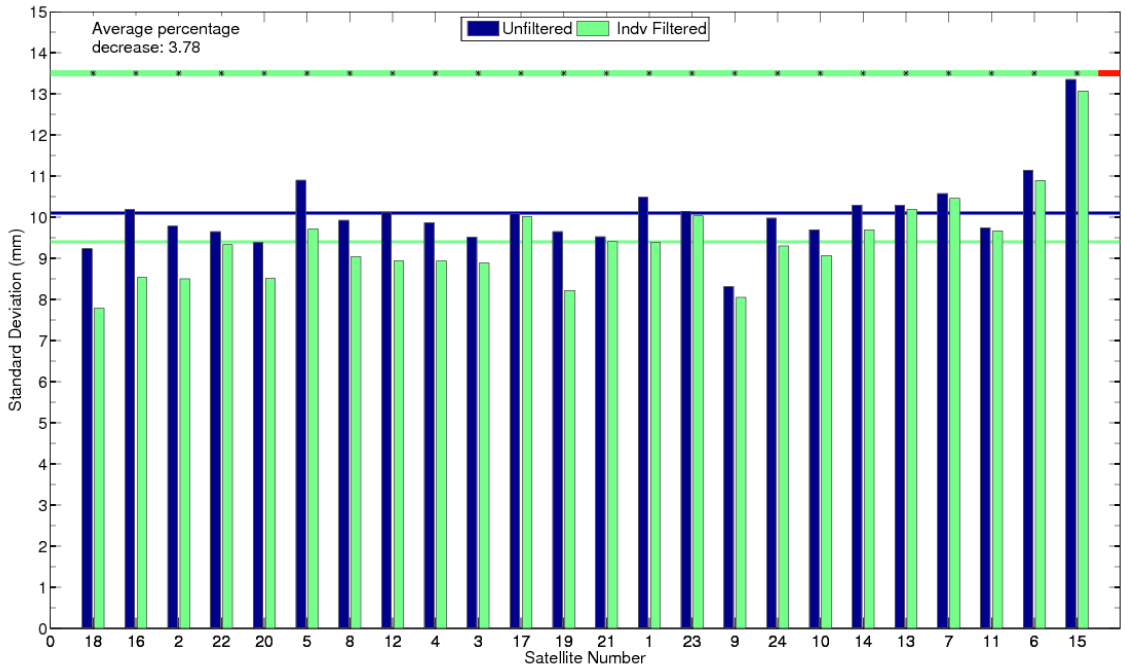

Figure 4.16: Comparison of standard deviations at site REDU, 2014, days 321 to 327 for unfiltered and GLONASS-only sidereally filtered carrier-phase residuals per satellite. Symbology as explained in Figure 3.12.

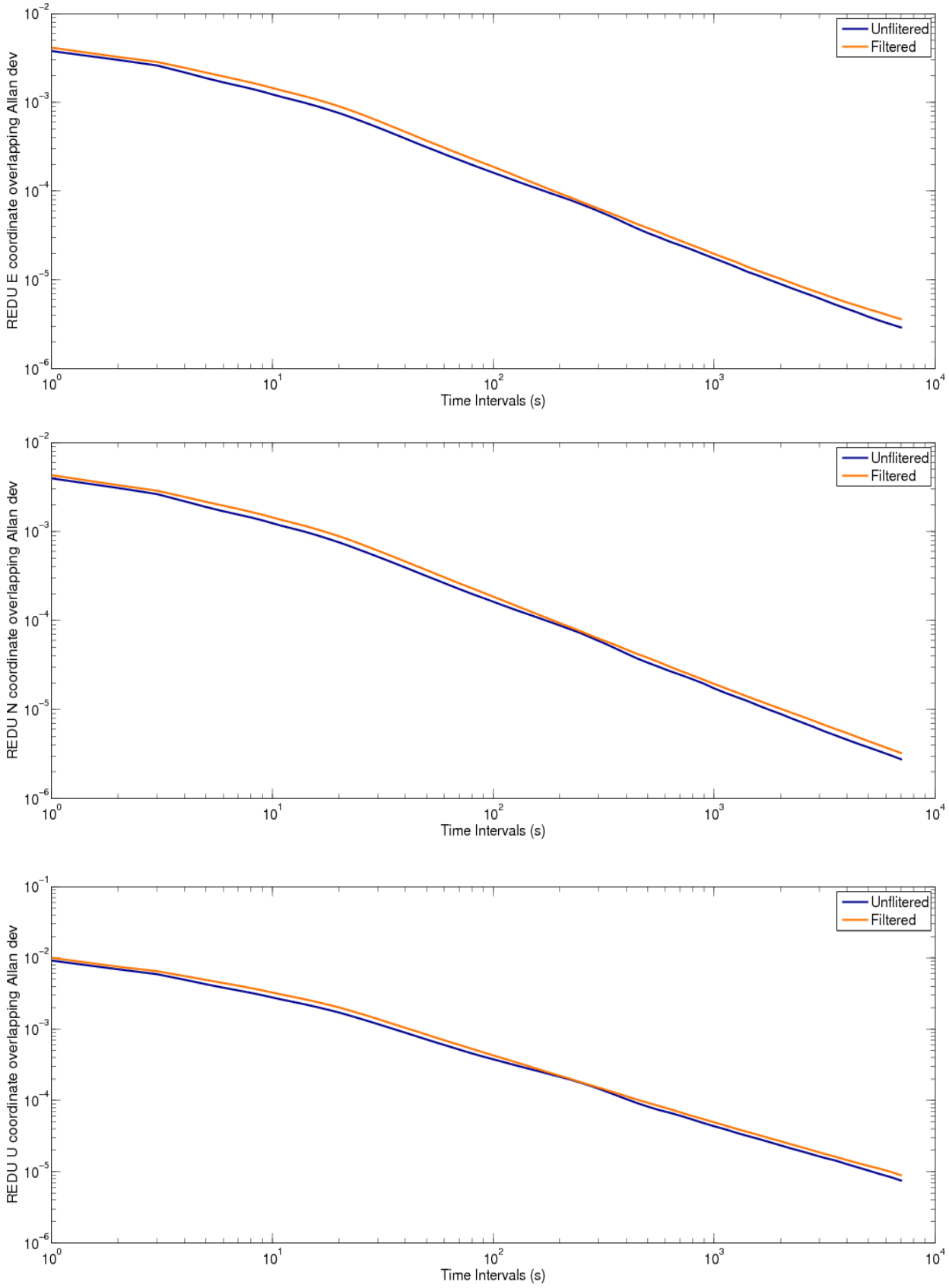

Figure 4.18: Allan deviation plots of the corresponding coordinate time series (East, North and Up) at site REDU.

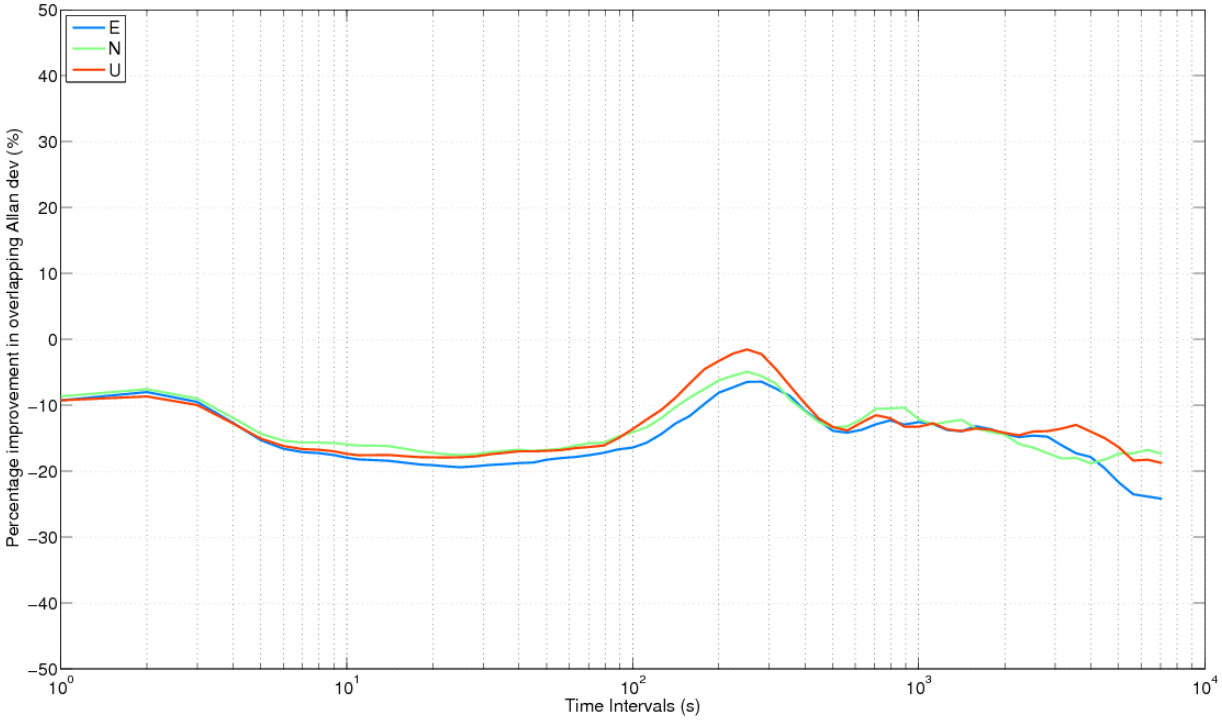

Figure 4.19: Percentage improvement (reduction), in Allan deviation at site REDU after GLONASS-only sidereal filtering.

4.4 Application of Filter using Elevation Angle Threshold

The effect of satellite elevation angle is taken into consideration when applying the GLONASS filter in this section. Prior to this section the filter has been applied to all elevation angles between 0° and 90°. It is expected that when satellites are at lower elevation angles they will experience higher levels of multipath; therefore only applying the filter at times of low satellite elevation should prevent adding or amplifying other noise at times experiencing little to no multipath. To explore this theory, high-level multipath (LC residual RMS >20 mm) for all five sites was sorted into two elevation angle categories; elevation angles of 30° or less and angles between 30° and 90°. The percentage of values in each category from the total was then computed. It is clear from Figure 4.20 that the majority of high-level multipath for GLONASS satellites does occur at low elevation angles, as was the case for GPS satellites seen in section 3.9.1. On average 87.2% of the sites' high-level multipath for GLONASS occurs at elevation angles of 30° or less, which is only 4% less than the average for GPS. This value is higher for site HUNG where about 96.4% of the total high level multipath occurs at elevation angles 30° or less, compared to only 80.6% for site MACY. Both of these sites were hence selected to test the effect of limiting the filter application to epochs where satellite elevation is 30° or less.

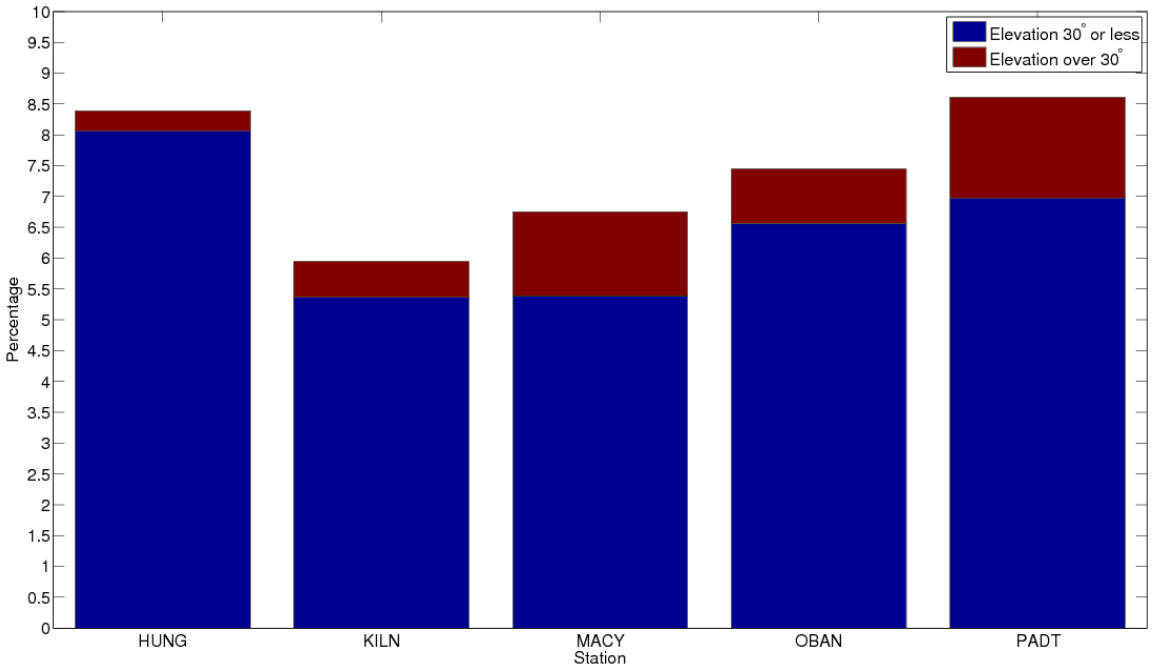

Figure 4.20: Percentage breakdown of elevation angles with GLONASS-only carrier-phase residuals RMS >20 mm.

4.4.1 Application of filter at elevation angles of 30° or less

The statistics in Table 4.7 show that the coordinates for site HUNG yield slightly lower standard deviations, about 0.6 mm on average for all three components, for 30° filter application (epochs with elevation angles of 30° or less) compared to the 90° filter (epochs with elevation angles between 0° and 90°). The overall 3D RMS improvement of the time series has also increased by about 2.61%, which may seem small but could prove important when measuring small displacements such as those required for accurate earthquake and tsunami magnitude estimates. For MACY on the other hand, thresholding filter application to lower elevation angles has not improved filter performance, instead causing the coordinate time series standard deviations to increase by about 2 mm in the horizontal components and over 10 mm in the vertical component. The 3D RMS improvement is also ~20% less than for the 90° application.

As well as the precision in coordinate time series, the stability has also improved at site HUNG when using a 30° filter. It can be seen from the Allan deviation plots in Figure 4.21 how the 30° filtered results consistently have a lower Allan deviation value than the 90° filter curve for all coordinate components. The 30° filter also shows improvement in stability at

shorter averaging intervals, about 3 mins shorter than for the 90° filter. This implies the filter is either better at removing high-frequency multipath or high-frequency noise is more likely not being amplified at the higher elevated satellites by filter application. The percentage improvement shown in the Allan deviation plot in Figure 4.22, more clearly exhibits this improvement. Although the low elevation filter yields greater stability throughout the averaging intervals, the maximum improvement in Allan deviation is similar in magnitude and averaging interval to the filter applied to all elevation angles, as seen in Table 4.8. This reiterates the fact that the majority of high-level multipath occurs at lower elevation angles at this site, from the assumption that the maximum improvement is due to more multipath being mitigated, due to there being higher levels of multipath to mitigate at this period.

The Allan deviation curves for site MACY as seen in Figure 4.23 also show that the 30° filter reduces the amplification of high-frequency noise at the short averaging intervals. The stability of the 30° filter is lower than the 90° filter for averaging intervals smaller than about 200 s where both filters have greater Allan deviation than the unfiltered case. After this interval the 90° filter Allan deviations get notably smaller than the unfiltered curve, whereas in comparison there is very little reduction in Allan deviation from the 30° filter. Again this is more evident from the percentage improvement in Allan deviation plots as was shown in Figure 4.22, where the 90° filter can be seen to rapidly improve stability whereas the 30° filter slowly increases before plateauing. This is mostly likely, as hypothesised, due to about 20% of the high-level multipath at MACY occurring at elevations greater than 30° so they are not filtered when using the elevation angle threshold filter of 30° or less. The GLONASS results for site MACY are in keeping with the results found when using GPS filtering at this site.

Table 4.7: Comparison of elevation angle filter thresholding statistics; coordinate standard deviations, percentage decrease in 3D coordinate RMS and percentage decrease in carrier-phase residuals standard deviations, for sites HUNG and MACY.

Site	Processing Method	East St.dev (mm)	North St.dev (mm)	Up St.dev (mm)	3D RMS filter % decrease	LC residuals St.dev % decrease
HUNG	90° filter	16.03	13.04	36.39	5.35	22.20
HUNG	30° filter	15.48	12.53	35.56	7.96	23.86
HUNG	38° filter	15.36	12.47	34.96	8.80	24.62
HUNG	Indv filter	15.37	12.61	35.48	7.88	23.97
MACY	90° filter	15.64	13.60	32.90	21.45	11.17
MACY	30° filter	17.46	15.91	43.37	1.05	5.56

Table 4.8: Comparison of elevation angle filter thresholding maximum percentage improvement in Allan deviation for sites HUNG and MACY.

Site	Processing Method	Maximum percentage improvement in Allan deviation		
		East	North	Up
HUNG	90° filter	17%	21%	20%
HUNG	30° filter	20%	21%	21%
HUNG	38° filter	21%	23%	22%
HUNG	Indv filter	20%	21%	21%
MACY	90° filter	21%	24%	29%
MACY	30° filter	8%	9%	6%

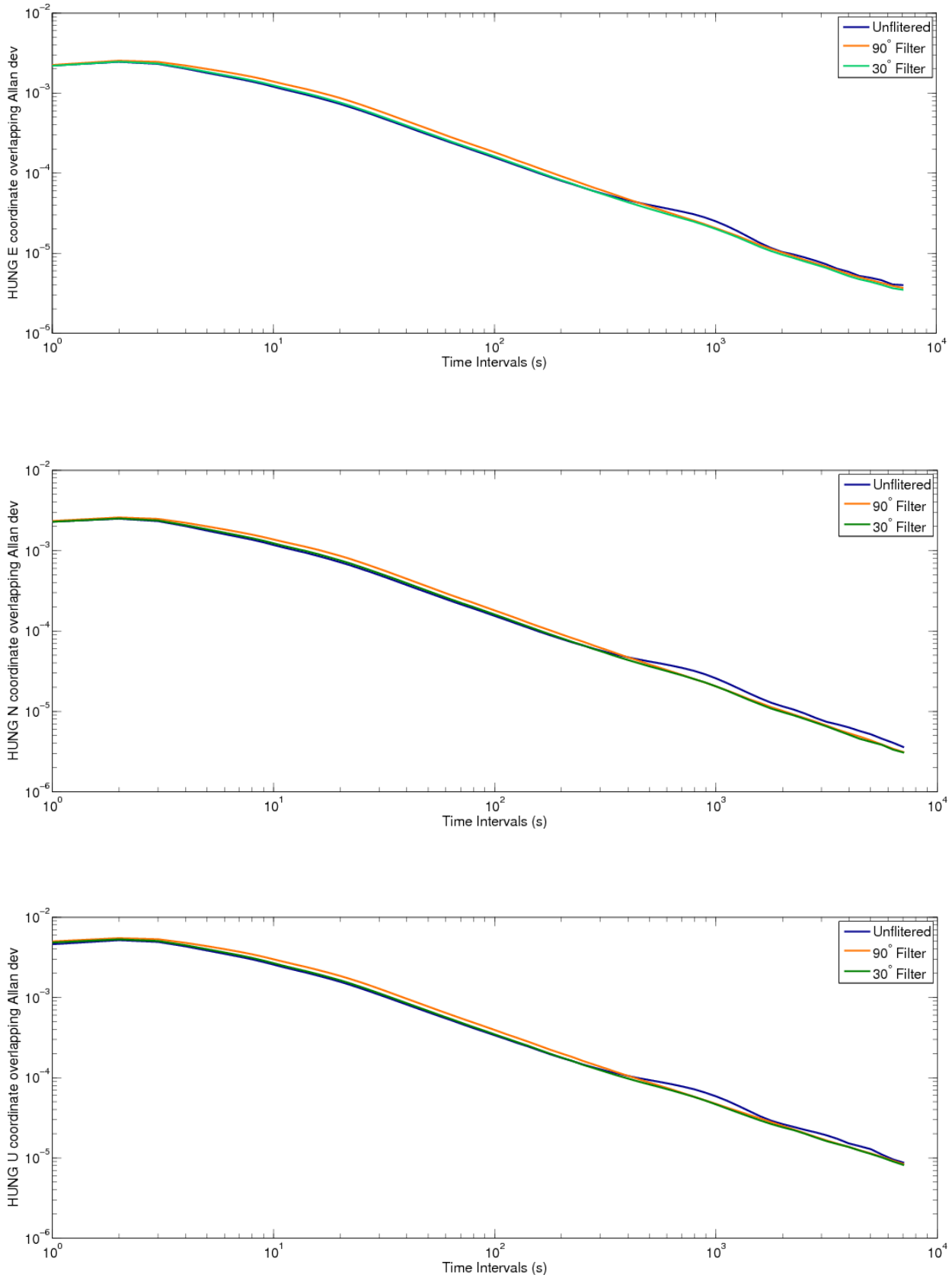

Figure 4.21: Comparison of elevation angle filter thresholding Allan deviation plots for GLONASS-only, site HUNG.

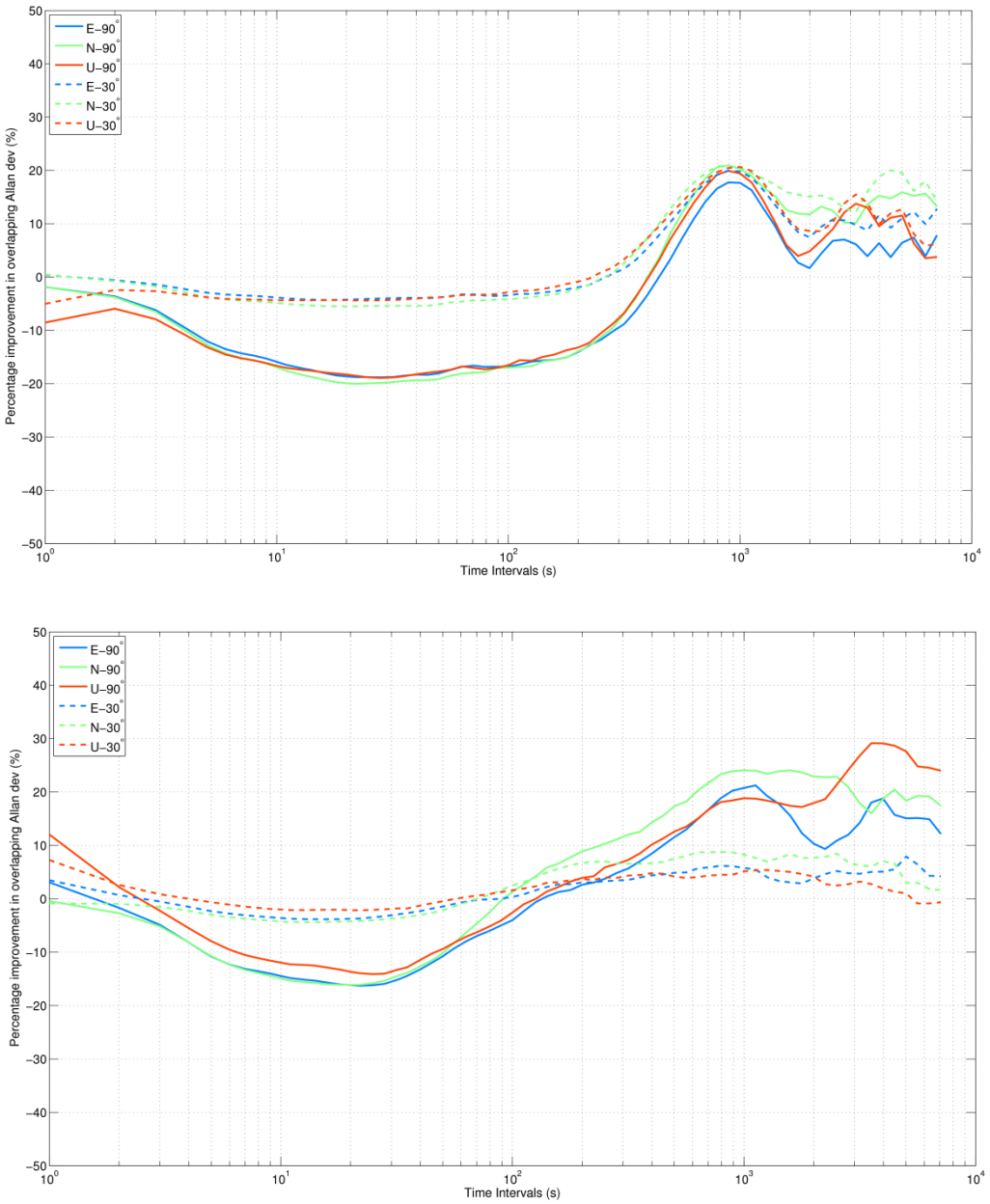

Figure 4.22: Comparison of elevation angle filter thresholding percentage improvement in Allan deviation for GLONASS-only, sites HUNG (top) and MACY (bottom) for a 90° and a 30° or less filter.

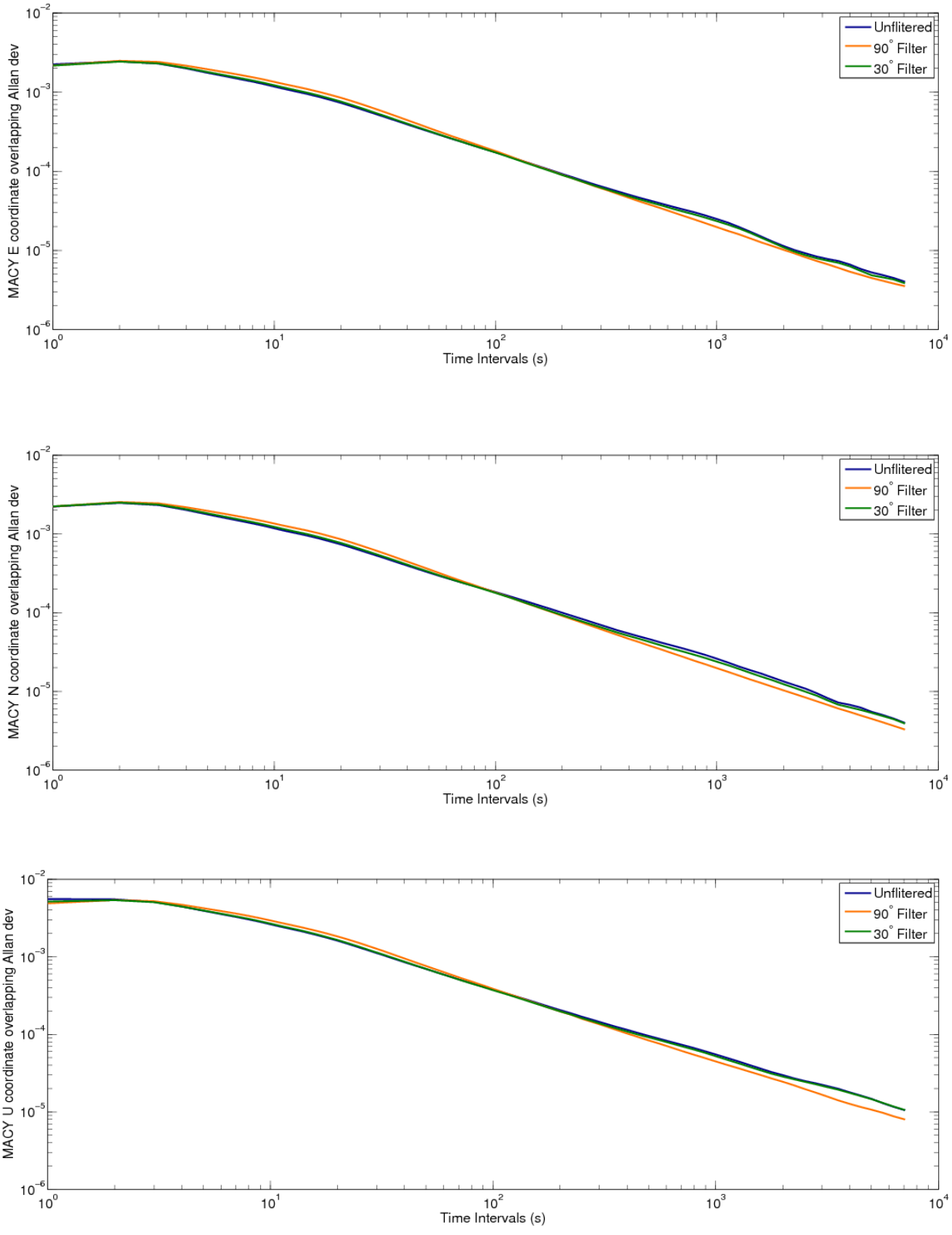

Figure 4.23: Comparison of elevation angle filter thresholding Allan deviation plots for GLONASS-only, site MACY, East, North and Up respectively.

4.4.2 Application of filter at elevation angles of 38° or less

The improvement at site HUNG from using a filter elevation of 30° or less indicates that sidereal filtering for GLONASS can additionally be enhanced by calculating the optimum elevation angle for filter application as well as using individual optimum lag periods. This theory was investigated further by calculating the optimum elevation angle for filter application for the constellation as a mean and for individual satellites at site HUNG. Optimum elevation angles were computed by correlating the optimum lag value for each satellite using elevation angles ranging initially from 20° to 90° incremented by 5° intervals. This range was then reduced to angles ranging from 20° to 40° incremented by 2° intervals. As with finding the optimum lag period, the elevation angle which gives the highest correlation value is deemed the optimum. As seen from Figure 4.25 the optimum elevation angle varies for each satellite and has a mean value of 38° at site HUNG. The filter was hence recomputed and only applied to epochs with elevation angles of 38° or less.

As seen from the statistics in Tables 4.7 and 4.8, the 38° or less filter reduces the coordinate standard deviations in all three components on average by 0.3 mm in comparison with the 30° or less filter which is itself an average reduction in standard deviation of 2.85 mm from the unfiltered case. The 3D RMS improvement has also increased to 8.8% and the average reduction in carrier-phase residuals standard deviations has increased to 24.62%, which is just under 1 percentage points more than for the 30° or less filter.

From the percentage improvement in Allan deviation plot shown in Figure 4.26, the increase in maximum improvement in time series stability on average of about 1 percentage point can be seen. However the improvement in time series stability at shorter averaging intervals has not been improved by the 38° or less filter, which indicates that high-frequency noise is still being amplified for certain satellites. Hence a filter with individual elevation thresholds was computed and tested to see if noise amplification could be reduced further. The constellation mean elevation threshold value has enhanced filter application for GLONASS satellites but did not improve GPS filter application, as discussed in section 3.10.1. This could be due to more variability in GPS satellite elevations than in GLONASS satellites, as seen in Figure 3.22 and Figure 4.24.

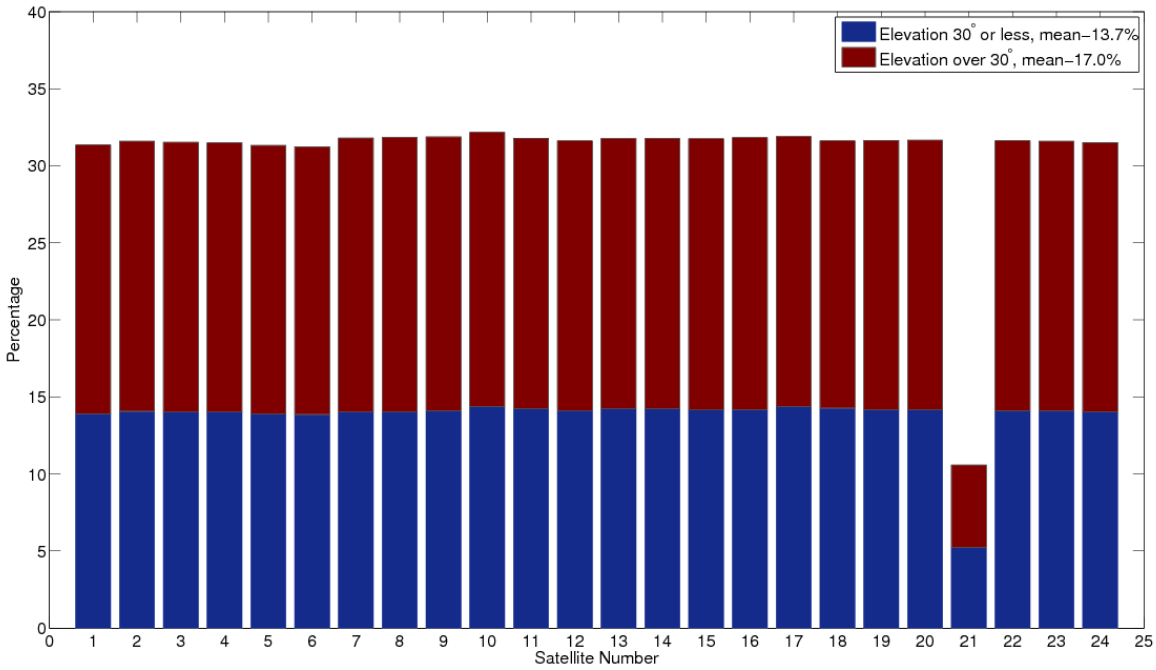

Figure 4.24: GLONASS satellite elevation angle variation at site HUNG, 2014, days 306-327 for RMS >20mm.

4.4.3 Application of filter at optimum elevation angles for each satellite

As seen from Figure 4.25 the optimum elevation angles for the constellation at site HUNG vary from 24° to 40° for individual satellites. The statistics in Tables 4.7 and 4.8 show that using individual elevation thresholds for individual satellites does not appear to improve the accuracy of the coordinate time series compared to using the constellation mean elevation angle threshold, nor does it improve the stability of the time series at the short time intervals, which was also the case for GPS filtering. This could be, as stated before in section 3.10.2, since optimum elevation angles are based on using the optimum lag periods calculated from using residuals with elevation angles between 0° and 90° rather than recalculating the optimum lag value at the elevation threshold.

For site HUNG it has been shown that GLONASS filtering can be improved by tailoring the filter by elevation angle, which prevents the amplification of high-frequency noise at higher elevation angles where less multipath is present. The effectiveness of this is site specific and should be tailored to individual sites, which although more time consuming produces more precise and stable results. For site HUNG the precision increased by 3.5 percentage points and stability by 2.5 percentage points on average, when using a mean elevation angle

threshold for filtering rather than applying the filter to all elevation angles. Reducing the elevation cutoff of site MACY to 30° or less however reduced filter performance drastically by 20 percentage points in accuracy and 17 percentage points in stability which for earthquake and tsunami applications could make a large difference to the overall earthquake and tsunami size magnitude estimates. Therefore elevation angle thresholding for filter application is recommended to be investigated but cannot be generalised for all sites as evident from the 30° angle or less filter at site MACY, so must only be used if computed first.

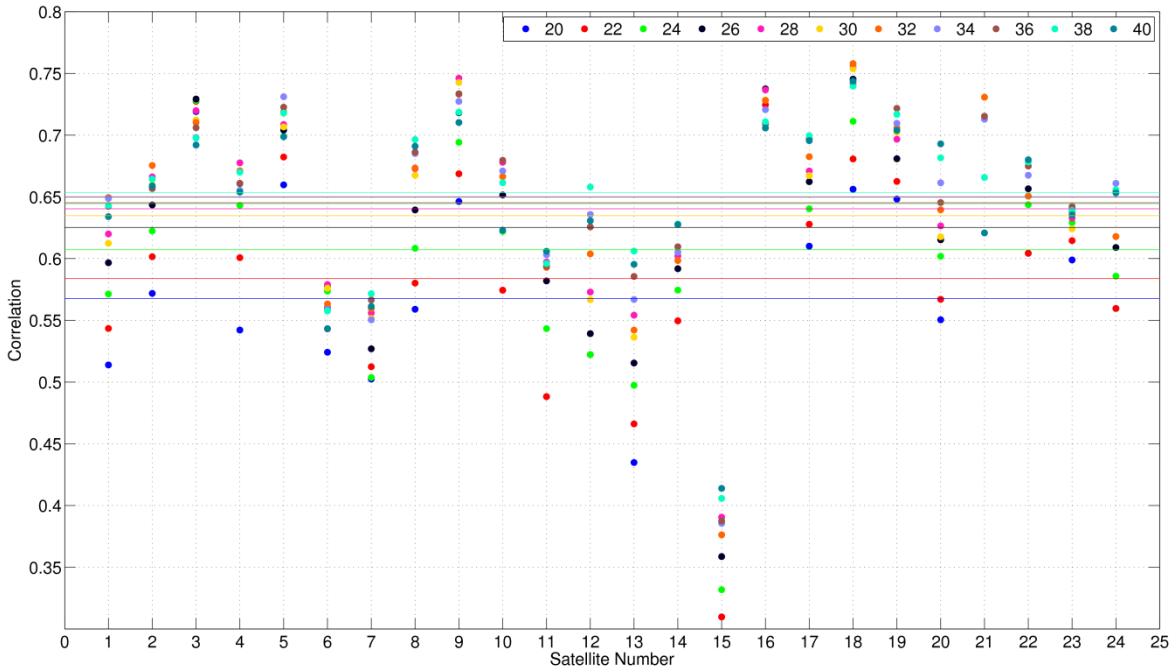

Figure 4.25: Correlation values of GLONASS carrier-phase residuals at a range of elevation angle thresholds at HUNG, 2014, days 306-327. Straight lines show elevation constellation mean values.

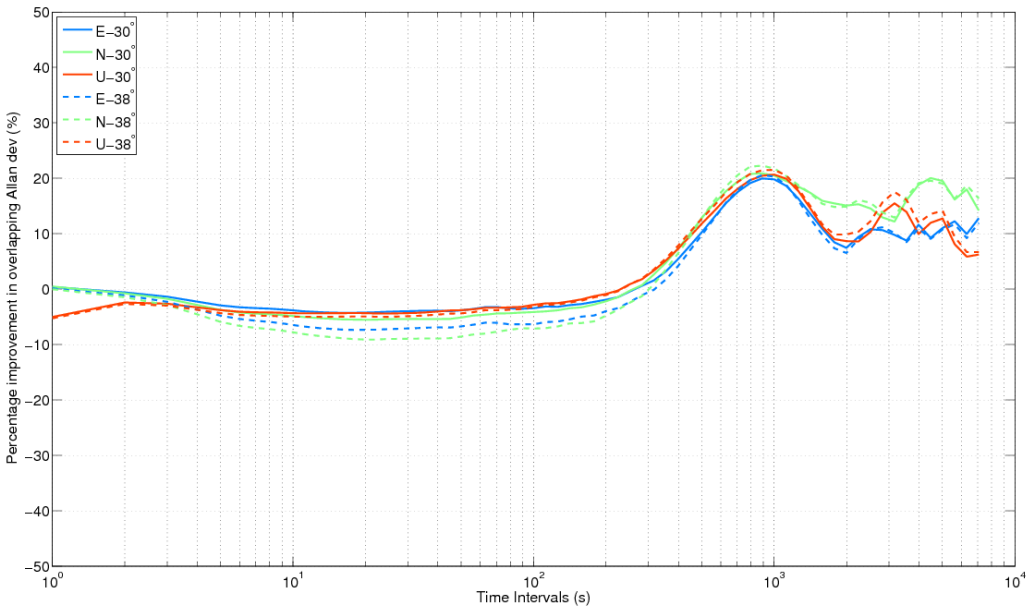

Figure 4.26: Comparison of elevation angle filter thresholding percentage improvement in Allan deviation for GLONASS-only at site HUNG for a 30 ° and a 38° or less filter.

4.5 GPS and GLONASS Combined Filtering Performance

Due to the difference in GPS and GLONASS satellite geometry repeat periods, the filter algorithm was created to be independent for each constellation. This allows the filter to be used during single constellation processing or dual constellation processing and to be expanded for multiple constellations and repeat periods. To see if a combined GPS and GLONASS (GR), solution would benefit from GPS and GLONASS multipath filtering rather than just a GPS or GLONASS filtering alone, using the same method as described previously, a GPS filter was created and applied to all elevation angles, as was a GLONASS filter for a GR PPP solution. For the same GR PPP solution, just the GPS-only filter was applied to assess the improvement made by the addition of GLONASS filtering.

As seen from the coordinate standard deviations in Table 4.9, there is an improvement in positioning solution from the combined use of GPS and GLONASS when compared with both the GPS-only and GLONASS-only unfiltered solutions. Using a GR solution has decreased the unfiltered coordinate standard deviations when compared with the GPS-only solutions by 35.6% and by 39.0% when compared with the GLONASS-only solution, Table 3.5 and Table

4.4 respectively. Thus the use of GPS and GLONASS enhances position performance for these sites even without filtering, when compared to single constellation solutions.

As seen from the coordinate standard deviations in Table 4.9, GR filtering improves the standard deviation in the horizontal components for all sites on average by 2.6 mm (22.0%) and 7.0 mm (25.1%) in the vertical component. When only using GPS filtering in the combined GR solution however, the standard deviations are only improved on average by 1.8 mm (15.1%) and 4.9 mm (17.2%) in the horizontal and vertical components. The combined GR filtering improves filtering by 7.5 percentage points on average for all sites in terms of coordinate standard deviation in comparison with just GPS filtering alone. The combined GR filtering improves the coordinate standard deviations in comparison with just the GPS-only, GPS filtered solutions by 24.7%, and the GLONASS-only, GLONASS filtered solutions by 43.2%. Hence a GR filtered solution is advised for these five sites if optimum coordinate precision is to be gained.

The difference between GR and GPS-only filtering for the 3D RMS coordinate difference is a similar size with GR filtering showing around 5.8 percentage points more improvement, with an average of 21.4% for all sites.

As an example, it can be seen from the GR coordinates for site PADT shown in Figure 4.27, how consecutive days show similar variation in coordinates in all three components over periods of a few minutes and to a few hours. In the East component there is a distinct near-sidereal pattern which peaks at about 0.04 m, which extends over 5 hours and starts at around 19:00 each day. The sidereal filter can be seen to smooth this crest which indicates that the filter has been successful in reducing low-frequency multipath in the order of a few hours. The standard deviations for site PADT show the largest improvements with GR filtering of 38.8% on average for all three coordinates and a 3D RMS improvement of 32.1%.

Table 4.9: Standard deviations, in millimetres, of coordinate from unfiltered PPP processing, GR PPP processing with GR filtering and GR PPP processing with GPS-only filtering.

Site	Processing Method	East St.dev	North St.dev	Up St.dev
HUNG	PPP unfiltered	8.83	10.23	24.33
HUNG	GR filtered	8.42	8.79	21.06
HUNG	GPS-only filtered	8.62	9.30	21.74
KILN	PPP unfiltered	10.38	10.56	24.92
KILN	GR filtered	8.76	9.28	20.83
KILN	GPS-only filtered	8.95	9.70	21.86
MACY	PPP unfiltered	10.06	11.85	25.38
MACY	GR filtered	8.09	8.99	19.48
MACY	GPS-only filtered	8.56	10.04	21.76
OBAN	PPP unfiltered	10.31	10.88	26.56
OBAN	GR filtered	7.37	7.90	17.91
OBAN	GPS-only filtered	8.49	9.18	21.35
PADT	PPP unfiltered	14.46	13.82	33.26
PADT	GR filtered	9.02	8.42	20.01
PADT	GPS-only filtered	10.76	9.87	23.49

Table 4.10: Comparison of GR and GPS-only filtering statistics; percentage decrease in 3D coordinate RMS and percentage decrease in carrier-phase residuals standard deviations.

Site	Processing Method	3D RMS filter % decrease	G LC residuals St.dev % decrease	R LC residuals St.dev % decrease
HUNG	GR filtered	11.89	36.15	26.70
HUNG	GPS-only filtered	8.97	33.29	4.81
KILN	GR filtered	14.47	27.60	19.03
KILN	GPS-only filtered	11.82	25.41	3.71
MACY	GR filtered	21.37	28.34	14.31
MACY	GPS-only filtered	14.75	25.08	4.66
OBAN	GR filtered	27.37	35.28	22.09
OBAN	GPS-only filtered	16.26	31.38	4.67
PADT	GR filtered	32.05	31.13	14.65
PADT	GPS-only filtered	26.31	28.37	5.87

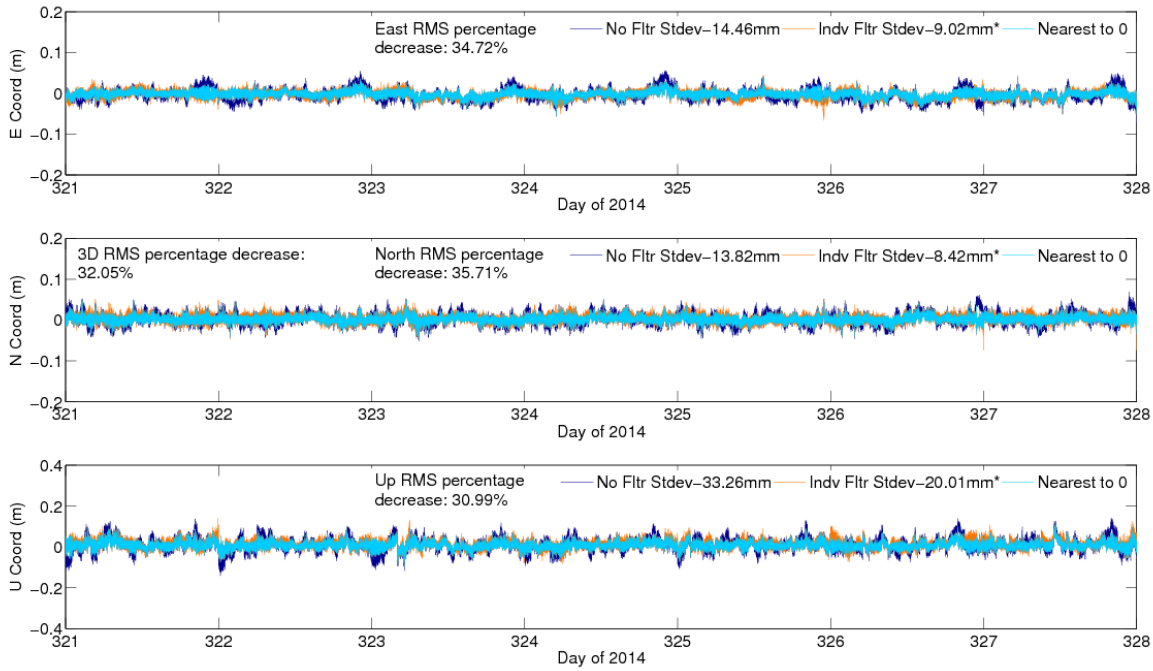

Figure 4.27: Coordinate comparison at site PADT of unfiltered GR PPP processing and GR filtered GR PPP processing, 2014, days 321 to 327.

Combined filtering can also be seen to reduce the standard deviation of the carrier-phase residuals to which the filter has been directly applied, as seen in Figure 4.28 for site PADT. The standard deviations of the GPS residuals at PADT have, on average, been reduced by 31.1% from 14.4 mm to 9.8 mm and the GLONASS residuals by 14.7% from 15.0 mm to 12.8 mm. The smaller reduction in GLONASS residuals compared to GPS residuals is again most likely due to the longer lag periods used for GLONASS filter creation, making it less effective. When only the GPS filter was applied to the GR solution the GPS residual standard deviations were reduced by 2.8 percentage points less, when compared to GR filtering. The GLONASS residuals, although no filter was directly applied to them during GPS-only filtering, were also reduced by 5.9 percentage points. This shows that GR filtering has improved the GLONASS residual standard deviations by over 8% when compared to GPS-only filtering. The improvement in GLONASS residuals, even though no filter was applied, could be due to the improvement in GPS residuals increasing the overall accuracy of the solution as a whole. The average increase in improvement across all five sites in GLONASS residual standard deviations is 14.6 percentage points from GR filtering compared to GPS-only filtering, as seen in Table 4.10.

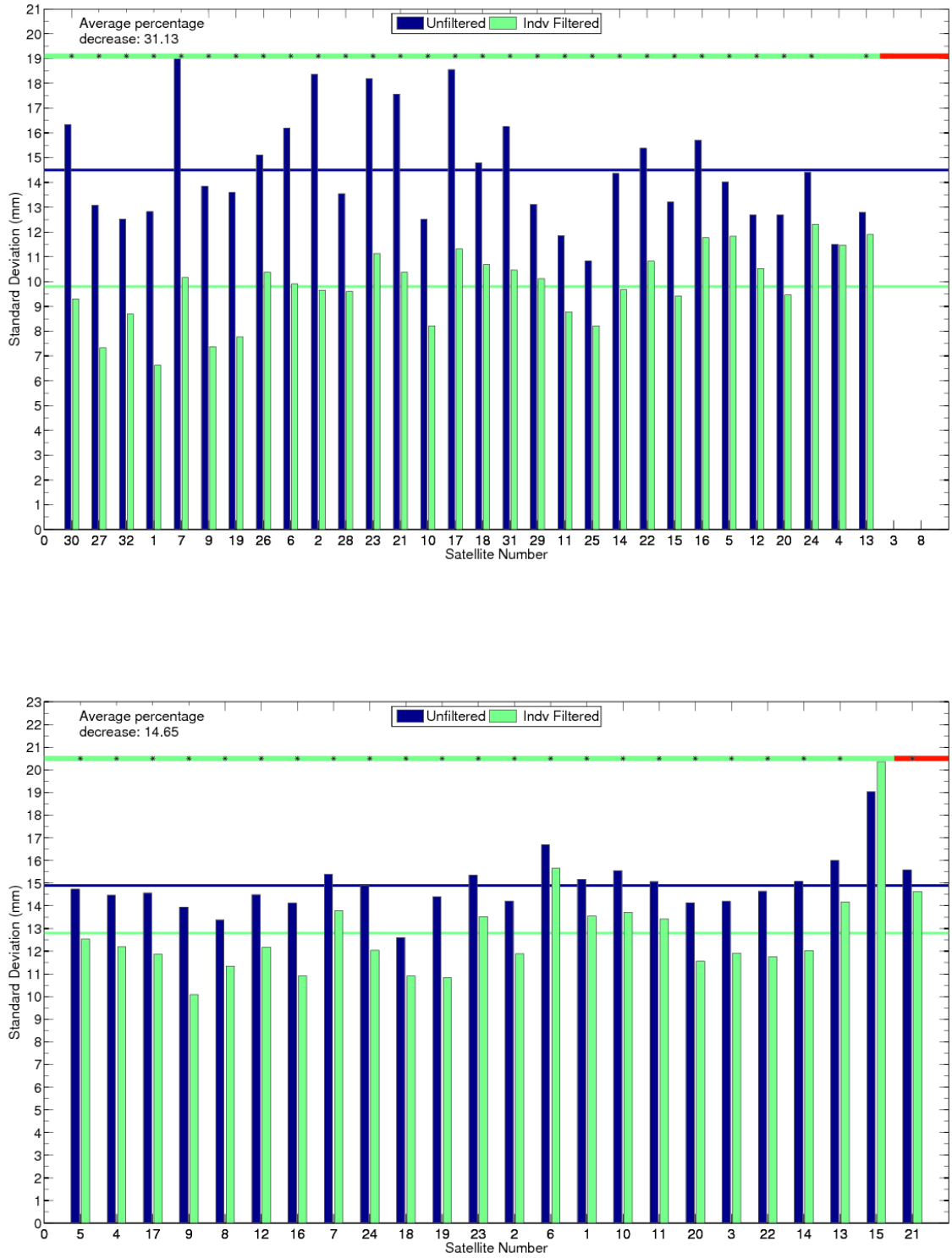

Figure 4.28: Comparison of standard deviations at site PADT, 2014, days 321 to 327 for unfiltered GR and GR filtered carrier-phase GPS (top) and GLONASS (bottom) residuals per satellite. Symbology as explained in Figure 3.12.

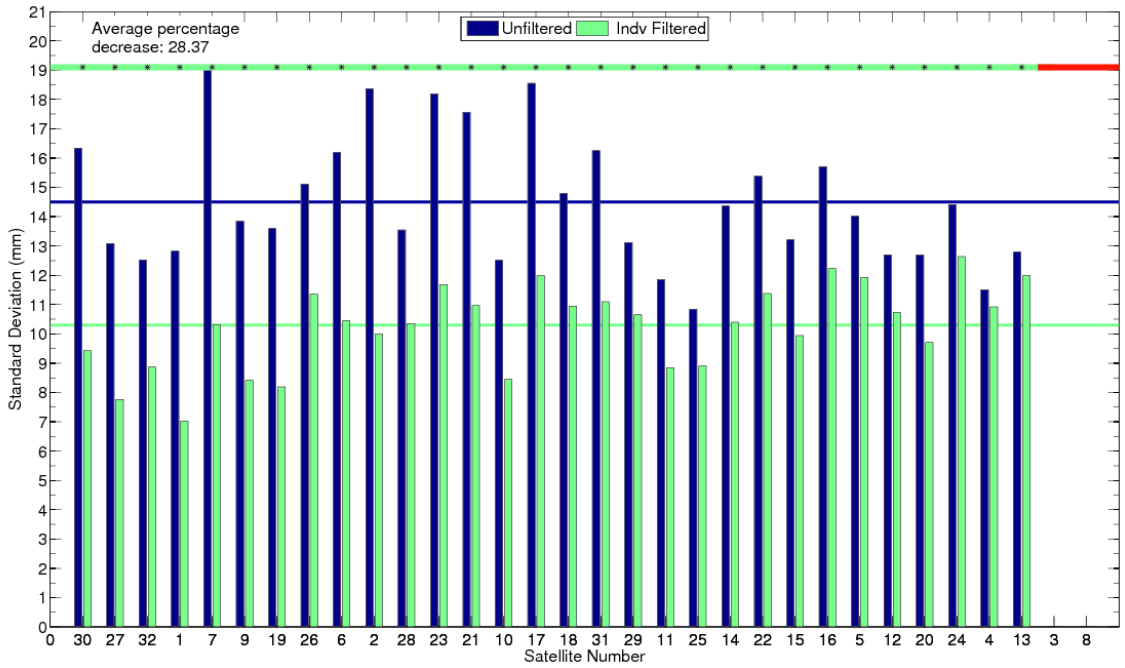

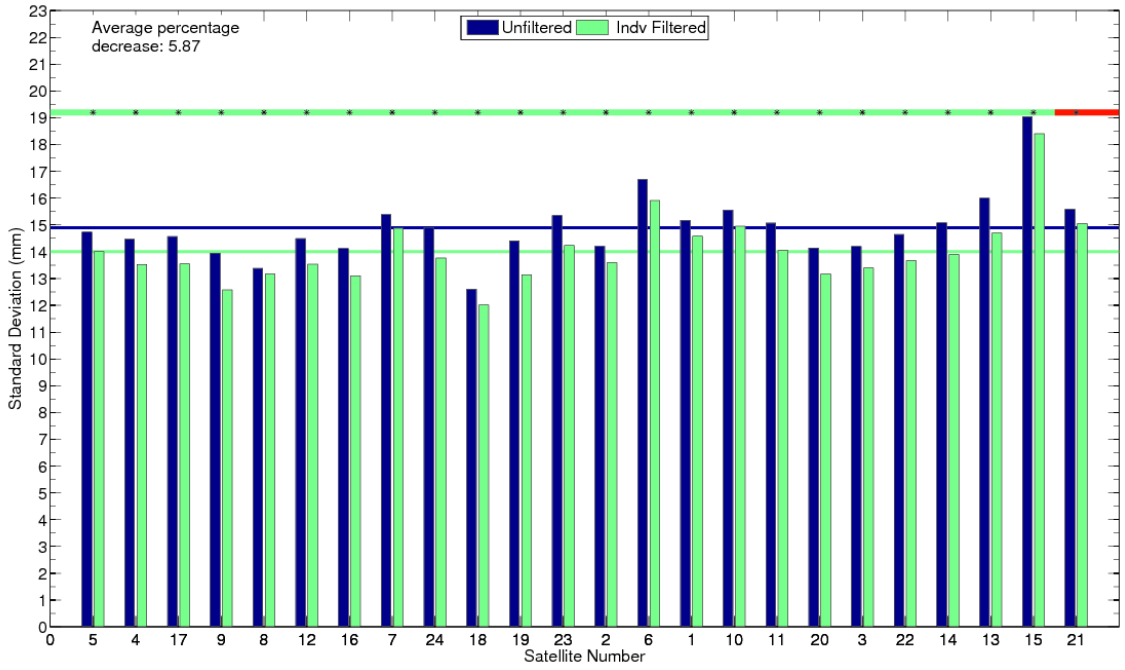

Figure 4.29: Comparison of standard deviations at site PADT, 2014, days 321 to 327 for unfiltered GR and GPS only filtered carrier-phase GPS (top) and GLONASS (bottom) residuals per satellite. Symbology as explained in Figure 3.10.

The coordinate Allan deviation plots for sites PADT and MACY can be seen in Figure 4.30 and Figure 4.31 respectively. The East coordinate Allan deviation plot for PADT shows that the GR filter increases the stability of the East component of the coordinate time series for averaging intervals larger than 380 s with maximum improvement at the largest averaging interval as shown in Figure 4.32. The GPS-only filter gives a more stable time series than the GR filter for intervals smaller than 800 s, when both filtered results are less stable than the unfiltered case. Again the reason for this instability is likely due to the filters amplifying high-frequency noise at short averaging intervals. The GPS-only filter improves the stability of the time series from averaging intervals about 2 minutes smaller than for the GR filter but is less stable than the GR filter at averaging intervals over 800 s. As seen from Figure 4.32, the East percentage improvement in Allan deviation for the GPS-only filter has more distinct peaks and troughs at the longer averaging intervals than the GR filter, indicating that a periodic component to the signal is still present which is likely due to strong GLONASS multipath still being present.

The East coordinate Allan deviation plot of MACY Figure 4.31 shows that the GR filter initially increases the stability of the coordinate time series for averaging intervals less than 2 s, before worsening the stability until averaging intervals of over 120 s. The maximum improvement for the GR filter occurs at around 1120 s, as seen in Figure 4.32. The improvement in stability at these short averaging intervals implies that high-frequency multipath has been successfully removed by the GR filter in the East component at this site. The GPS-only filter also shows success in filtering high-frequency multipath as the stability is better than the unfiltered case for 1-6 s averaging intervals, which is 4 s longer than for the GR filter. This indicates that the GLONASS filter is causing more high-frequency noise to be amplified with the additional filter application. The GPS-only filtering also shows a more stable time series than the unfiltered case for averaging intervals over 60 s, with maximum improvement at the same averaging interval as for the GR filter, but with a reduction in improvement of about 8 percentage points.

The North coordinate Allan deviation plot for PADT shows the GR filter increases the stability of the North component of the coordinate time series for averaging intervals larger than 380 s, similar to the East component, with maximum improvement at 3160 s averaging interval as seen in Figure 4.30 and Figure 4.32. The GPS-only filter increases the stability for

averaging intervals from 160 s, with a maximum improvement peaking at the same interval as the GR filter, but with a reduction in improvement of about 10 percentage points.

The North coordinate Allan deviation plot of MACY, Figure 4.31, shows that the GR filter increases the stability of the coordinate time series for averaging intervals over 80 s, with a maximum improvement peaking at averaging intervals around 890 s which is roughly 230 s before the East GR filter maximum improvement occurs. The GPS-only filter however, much like in the East coordinate, shows improvement in the North component of the time series stability between averaging intervals of 1-8 s, then again for averaging intervals over 50 s. Again this indicates that high-frequency noise is being amplified less by using a single constellation filter rather than the dual filter, and that high-frequency GPS multipath is being filtered.

The Up coordinate Allan deviation plot of PADT shows the GR filter improves stability from averaging intervals of 295 s, which is an interval that is 85 s shorter than for the horizontal coordinate components. Much like the East component, the maximum percent increase in stability is at the largest averaging interval. This implies that the GR filter is stable over very long averaging intervals. The GPS-only filter again shows reduced improvement in stability compared to the GR filter but only after averaging intervals of 640 s. The GPS-only filter shows better stability than the unfiltered case from averaging intervals over 160 s which was the case for the GPS-only filter in the North component. The maximum percent improvement in Allan deviation for the GPS-only filter is also at the maximum averaging interval but reduced by 13 percentage points in comparison to the GR filter.

The Up coordinate Allan deviation plot of MACY, Figure 4.31, shows the GR filter improves the stability in the Up coordinate from averaging intervals of 115 s, which is similar to that for the East coordinates at this site. The maximum improvement occurs at averaging intervals around 4470 s, which is longer than the horizontal coordinate components, as seen in Figure 4.32. Again, the GPS-only filter shows better stability than the GR filter at the shorter averaging intervals where both filtered cases are less stable than the unfiltered case. The GPS-only filter improves the stability of the time series for averaging intervals greater than 82 s and the maximum improvement peaks at the same interval as for the GR filter, but with a reduction in improvement of about 10 percentage points.

From looking at the percentage improvement in Allan deviation plot for site PADT and MACY, Figure 4.32, it can be seen that the GR filter improvement curves show less fluctuation at the longer averaging intervals in comparison with the GPS-only filter curves. This is most likely due to GLONASS multipath error causing oscillations in the position time series with periods greater than 1000 s, as no filter has been applied to the GLONASS residuals. It can also be seen for site MACY how the filter performance appears to deteriorate after averaging intervals over 2000 s. The variable performance of the filter at larger averaging intervals could be due to more non-multipath errors contributing to the measurement residuals at these periods. It is plausible that lower-frequency multipath could be being absorbed into other slowly varying parameters, such as receiver clocks, ambiguity resolution and wet tropospheric delay during the Kalman filter process. Hence, there is less multipath present at these periods in the residuals which are being used to create the multipath mitigation filters.

Table 4.11: Maximum percentage improvement in Allan deviations for GR filtered and GPS-only filtered GR PPP processing.

Site	Processing Method	Maximum Percentage Improvement in Allan Deviation		
		East	North	Up
HUNG	GR filtered	27%	32%	29%
HUNG	GPS-only filtered	18%	21%	21%
KILN	GR filtered	22%	16%	23%
KILN	GPS-only filtered	17%	11%	19%
MACY	GR filtered	21%	30%	24%
MACY	GPS-only filtered	13%	17%	14%
OBAN	GR filtered	27%	28%	32%
OBAN	GPS-only filtered	19%	17%	19%
PADT	GR filtered	35%	41%	43%
PADT	GPS-only filtered	23%	31%	30%

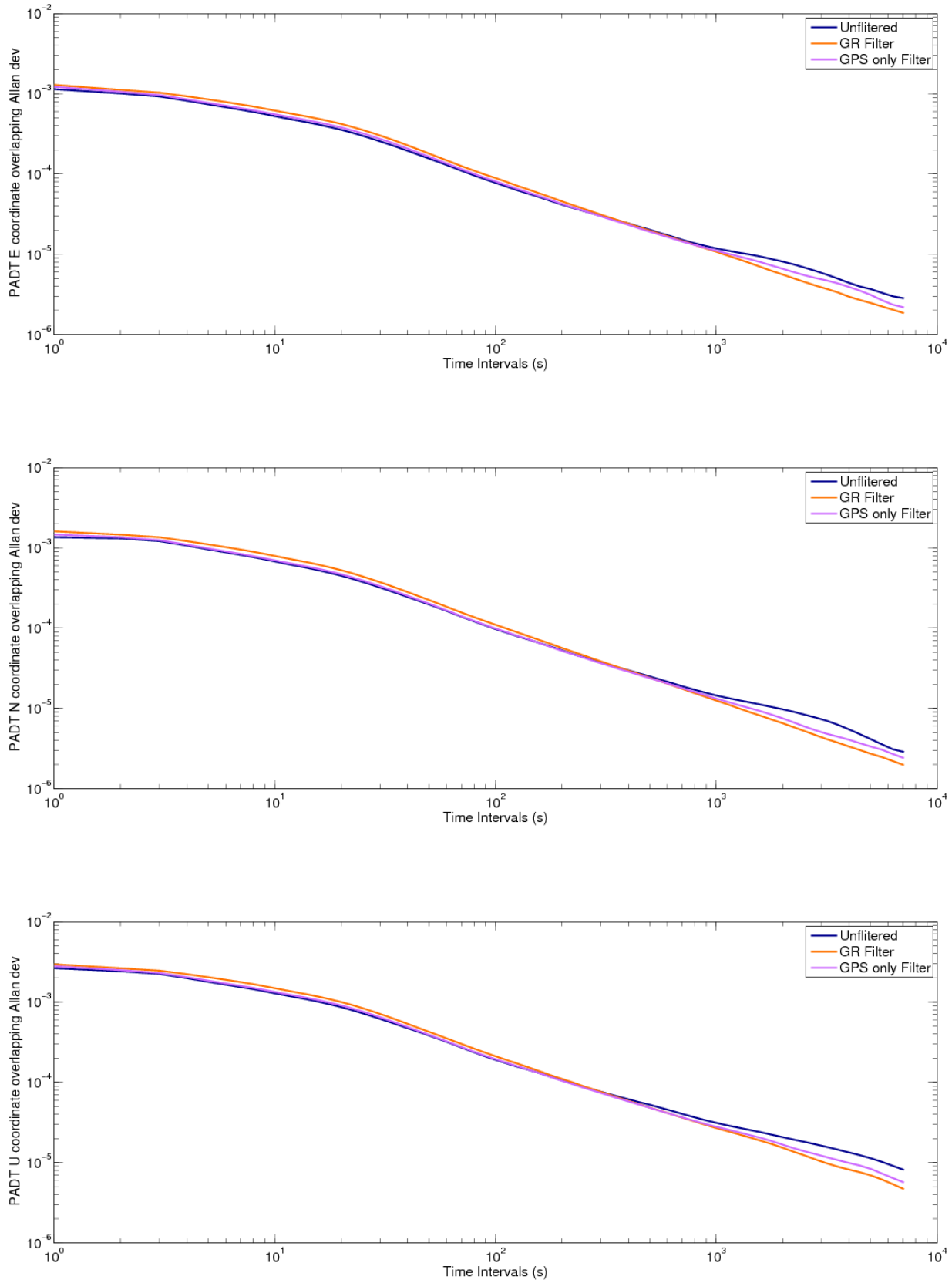

Figure 4.30: Comparison of GR PPP unfiltered (blue), GR filtered (orange) and GPS only filtered (lilac), Allan deviation plots for site PADT coordinate time series, for the East, North and Up components respectively.

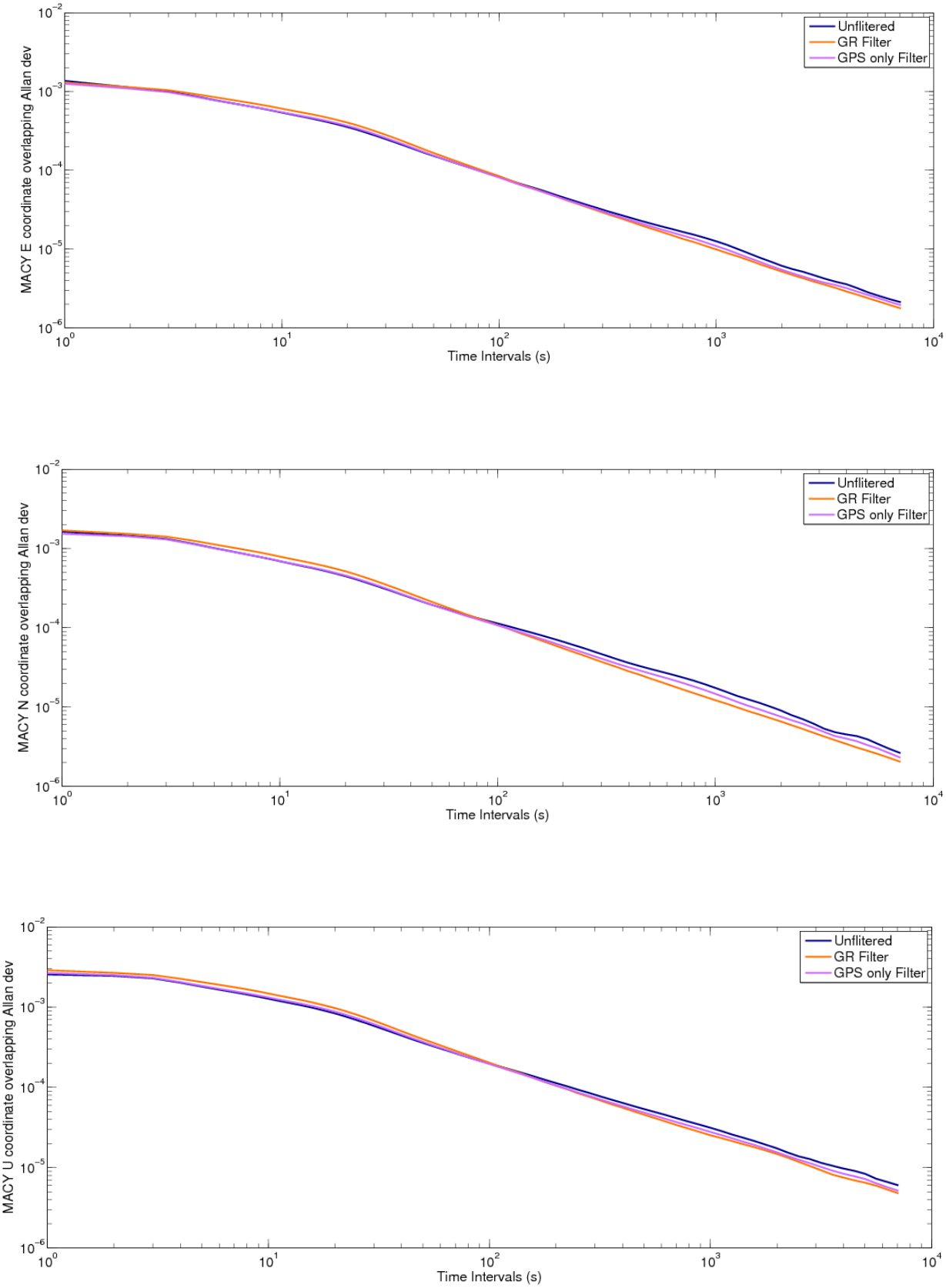

Figure 4.31: Comparison of GR PPP unfiltered (blue), GR filtered (orange) and GPS only filtered (lilac), Allan deviation plots for site MACY coordinate time series, for the East, North and Up components respectively.

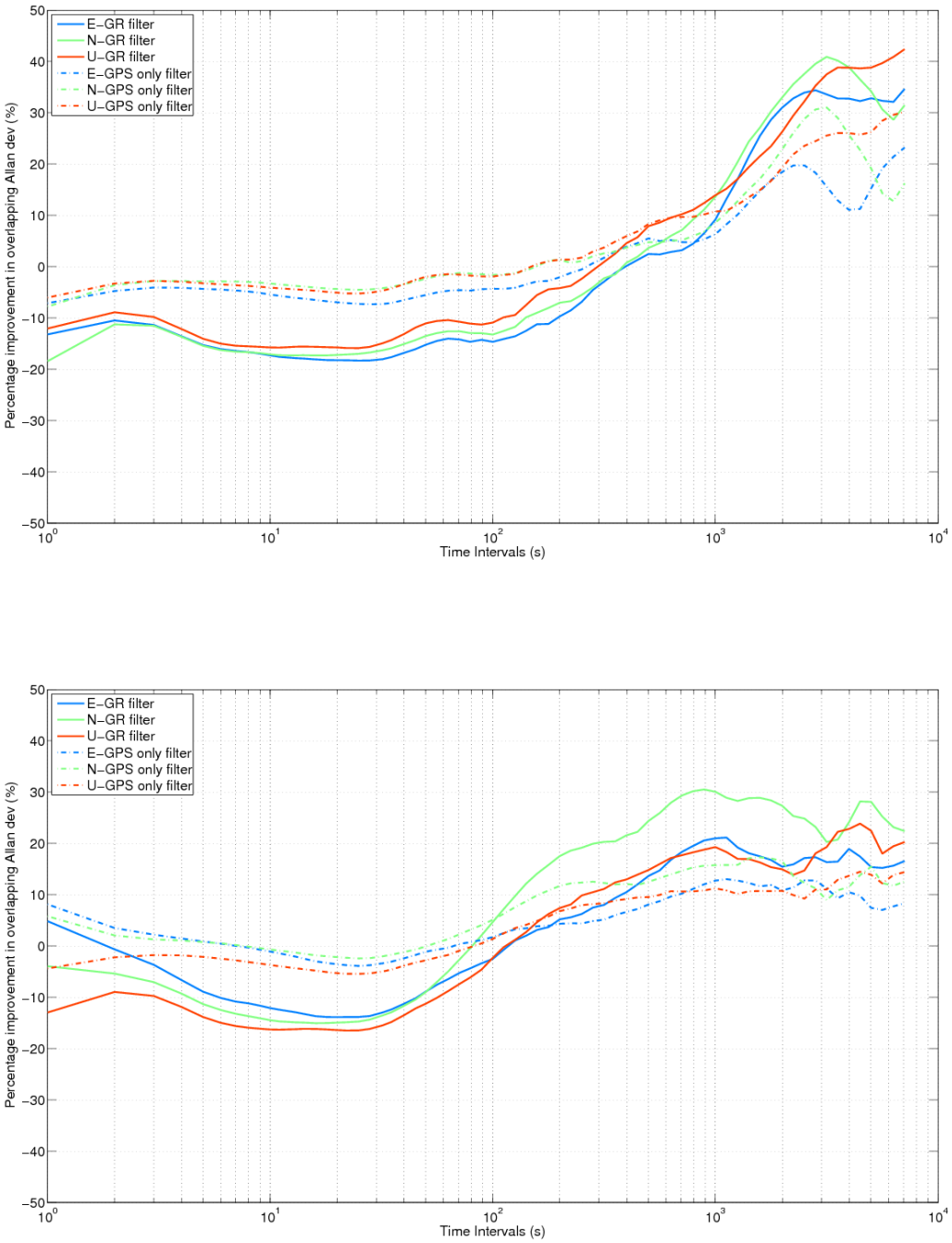

Figure 4.32: Comparison of GR PPP GR filtered and GPS-only filtered percentage improvement in Allan deviation at site PADT (top) and MACY (bottom).

As seen in the power spectral density plots, Figure 4.33, for site HUNG and in Appendix D for all other sites, the GPS and GLONASS filter improves the position estimates for frequencies roughly between 0.00002-0.002 Hz. Filtering has least effect at more extreme frequencies, either very low or very high. The result for GPS and GLONASS combined filtering are in keeping with the results found from individual constellation filtering, as discussed in section 3.8 and 4.3.

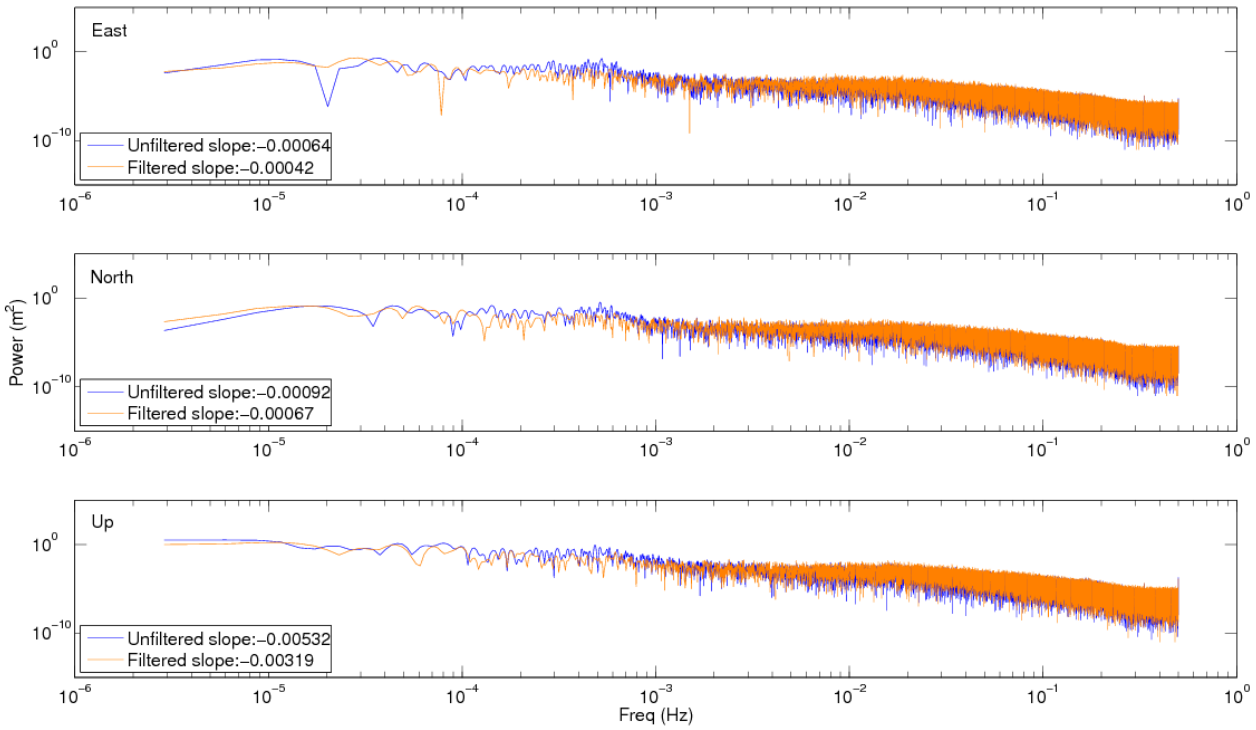

Figure 4.33: Power spectral density comparison of computed GR coordinates at site HUNG of unfiltered GR PPP processing, in dark blue, and GR sidereally filtered PPP processing, in orange, 2014, days 321 to 327.

4.6 Conclusion

The above analyses were devised to test the feasibility of observation domain GLONASS near 8 sidereal day filtering in PPP processing, both in a GLONASS-only and GPS and GLONASS combined solution, from continuously operating GNSS stations in contrasting environmental surroundings. The following conclusions from the analyses can be made:

-The GLONASS carrier-phase residuals were found to have an optimum mean lag period of 689,248 s for the five sites used in this study which roughly equates to 8 days, with a near-sidereal period of 86156 s. Individual satellite optimum lag periods for GLONASS range from 689238 s to 689253 s across all five sites and were found to be more effective in filtering than using a mean optimum lag period.

-GLONASS sidereal filtering has been shown to be most effective when observations are strongly affected by multipath. The greatest improvement with GLONASS filtering in a GLONASS-only PPP solution was found to be at site OBAN which has a high proportion of carrier-phase residuals with RMS values greater than 10 mm. On the other hand, GLONASS observations at site HUNG were not affected by strong multipath signals as given by the percentage breakdown of GLONASS-only carrier-phase residuals RMS, Figure 4.1, and hence did not yield as large improvement from filtering as site OBAN. Average improvement in coordinate time series 3D RMS for all five sites was found to be just under 18%. Despite the reduced improvement at site HUNG, the GLONASS filter was successful at increasing the stability of the PPP coordinate time series over averaging intervals starting between 30-700 s depending on the particular site. The improved stability of a coordinate time series of over just a few tens to hundreds of seconds is advantageous for earthquake and tsunami early-warning systems which require accurate and often small earthquake surface displacement measurements at low latency (within minutes of an event).

-The effectiveness of GLONASS filtering is dependent on multipath strength, the higher the level of multipath the better the filter works. If little to no multipath is present then the filter adds noise rather than subtracting a genuine multipath signal.

-The effectiveness of GLONASS filtering is dependent on the satellite elevation angle, as the majority of strong signal multipath arises from low elevation satellites. Thresholding the filter application to epochs under a certain elevation angle reduces the problem of high-

frequency noise being amplified by filter application at elevations experiencing little to no multipath. Thus coordinate time series stability is improved, particularly at short averaging intervals which are of most importance for early-warning systems as previously mentioned.

-For averaging intervals over about 2000 s the performance of GLONASS-only and GPS and GLONASS filtering becomes less stable as fluctuations in the percentage improvement Allan deviation plots occur at larger averaging intervals. As previously mentioned, low-frequency multipath error is probably being absorbed into other slowly varying parameters, such as the wet tropospheric delay. The fixing of the GPS and GLONASS carrier-phase integer ambiguities, as mentioned in section 2.6.1, could potentially enhance filter performance by refining the overall accuracy of the coordinates, wet tropospheric delay and clock terms. This could not be investigated further due to GPS and GLONASS ambiguity fixed PPP software not being available or used for this thesis.

-A GPS+GLONASS PPP solution improves the total precision, in terms of standard deviation of the unfiltered coordinate time series, for all five sites on average by 35.6% when compared with the GPS-only solutions and 39.0% when compared with the GLONASS-only solutions.

-A GPS+GLONASS PPP GR filtered solution also improves the total precision in terms of standard deviation of the filtered coordinate time series for all five sites. Precision is on average improved by 24.7%, when compared with the GPS-only, GPS filtered solutions and 42.3%, when compared with the GLONASS-only, GLONASS filtered solutions. Hence for highest precision coordinates a combined GR filter should be applied to a GPS+GLONASS PPP solution.

-The inclusion of GLONASS filtering into a GPS+GLONASS PPP solution improves the total precision, in terms of standard deviation and 3D RMS improvement, of the coordinate time series for the five sites on average by 23.2% and 21.4%, respectively. When just using GPS filtering in a GR PPP solution, the filter performance is reduced by 7.5 and 5.8 percentage points compared with the above-mentioned statistics. The maximum improvement in Allan deviation signifying coordinate time series stability is also reduced on average by 9 percentage points with the exclusion of GLONASS filtering. Hence, it is feasible to combine GPS and GLONASS observation domain filtering of PPP processing which offers enhanced performance over just GPS filtering alone.

Chapter 5. Measurement of Static Permanent Displacement

5.1 Introduction

The previous two chapters have indicated that applying near-sidereal filters in the observation domain can increase the precision and stability of GNSS coordinate positions of static receivers. A combined GR solution with GR filtering was found to yield the highest precision solution in terms of coordinate standard deviations out of the various solutions and filter combinations tested. As described in Chapter 2, determining the static permanent displacement induced by a seismic event with precision and speed is crucial for earthquake and tsunami early-warning systems. In this chapter a method is devised to evaluate the performance of near-sidereal filtering in an artificial dynamic situation where the true displacement is known, to demonstrate the enhancement of precision in detecting and measuring static permanent displacements of the order of a few millimetres to centimetres.

5.2 Experimental Design and Data Collection

In order to assess the precision of GNSS static permanent displacement measurements, an experiment took place on the flat rooftop of the Newcastle University Drummond Building. A secure rooftop location was chosen as it has a relatively unobscured view of the sky, and the Drummond Building already has the facilities to host multiple GNSS receivers. The roof is surrounded by parapet walls on three sides and another floor on the fourth side, clad with corrugated metal, as seen in Figure 5.1. The four corners of the roof contain concrete pillars, two of which were occupied by Leica GS10 receivers with Leica AS10 antennas which use firmware versions 5.501418/6.403 and Leica CS20 controllers. One receiver was mounted on to the South East concrete pillar directly and acts as a reference, Drummond Base (DRMB); the other was mounted to a moveable platform on top of the North East pillar, Drummond Shake (DRMS). The locations of both receivers can be seen in Figure 5.1 and the mounts in Figure 5.2. The platform DRMS was able to move in three directions using a manual turning handle. The location of DRMS was selected as it is in close proximity to multiple metal structures and signal reflecting objects as seen in Figure 5.3; thus there is a high-level of multipath present. The location of DRMB offers a relatively simple multipath environment and is used as a control receiver only.

Data collection took place over 13 consecutive days: 5th-18th November 2016 (days of year 310-323), to allow the GLONASS satellite orbits to repeat a whole 8 day cycle and hence provide single filter values as opposed to averaged filter values used in the previous chapters. The receivers were set to log GPS and GLONASS code and carrier-phase data at a 1 Hz rate for the whole data collection period. On day 322, the DRMS antenna was moved horizontally by increasing amounts at half hour intervals, as given in Table 5.1. On day 323, DRMS again was moved by the same amounts and time intervals as previously stated, but this time in the vertical direction. The antenna movement was recorded using a micrometre which acted as the known 'true' value of movement. This can be compared to the GNSS receiver values once post-processed in PPP kinematic mode and filtered, using the same methods outlined in Chapter 3 and Chapter 4. The timing of movement was recorded approximately, but due to the time taken to complete each manoeuvre could not be described exactly. Using a moving platform is similar to the method used by Ragheb *et al.* (2010) to assess the measurement of small displacements when using single-epoch switched antenna array GPS with sidereal filtering in a double-difference processing mode. Ragheb *et al.* (2010) were able to reduce the overall RMS of the coordinate residuals in the horizontal plane to 4.5 mm from 13.0 mm which was achieved from much longer observation periods.

It is noted that in this method the antenna's relative position to surrounding reflectors will change. In a real seismic event however, it is assumed that relative positions will remain unchanged provided that there is minimum damage and reflectors are of solid structure.

Figure 5.1: Aerial photograph of the Drummond building's flat roof, outlined in purple. The North East antenna location (DRMS) is in red and the South East antenna location (DRMB) in yellow. Copyright Google.

Figure 5.2: a) DRMB antenna and concrete pillar mount, looking South. b) DRMS antenna, concrete pillar and moving platform mount, looking North.

Figure 5.3: a) DRMS antenna environment looking North West. b) DRMS antenna environment looking North East.

Table 5.1: Antenna time interval offsets from 10:00 on days 322 and 323 and displacements for horizontal and vertical movements.

Time Offset (h)	0.0	0.5	1.0	1.5	2.0	2.5	3.0	3.5	4.0	4.5	5.0	5.5
Displacement (mm)	1	-1	2	-2	5	-5	10	-10	20	-20	50	-50

5.3 Pilot Study

GLONASS and GPS near-sidereal filtering of a static receiver was first tested at the Drummond roof site before the main experiment took place, to ensure that the site would benefit from near-sidereal filtering. The same Leica antenna and receiver as mentioned in section 5.2 was set up on the Drummond North East concrete pillar, for the 22 day data span as used in Chapter 3 and Chapter 4, i.e. November 2nd-23rd 2014, days of year 306 to 327. The antenna occupied the same pillar as DRMS, but was not mounted to the movable platform so is denoted as site DLNE to differentiate between pillar and platform mount and different observation periods. The data was processed and filtered using the same methodology as described in Chapters 3 and 4.

5.3.1 Optimum GLONASS Lag Period

GLONASS filtering was first conducted separately to find the correct lag period for individual GLONASS satellites at this site (DLNE). As seen from Figure 5.4, the mean lag period for the whole GLONASS constellation at site DLNE peaks around 689,248 s (7d 23h 27m 28s) for the 22 day time span correlated. This is the same repeat period that was found for the five OS sites in Chapter 4 for this time span. The mean peak correlation strength of the GLONASS constellation at this site is roughly 0.53, which is within the range found in Chapter 4.

Along with the mean for the whole constellation, the optimum lag periods per satellite were also computed to increase the filter's effectiveness. The individual GLONASS satellite optimum lag values for carrier-phase and code residuals at site DLNE have a similar spread from the mean as those from the OS sites, as seen in Table 5.2.

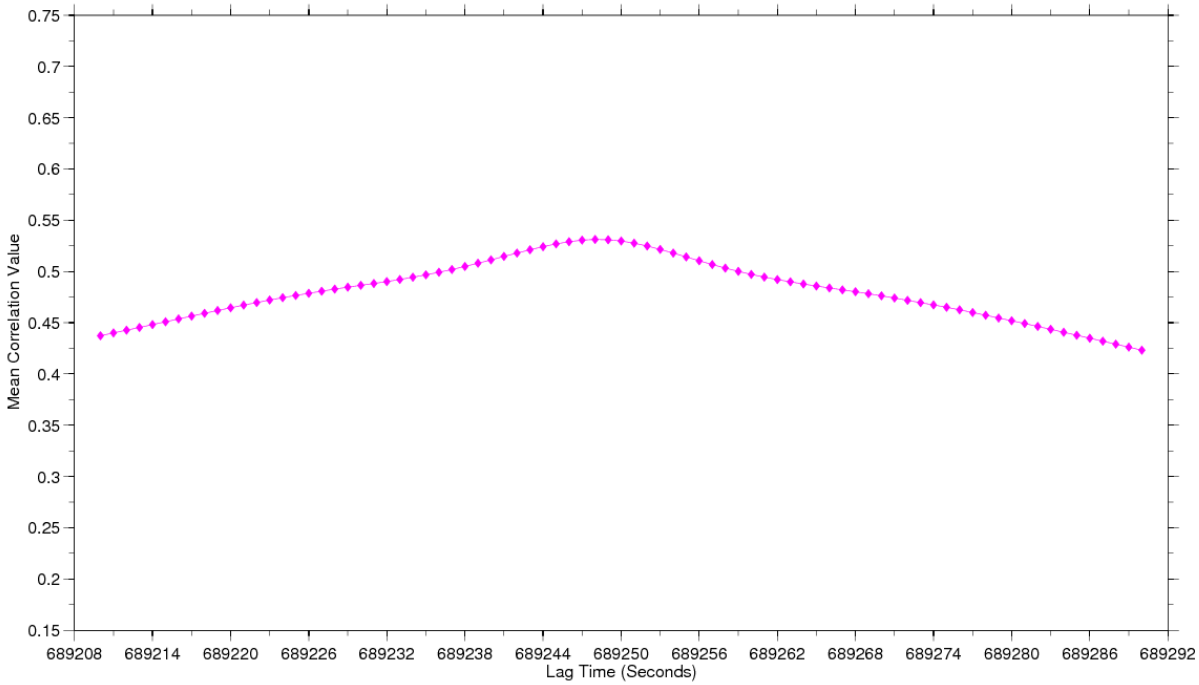

Figure 5.4: Mean GLONASS satellite constellation carrier-phase residual correlations at a range of near eight sidereal lag values for DLNE site, 2014, day of year 306 to 327.

Table 5.2: Standard deviations of the GLONASS carrier-phase and code residuals and optimum lag values per satellite at site DLNE, 2014, days 306-327. All values are given in seconds.

	Carrier	Code
Opt lag value St.dev	3.92	4.48
Sat 01	689244	689242
Sat 02	689250	689250
Sat 03	689250	689249
Sat 04	689250	689252
Sat 05	689249	689242
Sat 06	689251	689250
Sat 07	689251	689252
Sat 08	689249	689251
Sat 09	689249	689249
Sat 10	689250	689258
Sat 11	689250	689250
Sat 12	689248	689256
Sat 13	689249	689249
Sat 14	689252	689252
Sat 15	689242	689247
Sat 16	689250	689254
Sat 17	689247	689247
Sat 18	689243	689247
Sat 19	689236	689241
Sat 20	689240	689241
Sat 21	689245	689244
Sat 22	689249	689252
Sat 23	689249	689250
Sat 24	689248	689249

5.3.2 GLONASS Sidereal Filter Performance at site DLNE

Once the optimum lag period was determined, sidereal filters for the carrier-phase and code residuals were made by stacking the static residuals at the desired lag periods as outlined before in Chapters 3 and 4. Upon examination of Figure 5.6, which shows the coordinates for DLNE, the filter can be seen to produce smoother results than the unfiltered coordinate differences. The standard deviations for all three dimensions are significantly smaller and the 3D RMS decrease is 24.3%, which is 6.4 percentage points more than the mean improvement of the five OS sites. This is most likely due to a high multipath environment being selected hence there is more multipath to mitigate. The greatest improvement in RMS

is in the East; the North and Up components have similar slightly smaller levels of improvement as one another, which is also the case for the OS sites.

The average decrease in carrier-phase satellite residuals standard deviation for all the OS sites is about 14.7%. DLNE has an average reduction in carrier-phase satellite residuals standard deviation of 18.3% as seen in Figure 5.5, which is 3.6 percentage points higher than the OS sites' average.

As with previous analysis the Allan deviation of the coordinate time series is used to assess the increase in stability with filter application. The coordinate Allan deviation plots for DLNE can be seen in Figure 5.7 and show increasingly larger improvements in the East coordinate stability for time intervals greater than 50 s and greater than 100 s for the North and Up coordinates. The maximum improvement for all components peaks at the maximum 2 hour averaging interval and ranges between 25%-30% as seen in Figure 5.8, which is similar to the OS site results.

Overall it can be seen how GLONASS filtering has improved the coordinate standard deviations at DLNE in the East, North and Up by 5.7 mm, 4.2 mm and 10.8 mm respectively, and has improved the stability of the coordinate time series, which should enhance the measurement of small static permanent displacements.

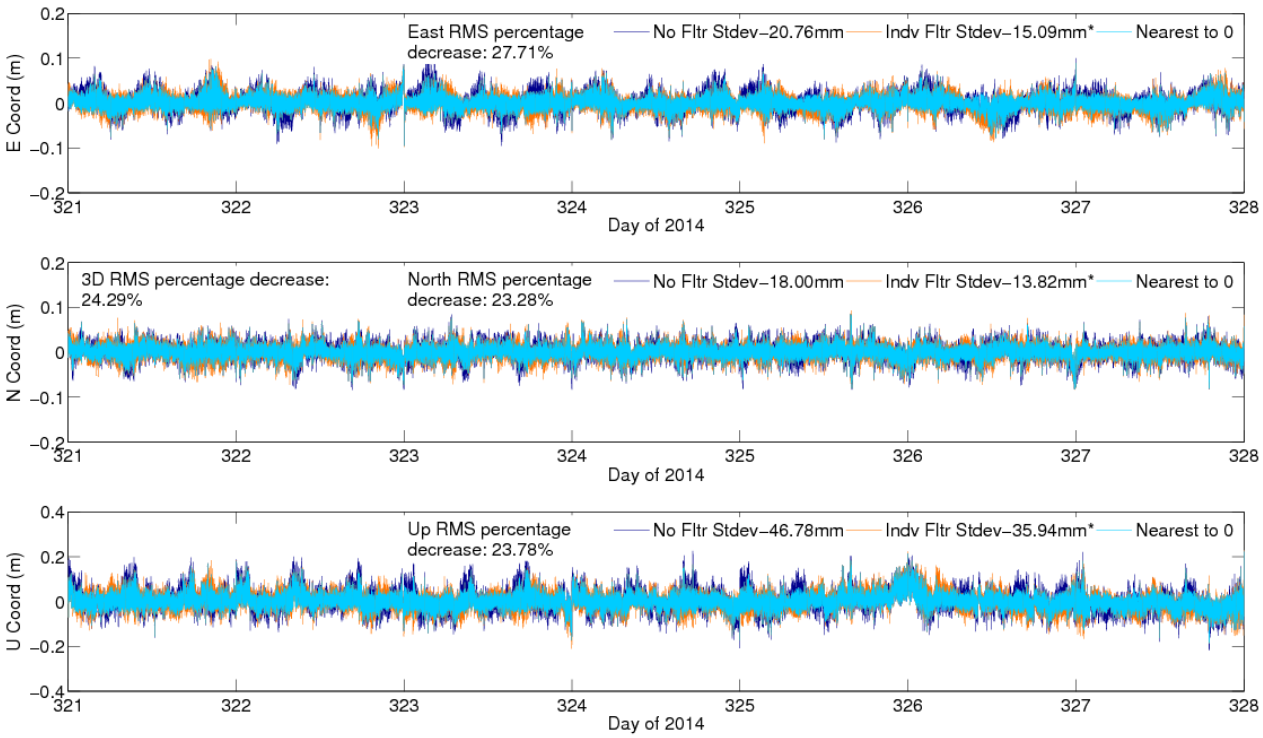

Figure 5.6: Coordinate comparison at site DLNE of unfiltered PPP and GLONASS-only sidereally filtered PPP processing, 2014, days 321 to 327.

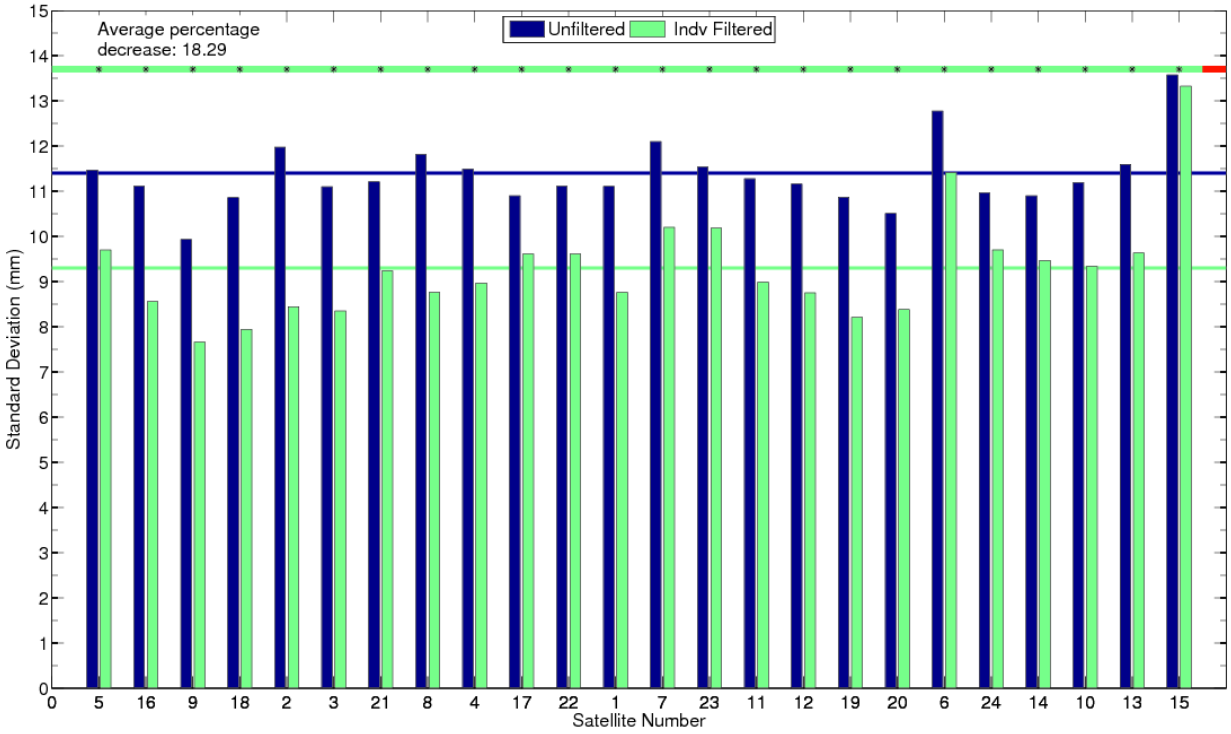

Figure 5.5: Comparison of standard deviations, at site DLNE, 2014, days 321 to 327 for unfiltered and GLONASS-only sidereally filtered carrier-phase residuals, where the blue horizontal lines represent the mean of the constellation carrier-phase residuals standard deviations for the unfiltered, in blue and filtered in green, scenarios. The asterisk signifies that the filtered residuals' standard deviations are significantly smaller than the unfiltered, at the 95% confidence level and the horizontal line behind them dictates if a filter was applied to that particular satellite (green) or not (red).

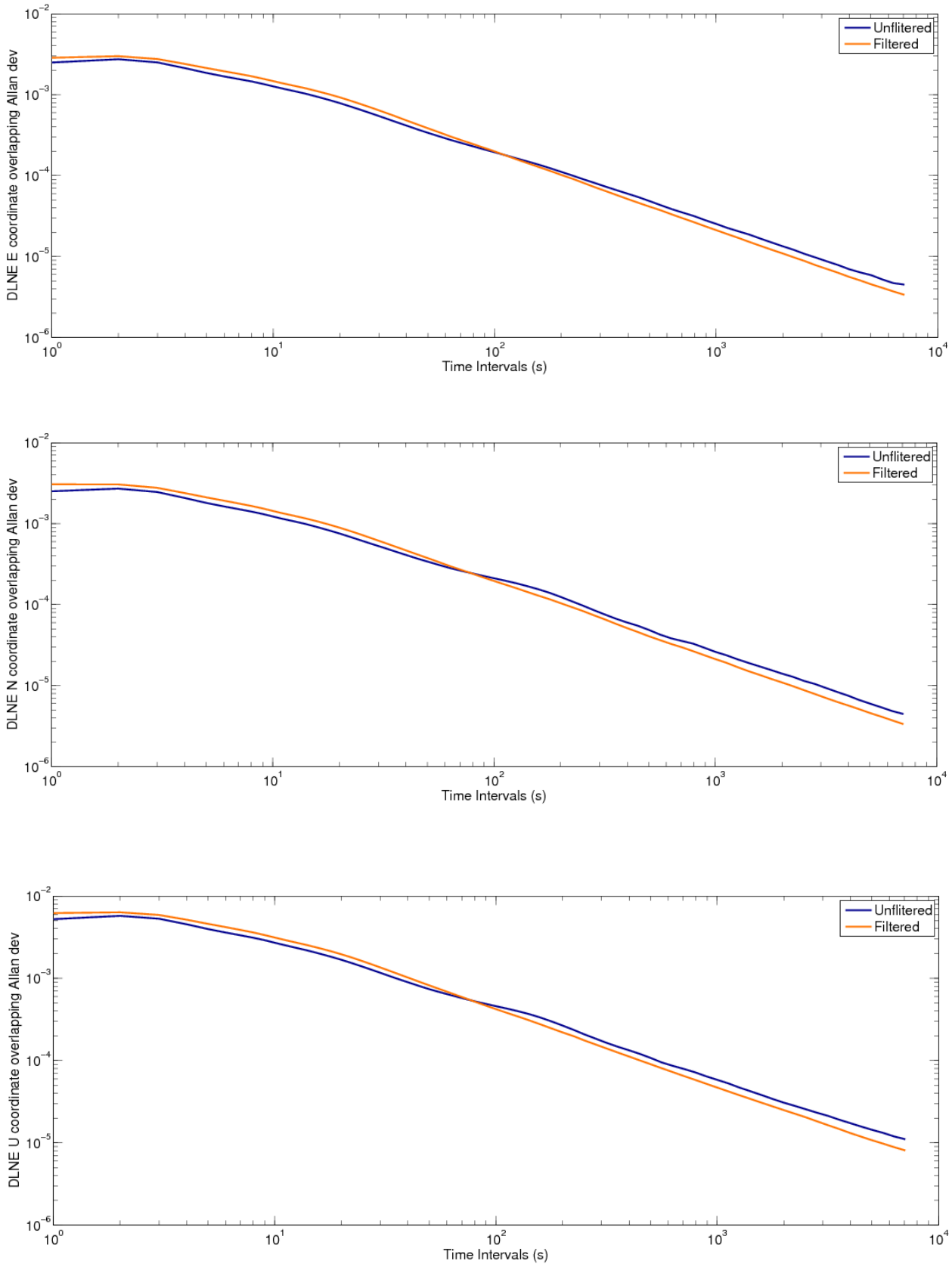

Figure 5.7: Allan deviation plots for GLONASS-only filtering, site DLNE, East, North and Up respectively.

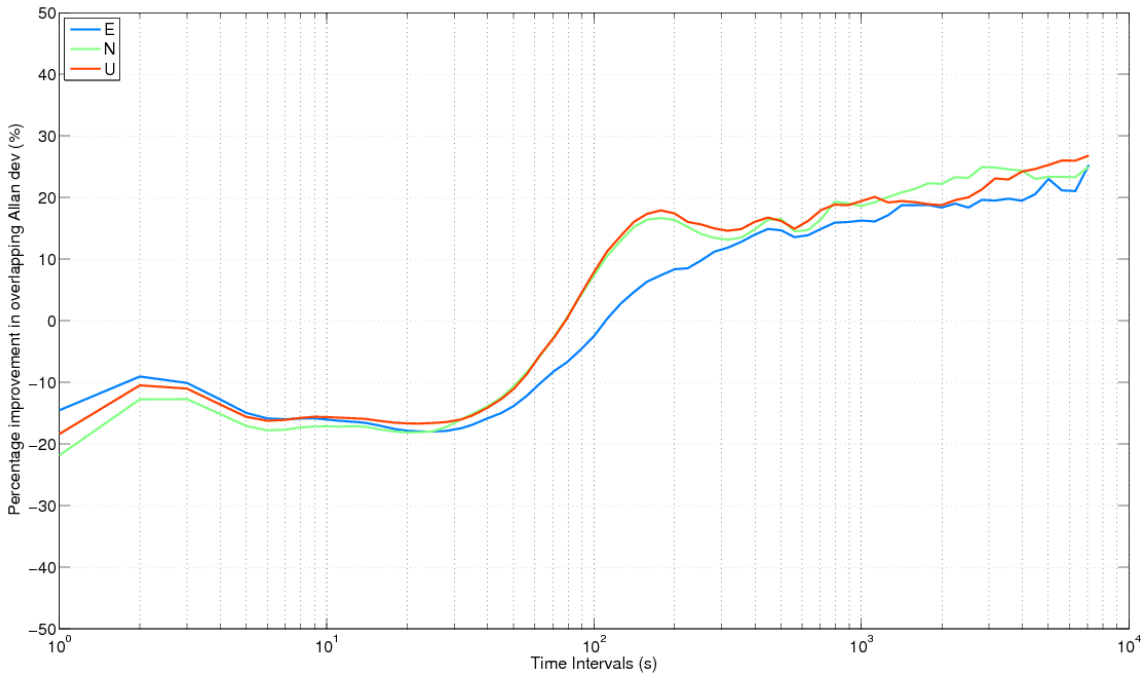

Figure 5.8: Percentage improvement (reduction), in Allan deviation for site DLNE, after GLONASS-only filtering, corresponding to Allan deviation curves.

5.3.3 GPS and GLONASS Sidereal Filter Performance at site DLNE

The improvement from applying a GPS and GLONASS filter to a GR solution was also tested for site DLNE. Figure 5.9 shows the standard deviations for all three coordinate dimensions are significantly smaller when filtered; the horizontal components are on average, improved by 28.6% and the vertical by 19.2%. The horizontal components show greater improvement than the OS site average, mentioned in section 4.6, but smaller improvement in the vertical. The North coordinate shows greater improvement than the East which is likely due to the location of the reflective air conditioning units at the front (North) of the antenna.

The 3D RMS decrease is 21.4% which is the same as the mean improvement of the five OS sites. The average decrease in GPS carrier-phase satellite residuals standard deviation for all the OS sites is about 31.3%. DLNE has an average reduction in GPS carrier-phase satellite residuals standard deviation of 33.9% as seen in Figure 5.10, which is slightly higher than the OS sites' average. This is also the case for the GLONASS carrier-phase satellite residuals standard deviation which shows a 19.9% decrease.

The coordinate Allan deviation plots for DLNE can be seen in Figure 5.11 and show improvements in the East coordinate stability for time intervals greater than 90 s and

greater than 65 s for the North and Up coordinates. The maximum improvement for the East components peaks around the averaging interval 1120 s, whereas the North and Up peak at the longest averaging interval. The maximum improvement ranges from 25% to 30% as seen in Figure 5.12, which is similar to the OS site results.

Overall it can be seen how GPS and GLONASS filtering has improved the coordinate standard deviations at DLNE in the East, North and Up by 2.9 mm, 3.7 mm and 5.5 mm respectively and has improved the stability of the coordinate time series. The reduction in standard deviation is less than for GLONASS-only filtering due to the GR coordinate time series benefitting from increased sky coverage, producing more precise unfiltered coordinates than GLONASS-only coordinates.

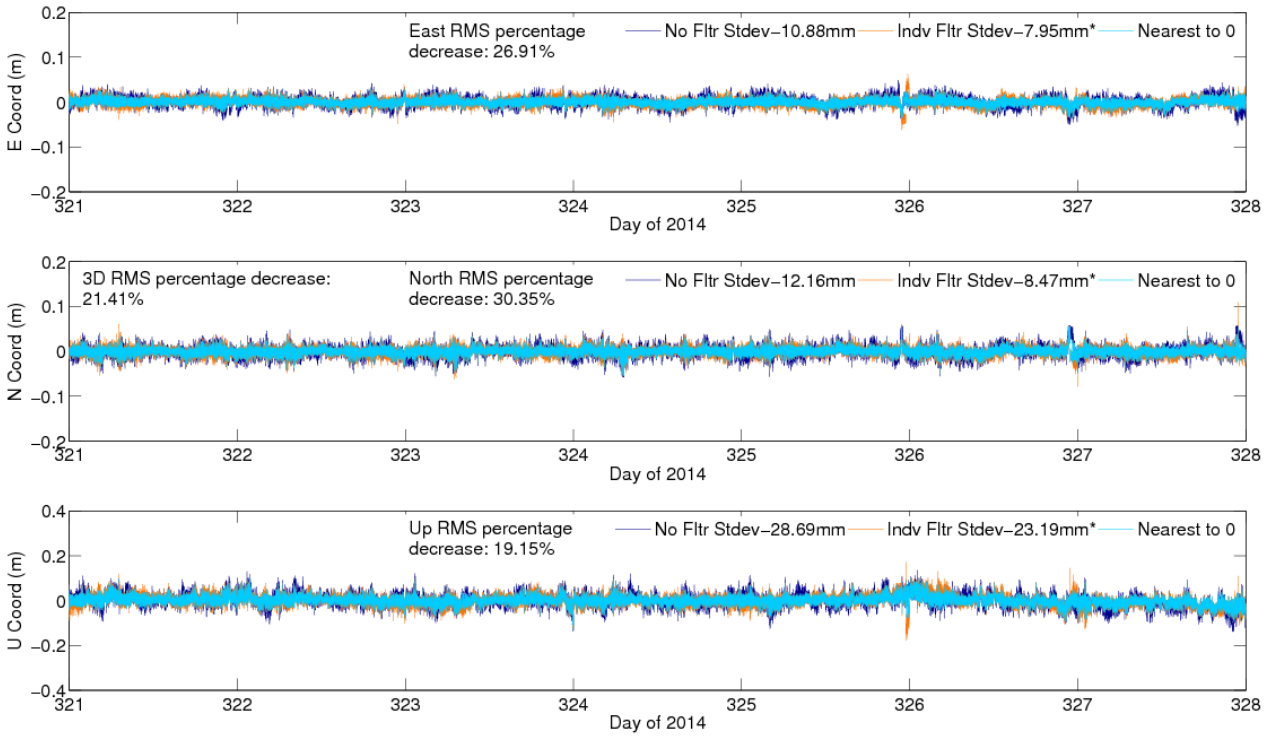

Figure 5.9: Coordinate difference comparison at site DLNE of unfiltered PPP and GR sidereally filtered PPP processing, 2014, days 321 to 327.

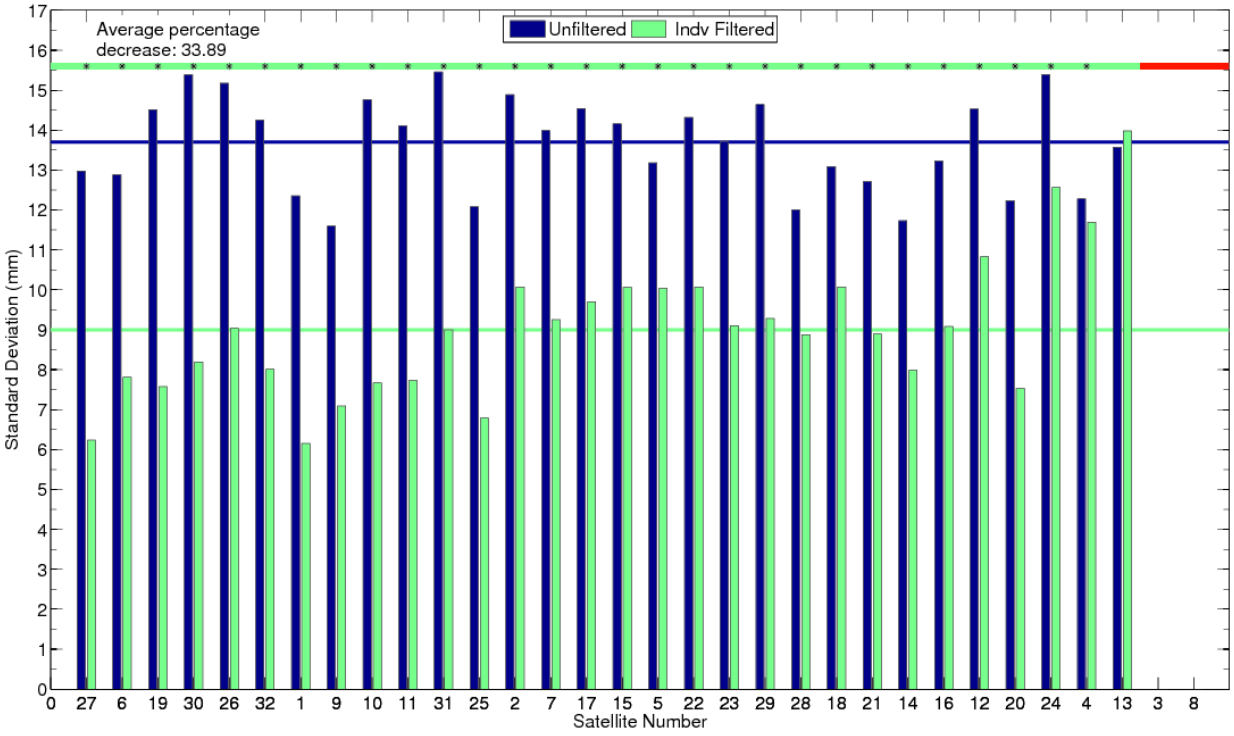

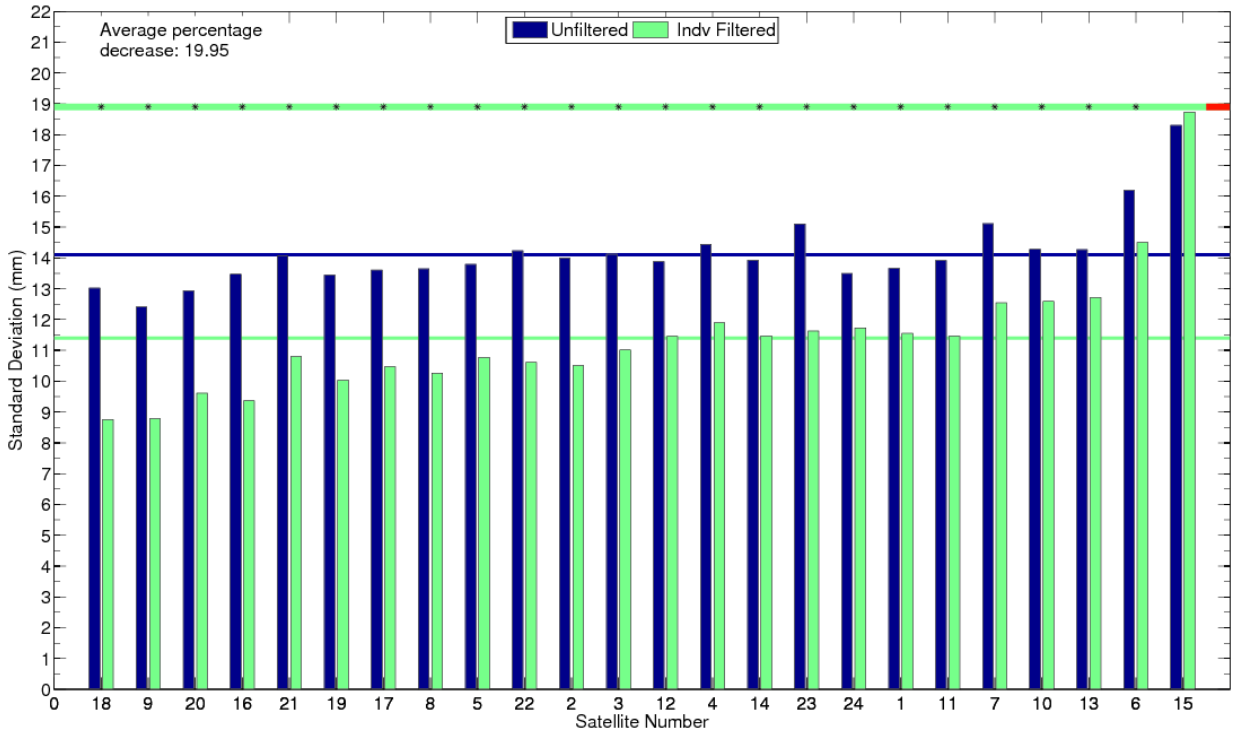

Figure 5.10: Comparison of standard deviations at site DLNE, 2014 days 321 to 327 for unfiltered and GR and GR filtered carrier-phase GPS (top) and GLONASS (bottom) residuals. Symbology as explained in Figure 5.6.

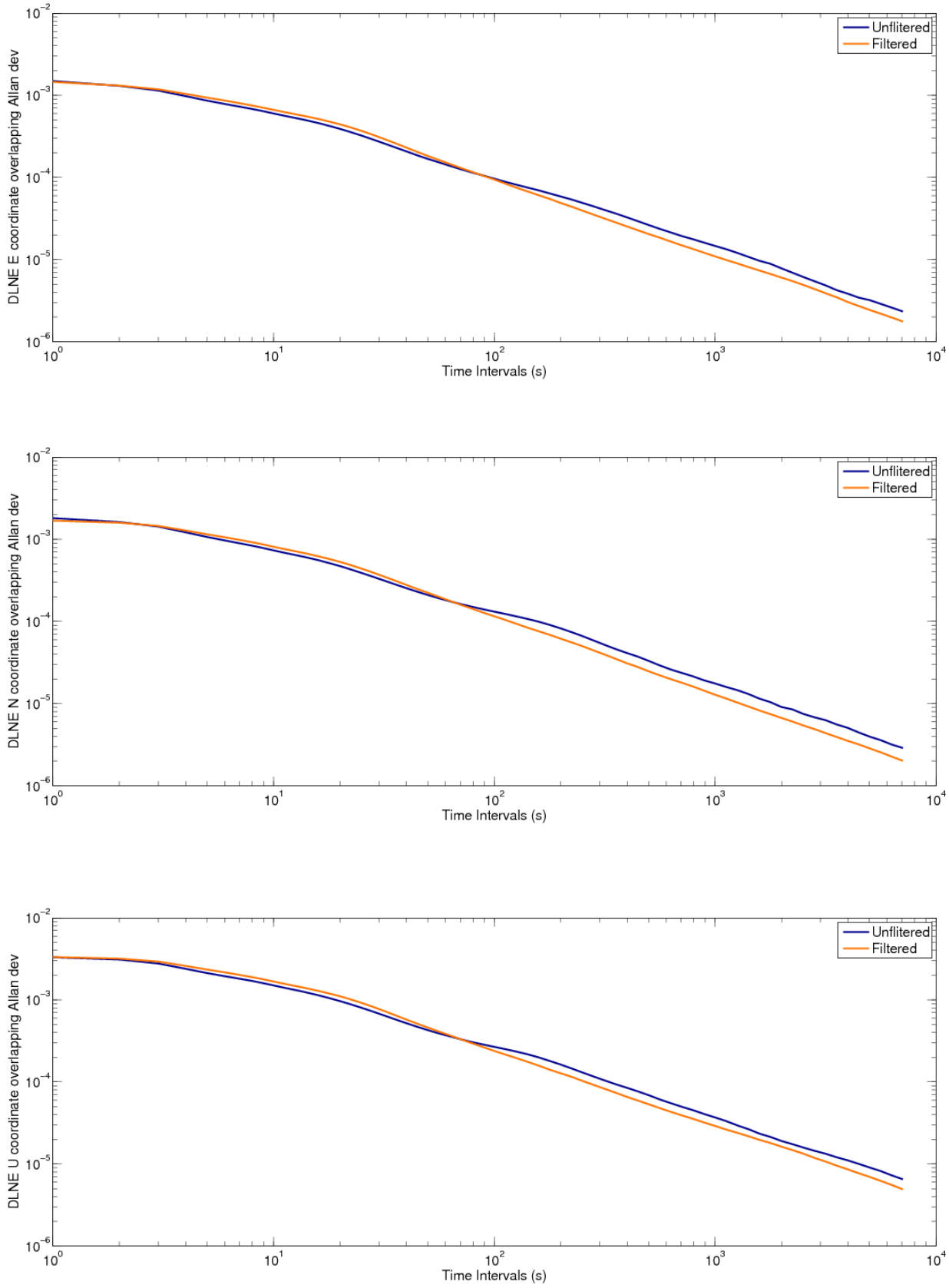

Figure 5.11: Allan deviation plots for GR filtering, site DLNE, East, North and Up respectively.

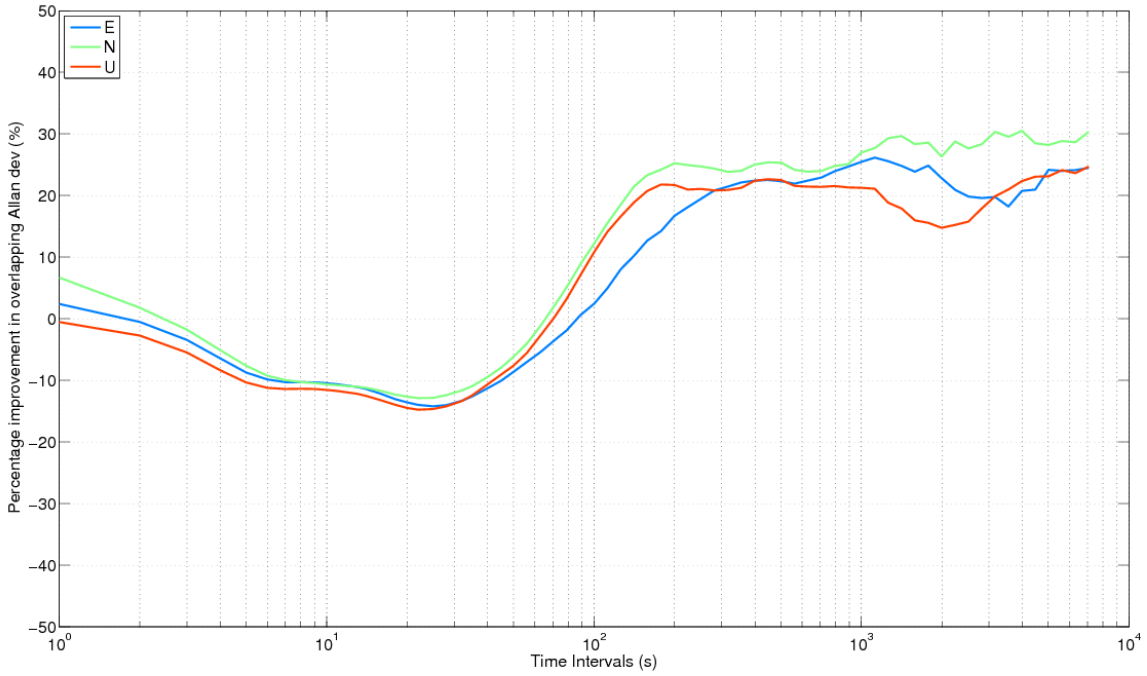

Figure 5.12: Percentage improvement (reduction), in Allan deviation for site DLNE, after GR filtering, corresponding to Allan deviation curves.

5.3.4 Filter Performance at Moving site DRMS and Static site DRMB

Figure 5.13 shows the results of GR filtering at site DRMS for the two day period when the antenna was moved as described in section 5.2. The standard deviations for all three coordinate dimensions are smaller when filtered; the horizontal components are on average, improved by 17.9% and the vertical by 5.2%. For site DRMB on the other hand as seen in Figure 5.14, filtering has not improved the East standard deviation, and has only improved the North and Up components on average by 6.3%. This could be due to the comparatively low multipath environment of DRMB site when compared to DRMS. The improvement with filtering at DRMS is less than the pilot study; this could be due to using 'Final Rapid' orbits and the antenna and surrounding environment relative position changing with antenna movement, which is unavoidable. CODE 'Final Rapid' products as the name suggests are generated with less latency then 'Final' products, they are generated daily, but at the cost of reduced accuracy, as seen in Table 2.2, (Dach *et al.*, 2016). 'Final Rapid' products use the middle of the long-arc solution computed from the 'Rapid' orbits on the current and previous day with the addition of the 'Ultra-Rapid' solution from the following day. The 3D RMS decrease is 7.63% and the average decrease in GPS and GLONASS carrier-phase satellite

residuals standard deviations are 21.68% and 6.52% respectively, as seen in Figure 5.15. The poorer GLONASS performance could be due to the limited availability of three of the satellites, reducing the filter application. These satellites were not in view of the antenna for long enough periods to compute filter values for; this could be due to obstructions impeding the sky view.

It should be noted that even with the application of near-sidereal filtering the standard deviation of the vertical component is still double that of the horizontal components due to worse satellite geometry. For this reason only the horizontal component is analysed in terms of antenna displacement detection as movement should be more apparent and hence easier to detect as background coordinate noise levels are lower.

The coordinate Allan deviation plots for DRMS can be seen in Figure 5.16 and show improvements in the East coordinate stability for time intervals greater than 110 s and greater than 60 s for the North and Up coordinates which is similar to the pilot study results. The maximum improvement for the East component peaks round the averaging interval 3550 s, whereas the North and Up components peak at a much smaller averaging interval, 220 s. The Up component improvement in stability also sharply decreases from averaging intervals over 3550 s which could be due to the noisier nature of the Up component masking the multipath error. The maximum improvement in stability ranges between 14%-18%, as seen in Figure 5.17, which again is smaller than the pilot study which could be due to using ‘Final Rapid’ orbits and single filter values.

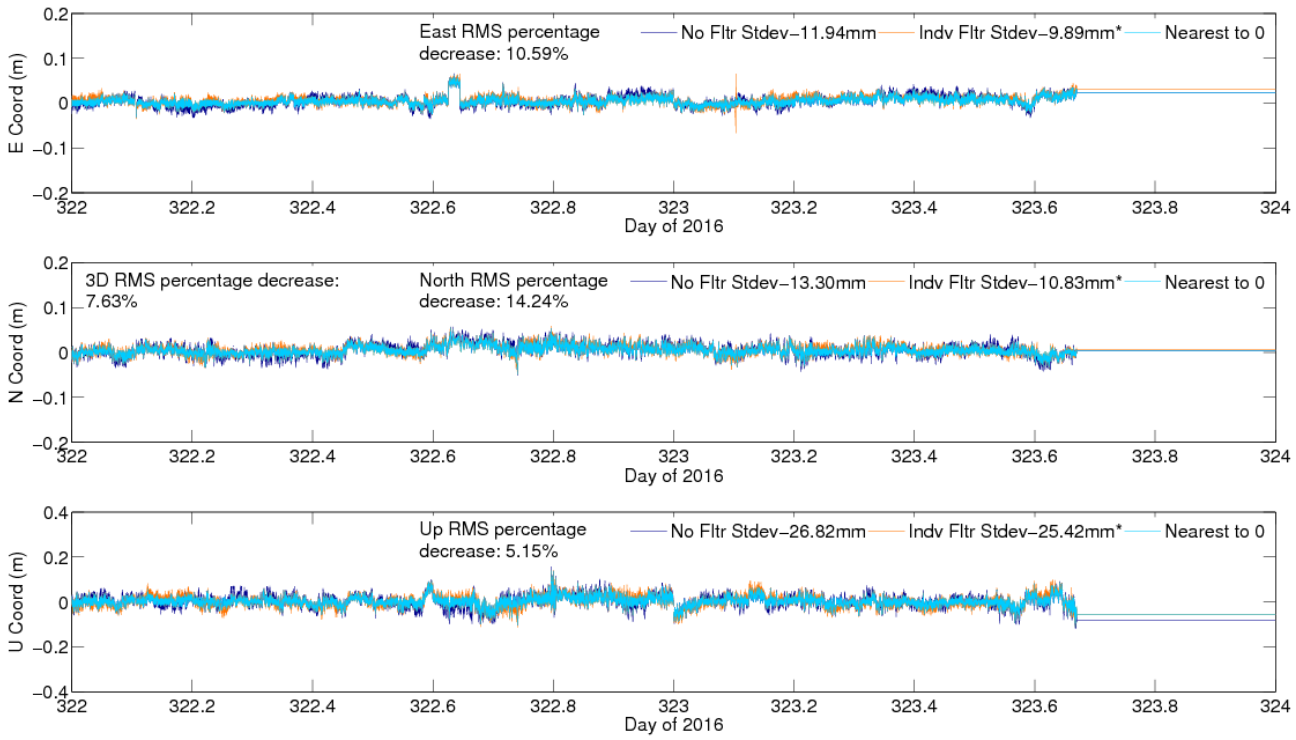

Figure 5.13: Coordinate comparison at site DRMS of unfiltered PPP and GR sidereally filtered PPP processing, 2016, day of year 322 to 323.

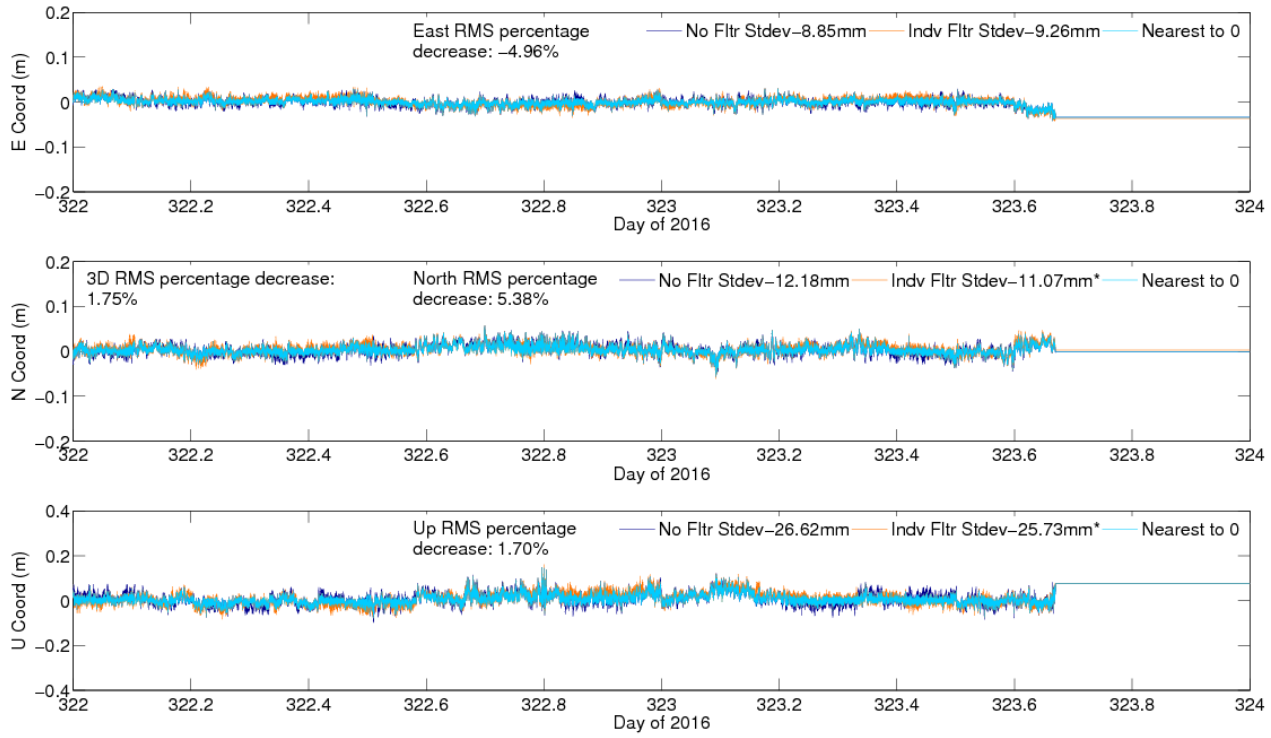

Figure 5.14: Coordinate comparison at site DRMB of unfiltered PPP and GR sidereally filtered PPP processing, 2016, day of year 322 to 323.

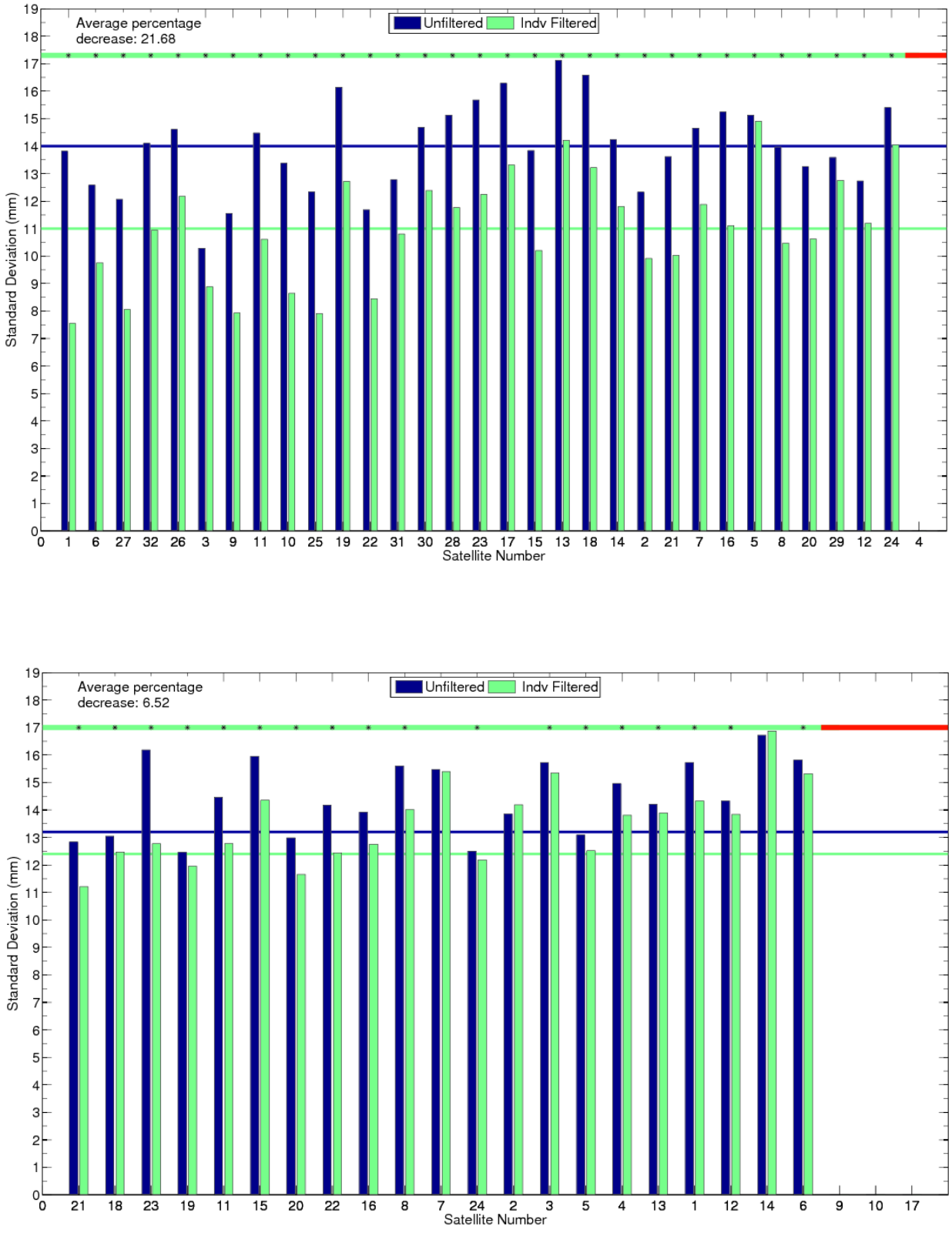

Figure 5.15: Comparison of standard deviations at site DRMS, 2016 days 322 to 323 for unfiltered and GR and GR filtered carrier-phase GPS (top) and GLONASS (bottom) residuals. Symbology as explained in Figure 5.6.

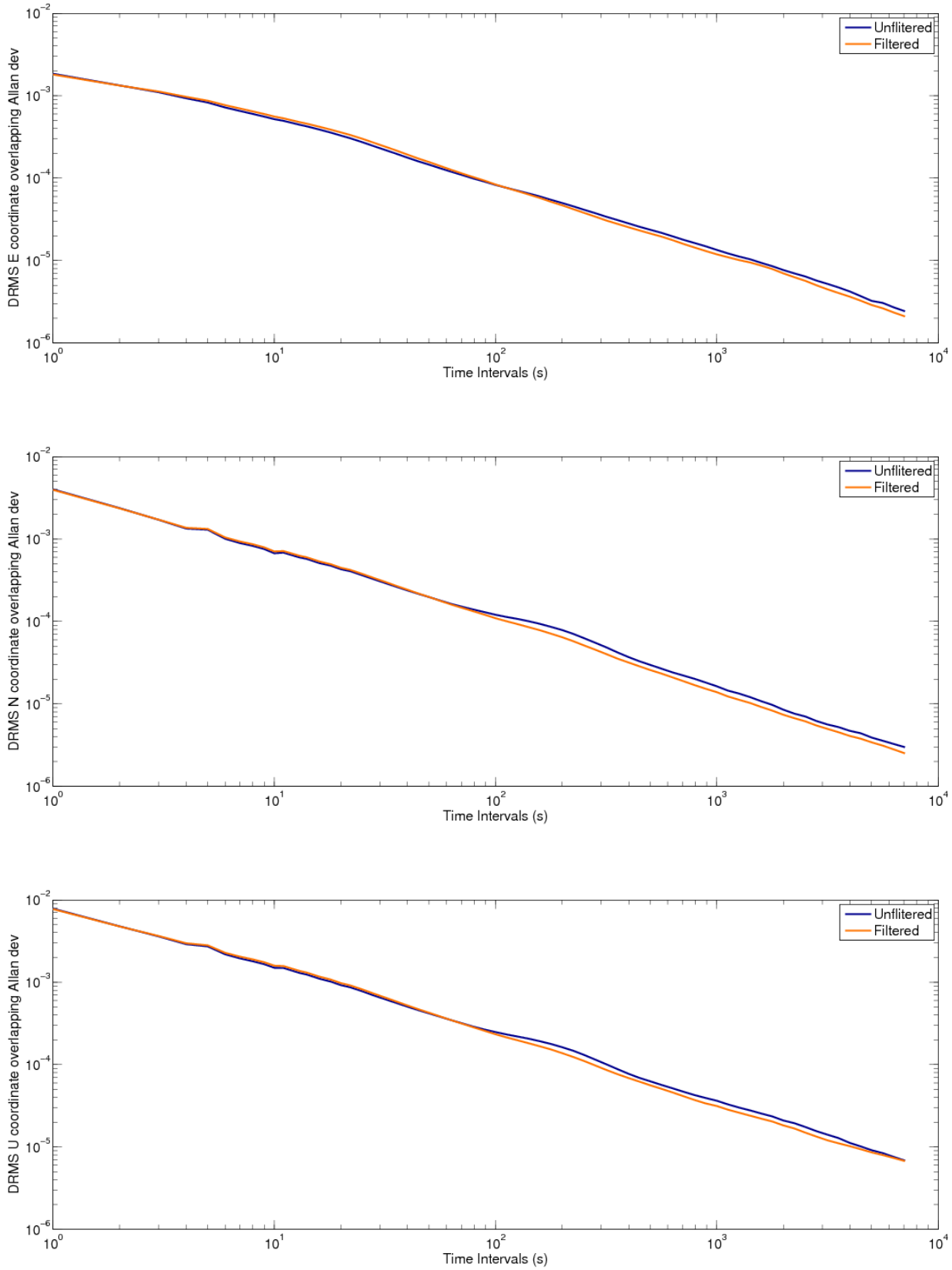

Figure 5.16: Allan deviation plots for GR filtering site DRMS East, North and Up respectively.

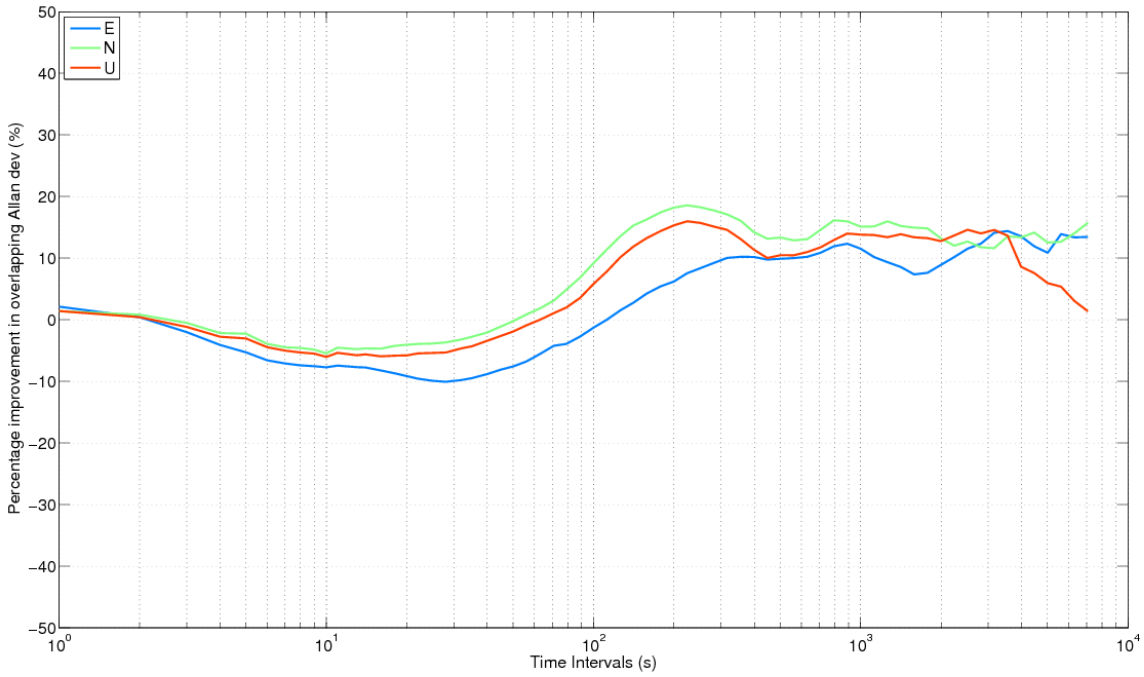

Figure 5.17: Percentage improvement (reduction), in Allan deviation for site DRMS, after GR filtering, corresponding to Allan deviation curves.

5.4 Detection and Measurement of Displacement

Earthquake warning is the detection of present earth movement and the rapid alert to those in harm's way without giving rise to false alarms. To assess the effect of sidereal filtering on displacement measurements, an algorithm was written to alert for antenna movement and measure the movement once a warning has been triggered. Although the data set here has been post-processed, the algorithm has been written such that it could be used in real-time.

The alert to antenna movement algorithm was loosely based on the algorithm proposed in Allen and Ziv (2011) to detect GNSS displacement from the 2010, M_w 7.2 El Mayor-Cucapah earthquake. In their study, earthquake arrival or the start of Earth surface displacement is assumed to be when a short term moving average, 2 s prior, exceeds a given threshold of a long term moving average, 100 s prior. In this study however, the antenna is not assumed to have moved instantaneously due to the time taken to manually wind the platform to each position. Therefore a propagation period of 1 minute (60 s) was included to allow for transient disturbances to subside before computing the displacement, as demonstrated in Figure 5.18. For a real earthquake situation, this propagation time would allow surface wave shaking to subside which could mask the true size of the static permanent displacement.

Only the 1 Hz East coordinate time series from section 5.3.4 is used in this movement study as the Up coordinates standard deviations, are larger in both the unfiltered and filtered time series when compared with the horizontal components, as seen in Tables 3.5, 4.4 and 4.9. Similarly the majority of the North coordinate standard deviations for the OS UK sites are larger than the East coordinates for unfiltered and filtered time series. The noisier vertical component can be attributed to the correlation with tropospheric and ionospheric effects and poor satellite geometry resulting from only seeing satellites in one hemisphere, as described in section 4.3. The noisier North coordinates on the other hand are due to the relatively high latitude of the UK in comparison to satellite inclination, resulting in less satellites being visible in the North-South direction than the East-West. Hence the higher noise levels in the North and Up are more likely to prevent small displacement measurements from being detected and are not used for this experiment.

Using the East coordinate time series and a propagation period of p seconds, the static permanent displacement $\widehat{\Delta E_{\alpha\beta}}$ using long term averaging windows of length α seconds ($300 \leq \alpha \leq 1200$) tested in increments of 300 s and short term averaging windows of length β seconds ($30 \leq \beta \leq 360$) tested in increments of 30 s, can be computed as follows:

$$\widehat{\Delta E_{\alpha\beta}} = E_{post} - E_{pre} \tag{5.1}$$

$$E_{pre} = med\ x_{i=p+1}^{p+\alpha} \tag{5.2}$$

$$E_{post} = med\ x_{i=p+\alpha+1}^{p+\alpha+\beta} \tag{5.3}$$

where med refers to calculating the median of the data set $x_{i=1}^{N}$, $\{x_1, x_2 \ldots x_N\}$.

The threshold to alert for displacement was set to be when the median difference is over 1.5 times the standard error of the difference ($\sigma_{MAD_{post-pre}}$), as given below:

(5.4)

$$\sigma_{MAD_{post-pre}} = \sqrt{\sigma^2_{MAD_{post}} + \sigma^2_{MAD_{pre}}}$$

where the MAD is calculated and scaled to give the equivalent of the standard deviation in the same way as given equation (3.10).

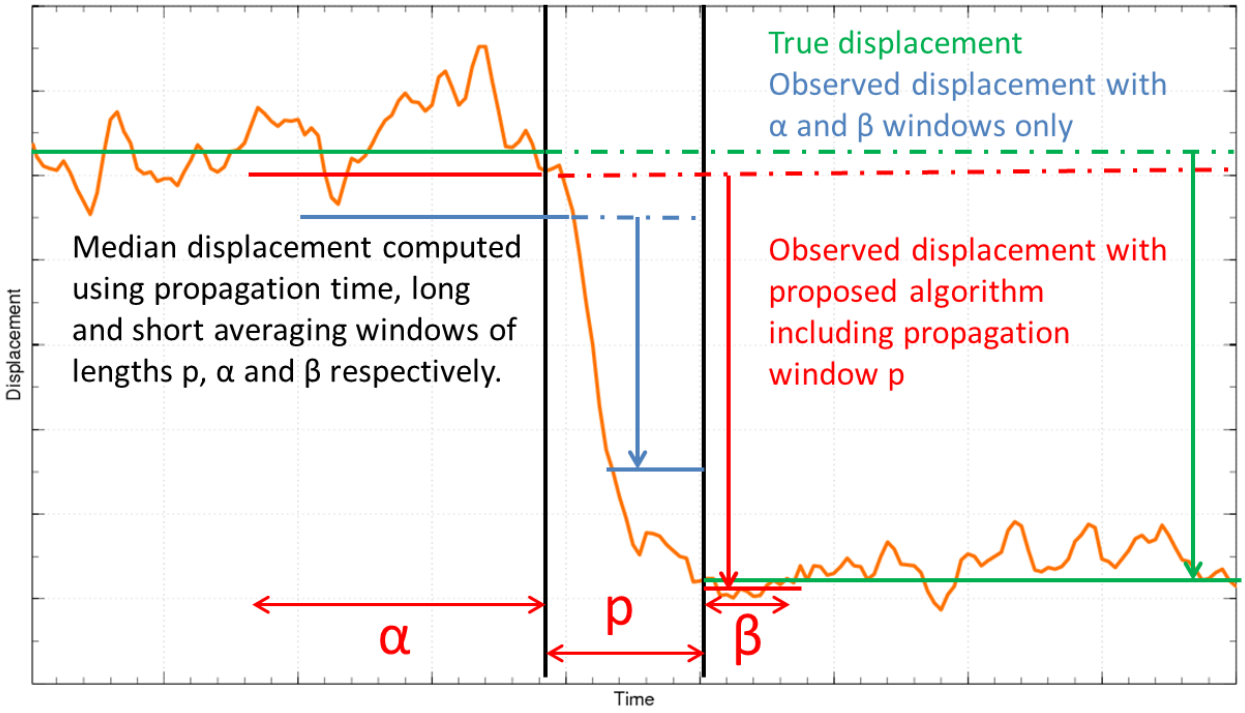

Figure 5.18: Diagram showing the computation of median displacement using long and short averaging windows, separated by a propagation time to ensure high amplitude transient waves are not erroneously measured. The green shows the true displacement that should be measured. Blue shows how the displacement is underestimated by not allowing the displacement to propagate to its true potential. Red shows how the propagation size allows an estimate closer to the true displacement to be observed.

The median was chosen to be used over the mean for each of the windows, as the mean would change gradually as the displacement propagates, whereas the change in coordinates should be more apparent or step like using the median, thus making the change in displacement easier to detect. The moving median suitability for the task of step recovery is demonstrated in Thun *et al.* (2015). The threshold of 1.5 times the standard error was selected by testing error ranges for all averaging window sizes between the values of 0.5-3, incremented in 0.5 steps. As demonstrated in Figure 5.19, the computed median difference, in vermillion peaks above one and a half times the standard error, in dark blue, at the six largest antenna movement times. The median difference peaks above the standard error threshold, in yellow, many times and rarely peaks above the standard error doubled, in cyan.

The value of 1.5 was able to pick out the six largest antenna movements with the fewest number of false alarms and therefore hereafter used.

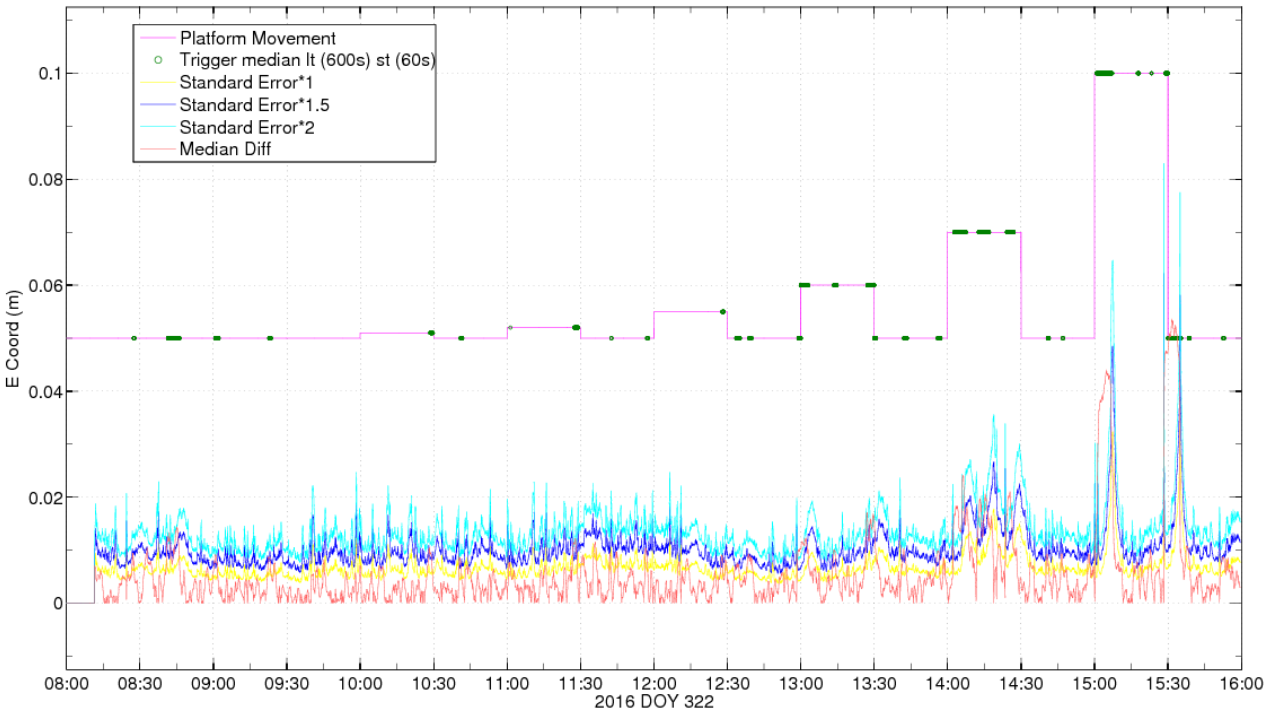

Figure 5.19: Absolute standard error thresholds for the computed absolute median displacements using a long term window of 600 s and a short term window of 60 s. Triggers are shown for the 1.5 standard error threshold only.

To reduce the number of false alarms, an additional threshold was used based on the number of consecutive alerts that have occurred. An alert was defined as any epoch where the median difference was larger than the standard error threshold. A warning is then triggered if this alert threshold is exceeded. The filtered East coordinate data from 00:20-06:10 of the same day (day 322) was used to assess the level of background noise in the data where no antenna movement is known to have occurred. The alert algorithm was run for 12 non overlapping 20 minute periods during this time span. On average, there were 6.25 alerts groups resulting in false alarms made per hour during this 4 hour time span. By taking the 95% percentile of the number of consecutive alerts in this time span, it is 95% certain that this number of alerts is due to noisy data and not displacement. Hence the algorithm only triggers a warning after this number has been breached. From analysis of all the long and short term windows used, a long term window of 600 s and a short term window of 60 s were deemed the most suitable. A short term window of 60 s was chosen as the stability of all coordinate components was found to be improved by filtering at averaging intervals of

60 s and over, as discussed in section 5.3.4. For a long term window of 600 s and a short term window of 60 s an alert threshold of 75 consecutive alerts or more was computed using the methodology described, as seen in Figure 5.20. As seen from Figure 5.22 and Figure 5.21, reducing the size of the short term median window to 30 s increases the number of alerts and allows the short term median to vary more rapidly which leads to a greater variation in calculated displacement measurements and thus displacement uncertainty. Increasing the size of the short term median window to 120 s, as seen in Figure 5.23, on the other hand, increases the warning latency as seen at 15:00, and does not detect the movement at 11:30 which the 60 s window size was able to detect. Reducing the long term median window to 300 s as seen in Figure 5.24, increases the number of alerts and number of movements undetected. The higher variability in long term median also causes multiple closely spaced separate triggers to occur; such is the case for the movement at 15:30. This could reduce confidence in the system if the movement is thought to have subsided. Increasing the long term median window to 1200 s, as seen in Figure 5.25, produces a very smooth long term medium time series which leads to movements being undetected and warnings being triggered for longer periods of time.

Once a warning has been triggered from the alerts the static permanent displacement was computed and updated every ten seconds until the alerts subside.

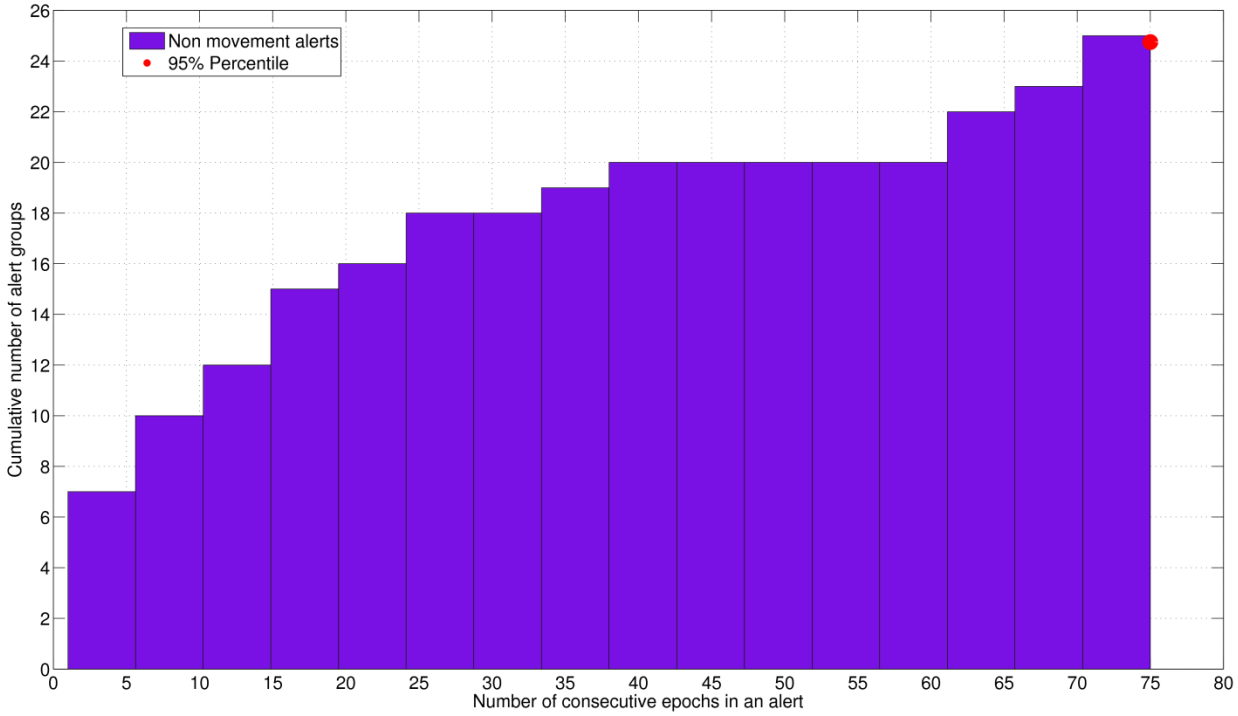

Figure 5.20: Number of consecutive epochs alerted due to East coordinate noise and its 95% percentile.

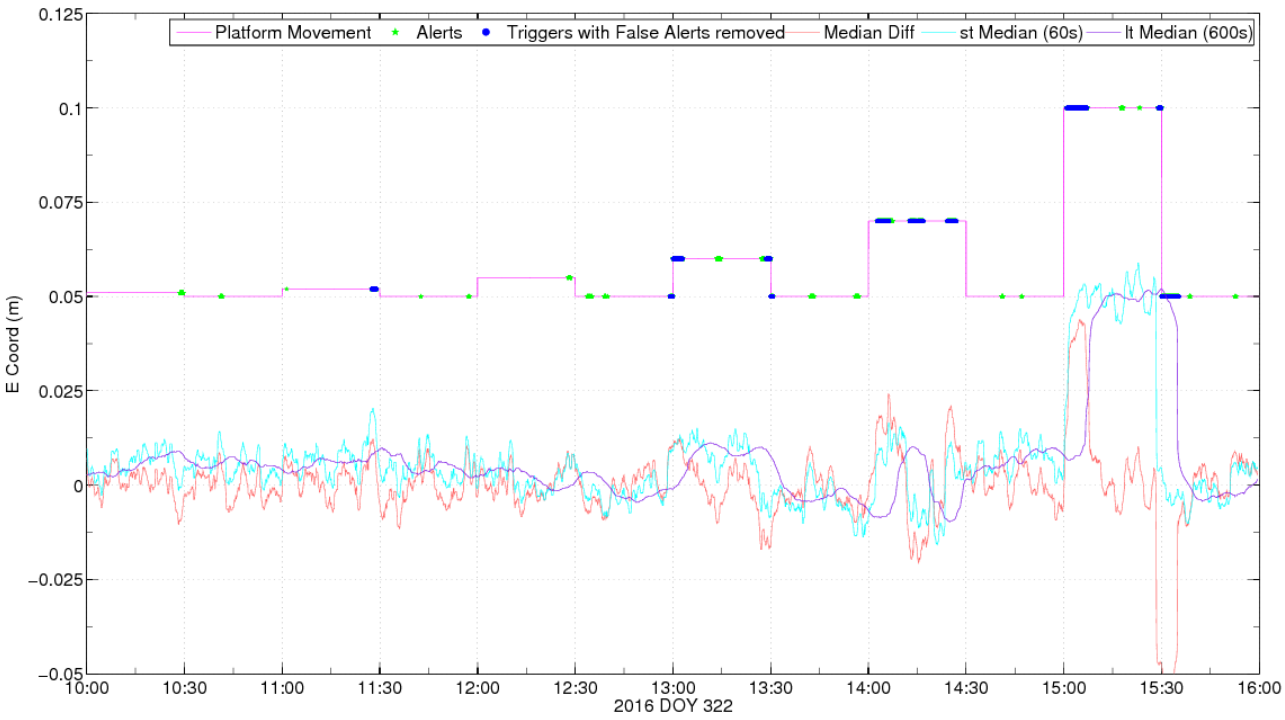

Figure 5.22: Platform movement detection using a long term median window of 600 s and a short term median window of 60 s. Alerts refers to any epoch where the median long term and short term difference is larger than the standard error threshold and a warning is only triggered when there has been more than consecutive 75 alerts.

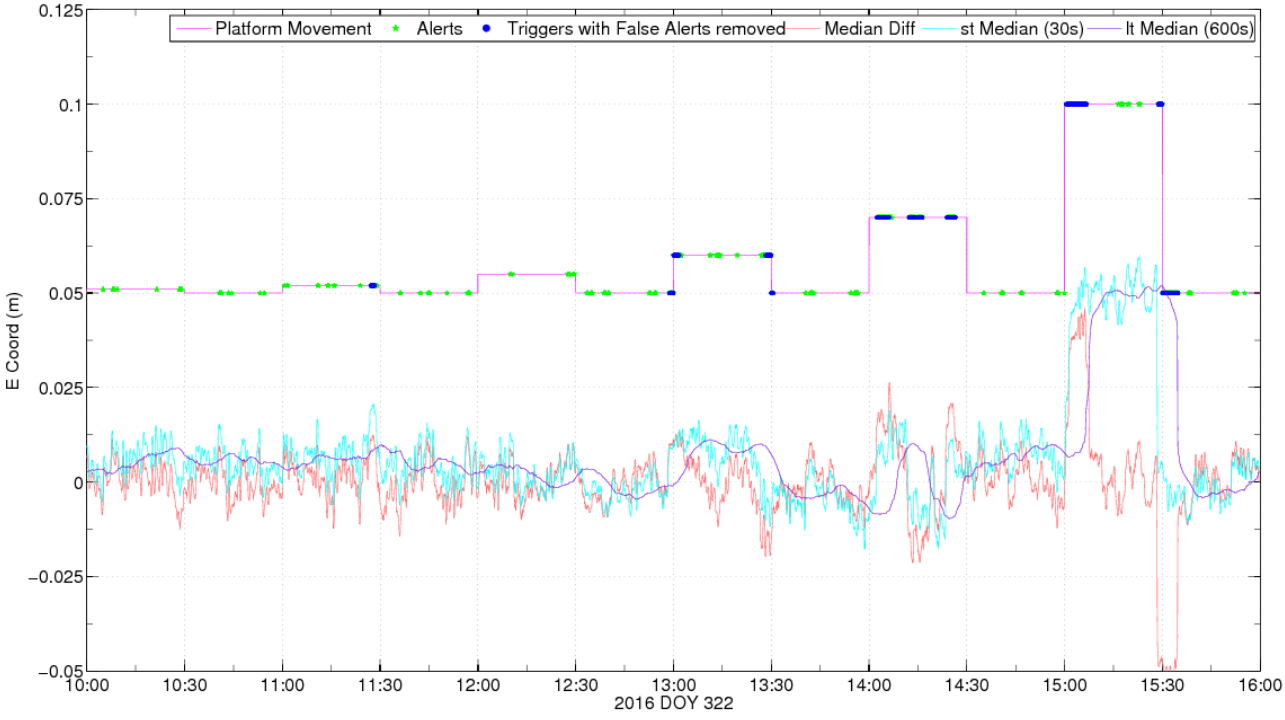

Figure 5.21: Platform movement detection using a long term median window of 600 s and a short term median window of 30 s.

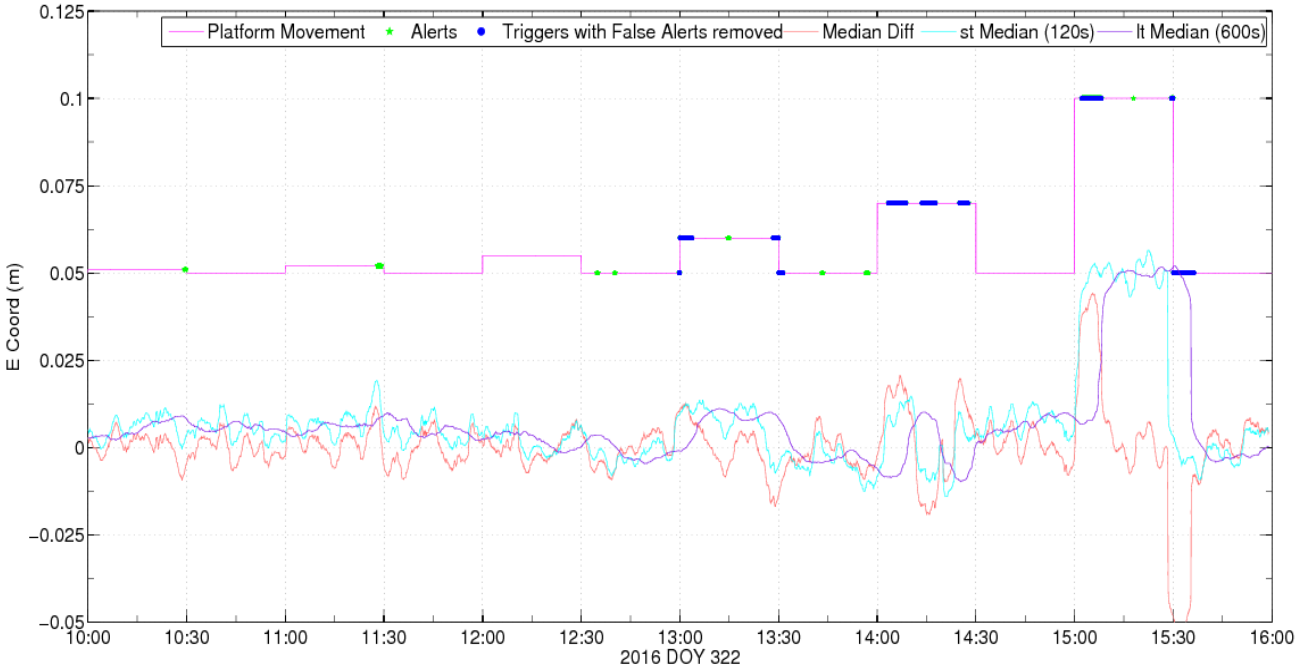

Figure 5.23: Platform movement detection using a long term median window of 600 s and a short term median window of 120 s.

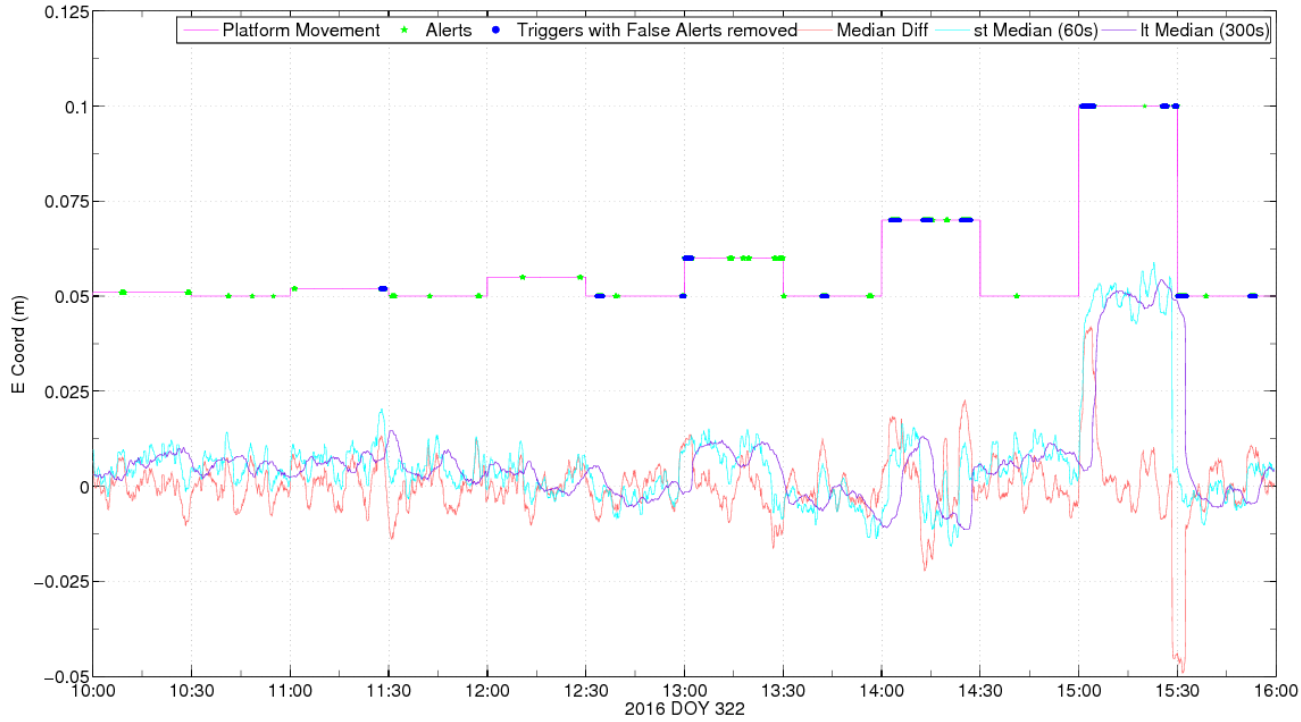

Figure 5.24: Platform movement detection using a long term median window of 300 s and a short term median window of 60 s.

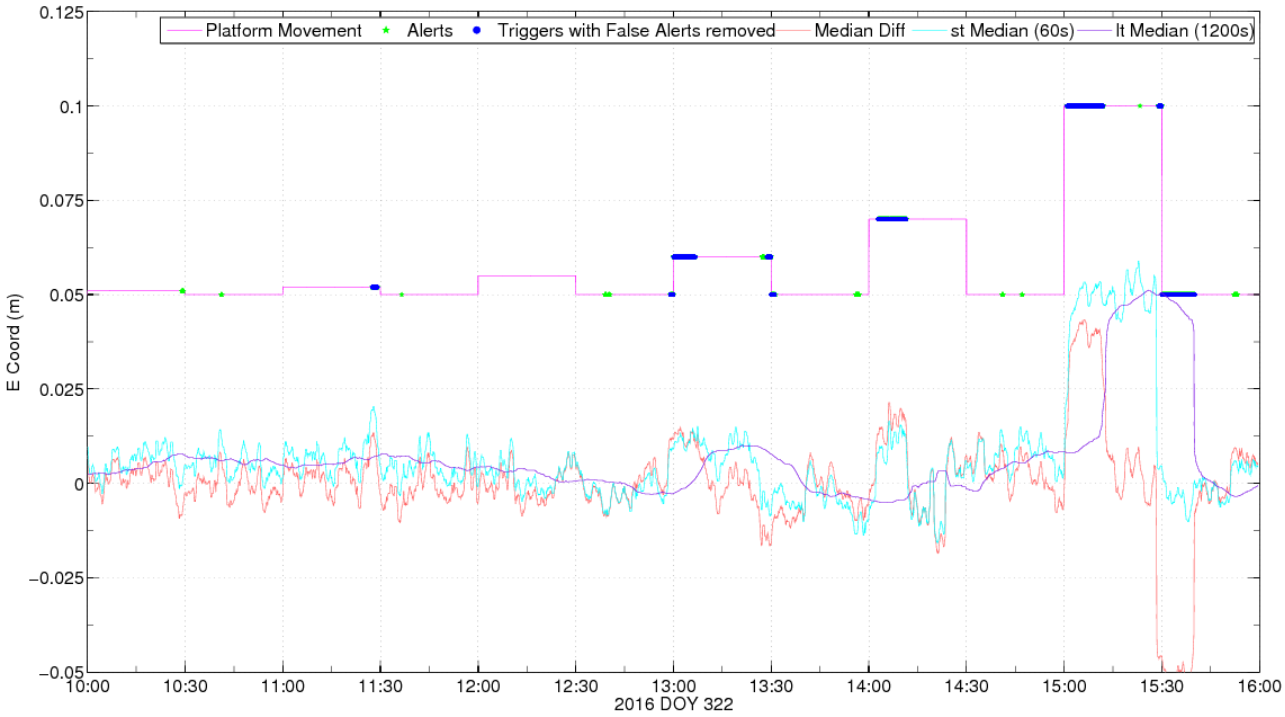

Figure 5.25: Platform movement detection using a long term median window of 1200 s and a short term median window of 60 s.

5.5 Displacement Detection and Measurement Results

Figure 5.26 shows how the algorithm is able to pick out the six largest antenna movements from the filtered East coordinate data set. After the additional alert to trigger threshold had been implemented the total number of false alarms for the filtered case is reduced to just 4, compared to 9 for the unfiltered case. It can be seen how filtering in the East coordinate has reduced the number of false alarms by just over half. Note that the incentive here is to assess the precision of static permanent displacements measured using PPP with and without near-sidereal filtering applied, not to find the optimum window sizes for displacement detection.

A visual comparison of Figure 5.27 shows how the filtered coordinates produce more precise results than the unfiltered coordinates, as seen from the tighter cluster of estimates. The filtered coordinate estimates are also more accurate which is particularly evident at time 15:30, where the estimates are closer to the known movement of the platform. It should be noted that the movement at 14:30 is not included in this results section due to equipment

failure at this time, preventing the actual antenna movement from being known. Table 5.3 shows the Root Mean Square Difference (RMSD) of the difference between N estimates and the known truth value of movement, as computed by:

$$RMSD = \sqrt{\frac{\sum_{i=1}^{n}(Computed - Truth)^2}{N}} \tag{5.5}$$

The RMSD shows how on average the filtered coordinate displacements are estimated with higher precision than the unfiltered based on the first trigger point and the 10 second updates thereafter. The filtered displacement estimates have an average RSMD value of 5 mm compared to 7 mm for the unfiltered estimates. The unfiltered coordinate estimates using just the first trigger points, estimate three out of the five movements with better accuracy then those coordinates that have been filtered. On average however, the filtered coordinates have a lower RMSD value for all five movements based on just the first trigger points. The average computed displacements in the East component for both the filtered and unfiltered case are given in Table 5.4.

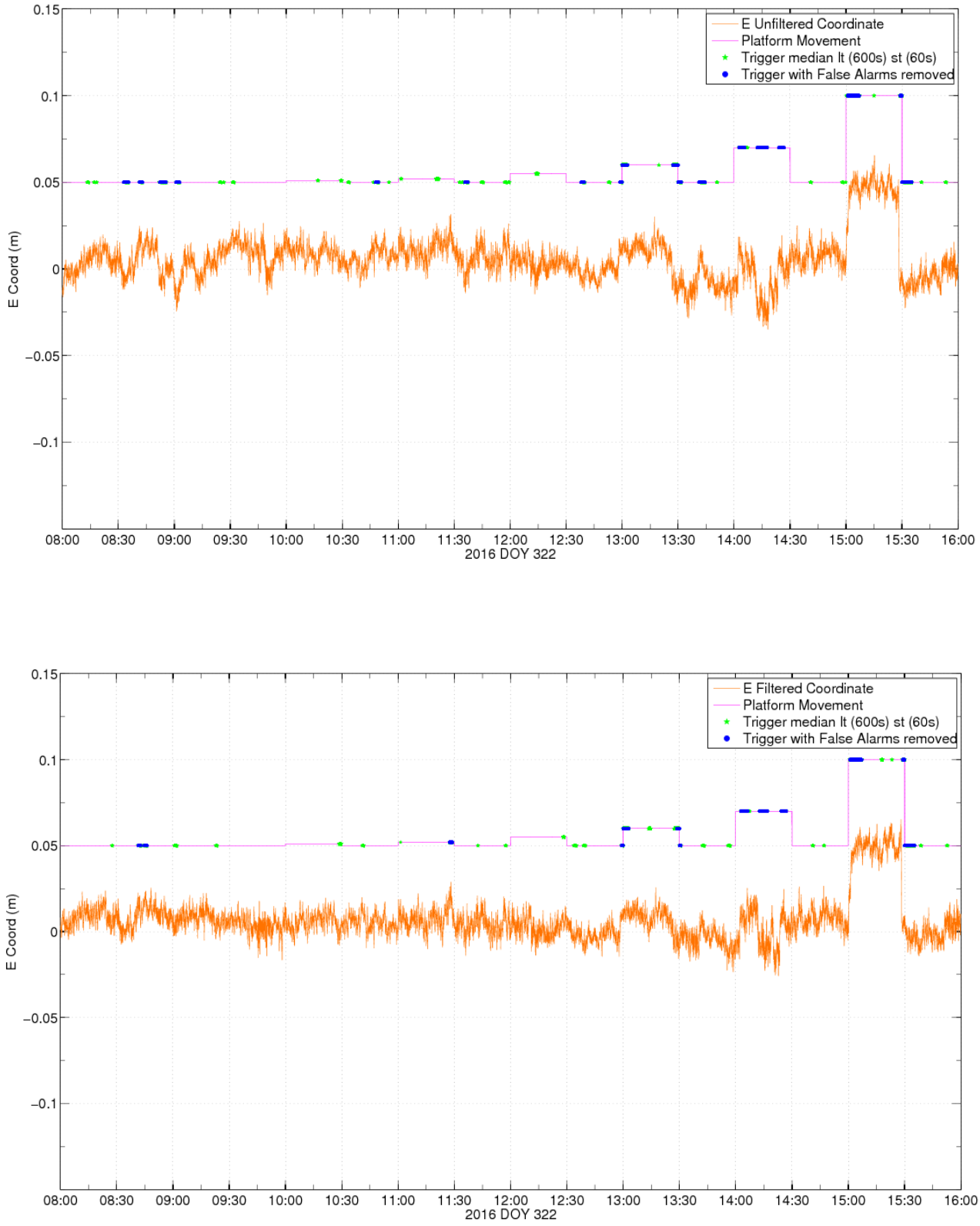

Figure 5.26: East coordinate time series between times 08:00 and 16:00 on day 322 2016 for DRMS receiver resulting from PPP GR unfiltered processing (top) and near-sidereally filtered processing (bottom). The magenta line shows the true platform movement and has been offset by 0.05 m for clarity.

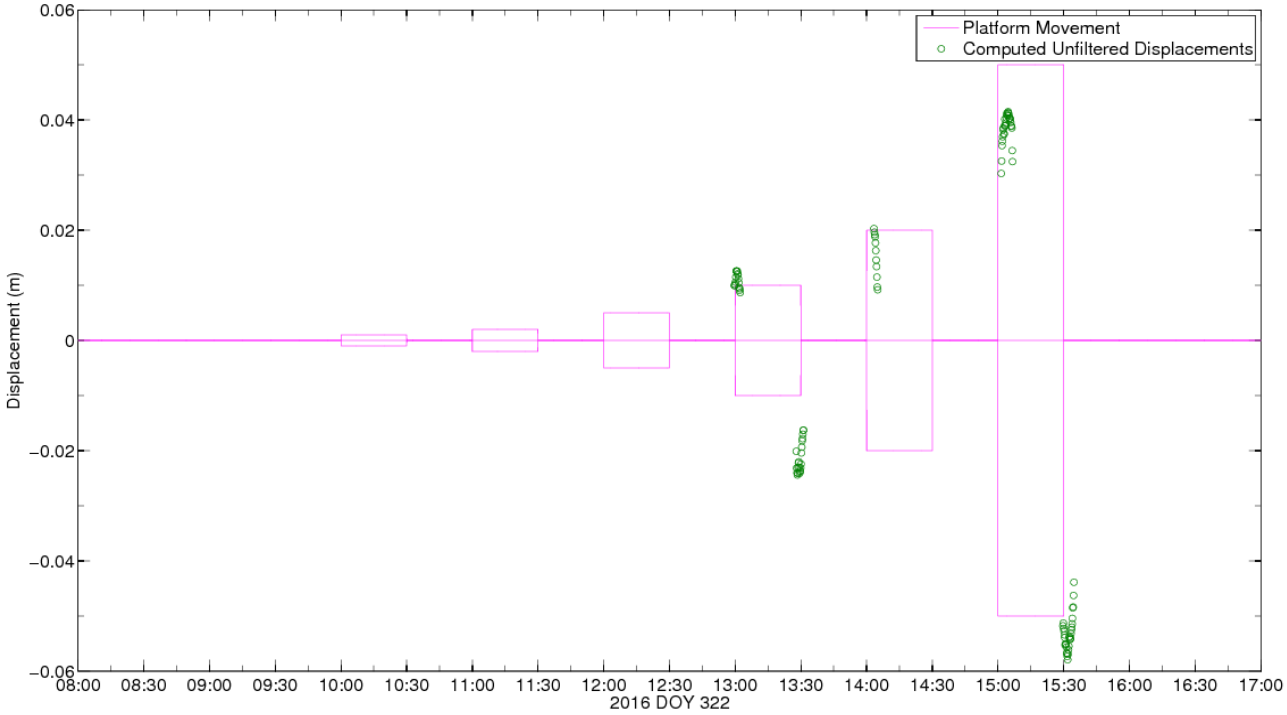

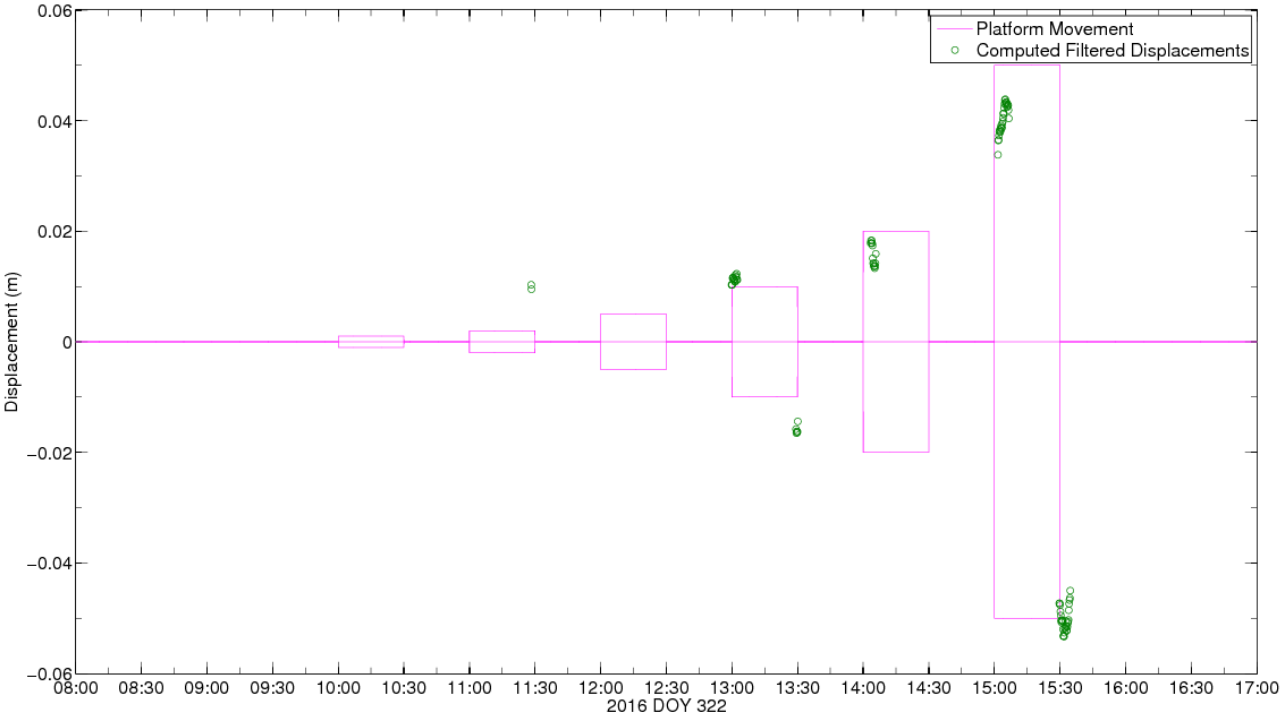

Figure 5.27: East coordinate computed displacements between times 08:00 and 16:00 on day 322 2016 for DRMS receiver resulting from PPP GR unfiltered processing (top) and near-sidereally filtered processing (bottom).

Table 5.3: RMSD values for sidereally filtered and unfiltered computed East coordinate platform displacements.

Platform Movement (mm)	-2	10	-10	20	50	-50
Unfiltered						
All triggers RMSD	-	2	12	6	12	5
1st Trigger RMSD	-	0	10	0	20	2
Filtered						
All triggers RMSD	12	1	6	5	10	2
1st Trigger RMSD	12	0	6	2	16	3

Table 5.4: Mean computed platform displacement values from sidereally filtered and unfiltered East coordinate GR PPP.

Platform Movement (mm)	-2	10	-10	20	50	-50
Unfiltered						
Mean Displacement (mm)	-	11	-21	15	38	-53
Filtered						
Mean Displacement (mm)	10	11	-16	16	40	-50

5.6 Conclusion

It has been demonstrated from the above results that it is possible to automatically detect antenna movements in the East component of size 1-5 cm using combined GPS and GLONASS PPP. The application of combined GPS and GLONASS near-sidereal filtering reduces the occurrence of false alarms to around half and improves the accuracy and precision of the displacement estimates on average by about 2 mm, in terms of the difference between filtered and unfiltered RMSD and mean displacement values. Even though near-sidereal filtering on average improves the precision and stability of a coordinate time series, it does not necessarily always improve the accuracy of the computed permanent static displacements, in some cases the unfiltered data outperformed the filtered data. This could be due to errors in the satellite orbit and clock models from using CODE 'Final Rapid' orbits to assess the feasibly of near real-time displacement detection. The use of long averaging

windows to compute the median displacement could also have a smoothing effect on high frequency multipath interference which could be decreasing the effectiveness of the near-sidereal filters at these frequencies. Also, as mentioned in section 5.2, during this experiment the antenna's relative position to surrounding reflectors changed as the antenna movements were made relative to the concrete pillar. This could reduce filter performance as the relative position of the antenna with respect to the reflecting objects has changed between filter creation and application. During an actual earthquake the concrete pillar would move with the antenna and thus the actual relative positions would remain largely unchanged. Hence, GNSS could be used in addition to seismic data to help prevent the occurrence of false alarms, the underestimation of static permanent displacements and thus the under estimation of earthquake and resulting tsunami magnitude.

Chapter 6. Conclusions

The research presented in this thesis has focused on sidereal filtering for multi-GNSS PPP, in particular GPS and GLONASS. The optimum geometry repeat period for the GLONASS constellation was determined and has allowed GLONASS-only and GPS and GLONASS observation domain, near-sidereal filtering in PPP. Filtering has been assessed both in a static and dynamic scenario for small displacement detection and measurement applications. This chapter will review the research undertaken and the conclusions drawn.

6.1 Review of Work

The limitations of early-warning systems at present and the requirements for GNSS enabled methods were introduced in Chapter 1. The benefit of the inclusion of GNSS data for early-warning systems was outlined and the current limitations of using GNSS highlighted in Chapter 2. The main limitation of GNSS, multipath and its mitigation methods were reviewed in Chapter 3.

The aims and objectives of this thesis were developed to provide research on the mitigation of GLONASS multipath in a GLONASS-only and GPS and GLONASS coordinate PPP solution, based on the orbital repeat geometry of both constellations. Emphasis was placed on how filtering improves the coordinate solution stability over short periods of time (a few tens to hundreds of seconds) for use in deformation monitoring, in particular the detection and measurement of small static displacements such as those induced by earthquakes.

The practicalities of combining GPS and GLONASS for near-sidereal filtering to fulfil the aims and objectives of the project were outlined in Chapters 3 and 4, along with a description of data collection and methodology validation. To enable near-sidereal filtering to be applied in the observation domain an amendment to the PANDA software was undertaken by Dr Ian Martin. An option was included to select if a filter was to be applied, and if so to which constellation(s) and satellite(s). An experiment to test the performance of the combined near-sidereal filter in a dynamic scenario was also conducted as outlined in Chapter 5, to assess the use of filtering to aid in the detection and measurement of small static displacements.

6.2 Summary of Results

-The method implemented in this study for finding the optimum repeat period of individual satellites is valid for PPP, as values computed for the GPS satellite constellation are in keeping with those found from previous research, which use a variety of different methodologies and processing strategies such as PPP or relative positioning. Optimum repeat period methods include in brief: finding the average orbit repeat time using the broadcast ephemeris and the orbital mean motion; interpolating precise orbit products to the equator crossing on successive days; finding when the dot product between two receiver-to-satellite unit vectors associated with the current epoch measurement and the prospective correction derived from the previous day's measurement is at a maximum; and using the day-to-day autocorrelation of coordinate and carrier-phase residuals

-The constellation mean optimum repeat period for the GLONASS constellation was found to be around 689,248 s which is roughly 8 days with a near-sidereal period of 86156 s.

-GPS-only near-sidereal filtering improves the 3D RMS of coordinates on average by 33.5%. The horizontal component standard deviations are on average reduced by 6.1 mm and the vertical by 15.9 mm, which is equivalent to about 33.0% and 35.7% improvement respectively. GPS filtering also increases the accuracy and stability of PPP coordinate time series, on average maximum improvement in Allan deviation was around 35%-38% in all coordinate components peaking at averaging intervals of about 1000 s.

-GLONASS-only near-sidereal filtering improves the 3D RMS of coordinate difference values on average by 17.9%. The horizontal component standard deviations are on average reduced by 4.3 mm and the vertical by 7.7 mm, which is equivalent to about 20.2% and 17.6% improvement respectively. GLONASS filtering also increases the accuracy and stability of PPP coordinate time series, on average maximum improvement in Allan deviation was around 19%-26% in all coordinate components at averaging intervals ranging from 650 s to the largest averaging interval of 2 hours.

-GPS and GLONASS near-sidereal filtering improves the 3D RMS of coordinate difference values on average by 21.4%. The horizontal component standard deviations are on average reduced by 2.6 mm and the vertical by 7.0 mm, which is equivalent to about 22.3% and 25.1% improvement respectively. GPS and GLONASS filtering also increases the accuracy and

stability of PPP coordinate time series, on average maximum improvement in Allan deviation was around 26%-30% in all coordinate components at similar averaging intervals as GPS-only filtering.

-Near-sidereal filtering was not very effective at removing errors which oscillate with periods of less than roughly 300 s. This is likely due to the filter amplifying high-frequency noise during periods where there is little to no multipath (see section 3.9).

-Near-sidereal filtering was also not as effective at removing errors which oscillate with periods exceeding a few thousand seconds. This could be due to more non-multipath errors contributing to the measurement residuals at these periods. It is plausible that lower-frequency multipath errors could be being soaked up by other slowly varying parameters, such as the wet tropospheric delay, during the Kalman filter process (see section 4.3).

-The elevation angle of filter application was investigated to try to reduce the amplification of high-frequency noise, to increase time series stability at short averaging intervals. The effectiveness of elevation angle thresholding was found to be site specific and more effective for GLONASS filtering than GPS filtering and did not benefit from individual elevation thresholds for each satellite. This could be due to a number of reasons, such as elevation dependant weighting in PANDA at low elevations angles or lack of the use of the optimum lag values for individual elevation threshold angles, as discussed in more detail in section 3.10.2. Section 4.4.3 however, does show that GLONASS-only filtering does benefit from only applying the filter to low elevation angle satellites.

-The automatic detection of small (up to <5 cm) artificially induced displacements using a GR PPP solution was investigated to assess the effectiveness of filter application in a dynamic situation. It was possible to create a displacement detection algorithm based on using long term and short term medians which could automatically detect displacements of 1 cm or larger from a filtered and unfiltered combined GPS and GLONASS East coordinate time series. The application of combined GPS and GLONASS near-sidereal filtering was found to reduce the occurrence of false alarms during automatic displacement detection by just over half. Filtering was found to improve the accuracy and precision of displacement estimates on average by 2 mm in terms of the difference between filtered and unfiltered RMSD and mean displacement values.

Overall this research has demonstrated the benefits of using combined GPS and GLONASS near-sidereal filtering for a GR PPP coordinate solutions and demonstrates the potential of using GNSS to aid in the detection and measurement of displacements such as those induced by an earthquake. Near-sidereally filtered GNSS offers enhanced coordinate time series stability, precision and reduces the number of false alarm that arise during displacement detection. It is hoped that the inclusion of near-sidereally filtered GNSS data would be able to reduce the occurrence of false alarms from early-warning systems which wholly use seismic data, and/or GNSS data that is strongly affected by multipath. The improvement from filtering could allow permanent static earth surface displacements to be estimated with a higher level of accuracy and hence prevent the underestimation of earthquake and resulting tsunami magnitude as well as improve warning response times.

6.3 Recommendations for Future Work

The potential of using sidereal filtering for multi-GNSS PPP with applications in deformation monitoring has been demonstrated in this thesis. A number of suggestions to expand this work further are outlined below:

-As mentioned in section 2.2, the positional accuracy of GNSS improves with the number of satellites included in the solution. With a larger number of satellites in the sky there is higher satellite availability and hence improved satellite geometry. Including satellites from other GNSSs such as Galileo and BeiDou when they become fully operational could be used to increase the positional accuracy of PPP (Cai *et al.*, 2015). The correlation method used in this research could easily be used to calculate the different geometry repeat periods of the Galileo and BeiDou constellations, especially the BeiDou constellation which consists of satellites with three different orbital repeat periods. The filters for GPS and GLONASS have been implemented separately in this research; therefore the method can be expanded to apply separate filters for the two additional constellations as PANDA already has the capabilities of processing multi-GNSSs in PPP.

-The results from thresholding filter application to lower elevation angles were inconclusive. A potential reason for this was due to using optimum elevation angles based on the optimum lag periods calculated from using residuals with elevation angles between 0° and 90°. Recalculating the optimum lag periods for each elevation threshold may help to give a more conclusive result.

-The PANDA software and PPP processing method used in this research does not fix the ionosphere-free phase ambiguity values; they are allowed to slowly change in the Kalman filter. PPP techniques where the GPS ambiguities can be fixed have recently been developed, which improves positional accuracy as mentioned in section 2.6.1. As well as the positional accuracy, slow varying parameter estimates such as the troposphere also benefit from ambiguity fixing. As discussed in section 4.3, filtering performed poorly at long averaging intervals due to lower-frequency multipath errors being soaked up by other slowly varying parameters, such as the troposphere. If the tropospheric delay could be better estimated then potential multipath will not be absorbed into this parameter and hence be filtered more effectively.

-Filter application was predominantly investigated using post-processed ESA 'Final' or CODE 'Final Rapid ' orbit and clock products, to show its full potential. Real-time products could conceal the true effectiveness of filtering due to erroneous satellite clock offsets. For tsunami early-warning near-real-time PPP processing and products are required. Since 2013 the IGS Real-time Service has allowed users to stream PPP orbit and clock corrections at a sampling rate of 5 seconds with typical latency of 25 seconds and orbit accuracy of ~5 cm (Grinter and Roberts, 2013). Commercial products are also available, e.g. Fugro were the first to offer a real-time service using GLONASS and have recently enhanced their product to include Galileo and BeiDou (Tegedor *et al.*, 2015). In addition to multi-GNSS real-time products now being available, the atomic clocks on-board new GPS satellites (Block IIF) are more stable than those on previous GPS blocks over short time intervals. The BeiDou and Galileo rubidium atomic frequency standards and passive hydrogen maser clocks are also more stable than the old GPS and GLONASS clocks (Griggs *et al.*, 2015). Hence near-real-time sidereal filtering in PPP should be possible at the required decimetre accuracy, provided that optimum satellite repeat periods are precomputed and near-sidereal filter values kept up to date.

-GLONASS satellite observations have low cross-correlation between each other due to inter-frequency biases from using the FDMA signal structure as opposed to CDMA which GPS uses. The new GLONASS-K satellites, the first operational satellite of which was launched in 2014, however, have an additional L3 band with CDMA capabilities. During this research GLONASS optimum repeat period correlations were weaker than GPS correlations due to their longer geometry repeat period (eight near-sidereal days). Previous research has found that filter life

time degrades from day 1 and at day 30 there is no coordinate improvement from filtering (Ragheb *et al.*, 2007a). Therefore the longer the repeat period the more likely environmental changes can occur and reduce the effectiveness of the filter. Hence, GLONASS filtering could benefit from using near-sidereal repeat periods of adjacent GLONASS satellite pairs rather than an eight near-sidereal repeat period for single satellites when the new GLONASS CDMA enabled satellites become operational.

-The use of GNSS near-sidereal filtering to enhance the measurement of small static displacements was only tested in this study using a simulated scenario, moving a platform by a known amount. Filtering was not tested for a real seismic event due to the lack of 1 Hz GPS and GLONASS data and ground truth displacement data being available, for an event with earthquake induced centimetre-level Earth surface displacements. Filtering could be applied to a variety of seismic events with varying magnitudes and fault rupture mechanisms. Provided that the 'true' displacement is known for the event to assess the performance of near-sidereal filtering, the computed static permanent displacements could then be used to estimate and compare earthquake magnitude and tsunami wave height.

References

Agnew, D. and Larson, K. (2007) 'Finding the repeat times of the GPS constellation', *GPS Solutions*, 11(1), pp. 71-76.

Aki, K. and Richards, P.G. (2002) *Quantitative Seismology*. 2nd edn. Sansalito, CA: University Science Books.

Alkan, R.M., İlçi, V., Ozulu, İ.M. and Saka, M.H. (2015) 'A comparative study for accuracy assessment of PPP technique using GPS and GLONASS in urban areas', *Measurement*, 69, pp. 1-8.

Allan, D.W. (1966) 'Statistics of atomic frequency standards', *Proceedings of the IEEE*, 54(2), pp. 221-230.

Allen, R.M. and Ziv, A. (2011) 'Application of real-time GPS to earthquake early warning', *Geophysical Research Letters*, 38(16).

Ashby, N. (2003) 'Relativity in the Global Positioning System', *Living Rev. Relativity*, 6.

Atkins, C. and Ziebart, M. (2015) 'Effectiveness of observation-domain sidereal filtering for GPS precise point positioning', *GPS Solutions*, 20(1), pp. 111-122.

Axelrad, P., Larson, K. and Jones, B. (2005) 'Use of the Correct Satellite Repeat Period to Characterize and Reduce Site-Specific Multipath Errors', *ION GNSS 18th International Technical Meeting of the Satellite Division*. Long Beach CA, 13-16 September. pp. 2638-2648.

Banville, S., Collins, P. and Lahaye, F. (2013) 'GLONASS ambiguity resolution of mixed receiver types without external calibration', *GPS Solutions*, 17(3), pp. 275-282.

Bilich, A., Cassidy, J.F. and Larson, K.M. (2008a) 'GPS seismology: Application to the 2002 Mw 7.9 Denali fault earthquake', *Bulletin of the Seismological Society of America*, 98(2), pp. 593-606.

Bilich, A. and Larson, K.M. (2007) 'Mapping the GPS multipath environment using the signal-to-noise ratio (SNR)', *Radio Science*, 42(6), p. RS6003.

Bilich, A., Larson, K.M. and Axelrad, P. (2008b) 'Modeling GPS phase multipath with SNR: Case study from the Salar de Uyuni, Boliva', *Journal of Geophysical Research: Solid Earth*, 113(B4).

Bisnath, S. and Collins, P. (2012) 'Recent Developments in Precise Point Positioning', *GEOMATICA*, 66(2), pp. 103-111.

Blewitt, G. (1990) 'An Automatic Editing Algorithm for GPS data', *Geophysical Research Letters*, 17(3), pp. 199-202.

Blewitt, G., Hammond, W.C., Kreemer, C., Plag, H.-P., Stein, S. and Okal, E. (2009) 'GPS for real-time earthquake source determination and tsunami warning systems', *Journal of Geodesy*, 83(3-4), pp. 335-343.

Blewitt, G., Kreemer, C., Hammond, W.C., Plag, H.P., Stein, S. and Okal, E. (2006) 'Rapid determination of earthquake magnitude using GPS for tsunami warning systems', *Geophysical Research Letters*, 33(11).

Bock, H., Dach, R., Jäggi, A. and Beutler, G. (2009) 'High-rate GPS clock corrections from CODE: support of 1 Hz applications', *Journal of Geodesy*, 83(11), pp. 1083-1094.

Bock, Y., Melgar, D. and Crowell, B.W. (2011) 'Real-Time Strong-Motion Broadband Displacements from Collocated GPS and Accelerometers', *Bulletin of the Seismological Society of America*, 101(6), pp. 2904-2925.

Bock, Y., Nikolaidis, R.M., de Jonge, P.J. and Bevis, M. (2000) 'Instantaneous geodetic positioning at medium distances with the Global Positioning System', *Journal of Geophysical Research: Solid Earth*, 105(B12), pp. 28223-28253.

Bock, Y., Prawirodirdjo, L. and Melbourne, T.I. (2004) 'Detection of arbitrarily large dynamic ground motions with a dense high-rate GPS network', *Geophysical Research Letters*, 31(6).

Boehm, J., Niell, A., Tregoning, P. and Schuh, H. (2006) 'Global Mapping Function (GMF): A new empirical mapping function based on numerical weather model data', *Geophysical Research Letters*, 33(7).

Boehm, J. and Schuh, H. (2004) 'Vienna mapping functions in VLBI analyses', *Geophysical Research Letters*, 31(1).

Bormann, P. and Saul, J. (2009) 'Earthquake Magnitude', in Meyers, R.A. (ed.) *Encyclopedia of Complexity and Systems Science*. Springer New York, pp. 2473-2496.

Cabinet Office, G.O.J. (2017) *Overview of the Quasi-Zenith Satellite System (QZSS)*. Available at: http://qzss.go.jp/en/overview/services/sv01_what.html.

Cai, C. and Gao, Y. (2009) 'A Combined GPS/GLONASS Navigation Algorithm for use with Limited Satellite Visibility', *The Journal of Navigation*, 62(04), pp. 671-685.

Cai, C. and Gao, Y. (2013) 'Modeling and assessment of combined GPS/GLONASS precise point positioning', *GPS Solutions*, 17(2), pp. 223-236.

Cai, C., Gao, Y., Pan, L. and Zhu, J. (2015) 'Precise point positioning with quad-constellations: GPS, BeiDou, GLONASS and Galileo', *Advances in Space Research*, 56(1), pp. 133-143.

Centre for Research on the Epidemiology of Disasters (2016) *The International Disaster Database*. Available at: http://www.emdat.be/disaster_list/index.html (Accessed: 18/07/2016).

Chen, K., Ge, M., Babeyko, A., Li, X., Diao, F. and Tu, R. (2016) 'Retrieving real-time co-seismic displacements using GPS/GLONASS: a preliminary report from the September 2015 Mw 8.3 Illapel earthquake in Chile', *Geophysical Journal International*, 206(2), pp. 941-953.

Choi, B.H., Hong, S.J. and Pelinovsky, E. (2006) 'Distribution of runup heights of the December 26, 2004 tsunami in the Indian Ocean', *Geophysical Research Letters*, 33(13).

Choi, K.H., Bilich, A., Larson, K.M. and Axelrad, P. (2004) 'Modified sidereal filtering: Implications for high-rate GPS positioning', *Geophysical Research Letters*, 31(22).

Collins, J.P. (1999) *Assessment and Development of a Tropospheric Delay Model for Aircraft Users of the Global Positioning System*. University of New Brunswick, Fredericton.

Collins, P., Lahaye, F., Héroux, P. and Bisnath, S. (2008) *ION GNSS 21st international technical meeting of the satellite division*. Savannah, US.

Colombo, O., Sutter, A.W. and Evans, A.G. (2004) *In Proceedings of the ION GPS GNSS 2004 Meeting*. Long Beach, California, September.

Crowell, B.W., Bock, Y. and Melgar, D. (2012) 'Real-time inversion of GPS data for finite fault modeling and rapid hazard assessment', *Geophysical Research Letters*, 39(9).

Crowell, B.W., Melgar, D., Bock, Y., Haase, J.S. and Geng, J. (2013) 'Earthquake magnitude scaling using seismogeodetic data', *Geophysical Research Letters*, 40(23), pp. 6089-6094.

Dach, R., Lutz, S., Walser, P. and Fridez, P. (2015) 'Bernese GNSS software version 5.2'. User manual, Astronomical Institute, University of Bern: Bern Open Publishing.

Dach, R., Schaer, S., Arnold, D., Orliac, E., Prange, L., Susnik, A., Villiger, A. and Jaeggi, A. (2016) 'CODE final product series for the IGS', [Online]. Available at: http://www.aiub.unibe.ch/download/CODE DOI: 10.7892/boris.75876 (Accessed: 18/07/2016).

Dai, W., Huang, D. and Cai, C. (2014) 'Multipath mitigation via component analysis methods for GPS dynamic deformation monitoring', *GPS Solutions*, 18(3), pp. 417-428.

Davis, J.P. and Smalley, R. (2009) 'Love wave dispersion in central North America determined using absolute displacement seismograms from high-rate GPS', *Journal of Geophysical Research: Solid Earth*, 114(B11).

Dong, D., Wang, M., Chen, W., Zeng, Z., Song, L., Zhang, Q., Cai, M., Cheng, Y. and Lv, J. (2015) 'Mitigation of multipath effect in GNSS short baseline positioning by the multipath hemispherical map', *Journal of Geodesy*, 90(3), pp. 255-262.

Edwards, S.J., Clarke, P.J., Penna, N.T. and Goebell, S. (2010) 'An Examination of Network RTK GPS Services in Great Britain', *Survey Review*, 42(316), pp. 107-121.

Ekström, G., Nettles, M. and Dziewoński, A.M. (2012) 'The global CMT project 2004–2010: Centroid-moment tensors for 13,017 earthquakes', *Physics of the Earth and Planetary Interiors*, 200–201, pp. 1-9.

El-Hattab, A.I. (2013) 'Influence of GPS antenna phase center variation on precise positioning', *NRIAG Journal of Astronomy and Geophysics*, 2(2), pp. 272-277.

Elósegui, P., Davis, J.L., Jaldehag, R.T.K., Johansson, J.M., Niell, A.E. and Shapiro, I.I. (1995) 'Geodesy using the Global Positioning System: The effects of signal scattering on estimates of site position', *Journal of Geophysical Research: Solid Earth*, 100(B6), pp. 9921-9934.

Elósegui, P., Davis, J.L., Oberlander, D., Baena, R. and Ekström, G. (2006) 'Accuracy of high-rate GPS for seismology', *Geophysical Research Letters*, 33(11).

Enderle, W. and Springer, T. (2015) *ESOC IGS ANALYSIS STRATEGY SUMMARY*. Available at: https://igscb.jpl.nasa.gov/igscb/center/analysis/esa.acn.

European-Commission (2015) *Galileo system*. Available at: http://ec.europa.eu/growth/sectors/space/galileo/launches/index_en.htm.

Ferre-Pikal, E.S. and Walls, F.L. (2005) 'Frequency Standards, Characterization', in *Encyclopedia of RF and Microwave Engineering*. John Wiley & Sons, Inc.

Ferreira, L.D.D. and de Moraes, R.V. (2009) 'GPS Satellites Orbits: Resonance', *Mathematical Problems in Engineering*, 2009, p. 12.

Filippov, V., Tatarnicov, D., Ashjaee, J., Astakhov, A. and Sutiagin, I. (1998) *Proceedings of the 11th International Technical Meeting of the Satellite Division of The Institute of Navigation* Nashville, TN.

Fowler, C.M.R. (2004) *The Solid Earth*. University Press Cambridge Books(Accessed: 01 June 2015).

Friederichs, T. (2010) 'Analysis of geodetic time series using Allan variances'.

Fuhrmann, T., Luo, X., Knöpfler, A. and Mayer, M. (2015) 'Generating statistically robust multipath stacking maps using congruent cells', *GPS Solutions*, 19(1), pp. 83-92.

Fund, F., Perosanz, F., Testut, L. and Loyer, S. (2013) 'An Integer Precise Point Positioning technique for sea surface observations using a GPS buoy', *Advances in Space Research*, 51(8), pp. 1311-1322.

Garin, L., F, V.D. and Rousseau, J. (1996) *ION GPS-96*. Kansas City,MO, September 17th-20th.

Garin, L. and Rousseau, J. (1997) 'Enhanced Strobe Correlator Multipath Rejection for Code and Carrier', *ION GPS-97*. Kansas City, MO, September 16-19. pp. 559-568.

Garrido, M.S., Gimenez, E., De Lacy, M.C. and Gil, A.J. (2011) 'Testing precise positioning using RTK and NRTK corrections provided by MAC and VRS approaches in SE Spain', *Journal of Spatial Science*, 56(2), pp. 169-184.

Ge, M., Gendt, G., Dick, G., Zhang, F.P. and Rothacher, M. (2006) 'A New Data Processing Strategy for Huge GNSS Global Networks', *Journal of Geodesy*, 80(4), pp. 199-203.

Ge, M., Gendt, G., Rothacher, M., Shi, C. and Liu, J. (2008) 'Resolution of GPS carrier-phase ambiguities in Precise Point Positioning (PPP) with daily observations', *Journal of Geodesy*, 82(7), pp. 389-399.

Geller, R.J. (1976) 'Scaling relations for earthquake source parameters and magnitudes', *Bull. Seismol. Soc. Am.*, 66, pp. 1501–1523.

Geng, J., Bock, Y., Melgar, D., Crowell, B.W. and Haase, J.S. (2013) 'A new seismogeodetic approach applied to GPS and accelerometer observations of the 2012 Brawley seismic

swarm: Implications for earthquake early warning', *Geochemistry, Geophysics, Geosystems*, 14(7), pp. 2124-2142.

Geng, J., Meng, X., Teferle, F. and Dodson, A. (2010a) 'Performance of Precise Point Positioning with Ambiguity Resolution for 1- to 4-Hour Observation Periods', *Survey Review*, 42(316), pp. 155-165.

Geng, J., Teferle, F.N., Meng, X. and Dodson, A.H. (2010b) 'Kinematic precise point positioning at remote marine platforms', *GPS Solutions*, 14(4), pp. 343-350.

Geng, J., Teferle, F.N., Shi, C., Meng, X., Dodson, A.H. and Liu, J. (2009) 'Ambiguity resolution in precise point positioning with hourly data', *GPS Solutions*, 13(4), pp. 263-270.

Genrich, J.F. and Bock, Y. (1992) 'Rapid resolution of crustal motion at short ranges with the global positioning system', *Journal of Geophysical Research: Solid Earth*, 97(B3), pp. 3261-3269.

Genrich, J.F. and Bock, Y. (2006) 'Instantaneous geodetic positioning with 10–50 Hz GPS measurements: Noise characteristics and implications for monitoring networks', *Journal of Geophysical Research: Solid Earth*, 111(B3).

GLONASS, I. (2008) *Global navigation satellite system GLONASS interface control document* (5.1). Available at: gauss.gge.unb.ca/GLONASS.ICD.pdf.

Görres, B., Campbell, J., Becker, M. and Siemes, M. (2006) 'Absolute calibration of GPS antennas: laboratory results and comparison with field and robot techniques', *GPS Solutions*, 10(2), pp. 136-145.

Griggs, E., Kursinski, E.R. and Akos, D. (2015) 'Short-term GNSS satellite clock stability', *Radio Science*, 50(8), pp. 813-826.

Grinter, T. and Roberts, C. (2013) 'Real Time Precise Point Positioning: Are We There Yet?', *International Global Navigation Satellite Systems Society GNSS Symposium 2013*. Outrigger Gold Coast, Qld, Australia, July 16th-18th.

Groves, P.D. (2013) *Principles of GNSS, Inertial, and Multisensor Integrated Navigation Systems*. London: Artech House.

Hanks, T.C. and Kanamori, H. (1979) 'A moment magnitude scale', *Journal of Geophysical Research: Solid Earth*, 84(B5), pp. 2348-2350.

Hernández-Pajares, M., Aragón-Ángel, À., Defraigne, P., Bergeot, N., Prieto-Cerdeira, R. and García-Rigo, A. (2014) 'Distribution and mitigation of higher-order ionospheric effects on precise GNSS processing', *Journal of Geophysical Research: Solid Earth*, 119(4), pp. 3823-3837.

Hernández-Pajares, M., Juan, J.M., Sanz, J., García-Rodríguez, A. and Colombo, O.L. (2004) *ION-GNSS meeting*. Portland, Oregon

Hernandez-Pajares, M., Juan, J.M., Sanz, J., Ramos-Bosch, P., Rovira-Garcıa, A., Salazar, D., Ventura-Traveset, J., López-Echazarreta, C. and Hein, G. (2010) *Proc. of the 5th ESA*

Workshop on Satellite Navigation Technologies (NAVITEC'2010), ESTEC, Noordwijk, The Netherlands.

Hesselbarth, A. and Wanninger, L. (2008) *Proceedings of the ION GNSS 2008*. Savannah, GA, USA.

Hirshorn, B., Weinstein, S. and Tsuboi, S. (2013) 'On the application of Mwp in the near field and the March 11, 2011 Tohoku earthquake', *Pure and Applied Geophysics*, 170(6-8), pp. 975-991.

Hofmann-Wellenhof, B., Lichtenegger, H. and Wasle, E. (2008) *GNSS – Global Navigation Satellite Systems: GPS, GLONASS, Galileo, and More*. Springer.

Hopfield, H.S. (1969) 'Two-quartic tropospheric refractivity profile for correcting satellite data', *Journal of Geophysical Research*, 74(18), pp. 4487-4499.

Hung, H.-K. and Rau, R.-J. (2013) 'Surface waves of the 2011 Tohoku earthquake: Observations of Taiwan's dense high-rate GPS network', *Journal of Geophysical Research: Solid Earth*, 118(1), pp. 332-345.

Hwang, C., Tseng, T.-P., Lin, T., Švehla, D. and Schreiner, B. (2009) 'Precise orbit determination for the FORMOSAT-3/COSMIC satellite mission using GPS', *Journal of Geodesy*, 83(5), pp. 477-489.

IGS (2015) *IGS Products*. Available at: http://www.igs.org/products (Accessed: 18/07/2016).

Jean, Y. and Dach, R. (2013) 'IGS 2013 Technical Report', [Online]. Available at: http://kb.igs.org/hc/en-us/articles/202459446-Technical-Report-2013.

Jing-nan, L. and Mao-rong, G. (2003) 'PANDA software and its preliminary result of positioning and orbit determination', *Wuhan University Journal of Natural Sciences*, 8(2), p. 603.

Kamatham, Y., Sarma, A.D., Kumar, A. and Satyanarayana, K. (2012) 'Spectral Analysis and Mitigation of GPS Multipath Error Using Digital Filtering for Static Applications', *IETE Journal of Research*, 59(2), p. 10.

Kanamori, H. (1977) 'The energy release in great earthquakes', *Journal of Geophysical Research*, 82(20), pp. 2981-2987.

Kaplan, E.D. and Hegarty, C.J. (2006) *Understanding GPS: Principles and Applications*. Norwood, MA: Artech House, INC.

Klobuchar, J.A. (1987) 'Ionospheric Time-Delay Algorithm for Single-Frequency GPS Users', *Aerospace and Electronic Systems, IEEE Transactions on*, AES-23(3), pp. 325-331.

Knöpfler, A., Masson, F., Mayer, M., Ulrich, P. and Heck, B. (2010) *FIG congress*.

Kouba, J. (2009) *A guide to using International GNSS Service (IGS) Products*. Available at: http://igscb.jpl.nasa.gov/components/usage.html

Kouba, J. and Héroux, P. (2001a) 'GPS precise point positioning using IGS orbit products', *Physics and Chemistry of the Earth, Part A: Solid Earth and Geodesy*, 26(6–8), pp. 573-578.

Kouba, J. and Héroux, P. (2001b) 'Precise Point Positioning Using IGS Orbit and Clock Products', *GPS Solutions*, 5(2), pp. 12-28.

Larson, K.M., Bilich, A. and Axelrad, P. (2007) 'Improving the precision of high-rate GPS', *Journal of Geophysical Research: Solid Earth*, 112(B5), p. B05422.

Lau, L. (2012) 'Comparison of measurement and position domain multipath filtering techniques with the repeatable GPS orbits for static antennas', *Survey Review*, 44(324), pp. 9-16.

Lau, L. and Cross, P. (2006) *IONS GNSS 19th International TechnicalMeeting of the Satellite Division*. Fort Worth, TX, 26th-29th September.

Laurichesse, D., Mercier, F., Berthias, J.-P., Broca, P. and Cerri, L. (2009) 'Integer Ambiguity Resolution on Undifferenced GPS Phase Measurements and Its Application to PPP and Satellite Precise Orbit Determination', *Navigation*, 56(2), pp. 135-149.

Leandro, R.F., Santos, M.C. and Langley, R.B. (2007) *Proc. ION GNSS*.

Leick, A. (2004) *GPS Satellite Surveying*. New York: John Wiley & Sons Inc.

Leys, C., Ley, C., Klein, O., Bernard, P. and Licata, L. (2013) 'Detecting outliers: Do not use standard deviation around the mean, use absolute deviation around the median', *Journal of Experimental Social Psychology*, 49(4), pp. 764-766.

Li, P. and Zhang, X. (2014) 'Integrating GPS and GLONASS to accelerate convergence and initialization times of precise point positioning', *GPS Solutions*, 18(3), pp. 461-471.

Li, X., Ge, M., Lu, C., Zhang, Y., Wang, R., Wickert, J. and Schuh, H. (2014) 'High-Rate GPS Seismology Using Real-Time Precise Point Positioning With Ambiguity Resolution', *Geoscience and Remote Sensing, IEEE Transactions on*, 52(10), pp. 6165-6180.

Liu, H., Shah, S. and Jiang, W. (2004) 'On-line outlier detection and data cleaning', *Computers & Chemical Engineering*, 28(9), pp. 1635-1647.

Luo, X., Mayer, M. and Heck, B. (2009) 'Improving the Stochastic Model of GNSS Observations by Means of SNR-based Weighting', in Sideris, M. (ed.) *Observing our Changing Earth*. Springer Berlin Heidelberg, pp. 725-734.

Lyard, F., Lefevre, F., Letellier, T. and Francis, O. (2006) 'Modelling the global ocean tides: modern insights from FES2004', *Ocean Dynamics*, 56(5), pp. 394-415.

McCloskey, J., Antonioli, A., Piatanesi, A., Sieh, K., Steacy, S., Nalbant, S.S., Cocco, M., Giunchi, C., Huang, J.D. and Dunlop, P. (2007) 'Near-field propagation of tsunamis from megathrust earthquakes', *Geophys. Res. Lett.*, 34(14).

Melgar, D., Bock, Y. and Crowell, B.W. (2012) 'Real-time centroid moment tensor determination for large earthquakes from local and regional displacement records', *Geophysical Journal International*, 188(2), pp. 703-718.

Melgar, D., Crowell, B.W., Bock, Y. and Haase, J.S. (2013) 'Rapid modeling of the 2011 Mw 9.0 Tohoku-oki earthquake with seismogeodesy', *Geophysical Research Letters*, 40(12), pp. 2963-2968.

Miller, J. (1991) 'Short report: Reaction time analysis with outlier exclusion: Bias varies with sample size', *The Quarterly Journal of Experimental Psychology Section A*, 43(4), pp. 907-912.

Mimura, N., Yasuhara, K., Kawagoe, S., Yokoki, H. and Kazama, S. (2011) 'Damage from the Great East Japan Earthquake and Tsunami - A quick report', *Mitigation and Adaptation Strategies for Global Change*, 16(7), pp. 803-818.

Nikolaidis, R.M., Bock, Y., de Jonge, P.J., Shearer, P., Agnew, D.C. and Van Domselaar, M. (2001) 'Seismic wave observations with the Global Positioning System', *J. Geophys. Res.*, 106(B10), pp. 21897-21916.

Ning, T., Elgered, G. and Johansson, J.M. (2011) 'The impact of microwave absorber and radome geometries on GNSS measurements of station coordinates and atmospheric water vapour', *Advances in Space Research*, 47(2), pp. 186-196.

Niu, X., Chen, Q., Zhang, Q., Zhang, H., Niu, J., Chen, K., Shi, C. and Liu, J. (2014) 'Using Allan variance to analyze the error characteristics of GNSS positioning', *GPS solutions*, 18(2), pp. 231-242.

Ogaja, C. and Satirapod, C. (2007) 'Analysis of high-frequency multipath in 1-Hz GPS kinematic solutions', *GPS Solutions*, 11(4), pp. 269-280.

Okada, Y. (1985) 'Surface deformation due to shear and tensile faults in a half-space', *Bulletin of the Seismological Society of America*, 75(4), pp. 1135-1154.

Pandey, D., Dwivedia, R., Dikshit, O. and Singh, A.K. (2016) 'GPS AND GLONASS COMBINED STATIC PRECISE POINT POSITIONING (PPP)', *International Archives of the Photogrammetry, Remote Sensing & Spatial Information Sciences*, 41.

Psimoulis, P., Houlié, N., Meindl, M. and Rothacher, M. (2015) 'Consistency of GPS and strong-motion records: case study of Mw9. 0 Tohoku-Oki 2011 earthquake', *Smart Structures and Systems*, 16(2), p. 19.

Ragheb, A.E. (2007) *Filtered and semi-continuous single epoch GPS for deformation monitoring*. PhD thesis. Newcastle University.

Ragheb, A.E., Clarke, P.J. and Edwards, S.J. (2007a) *Proceedings of the Institute of Navigation, National Technical Meeting*. San Diego, CA, January 2007.

Ragheb, A.E., Clarke, P.J. and Edwards, S.J. (2007b) 'GPS sidereal filtering: coordinate- and carrier-phase-level strategies', *Journal of Geodesy*, 81(5), pp. 325-335.

Ragheb, A.E., Edwards, S.J. and Clarke, P.J. (2010) 'Using Filtered and Semicontinuous High Rate GPS for Monitoring Deformations', *Journal of Surveying Engineering*, 136(2), pp. 72-79.

Ray, J., Cannon, M. and Fenton, P. (1998) 'Mitigation of Static Carrier Phase Multipath Effects Using Multiple Closely-Spaced Antennas', *11th International Technical Meeting of the*

Satellite Division of the Institute of Navigation, ION - GPS98. Nashville, Tennessee, September 15-18. pp. 1025-1034.

Reuveni, Y., Kedar, S., Owen, S.E., Moore, A.W. and Webb, F.H. (2012) 'Improving sub-daily strain estimates using GPS measurements', *Geophysical Research Letters*, 39(11), pp. 1-7.

Riley, W.J. (2008) *Handbook of Frequency Stability Analysis*. Boulder, CO.

Roger, J. and Gunnell, Y. (2012) 'Vulnerability of the Dover Strait to coseismic tsunami hazards: insights from numerical modelling', *Geophysical Journal International*, 188(2), pp. 680-686.

Saastamoinen, J. (1972) 'Atmospheric correction for the troposphere and stratosphere in radio ranging satellites', *The use of artificial satellites for geodesy*, pp. 247-251.

Sanchez, D.M., Yokoyama, T. and Prado, A.F.B.d.A. (2015) 'Study of some strategies for disposal of the GNSS satellites', *Mathematical Problems in Engineering*, 2015.

Sardón, E. and Zarraoa, N. (1997) 'Estimation of total electron content using GPS data: How stable are the differential satellite and receiver instrumental biases?', *Radio Science*, 32(5), pp. 1899-1910.

Satirapod, C., Rizos, C. and Wang, J. (2001) 'GPS SINGLE POINT POSITIONING WITH SA OFF: HOW ACCURATE CAN WE GET?', *Survey Review*, 36(282), pp. 255-262.

Seepersad, G. and Bisnath, S. (2015) *Proceedings of the 28th International Technical Meeting of The Satellite Division of the Institute of Navigation (ION GNSS+ 2015)*. Tampa, Florida.

Shi, C., Li, M., Lou, Y. and Zou, R. (2008a) 'Near real-time orbit determination of navigation satellite using regional tracking network', *Geo Inf Sci Wuhan Univ*, 33(7), pp. 697-700.

Shi, C., Lou, Y., Zhang, H., Zhao, Q., Geng, J., Wang, R., Fang, R. and Liu, J. (2010) 'Seismic deformation of the Mw 8.0 Wenchuan earthquake from high-rate GPS observations', *Advances in Space Research*, 46(2), pp. 228-235.

Shi, C., Zhao, Q., Geng, J., Lou, Y., Ge, M. and Liu, J. (2008b). Available at: http://dx.doi.org/10.1117/12.816261.

Simons, M., Minson, S.E., Sladen, A., Ortega, F., Jiang, J., Owen, S.E., Meng, L., Ampuero, J.-P., Wei, S., Chu, R., Helmberger, D.V., Kanamori, H., Hetland, E., Moore, A.W. and Webb, F.H. (2011) 'The 2011 Magnitude 9.0 Tohoku-Oki Earthquake: Mosaicking the Megathrust from Seconds to Centuries', *Science*, 332(6036), pp. 1421-1425.

Smalley, R. (2009) 'High-rate GPS: How High Do We Need to Go?', *Seismological Research Letters*, 80(6), pp. 1054-1061.

Sobolev, S.V., Babeyko, A.Y., Wang, R., Hoechner, A., Galas, R., Rothacher, M., Sein, D.V., Schröter, J., Lauterjung, J. and Subarya, C. (2007) 'Tsunami early warning using GPS-Shield arrays', *J. Geophys. Res.*, 112(B8).

Soycan, M. and Ata, E. (2011) 'Precise point positioning versus traditional solution for GNSS networks', *Scientific Research and Essays*, 6(4), pp. 799-808.

Springer, T. and Dach, R. (2010) 'GPS, GLONASS, and More', *GPS World*, 21(6), pp. 48-58.

Stiros, S.C. (2008) 'Errors in velocities and displacements deduced from accelerographs: An approach based on the theory of error propagation', *Soil Dynamics and Earthquake Engineering*, 28(5), pp. 415-420.

Takahashi, N., Ishihara, Y., Ochi, H., Fukuda, T., Tahara, J.i., Maeda, Y., Kido, M., Ohta, Y., Mutoh, K., Hashimoto, G., Kogure, S. and Kaneda, Y. (2014) 'New buoy observation system for tsunami and crustal deformation', *Marine Geophysical Research*, 35(3), pp. 243-253.

Tegedor, J., de Jong, K., Liu, X., Vigen, E. and Øvstedal, O. (2015) 'Real-Time Precise Point Positioning Using BeiDou'.

Thong, Y.K., Woolfson, M.S., Crowe, J.A., Hayes-Gill, B.R. and Challis, R.E. (2002) 'Dependence of inertial measurements of distance on accelerometer noise', *Measurement Science and Technology*, 13(8), p. 1163.

Thun, J., Lokmer, I. and Bean, C.J. (2015) 'New observations of displacement steps associated with volcano seismic long-period events, constrained by step table experiments', *Geophysical Research Letters*, 42(10), pp. 3855-3862.

Tobías, G., Calle, J.D., Navarro, P., Rodríguez, I. and Rodríguez, D. (2014) *Proceedings of the 27th International Technical Meeting of The Satellite Division of the Institute of Navigation (ION GNSS+ 2014)*.

Tranquilla, J.M. and Al-Rizzo, H.M. (1994) 'Range errors in global positioning system during ice cloud and snowfall periods', *Antennas and Propagation, IEEE Transactions on*, 42(2), pp. 157-165.

USGS (2016) *Earthquake Statistics*. Available at: http://earthquake.usgs.gov/earthquakes/browse/stats.php (Accessed: 18/07/2016).

Van Dierendonck, A.J., Fenton, P.A.T. and Ford, T.O.M. (1992) 'Theory and Performance of Narrow Correlator Spacing in a GPS Receiver', *Navigation*, 39(3), pp. 265-283.

Van Nee, R.D.J., Siereveld, J., Fenton, P.C. and Townsend, B.R. (1994) *Position Location and Navigation Symposium, 1994., IEEE*. 11-15 Apr 1994.

Vasudha, M.P. and Raju, G. (2017) 'Comparative evaluation of IRNSS performance with special reference to positional accuracy', *Gyroscopy and Navigation*, 8(2), pp. 136-149.

Wang, G.-Q., Boore, D.M., Tang, G. and Zhou, X. (2007) 'Comparisons of Ground Motions from Colocated and Closely Spaced One-Sample-per-Second Global Positioning System and Accelerograph Recordings of the 2003 M 6.5 San Simeon, California, Earthquake in the Parkfield Region', *Bulletin of the Seismological Society of America*, 97(1B), pp. 76-90.

Wanninger, L. (2012) 'Carrier-phase inter-frequency biases of GLONASS receivers', *Journal of Geodesy*, 86(2), pp. 139-148.

Wanninger, L. and May, M. (2001) 'Carrier-Phase Multipath Calibration of GPS Reference Stations', *Navigation*, 48(2), pp. 112-124.

Welch, G. and Bishop, G. (1995) 'An introduction to the Kalman filter' *TR 95-041*. University of North Carolina at Chapel Hill, Chapel Hill, NC 27599-3175, p. 16.

Whitmore, P.M., Tsuboi, S., Hirshorn, B. and Sokolowski, T.J. (2002) 'Magnitude-dependent correction for Mwp', *Science of Tsunami Hazards*.

Wielandt, E. (2012) 'Seismic Sensors and their Calibration', in Bormann, P. (ed.) *New Manual of Seismological Observatory Practice 2 (NMSOP-2)*. Potsdam : Deutsches GeoForschungsZentrum GFZ, pp. 1-51.

Wieser, A. and Brunner, F.K. (2002) *International Association of Geodesy Symposia, 125, Vistas for Geodesy in the New Millennium*. Springer Verlag.

Wright, T.J., Houlié, N., Hildyard, M. and Iwabuchi, T. (2012) 'Real-time, reliable magnitudes for large earthquakes from 1 Hz GPS precise point positioning: The 2011 Tohoku-Oki (Japan) earthquake', *Geophysical Research Letters*, 39(12).

Wu, J.T., Wu, S.C., Hajj, G.A., Bertiger, W.I. and Lichten, S.M. (1993) 'Effects of antenna orientation on GPS carrier phase', *Manuscripta Geodaetica*, 18, pp. 91-98.

Wübbena, G., Schmitz, M. and Matzke, N. (2010) *International Symposium on GNSS space-based and ground-based Augmentation Systems and Aplications*. Brussels, Belgium, 29th-30th November.

Yamada, H., Takasu, T., Kubo, N. and Yasuda, A. (2010) *23rd International Technical Meeting of The Satellite Division of the Institute of Navigation*. Portland,Oregon, 21-24 September.

Ye, S., Chen, D., Liu, Y., Jiang, P., Tang, W. and Xia, P. (2015) 'Carrier phase multipath mitigation for BeiDou navigation satellite system', *GPS Solutions*, 19(4), pp. 545-557.

Yi, T.H., Li, H.N. and Gu, M. (2011) 'Characterization and extraction of global positioning system multipath signals using an improved particle-filtering algorithm', *Measurement Science & Technology*, 22(7).

Yigit, C.o. (2014) 'Experimental assessment of post-processed kinematic Precise Point Positioning method for structural health monitoring', *Geomatics, Natural Hazards and Risk*, pp. 1-24.

Zhang, X. and Andersen, O.B. (2006) 'Surface Ice Flow Velocity and Tide Retrieval of the Amery Ice Shelf using Precise Point Positioning', *Journal of Geodesy*, 80(4), pp. 171-176.

Zhang, X., Liu, J. and Forsberg, R. (2008) 'PPP for Long-Range Airborne GPS Kinematic Positioning', in Xu, P., Liu, J. and Dermanis, A. (eds.) *VI Hotine-Marussi Symposium on Theoretical and Computational Geodesy*. Springer Berlin Heidelberg, pp. 211-215.

Zheng, D.W., Zhong, P., Ding, X.L. and Chen, W. (2005) 'Filtering GPS time-series using a Vondrak filter and cross-validation', *Journal of Geodesy*, 79(6-7), pp. 363-369.

Zhong, P., Ding, X., Yuan, L., Xu, Y., Kwok, K. and Chen, Y. (2010) 'Sidereal filtering based on single differences for mitigating GPS multipath effects on short baselines', *Journal of Geodesy*, 84(2), pp. 145-158.

Zumberge, J.F., Heflin, M.B., Jefferson, D.C., Watkins, M.M. and Webb, F.H. (1997) 'Precise point positioning for the efficient and robust analysis of GPS data from large networks', *Journal of Geophysical Research-Solid Earth*, 102(B3), pp. 5005-5017.

Appendix A

OS Net sites' local environment

HUNG-Hungerford

HUNG antenna installation which is approximately 5m above ground level.

KILN-Killin

KILN antenna installation which is approximately 2m above ground level.

MACY-Machynlleth

MACY antenna installation which is approximately 12m above ground level.

OBAN-Oban

OBAN antenna installation which is approximately 15m above ground level.

PADT- Padstow

PADT antenna installation which is approximately 5m above ground level.

All images are from: http://www.bigf.ac.uk/files/network_maps/script_all_pcsn_30s.html

Appendix B

Power spectral density plots of OS Net sites, GPS-only filter

KILN

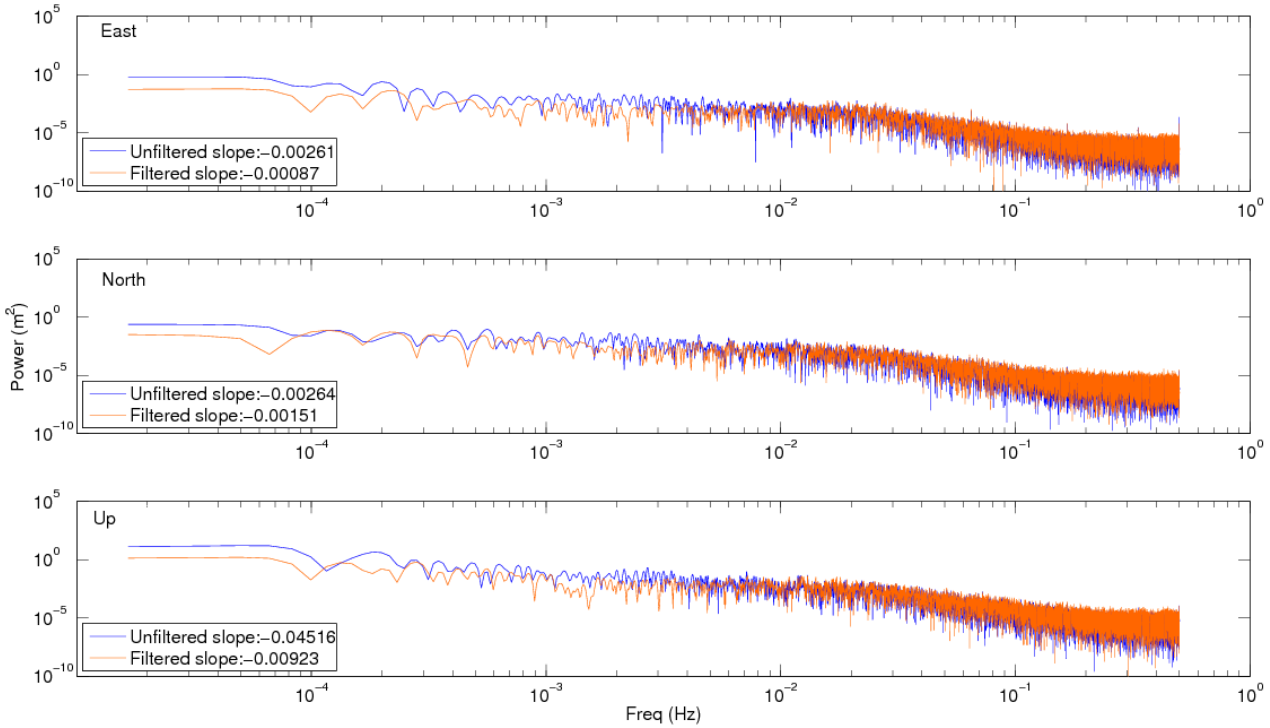

Power spectral density comparison of computed GPS coordinates at site KILN of unfiltered GPS PPP processing, in dark blue, and GPS-only sidereally filtered PPP processing, in orange, 2014, days 321 to 327.

MACY

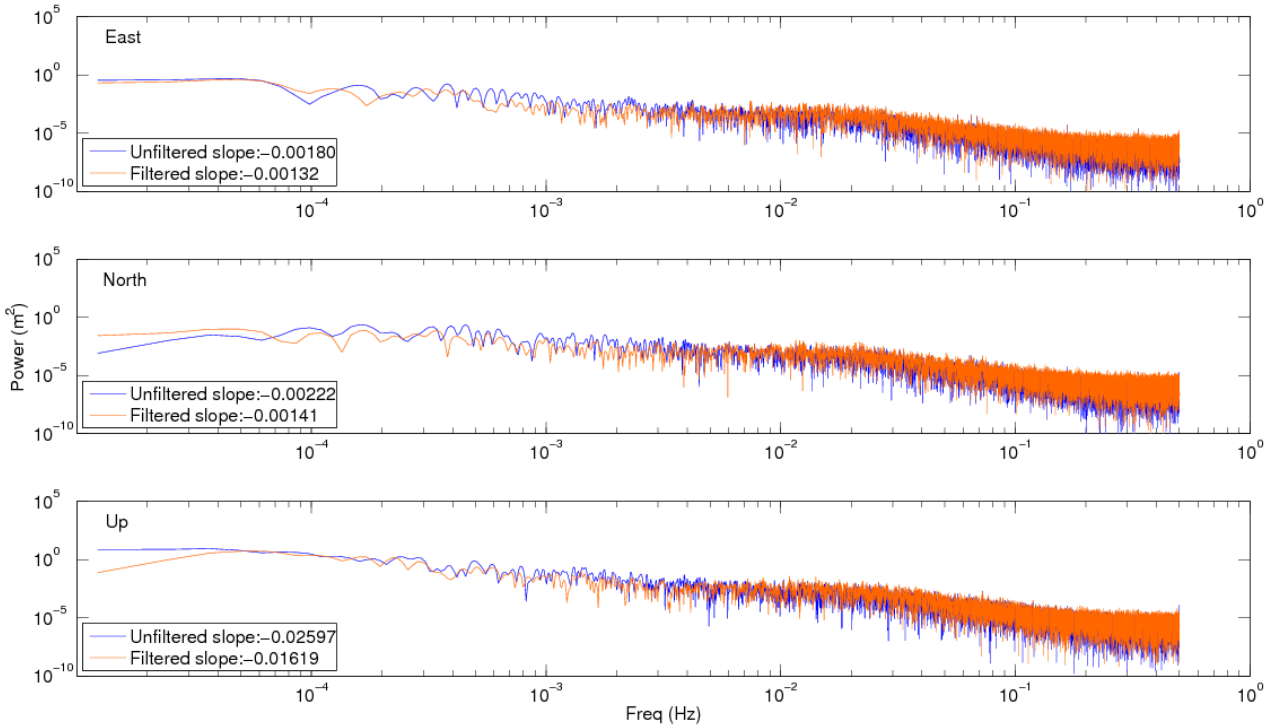

Power spectral density comparison of computed GPS coordinates at site MACY of unfiltered GPS PPP processing, in dark blue, and GPS-only sidereally filtered PPP processing, in orange, 2014, days 321 to 327.

OBAN

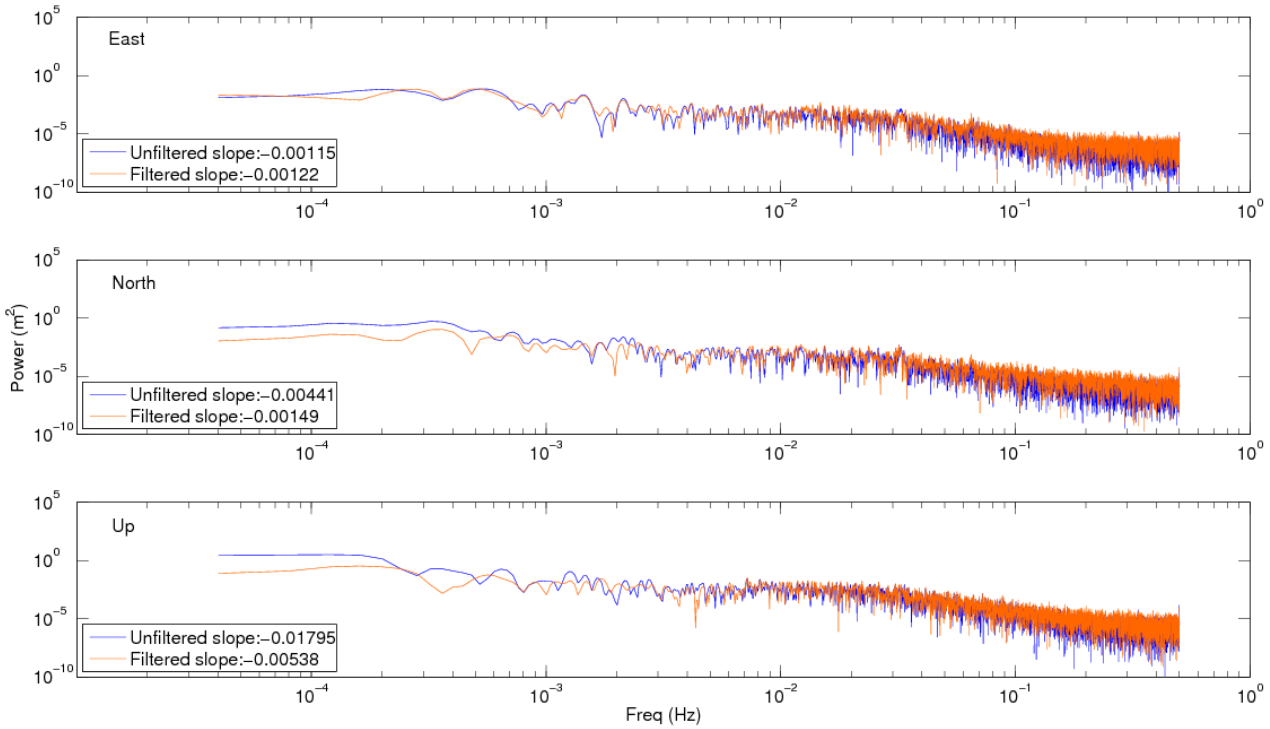

Power spectral density comparison of computed GPS coordinates at site OBAN of unfiltered GPS PPP processing, in dark blue, and GPS-only sidereally filtered PPP processing, in orange, 2014, days 321 to 327.

PADT

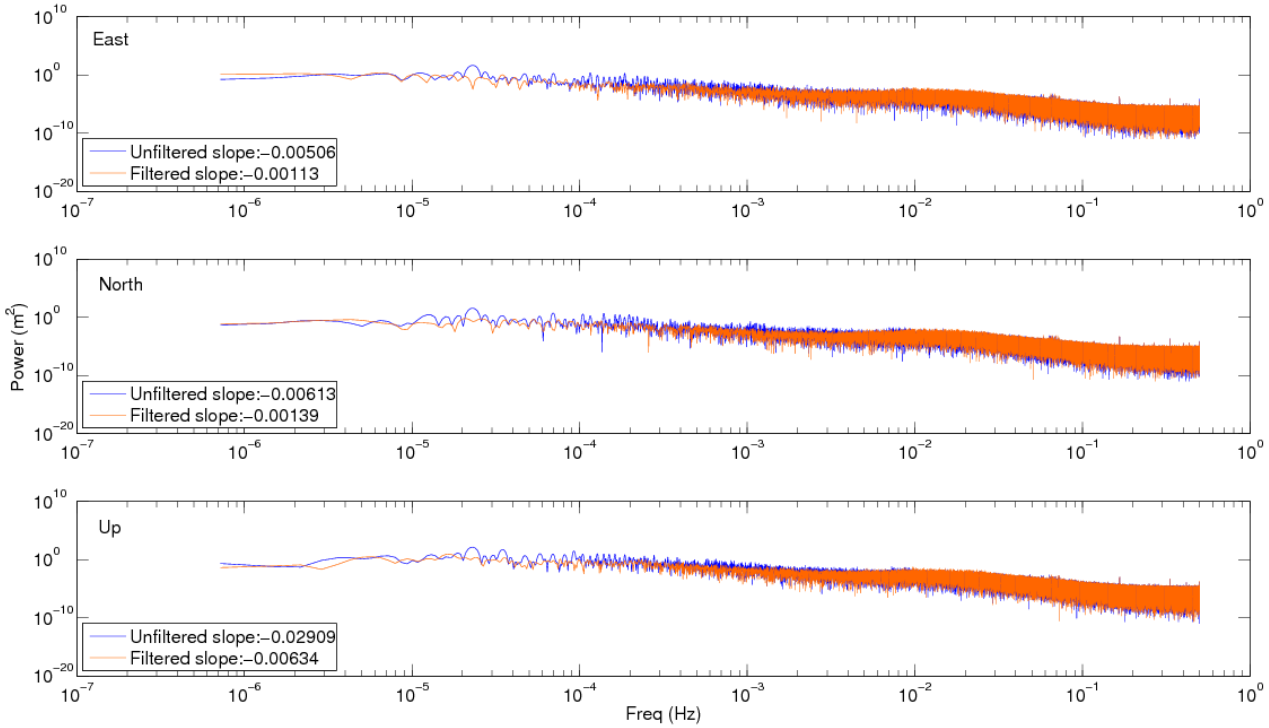

Power spectral density comparison of computed GPS coordinates at site PADT of unfiltered GPS PPP processing, in dark blue, and GPS-only sidereally filtered PPP processing, in orange, 2014, days 321 to 327.

Appendix C

Power spectral density plots of OS Net sites, GLONASS-only filter

KILN

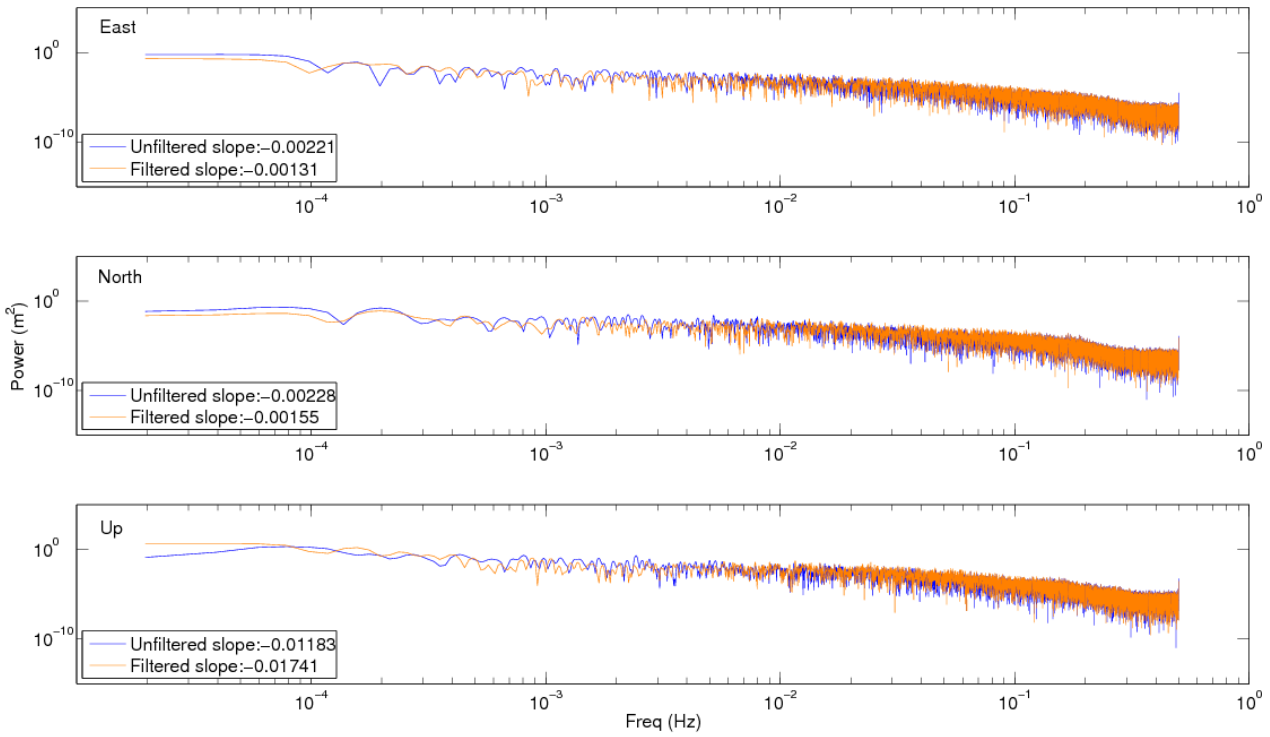

.Power spectral density comparison of computed GLONASS coordinates at site KILN of unfiltered GLONASS PPP processing, in dark blue, and GLONASS-only sidereally filtered PPP processing, in orange, 2014, days 321 to 327.

MACY

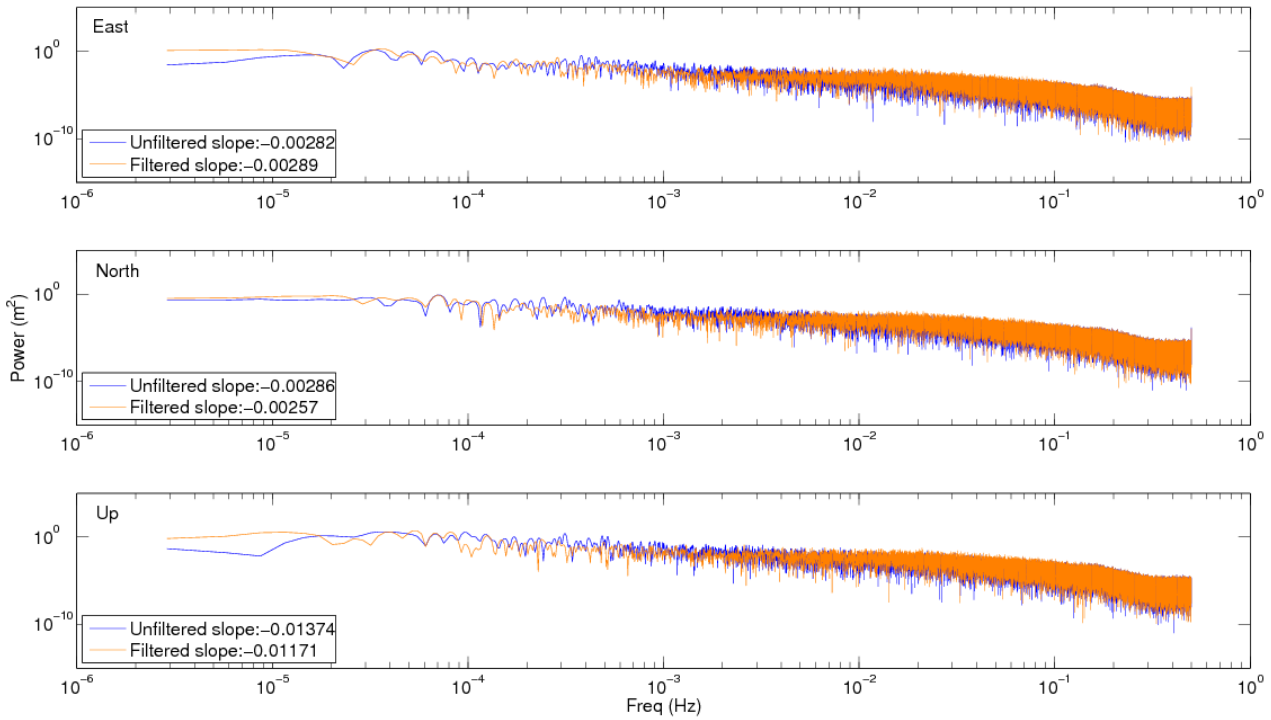

Power spectral density comparison of computed GLONASS coordinates at site MACY of unfiltered GLONASS PPP processing, in dark blue, and GLONASS-only sidereally filtered PPP processing, in orange, 2014, days 321 to 327.

OBAN

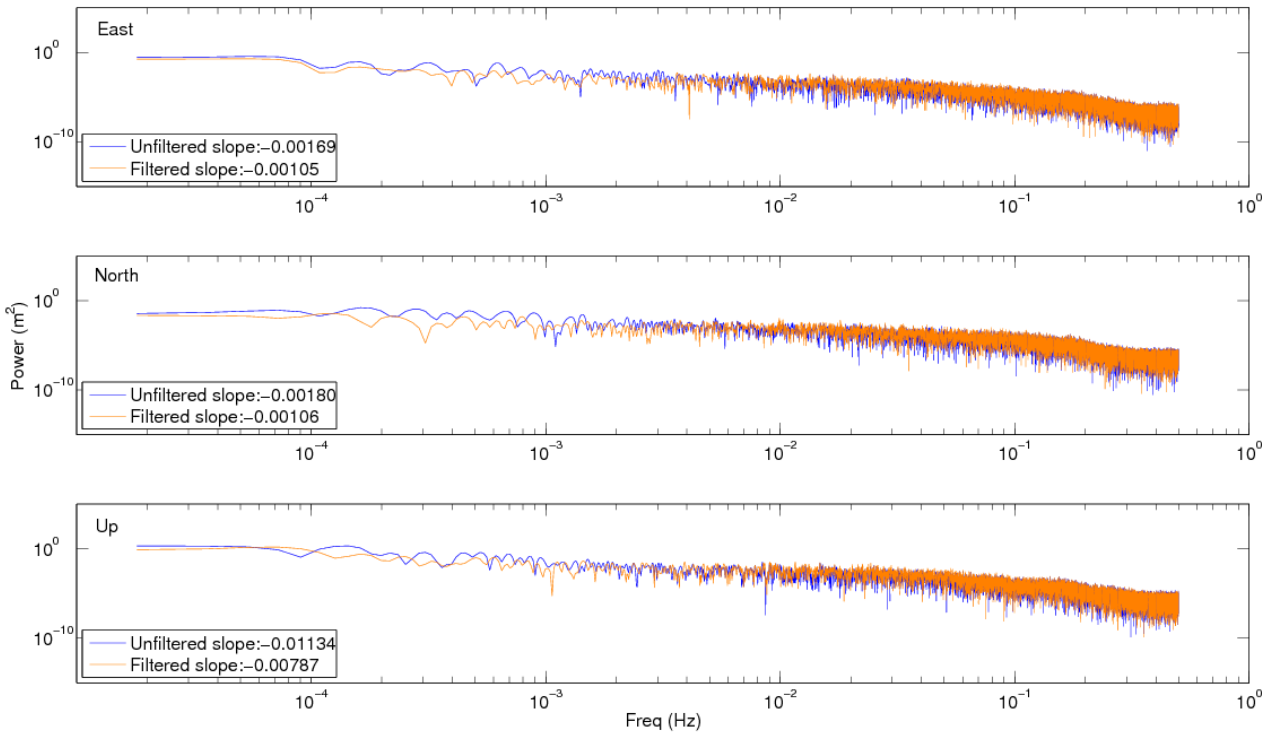

Power spectral density comparison of computed GLONASS coordinates at site OBAN of unfiltered GLONASS PPP processing, in dark blue, and GLONASS-only sidereally filtered PPP processing, in orange, 2014, days 321 to 327.

PADT

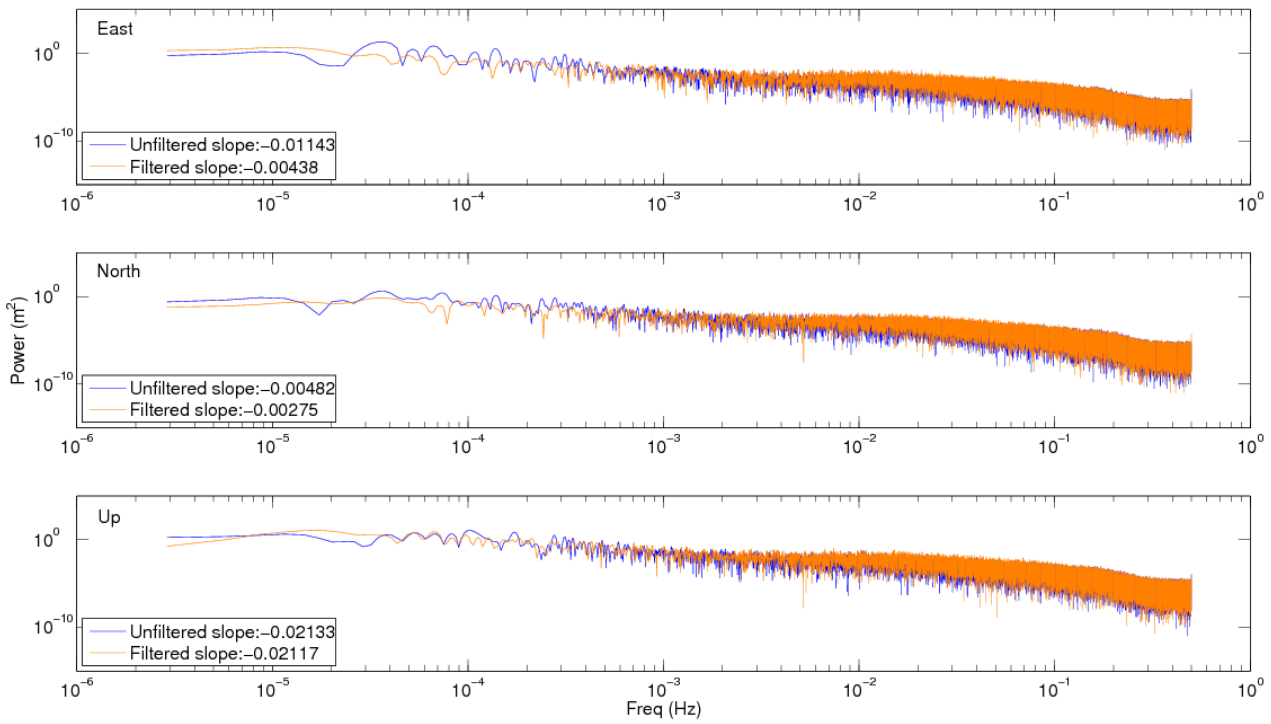

Power spectral density comparison of computed GLONASS coordinates at site PADT of unfiltered GLONASS PPP processing, in dark blue, and GLONASS-only sidereally filtered PPP processing, in orange, 2014, days 321 to 327.

Appendix D

Power spectral density plots of OS Net sites, GR filter

KILN

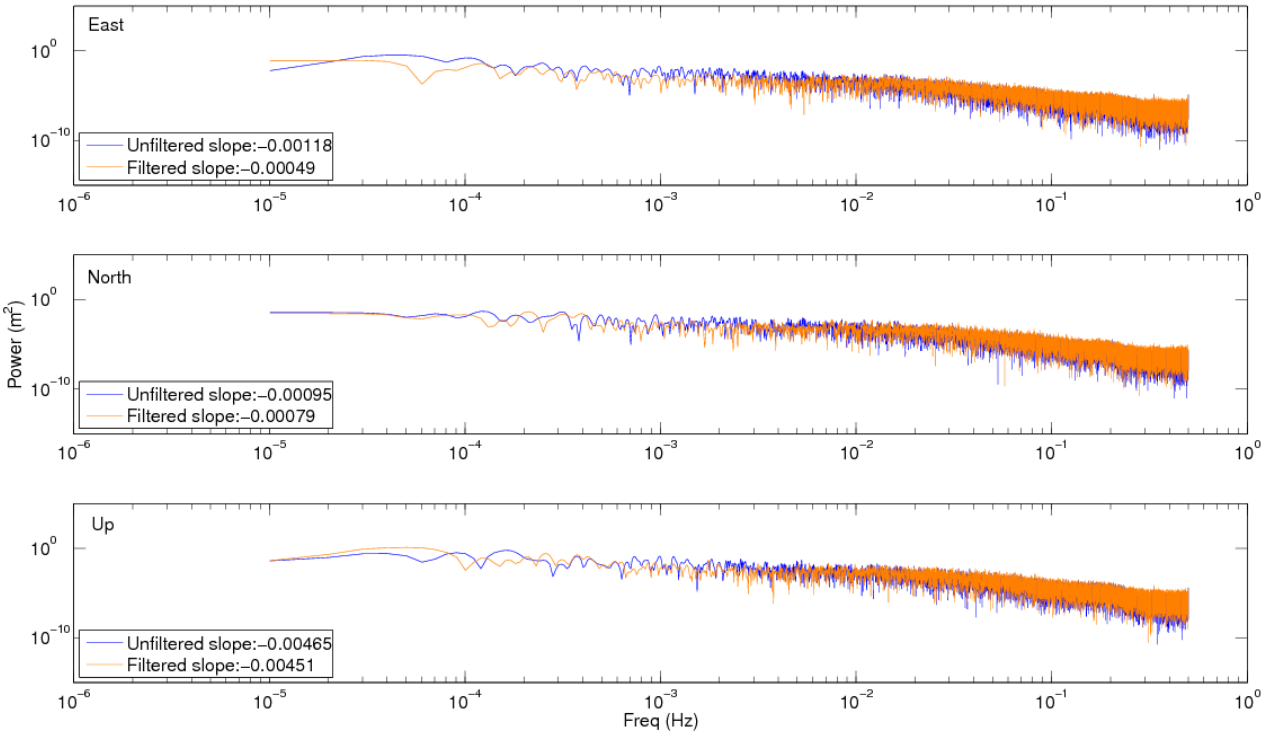

Power spectral density comparison of computed GR coordinates at site KILN of unfiltered GR PPP processing, in dark blue, and GR sidereally filtered PPP processing, in orange, 2014, days 321 to 327.

MACY

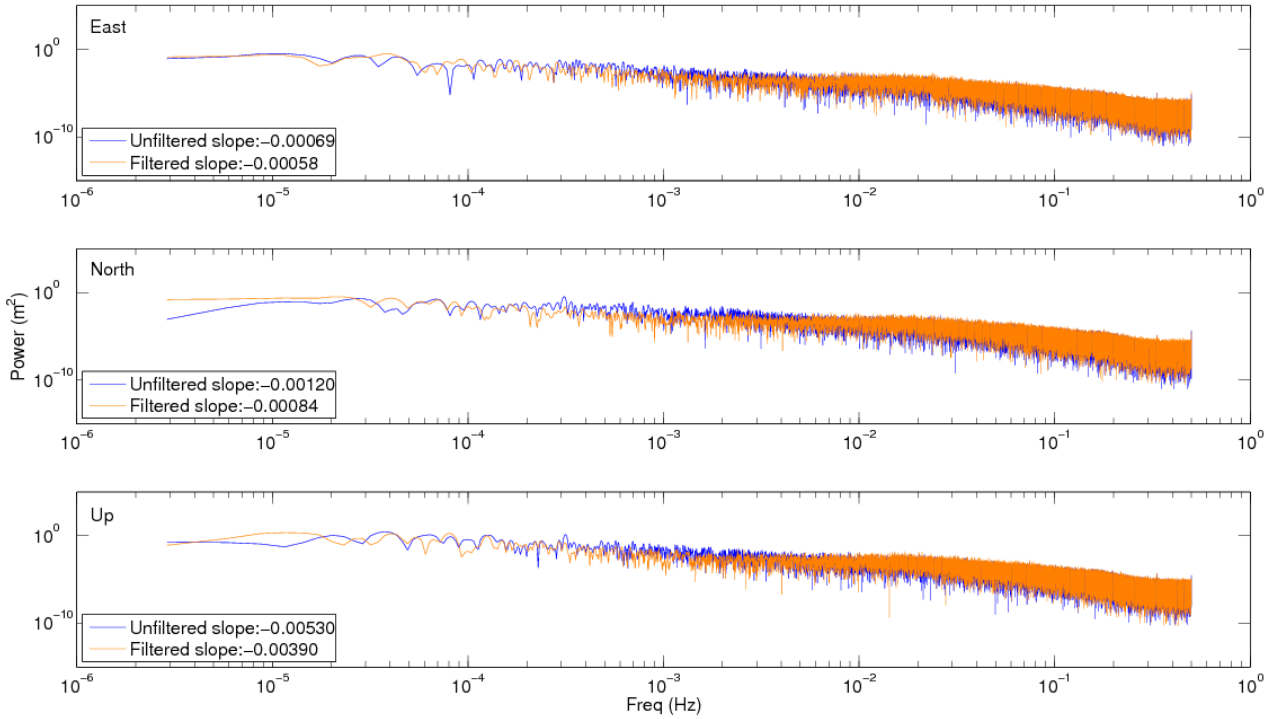

Power spectral density comparison of computed GR coordinates at site MACY of unfiltered GR PPP processing, in dark blue, and GR sidereally filtered PPP processing, in orange, 2014, days 321 to 327.

OBAN

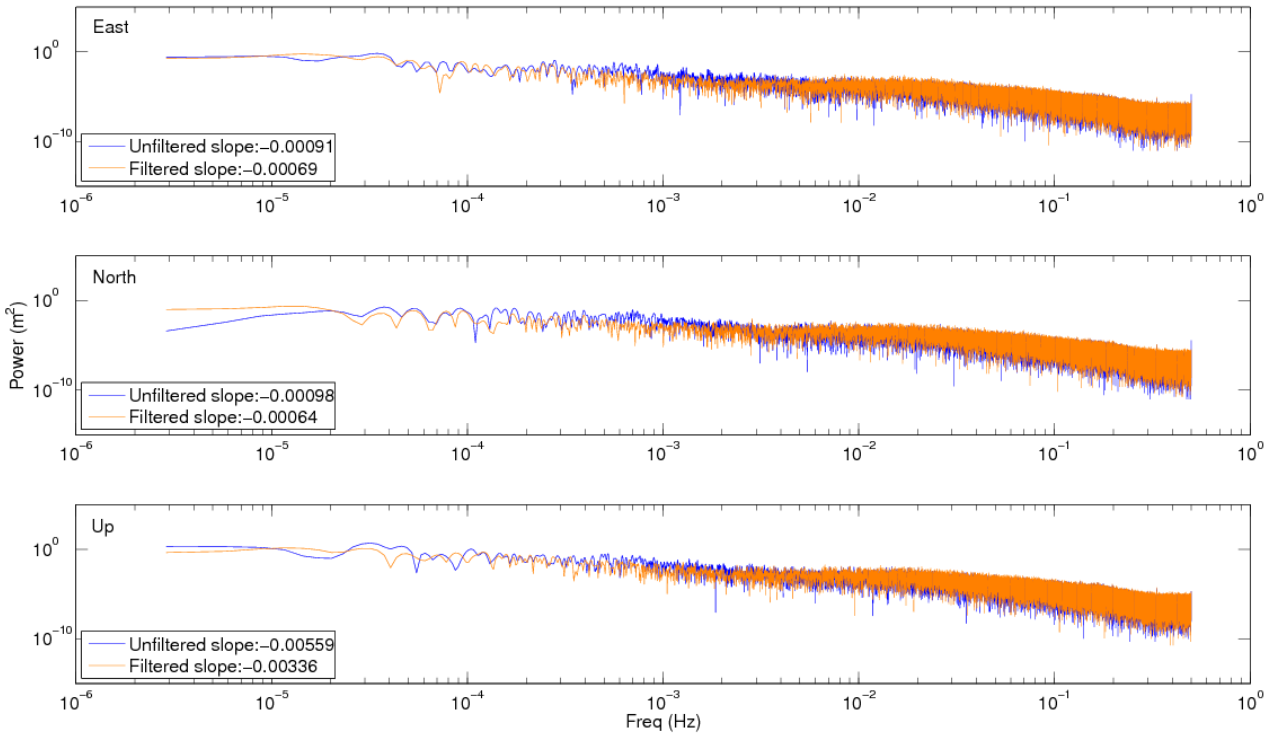

Power spectral density comparison of computed GR coordinates at site OBAN of unfiltered GR PPP processing, in dark blue, and GR sidereally filtered PPP processing, in orange, 2014, days 321 to 327.

PADT

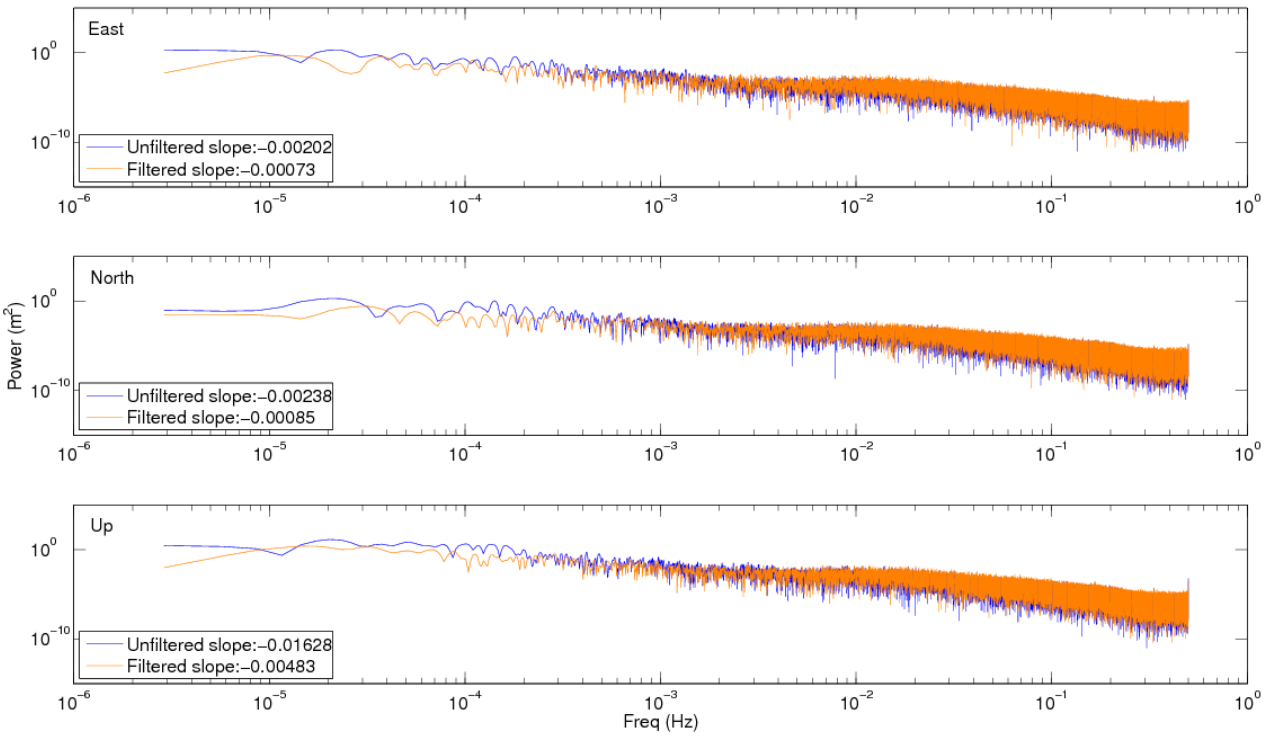

Power spectral density comparison of computed GR coordinates at site PADT of unfiltered GR PPP processing, in dark blue, and GR sidereally filtered PPP processing, in orange, 2014, days 321 to 327.